# Chiral interactions for nuclear reactions and heavy nuclei

**Chirale Wechselwirkungen für Kernreaktionen und schwere Kerne**
Zur Erlangung des Grades eines Doktors der Naturwissenschaften (Dr. rer. nat.)
genehmigte Dissertation von M.Sc. Victoria Durant Sanjinés-Uriarte aus Peru
Tag der Einreichung: 12.11.2018, Tag der Prüfung: 03.12.2018
Darmstadt — D 17

1. Gutachten: Prof. Ph.D. Achim Schwenk
2. Gutachten: Apl. Prof. Dr. Ir. Pierre Capel

TECHNISCHE
UNIVERSITÄT
DARMSTADT

Fachbereich Physik
Institut für Kernphysik

Chiral interactions for nuclear reactions and heavy nuclei
Chirale Wechselwirkungen für Kernreaktionen und schwere Kerne

Genehmigte Dissertation von M.Sc. Victoria Durant Sanjinés-Uriarte aus Peru

1. Gutachten: Prof. Ph.D. Achim Schwenk
2. Gutachten: Apl. Prof. Dr. Ir. Pierre Capel

Tag der Einreichung: 12.11.2018
Tag der Prüfung: 03.12.2018

Darmstadt — D 17

Bitte zitieren Sie dieses Dokument als:
URN: urn:nbn:de:tuda-tuprints-85197
URL: http://tuprints.ulb.tu-darmstadt.de/8519

*A mi madre, por su apoyo incondicional.*
*Y por servirme de inspiración siempre.*

# Abstract

In this Thesis, we study nuclear reactions and interactions for heavy nuclei based on chiral effective field theory interactions. Thus, long-range nucleon interactions are described through pion exchanges, while the unresolved short-distance physics is encapsulated into low-energy constants that are typically fitted to few-body data. As a result of the systematic expansion of chiral effective field theory, the inclusion of many-body forces enters naturally at higher orders. At the same time, chiral effective field theory also enables order-by-order improvable calculations, as well as estimates of theoretical uncertainties.

The determination of nucleus-nucleus potentials is important not only to describe the nuclear reaction mechanism, but also to extract nuclear-structure information and for modeling nuclear reactions for astrophysics. We present the first determination of double-folding potentials based on chiral effective field theory at leading, next-to-leading, and next-to-next-to-leading order. To this end, we construct new soft local chiral effective field theory interactions. We benchmark this approach in the $^{16}$O–$^{16}$O system, and present results for cross sections computed for elastic scattering up to 700 MeV in energy, as well as for the astrophysical $S$-factor of the fusion reaction. We also explore the impact of the density profile involved in the construction of the double-folding potentials. A first estimation of the impact of three-nucleon interactions as a triple-folding potential is presented as well.

For heavy nuclei, we focus on the calculation of three-nucleon interactions in their two-body normal-ordered form to be included in nuclear structure calculations. We develop a novel technique to perform the normal ordering directly in Jacobi basis, enabling the extension of the three-body model space in which these interactions can be included, as well as the storage of the matrix elements in all the steps of the calculation. To assess the validity of this new approach, we benchmark our matrix elements in $JT$-coupled basis against existing normal-ordered matrix elements using $^{4}$He and $^{16}$O as reference states in a harmonic oscillator basis. Additionally, we present first applications of these normal-ordered matrix elements in calculations of finite nuclei. Using the in-medium similarity renormalization group, we perform benchmarks for the $^{16}$O ground-state energy and charge radius. We also test the convergence of our results with respect to the inclusion of high partial waves.

Moreover, we present results for $sd$-shell Hamiltonians constructed from chiral effective field theory operators using the machinery developed for the transformation of matrix elements. Finally, we discuss an approximation for harmonic oscillator radial wave functions, which could further optimize future calculations of normal-ordered matrix-elements for heavy nuclei.

# Zusammenfassung

Diese Arbeit untersucht Reaktionen und Wechselwirkungen schwerer Kerne basierend auf der Chiralen effektiven Feldtheorie. Darin werden langreichweitige Wechselwirkungen zwischen Nukleonen durch den Austausch von Pionen beschrieben, wohingegen nicht auflösbare, kurzreichweitige Effekte in Niedrig-Energie-Konstanten aufgenommen werden, die typischerweise an Wenig-Teilchen-Systeme angepasst sind. Die Chirale effektive Feldtheorie erlaubt eine systematische Beschreibung von Vielteichen-Kräften, die bei höheren Ordnungen auftreten. Weiterhin bietet die Chirale effektive Feldtheorie ein sogenanntes "order-by-order improvement", was bedeutet das Berechnungen mit steigender Ordnung verfeinert/verbessert werden können, und sie ermöglicht es den Ergebnissen theoretische Unsicherheiten zuzuweisen.

Die Bestimmung von Atomkern-Atomkern-Potentialen ist nicht nur essenziell um nukleare Reaktionen zu beschreiben, sondern auch um Kernstruktur-Informationen zu extrahieren und um Kernreaktionen für astrophysikalische Systeme zu modellieren. In dieser Arbeit werden zum ersten mal Double-Folding Potentiale verwendet die auf chiralen Wechselwirkungen in führender Ordnung (leading-), next-to-leading- und next-to-next-to-leading-order basieren. Dafür wurden neue softe und lokale chirale Wechselwirkungen konstruiert. Als erster Benchmark wird das $^{16}\mathrm{O} -^{16}\mathrm{O}$ System betrachtet und Berechnungen erster Ergebnisse für Wirkungsquerschnitte von elastischen Streuexperimenten für Energien bis zu 700 MeV, sowie der astrophysikalische S-factor von Fusionsreaktionen gezeigt. Weiterhin wird der Einfluss des Dichte-Profils, welches in der Konstruktion der Double-Folding Potentialen verwendet wird, betrachtet. Abschließend werden erste Schätzungen für den Einfluss von Drei-Teilchen Wechselwirkungen in Triple-Folding Potentialen präsentiert.

In dieser Arbeit wird die Drei-Nukleon Wechselwirkung in Kernstrukturberechnungen von schweren Kernen in der sogenannten Zwei-Teilchen normalgeordneten Form verwendet. Im Zuge dieser Arbeit wurde eine neue Technik entwickelt mit der die Normalordnung direkt in der Jacobi-Basis berechnet wird, was es ermöglicht den Drei-Teilchen-Modellraum, in dem sich die Berechnungen abspielen, zu erweitern und gleichzeitig den Speicherbedarf der Matrix-Elemente zu reduzieren.

Um diese neue Methode zu validieren, werden die erzeugten Matrixelemente in einer $JT$-gekoppelten Basis mit bereits existierenden, normalgeordneten Matrixelementen für $^{4}$He and $^{16}$O Referenzzustände in harmonischer Oszillator-Basis verglichen. Erste Anwendungen der neuen normalgeordneten Matrixelemente in endlichen Kernen werden gezeigt. Mithilfe der In-Medium Similarity-Renormalization-Group werden Vergleichsrechnungen für die $^{16}$O Grundzustandsenergie und den Ladungsradius angefertigt. Die Konvergenz der Ergebnisse wird unter Hinzunahme höherer Partialwellen überprüft.

Zudem werden mithilfe dieser Methode Ergebnisse in der $sd$-Schale für Hamilitonians mit Operatoren aus der chiralen effektiven Feldtheorie gezeigt.

Abschließend wird eine Näherungsrechnung für Radialwellenfunktionen des harmonischen Oszillators besprochen, welche in Zukunft eine zusätzliche Verbesserung der normalgeordneten Matrixelemente schwerer Kerne bewirken könnte.

# Contents

# 1 Introduction

## 1.1 Nuclear forces

Since the discovery of the atomic nucleus in 1911 by E. Rutherford [1], great efforts have been invested in the exploration of its properties. The discovery of the neutron by J. Chadwick in 1932 [2] was a major breakthough, establishing the atomic nucleus as a system composed of two types of nucleons, protons and neutrons. One of the first formulations to quantify nuclear properties as a function of proton and neutron numbers was made by Bethe and Weizsäcker in 1935, in the form of a semi-empirical mass formula within the liquid-drop model [3, 4].

The main concern between the 1950's and the 1960's was to formulate realistic potentials between two nucleons ($NN$ potentials), mainly by using phenomenological descriptions or meson-exchange models inspired by the theory proposed by Yukawa [5]. Historically, a potential is regarded as realistic if it reproduces experimental scattering data.

It was not until the 1990's that $NN$ interactions were modeled fitting both neutron and proton scattering data, hence taking into account the charge-independence breaking that affects the strong interaction. The first $NN$ microscopic potentials that were able to reproduce both $pp$ and $nn$ scattering up to an energy $E_{\mathrm{lab}}$=350 MeV are the Nijmegen I/II and Reid 93 [6, 7], constructed in momentum space; and Argonne $v18$ [8], represented in coordinate space. All these potentials are expanded in terms of the operators allowed by the symmetries of the underlying two-body force. Alternatively, the first forces constructed as meson-exchanges in momentum space are Bonn and CD-Bonn [9], the latter of which includes charge dependence. For a chronological overview on the main ideas used to describe nuclear forces, see Table 1.1. For more details, see Ref. [10].

There are observables that cannot be accurately described with $NN$ interactions only, such as nuclear matter saturation [11] as well as properties of finite nuclei such as binding energies, separation energies or form factors [12, 13]. Therefore, at the same time that $NN$ potentials were developed and refined, notable efforts were made to describe $3N$ forces. The first formulation of three-body forces expressed as meson-exchanges was made in 1957 by Fujita and Miyazawa [14] and consisted of a term describing a pion exchanged by the first two nucleons scattering with the third nucleon through a $\Delta$ ressonance in a $P$-wave.

At the end of the 1970's, Quantum Chromodynamics (QCD) was formulated as the theory that describes the interactions between quarks and gluons, constituents of protons and neutrons, responsible for the nuclear force. It was also understood that a better connection of nuclear forces with the strong interaction is crucial for the investigation of open questions concerning the physics of nuclei. In 1979, Steven Weinberg formulated phenomenological Lagrangians consistent with chiral symmetries [15], which present the systematic scheme that expresses nuclear forces in a power counting expansion,

| | |
|---|---|
| 1935 | **Yukawa: Meson theory** |
| 1950's | *The "Pion Theories"*. One-pion exchange: good; multi-pion exchange: disaster. |
| 1960's | Many pions ≡ multi-pion resonances: $\boldsymbol{\sigma}$, $\boldsymbol{\rho}$, $\boldsymbol{\omega}$,.... The One-Boson-Exchange Model: success. |
| 1970's | Diverse two-pion-exchange models: Partovi–Lomon, Stony Brook, Paris, Bonn. |
| 1980's | Nuclear physicists discover **QCD**: Quark Models. |
| 1990's and beyond | Nuclear physicists discover **EFT**; Weinberg, van Kolck, ..., **Back to Meson (Pion) Theory!** *But, constrained by Chiral Symmetry.* |

**Table 1.1:** *The theory of nuclear forces: eight decades of struggle*. Taken from Ref. [10].

where the dominant terms of the Lagrangian are given by the lowest powers of momentum, and coined his many times cited quote "*If one writes down the most general possible Lagrangian, including all terms consistent with assumed symmetry principles, and then calculates matrix elements with this Lagrangian to any given order of perturbation theory, the result will simply be the most general possible S-matrix consistent with analyticity, perturbative unitarity, cluster decomposition and the assumed symmetry principles.*" This power counting expansion idea is the same used nowadays in chiral effective field theory (EFT), formally derived also by Weinberg in the early 1990's [16, 17]. This EFT allows to account for two-, three- and higher-body interactions in a natural and systematic way. A consequence of this systematic construction is the possibility to estimate the theoretical errors of the calculations at a certain order of the expansion [18, 19]. For these reasons, chiral EFT has become the standard method for developing systematic nuclear forces rooted in the symmetries of QCD.

Given its nature, Chiral EFT opens up a systematic path to investigate many-body forces. In particular, two- and many-body interactions can be studied consistently, constraining all the necessary parameters using only few-nucleon data.

Since the birth of nuclear physics as a field, the collaboration between theory and experiment has proven itself to be crucial for the progress of theoretical nuclear physics. A main goal of theory is to develop a systematic description of strong interactions in order to predict testable results that can be benchmarked by experiment. In the context of chiral EFT interactions, since they are base on an effective theory, their construction involves low-energy constants (LECs) that have to be fitted to experimental data, which makes experiment indispensable for important information that cannot be theoretically derived (yet).

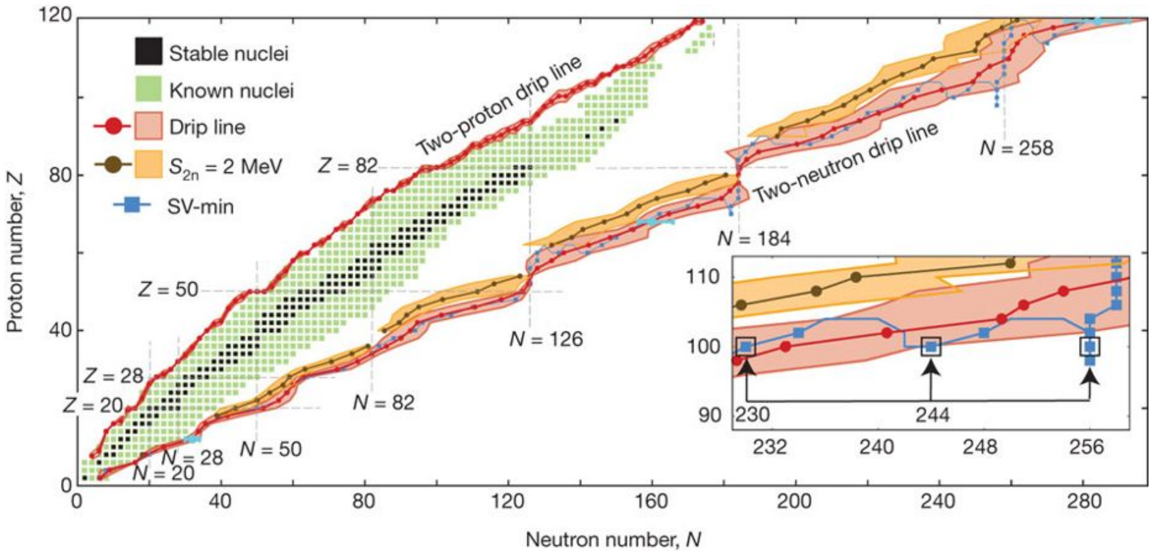

**Figure 1.1:** *Map of bound even-even nuclei as a function of $Z$ and $N$*: Stable (black squares) and radioactive (green squares) even-even isotopes known experimentally by 2012. Mean proton- and neutron-drip lines and their uncertainties obtained by averaging the results of different models are shown in red and blue. The $S_{2n} = 2$ MeV line is also shown in brown. The inset shows the two-neutron drip line around Z = 100. Figure from Ref. [20].

## 1.2 Structure and reactions of nuclei

The current status of known nuclei (from 2012) is presented in Fig. 1.1 [20], arranged as a function of proton and neutron numbers, $Z$ and $N$, respectively. The figure includes 767 isotopes, the stable ones shown as black squares, while the rest of experimentally known nuclei are depicted by green squares. The mean two-neutron and -proton driplines and their uncertainties (obtained as an average of results from different density functional theory models) are shown in red. The two-neutron separation energy is defined as the difference in binding energy between the isotope $(Z,N-2)$ and the isotope $(Z,N)$, being the case analogous for the two-proton separation energy. Therefore, a nucleus $(Z,N)$ for which the two-neutron or two-proton separation energy is negative will be unbound when adding neutrons or protons, respectively. The set of these nuclei define the limits of the nuclear chart. From the gap in the neutron-rich region of the figure, it is clear that collaboration between experimental results and theoretical predictions for medium-mass and heavy nuclei is crucial for the development of nuclear physics as a field.

While the direct solution of the nucleus starting from quarks and gluons as fundamental degrees of freedom is currently being pursued for light nuclei, see, e.g., Refs. [21, 22], this description still presents large systematic errors that make the comparison with experimental data challenging. For this reason, in the context of this thesis, we refer to *ab initio* to those few- or many-body methods that start from realistic interactions between nucleons, which are considered the degrees of freedom of the problem. Until the early 2000s, the possibilities to solve the many-body Schrödinger equation with *ab initio* methods was restricted to light systems up to $A \approx 12$ using, for example, Monte Carlo methods like Variational Monte Carlo (VMC), Auxiliary Field Diffusion Monte Carlo (AFDMC) or Green's Function Monte Carlo (GFMC), all of them reviewed in Ref. [23]. Shell model calculations, first presented in 1966 by Tom Kuo and Gerry Brown [24], were used to describe medium mass and some heavy nuclei at near-closed shells [25], while using energy density functionals like Skyrme, Gogny or relativistic mean field model (RMF) with different methods like self-consistent mean-field model made it possible to calculate nuclear properties for a wider range of masses (for a review on this topic, see Ref. [26]). Nowadays we have *ab initio* for medium-heavy mass [27], towards *ab initio* shell model [28, 29], and energy density functionals [20, 30]. The evolution of the reach of *ab initio* calculations in terms of the mass number $A$ as a function of the years can be seen in Fig. 1.2 [31]. It is clear from the figure that up to the early 2010's the progress was linear, since the increase of computing power was exponential with $A$, while in recent years there has been an exponential increase with $A$, thanks to the development of polynomial scaling algorithms [31].

The consistent inclusion of three-body interactions has been found to be crucial for the reproduction of experimental data (see, e.g., Ref. [12] for a review). One of the most prominent examples of this phenomenon can be seen in Fig. 1.3, that depicts the change of the location of the theoretically derived neutron drip-line from $^{28}$O (considering only $NN$ microscopic interactions) to the experimentally observed $^{24}$O (when $NN+3N$ interactions are considered), due to the repulsive $3N$ contributions to the interactions among excess neutrons [32]. Examples of this effect can be seen for both a $G$-matrix interaction, which describes in an effective way the interaction between two nucleons taking into account in-medium effects [33] (panel (b)), and $NN$ interactions coming from chiral EFT (panel (c)).

It has been proven that the inclusion of $3N$ forces throughout the neutron-rich region of the nuclear chart is strictly necessary to correctly describe observables from calculations starting from microscopic interactions. Prominent examples of these cases are the discovery of new shell closures in the calcium region [34, 35], or the correct reproduction of the trend of binding energies throughout Ar, K, Ca, Sc, and Ti isotopic chains [36], amongst others. Complementary to finite systems, it is also known that, for calculations with chiral EFT, saturation in nuclear matter is driven by three-nucleon interactions [37]. For this reason, most current *ab initio* nuclear structure calculations use $NN$ and $3N$ interactions as starting point. This approach has many advantages: aside from being an ideal way

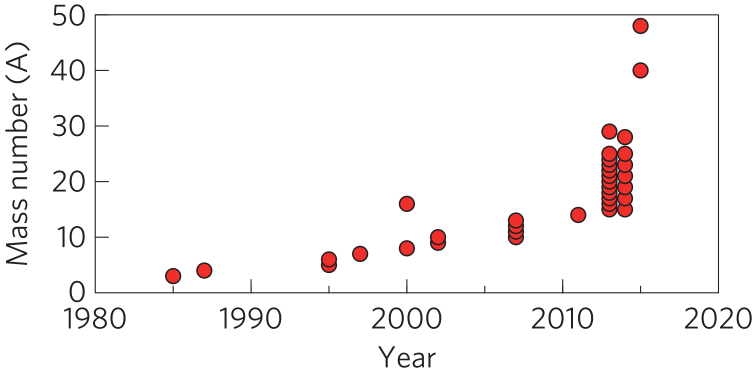

**Figure 1.2:** The figure reflects the linear progress in the early years, due to the exponentially increasing computing power that was applied to exponentially expensive numerical algorithms. The algorithms of the recent years, which have polynomial scaling in $A$, have exponentially increased the reach. Figure from Ref. [31].

of testing our understanding of $NN$ and $3N$ forces, it allows to find an exact solution of three- and four-body systems with, e.g., Faddeev and Faddeev-Yabukowsky equations [38] or hyperspherical harmonics [39], while using interactions from chiral EFT also makes it possible to perform reliable extrapolations and error estimations from theory [18, 19].

One of the most challenging aspects of expanding the frontier of *ab initio* methods in order to describe nuclei beyond the $sd$ shell is the consistent inclusion of three-body elements in every step of the calculation. Amongst the most successful ways of performing this inclusion we have the introduction of controlled approximations, being the normal-ordering technique (NO) one of the most used, since it includes $3N$ interactions in the form of effective $NN$ matrix elements. The main advantage of the NO is that it makes it possible to account for $3N$ effects in a many-body formalism at $NN$ level.

Since realistic interactions cause correlations amongst the nucleons, most many-body methods that take a matrix representation of the Hamiltonian as an input require large model spaces in order to be able to account for said correlations. The usual way of dealing with this problem is to soften the interaction by applying a renormalization group (RG) evolution, such as low-momentum $NN$ interactions $V_{\text{low k}}$, given by the low-momentum block of a block-diagonal Hamiltonian in momentum space [40], or using unitary transformations such as the unitary correlation operator method (UCOM) [41] or the similarity renormalization group (SRG) [42, 43], which yield a diagonal band interaction by decoupling high- and low- momentum states. While it is not possible, in general, to apply the $V_{\text{low k}}$ or UCOM formalisms beyond the $NN$ space, the extension of the SRG evolution to the three-body space [44–46] along with advances in the computational treatment of three-body matrix elements allow for applications of chiral $NN + 3N$ interactions in different many-body methods. Using these softer interactions also accelerates the convergence of the calculations, which makes it also possible to study different observables in a large number of systems, such as properties of neutron matter important for finite nuclei like pairing [47] and neutron drops [48, 49].

Some of the possible applications to finite nuclei are nuclear spectroscopy both in conventional nuclei [45, 50, 51] or hypernuclei [52, 53]. These applications beyond the $sd$ shell are possible to perform thanks to the great improvement in many-body methods. Examples of those are the importance-truncated Large-Scale Shell Model [54], coupled-cluster (CC) methods [55–59], the in-medium similarity renormalization group (IM-SRG) [60–63], many-body perturbation theory (MBPT) [64, 65], or the self-consistent Green's function (SCGF) methods [66–68]. Efforts have also been made with multi-reference extensions and further developments to describe open shell nuclei [69–71].

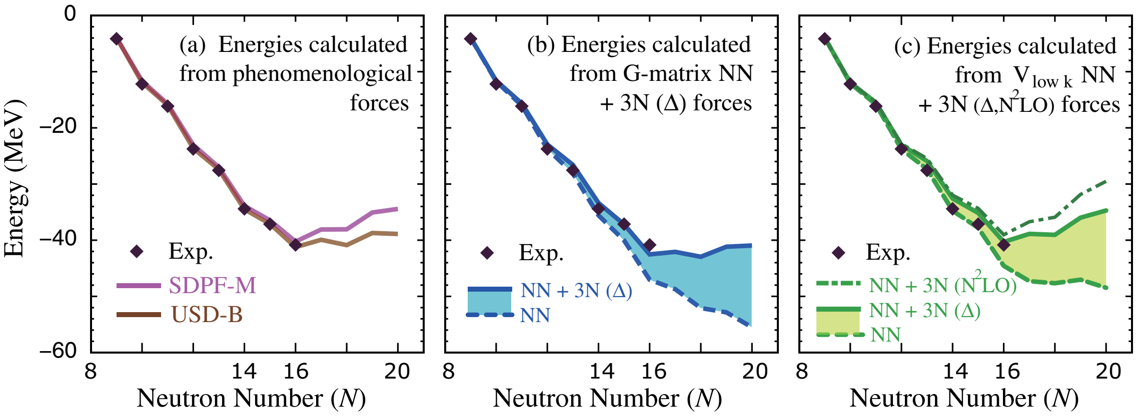

**Figure 1.3:** Ground-state energies of oxygen isotopes (measured from $^{16}$O) as function of their neutron number $N$ for (a) SDPF-M and USD-B phenomenological forces, (b) $NN$ and $3N$ G-matrix interaction, and (c) $V_{\mathrm{low}\,k}$ interaction including $NN$ only and $3N$ forces from chiral EFT. In panels (b) and (c) the changes due to $3N$ forces based on $\Delta$ excitations are highlighted by the shaded areas. Figure from Ref. [32].

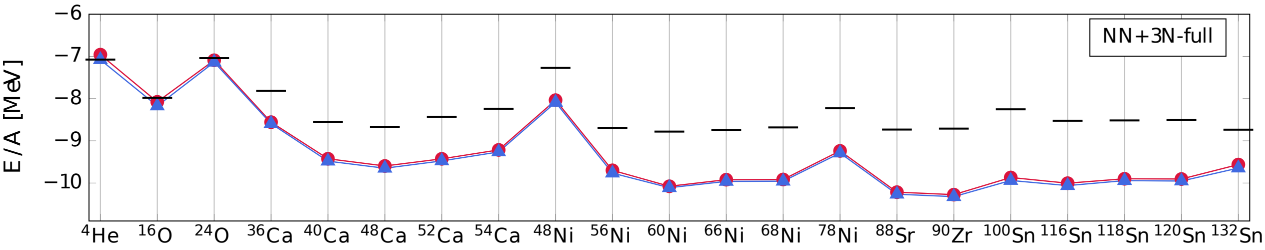

**Figure 1.4:** Ground-state energies per nucleon from HF-MBPT (red circles) in comparison to CC calculations (blue triangles) for selected closed-shell nuclei. Experimental values are indicated by black bars. For details in the calculations, see Ref. [72], from where the figure was taken.

Even though there have been tremendous advances in the calculations for medium-mass and heavy nuclei and results for isotopes up to tin are available [59, 72, 73], there are still severe challenges to overcome related to the description of the Hamiltonian, the SRG-induced many-body contributions, and the truncations of the model space in which $3N$ interactions can be included. In all the many-body methods mentioned before, a strict truncation in the three-body energy has to be applied due to computational restrictions. The neglected contributions can have sizable effects depending on the nucleus considered, and present a limitation for the calculation of observables of heavier nuclei. An example of results for ground-state energies of closed nuclei using Hatree-Fock-MBPT and CC for nuclei up to $^{132}$Sn is shown in Fig. 1.4 [72]. This figure exemplifies the great and promising improvement in the reach of *ab initio* techniques, while showing at the same time the difficulty to reproduce experimental values as $A$ grows.

On the other hand, the use of nuclear interactions as only input allows us to work towards a common framework for *ab initio* structure and reactions [74, 75]. In order to gather information on the nucleus itself, the study of nucleus-nucleus reactions is crucial, since the forces that act between them originate from those between nucleons. Determining this interaction between two nuclei is a long-standing and challenging problem [76]. It constitutes a crucial input in the modelling of nuclear reactions, which provide key information about the structure of nuclei and are relevant for many astrophysical problems, including the stellar synthesis of elements or the birth of neutron stars. This interaction between two nuclei can be regarded, in first approximation, as a one-body potential (optical potential) [76,77]. The optical potential is usually a complex quantity that describes the attractive interaction that mediates elastic scattering between the nuclei, while also simulates the absorption of the incoming elastic channel to other possibly open non-elastic channels, without explicitly dealing with the excitation of internal degrees of freedom of the colliding nuclei. The interaction between nuclei has been historically modeled by phenomenological potentials, e.g., of Woods-Saxon form [78]. The standard form of a phenomenological optical potential can consist of up to three real and three imaginary nuclear terms (volume, surface, and spin-orbit terms) plus a Coulomb term. All these are defined by parameters that are adjusted to reproduce elastic-scattering data at different energies, see, e.g., Ref. [79]. Albeit precise when experimental data exist, these potentials lack predictive behavior and do not have controlled uncertainties.

Alternatively, it has been suggested to construct nucleus-nucleus potentials from the densities of the colliding nuclei and a given nucleon-nucleon interaction using a double-folding procedure [80]. It is known that this framework provides more realistic potentials for the nucleon-nucleus interactions than for the nucleus-nucleus case [81]. Nevertheless, it constitutes a first-order approximation to optical potentials derived from Feshbach's reaction theory [76]. Promising results have been obtained in such a way, e.g., by considering the M3Y interaction [80], zero-range contact $NN$ interactions [82, 83] or using a $G$-matrix approach, see, e.g., Refs. [84, 85] for recent work. Examples of elastic-scattering cross sections obtained from double-folding interactions can be seen in Fig. 1.5. In the left panel, results for the reaction $^{16}$O–$^{40}$Ca at different energies were obtained using the double-folding potential from the M3Y interaction for the real part of the total potential, and fitting a Woods-Saxon potential to reproduce its imaginary part [80]. In contrast, the right panel shows results for the elastic scattering of $^{16}$O by $^{28}$Si, $^{40}$Ca, $^{90}$Zr, and $^{208}$Pb using a double-folding potential generated from a $G$-matrix interaction, which already renders a complex double-folding potential [84]. Even though these examples do no provide parameter-free optical potentials, they make it clear that the double-folding technique is a promising approach to describe nuclear reactions.

During the last decade, there have been great advances also in nuclear reactions based on effective field theories. Efforts have been made to derive nucleon-nucleus optical potentials using chiral EFT interactions from perturbation theory [86, 87] and self-consistent Green's function calculations [88, 89]. It is clear from all the progress in this field that the derivation of nucleus-nucleus potentials from microscopic $NN$ interactions is a promising direction of research towards *ab initio* nuclear reactions.

## 1.3 Motivation for this thesis

As it could be seen in the previous section, in spite of the tremendous advances and breakthroughs achieved in the last years, there are still necessary improvements to accurately describe nuclear reactions and structure from an *ab initio* point of view. For this reason, in this work we develop nucleus-nucleus interactions calculated from chiral EFT in order to work towards an *ab initio* description of reaction observables. This approach provides a systematic construction by using $NN$ potentials at increasing orders in the chiral expansion. This systematic nature has two main advantages: it shows a clear path to improve the potential, while also offering the possibility to estimate theoretical uncertainties in the interaction between two nuclei. At the same time, this approach offers the possibility to consistently include $3N$ interactions to describe nuclear reactions.

On the other hand, we also work towards increasing the model space in which three-body interactions can be included in the form of normal-ordered two-body matrix elements, since this is a necessary step to describe observables for heavy nuclei. The study of a new method to calculate these effective $NN$ interactions that circumvents the existing challenges to introduce larger model spaces is necessary to work towards a better description and prediction of the nuclear chart from *ab initio* methods.

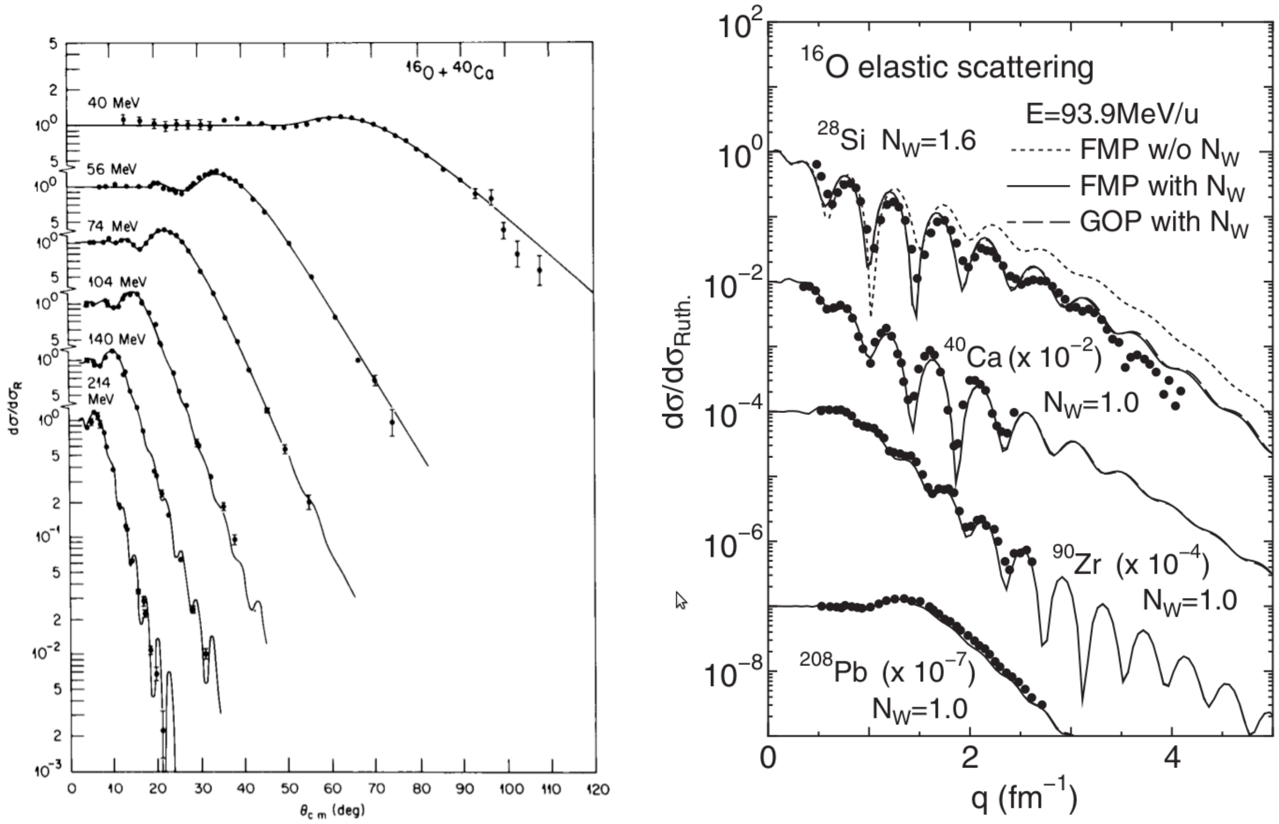

**Figure 1.5:** Examples of elastic nucleus-nucleus scattering cross sections (normalized to the Rutherford cross section) obtained with double-folding potentials. The left panel shows results for the reaction $^{16}$O–$^{40}$Ca obtained with phenomenological $NN$ potentials at a range of energies from 40 to 214 MeV (from Ref. [80]), while the right panel shows results for scattering of $^{16}$O off $^{28}$Si, $^{40}$Ca, $^{90}$Zr, and $^{208}$Pb using a double-folding potential generated from microscopic $G$-matrix interactions (from Ref. [84]).

This thesis is organized as follows: more details on QCD and chiral EFT will be given in Ch. 2. The local representation of chiral EFT for two- and three-body interactions up to N$^2$LO is presented in Ch. 3. Chapter 4 contains the theoretical basics of scattering theory for nucleus-nucleus reactions, which will be applied to calculate the observables using double-folding potentials from $NN$ chiral EFT local interactions. The derivation of such potentials, as well as results for elastic scattering and fusion of the $^{16}$O–$^{16}$O system are presented in Ch. 5. A first approach to include $3N$ interactions using a triple-folding technique is also studied. We continue with the focus on three-body interactions in Ch. 6, where we discuss the normal-ordering approximation, usually applied in calculations of nuclear structure. Chapter 7 follows this idea, presenting details on the novel approach developed to calculate two-body normal-ordered matrix elements in Jacobi basis and the results for benchmarks against existing reference matrix-elements in medium-mass nuclei. In Ch. 8, we present results for binding energies of $^{16}$O within the IM-SRG many-body method using this novel approach to calculate normal-ordered matrix-elements, comparing them to results using existing reference matrix-elements. On the other hand, Ch. 8 presents also a possible approximation for the wave functions to be applied in calculations of heavy nuclei observables, and results of shell-model interactions that benefit from the transformation used for the calculation of the matrix elements of Ch. 7. Finally, a summary of the thesis as well as an outlook are contained in Ch. 9.

# 2 Strong interactions and chiral effective field theory

## 2.1 Quark model

The diversity of hadrons observed in nature suggests that it is unlikely that they are fundamental entities of nature. In fact, the existence of quarks (and antiquarks) as subatomic particles, constituent of baryons and mesons, was postulated in 1964 by M. Gell-Mann [90] and G. Zweig [91]. Although this model was postulated assuming the existence of three quarks, nowadays there are a total of six known quarks in nature: up (u), down (d), strange (s), charm (c), top (t), and bottom (b). These are referred to as different quark flavors.

In the quark model, baryons are composed of three quarks, and mesons are composed by one quark and one antiquark. Each hadron is characterized by its mass, its charge and its quantum numbers (angular momentum, parity, isospin...). Experimental observations show that hadrons appear in isospin multiplets, but the particles of a given multiplet do not have the same mass. This observation indicates that the strong interaction is approximately invariant under isospin transformations, but not exactly invariant under flavor transformations. Mathematically, this implies that $SU(3)_{\text{flavor}}$ is only an approximate symmetry.

In order to ensure that baryons have an antisymmetric wave function when a hadron is composed by three quarks of the same flavor (in case of, for example, the $\Delta$ resonances), a color degree of freedom was introduced by O. W. Greenberg in 1964 [92]. This implies that aside from flavor, quarks also carry color, which can be red, green or blue and is not an observable. Therefore, any observable state must be a color singlet, or colorless, leading to baryons being composed by a sum of one red, one blue and one green quark, while mesons are composed by a quark and an antiquark of a color and its corresponding anticolor.

Color is an exact local symmetry of the model, represented by the group $SU(3)_{\text{color}}$, and explains the lack of observation of states formed by a number different to three quarks and/or the combination quark-antiquark.

## 2.2 QCD Lagrangian

Quantum Chromodynamics (QCD) is the non-Abelian gauge theory that describes the group $SU(3)$ of color. Given this symmetry, the interaction is governed by massless bosons of spin 1, the gluons, that only couple particles that have color. Therefore, QCD is the theory that describes the nuclear force through the interaction of color carrying quarks via gluon exchanges. This implies that considering a fermionic field of spin 1/2, $q$, we can write the interaction part of a Lagrangian for $N$ quarks as

$$\mathscr{L} = \bar{q}_1(i\gamma^\mu D_\mu - m_1)q_1 + \bar{q}_2(i\gamma^\mu D_\mu - m_2)q_2 + \ldots + \bar{q}_N(i\gamma^\mu D_\mu - m_N)q_N\,, \tag{2.1}$$

where $D_\mu = \partial_\mu - i g_s \frac{\lambda_a}{2} \mathscr{A}_{\mu a}$ is the gauge covariant derivative. $D_\mu$ ensures that the Lagrangian is symmetric under global transformations by introducing the Gell-Mann matrices $\lambda_a$ and a Gauge field $\mathscr{A}_{\mu a}$ for each of the eight generators of $SU(3)_{\text{color}}$.

It is important to notice that $D_\mu$ also depends on the strong coupling constant, $g_s$, which is the only free parameter of the Lagrangian. Even though it is referred to as constant, this coupling strength

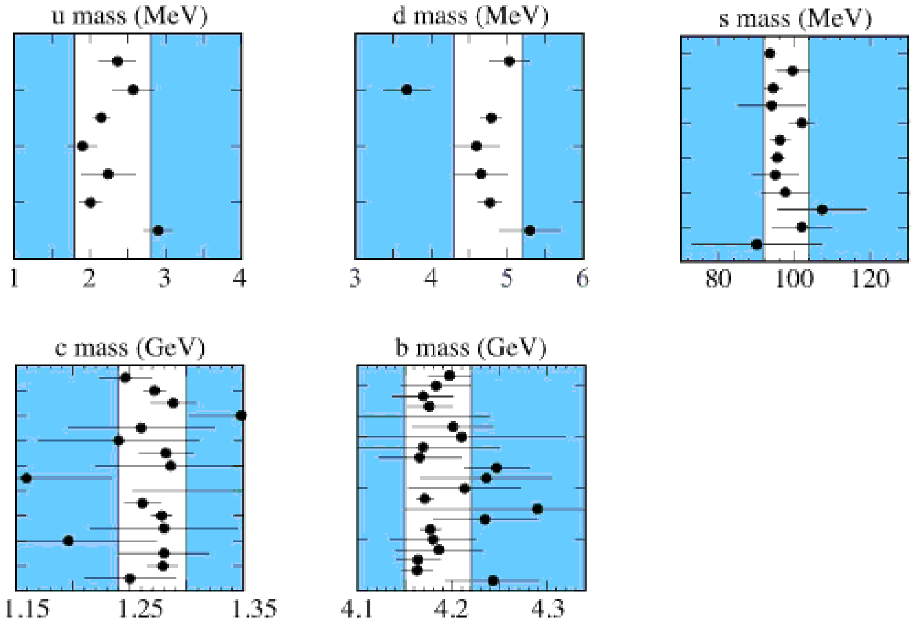

**Figure 2.1:** *The values of each quark mass parameter taken from the Data Listings*: points shown in chronological order with the more recent measurements at the top. The figure for mass measurements of the heaviest quark (t) is not available. Figure modified from Ref. [93].

varies as a function of the energy scale or, equivalently, the typical momentum transfer of the process, $Q$. An important particularity of $g_s(Q)$ is that it decreases for increasing momenta, leading to the asymptotic freedom that characterizes QCD [94]. $g_s$ also depends on a constant $\Lambda^{\mathrm{QCD}}$ that is determined experimentally to be $\Lambda^{\mathrm{QCD}} \approx 200$ MeV [93] and determines the mass scale that separates the world of hadrons (non-perturbative region) and the world of quarks and gluons, which are in the free regime (perturbative region).

The Lagrangian in Eq. (2.1) can be rewritten in a more compact way using the mass matrix, $\mathscr{M} = \mathrm{diag}(m_1, m_2, \ldots, m_N)$. Adding also the kinetic term $[D_\mu, D_\nu]$, we have that

$$\mathscr{L}_{\mathrm{QCD}} = \bar{q}(i\gamma^\mu D_\mu - \mathscr{M})q - \frac{1}{4} G_{\mu\nu,a} G_a^{\mu\nu} , \tag{2.2}$$

where $G_{\mu\nu,a}$ is the gluon field strength tensor, related to the Gauge field and the structure constants of the $SU(3)_{\mathrm{color}}$ algebra, $f_{abc}$, as

$$G_{\mu\nu,a} = \partial_\mu \mathscr{A}_{\nu,a} - \partial_\nu \mathscr{A}_{\mu,a} + g f_{abc} \mathscr{A}_{\mu,b} \mathscr{A}_{\nu,c} \, . \tag{2.3}$$

| Quark | u | d | s | c | b | t |
|---|---|---|---|---|---|---|
| Mass | $2{,}2\,^{+0{,}6}_{-0{,}4}$ | $4{,}7\,^{+0{,}5}_{-0{,}4}$ | $96\,^{+8}_{-4}$ | $1{,}27\,^{+0{,}06}_{-0{,}06}$ | $4{,}18\,^{+0{,}04}_{-0{,}03}$ | $160\,^{+5}_{-4}$ |

**Table 2.1:** Quark masses. The lightest quarks (u, d and s) have masses with units of MeV, while the masses of the heaviest quarks (c, b and t) are given in GeV. Values taken from Ref. [93].

### 2.2.1 Chiral symmetry

The QCD Lagrangian presents a very important symmetry: chirality, which represents the generalization of helicity for ultra-relativistic particles. Since the quarks up and down are at least 20 times lighter than the rest of quarks (see Fig. 2.1 and Table 2.1), we can approximately write the ud QCD Lagrangian in the limit of vanishing quark masses

$$\mathscr{L}_{QCD}^{\mathscr{M}=0} = \bar{q} i \gamma^{\mu} \mathscr{D}_{\mu} q - \frac{1}{4} G_{\mu\nu,a} G_{a}^{\mu\nu} , \tag{2.4}$$

and rewrite it as

$$\mathscr{L}_{QCD}^{\mathscr{M}=0} = \bar{q}_R i \gamma^{\mu} \mathscr{D}_{\mu} q_R + \bar{q}_L i \gamma^{\mu} \mathscr{D}_{\mu} q_L - \frac{1}{4} G_{\mu\nu,a} G_{a}^{\mu\nu} , \tag{2.5}$$

where $q_R = \frac{1}{2}(1+\gamma_5)q$ and $q_L = \frac{1}{2}(1-\gamma_5)q$ are, respectively, right- and left-handed chirality eigenstates.

In this massless quarks approximation, the theory has a high degree of symmetry originated in the fact that the interaction between quarks and gluons does not depend on quark flavor and there is a conservation of helicity: $\mathscr{L}_{QCD}^{\mathscr{M}=0}$ is invariant under independent rotations of left- and right-handed quarks. This means that there is a $SU(2)_R \times SU(2)_L$ symmetry. Therefore, the right- and left-handed components of massless quarks do not mix. This property is known as chirality or chiral symmetry.

#### Explicit symmetry breaking

Since in nature the up and down quark masses are non-vanishing, the mass term of the Lagrangian, $-\bar{q}\mathscr{M}q$, explicitly breaks chiral symmetry. In this two flavor case this term can be rewritten as

$$\mathscr{M} = \begin{pmatrix} m_u & 0 \\ 0 & m_d \end{pmatrix} = \frac{1}{2}(m_u + m_d)\mathbb{1} + \frac{1}{2}(m_u - m_d)\tau_3 , \tag{2.6}$$

where $\mathbb{1}$ is the identity matrix and $\tau_3$ is the Pauli matrix of the third isospin component. In this expression, it can easily be seen that the first term is invariant under $SU(2)_{\text{isospin}}$, while the second vanishes for $m_u = m_d$. Therefore, even though chirality is only an approximated symmetry, isospin is an exact symmetry in the case $m_u = m_d$.

#### Spontaneous symmetry breaking

There is evidence that the (approximated) chiral symmetry of the Lagrangian is not realized on the ground state of the system, i.e. spontaneously broken. This symmetry is dynamically broken due to the creation of a fermionic condensate; the quark condensate in the case of chirality.

Since there is a symmetry, according to Noether's theorem there will be three right- and three left-handed conserved currents. These can be equivalently written as three axial-vector and three vector conserved currents that will generate conserved charges: one axial-vector, $Q_A$, and one vector, $Q_V$, that will commute with the Hamiltonian. As it was demonstrated by Vafa and Witten in 1984 [95], the lowest energy state is invariant under vector charges, which implies $Q_V|0\rangle = 0$. Nevertheless, this is not the case for the axial-vector currents, since $Q_A|0\rangle = 0$ would imply that baryons of positive and negative parity would have the same mass (parity doublets). Given that there are no observations

| Particle | Quark composition | $J^P$ | Mass [MeV] |
|---|---|---|---|
| p | uud | $1/2^+$ | $938{,}272081 \pm 6{\cdot}10^{-5}$ |
| $N^+$ | uud | $1/2^-$ | $1535^*$ |
| n | ddu | $1/2^+$ | $939{,}565413 \pm 6{\cdot}10^{-5}$ |
| $N^0$ | ddu | $1/2^-$ | $1535^*$ |
| $\Sigma^+$ | suu | $1/2^+$ | $1189{,}37 \pm 0{,}07$ |
| $\Sigma^-$ | sdd | $1/2^+$ | $1197{,}449 \pm 0{,}030$ |
| $\Sigma^0$ | uds | $1/2^+$ | $1192{,}642 \pm 0{,}024$ |
| $\Sigma(1750)$ | uds | $1/2^-$ | $1750^*$ |
| $\Lambda^0$ | uds | $1/2^+$ | $1115{,}683 \pm 0{,}006$ |
| $\Lambda(1405)$ | uds | $1/2^-$ | $1405.1\,^{+1.3}_{-1.0}$ |
| $\Xi^-$ | ssd | $1/2^+$ | $1314{,}86 \pm 0{,}20$ |
| $\Xi^0$ | ssu | $1/2^+$ | $1321{,}71 \pm 0{,}07$ |

**Table 2.2:** Masses of the components of the light baryon octet with $J^P = (1/2)^+$ and their counterparts with negative parity, except for $\Xi$ baryons with $J^P = (1/2)^-$, whose mass have not yet been determined. The masses marked with $^*$ indicate the mean value of the Breit-Wigner mass. Values taken from Ref. [93].

of parity doublets in the known low-mass hadrons (see Table 2.2), we can say that the fundamental state of QCD does not have the symmetry of the Lagrangian, which implies that there is a spontaneous breaking of chiral symmetry (even though this symmetry could be restored for highly-excited nucleon and $\Delta^*$ resonances [96]).

Given the Goldstone theorem [97], a spontaneously broken symmetry has associated bosons that generate it. In this case, they are the pseudoscalar pion triplet: $\pi^+$, $\pi^-$, and $\pi^0$.

## 2.3 Chiral effective field theory

Since chirality is a broken symmetry that has pions as generators, it is possible to develop an effective theory that is rooted in this symmetry, while describing the system in the low-energy region of interest for nuclear physics.

An effective theory is a systematic approximation of the dynamics that governs a physical process. As such, it is valid in a certain energy regime. It is important to notice that it is not a model, since it has a systematic character that allows making predictions with an arbitrary precision.

For this to be possible, there must exist a small parameter that determines an expansion. In most physical processes, this parameter is determined by the ratio between two clearly separated scales that are involved in said process. The physical processes can then be described with a finite number of parameters, up to effects that are suppressed by $(Q/\Lambda)^\nu$, where $Q$ is the momentum of the particles in our effective theory, $\nu$ is the arbitrary expansion order, and $\Lambda$ is determined by the break-down scale of the theory.

### 2.3.1 Principles of effective field theory for nucleons

The energy gap in the mesonic spectrum can be clearly determined by noticing the mass difference between pions, with a mass of around 140 MeV, and vector mesons, with masses of at least 770 MeV (see Table 2.3). Since nucleon in nuclei and nuclear matter have typical momenta of around 100 MeV, we can identify the characteristic momentum of our theory as the pion mass, $m_\pi$, and set the hard

| Particle | $\pi^+$ | $\pi^-$ | $\pi^0$ | $\rho$ | $\omega$ |
|---|---|---|---|---|---|
| Mass [MeV] | 139,57018<br>(±0,000035) | 139,57018<br>(±0,000035) | 134,97668<br>(±0,00006) | 775,26<br>(±0,25) | 782,65<br>(±0,12) |

**Table 2.3:** Masses of lightest unflavored mesons. All of them are composed by combinations of u, d, ū and d̄. Values taken from Ref. [93].

scale to be of the order of the mass of lightest vector meson, $m_\rho$. it is important to note that the mass difference between $\Delta$ resonances ( with $m_\Delta \approx 1232$ MeV) and nucleons is approximately 300 MeV. Therefore, it is of the order of the breakdown scale, and we can have $\Delta$-full chiral interactions, that explicitly include intermediate $\Delta$-excitations as degrees of freedom [98–100]. In this work, we will focus on $\Delta$-less ChEFT, where the $\Delta$ excitations are absorbed into the low-energy constants.

With this idea in mind, the nucleon-nucleon interaction can be modeled as meson exchanges, basing this approach in symmetries of QCD. Taking the simplest case of one meson exchange (OME), using Feynman rules we can describe their interaction diagram proportionally to a factor $\frac{1}{\mathbf{q}^2+m^2}$. For mesons heavier than the pion, this factor $\frac{1}{\mathbf{q}^2+m^2_{\text{heavy}}}$ can be expanded at low energies

$$\frac{1}{m^2_{\text{heavy}}}\frac{1}{1+\mathbf{q}^2/m^2_{\text{heavy}}} \approx \frac{1}{m^2_{\text{heavy}}} + \frac{\mathbf{q}^2}{m^4_{\text{heavy}}} + \ldots \tag{2.7}$$

Since the first term is dominant in the expansion (the second term gives approximately a 3% correction if $q = m_\pi$ and $m_{\text{heavy}} = m_\rho$), we can concentrate on it to understand what an interaction mediated by heavy mesons means in this theory. Taking the Fourier transform ($\mathscr{F}$) of this term, it is easy to interpret that since $\mathscr{F}\left(1/m^2_{\text{heavy}}\right) \propto \delta(r)$, the exchange of heavy mesons can be absorbed in contact terms of the potential. These terms account for short-range interactions without explicitly dealing with their dynamical origin. The strength of these contact interactions is determined by the so-called low-energy constants (LECs), whose values are typically fitted to reproduce experimental $\pi\pi$, $\pi N$ or $NN$ data in the two-body sector. The scattering solution of the Lippmann-Schwinger equation [77, 101] is usually fitted to data or some phase shifts from the Nijmegen partial wave analysis (PWA) [6]. More details on the determination of LECs will be given at the end of this chapter and in Chapter 3.

Therefore, the idea of this effective theory is to provide a systematic expansion for nuclear forces with:

- Pion exchanges to build the long range part.
- $\delta$-functions (and derivatives of delta functions) for the short range part.

As mentioned before, one of the main advantages of chiral EFT is its systematic expansion nature. For interactions in three dimensions, the $\delta$-like interactions that arise from the exchange of heavy mesons give infinities when, e.g., solving the Lippmann-Schwinger equation or applying perturbation theory to determine nuclear properties. This issue can be easily exemplified in the second case

$$\sum_{n\neq 0}\frac{\langle 0|V|n\rangle\langle n|V|0\rangle}{E_0-E_n} \propto |V|^2\sum_{n\neq 0}\frac{1}{E_0^{(0)}-E_n^{(0)}} \propto \frac{1}{m^4_{\text{heavy}}}\int d^3p\frac{1}{-p^2/2m} \propto \frac{1}{m^4_{\text{heavy}}}\int_0^\infty dp = \infty \tag{2.8}$$

To solve this problem, $\delta$-function interactions are regularized (at mean field, $\delta$-interactions can be handled, but not its corrections). Even though there are multiple possible choices for the regulator

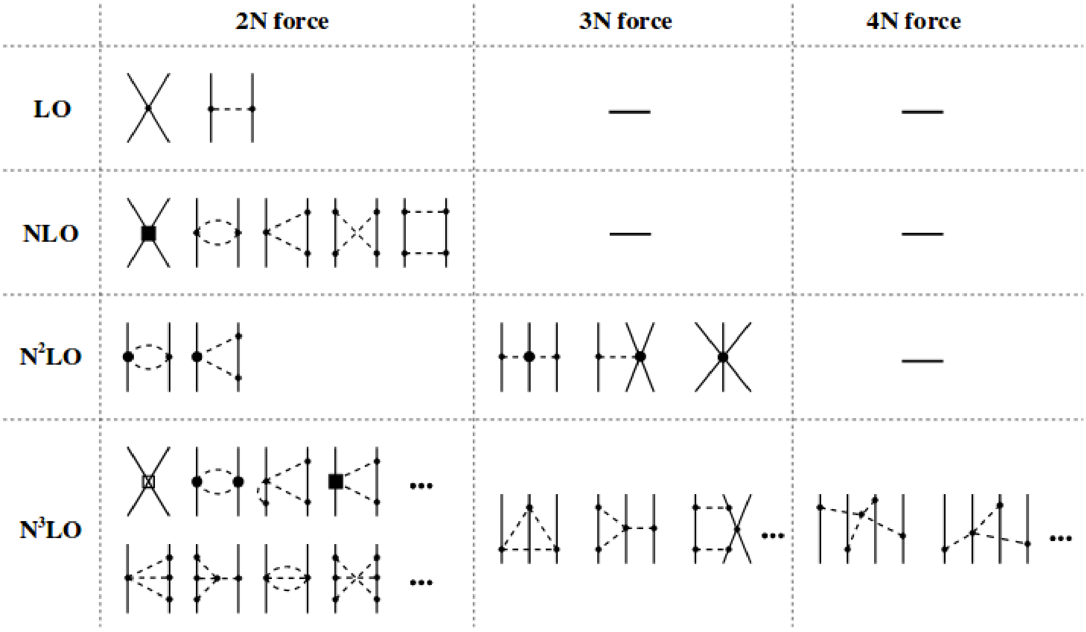

**Figure 2.2:** Two-, three- and four-body forces in the chiral expansion up to fourth order in Weinberg's power counting (N$^3$LO). Solid lines represent nucleons while dashed lines correspond to pions. Figure taken from Ref. [102].

function, this regularization has been historically made via a factor $f(p,p') = e^{-((p+p')/\Lambda)^{2n}}$, where $\Lambda$ is the regulator cutoff, $Q$ is related to the nucleon momentum and $n$ is an integer large enough to ensure that the regulator does not allow contributions beyond the given chiral order. In the recent years, different regularization schemes have been proposed and tested, namely non-local, local, and semilocal (see, e.g., [18]).

We can now see the general idea of chiral EFT is to expand long-range parts in pion exchanges and short-range parts in (regularized) contact-like interactions. As mentioned at the beginning of this section, this is done in in powers of $(Q/\Lambda)^{\nu}$ with $\nu \geq 0$ the index that defines the power counting of this theory [15]

$$\nu = 2 - N + 2L + \sum_i V_i \left( d_i + \frac{1}{2} n_i - 2 \right) . \tag{2.9}$$

This formula is interpreted as the contribution to the potential between $N$ nucleons of a diagram with $L$ loops and $V_i$ vertices that involve $n_i$ nucleon lines and $d_i$ derivatives.

As a result, the systematic expansion leads to a hierarchy of nucleon interactions that naturally include many-nucleon contributions, with $NN$ interactions starting at leading order (LO, $\nu = 0$) followed by a contribution at next-to-leading order (NLO, $\nu = 2$), whereas three-nucleon interactions enter at next-to-next-to leading order (N$^2$LO, $\nu = 3$), and higher-body contributions are also naturally incorporated as $\nu$ grows. This order-by-order expansion can be seen in Fig. 2.2 where the diagrammatic contributions for the chiral two-, three-, and four-nucleon forces are illustrated up to N$^3$LO ($\nu = 4$).

### 2.3.2 Two-nucleon interactions up to N$^2$LO

Without giving details of their derivation, we will present here the expressions that characterize the different order-by-order contributions of the chiral $NN$ interaction.

For the LO contact potential, we have

$$V_{\text{cont}}^{(0)} = C_S + C_T \boldsymbol{\sigma}_1 \cdot \boldsymbol{\sigma}_2 \,. \tag{2.10}$$

Additionally, as can be seen in Fig. 2.2, the one-pion exchange interaction contributes at LO

$$V_{\text{OPE}}^{(0)} = -\frac{g_A^2}{4f_\pi^2} \frac{\boldsymbol{\sigma}_1 \cdot \mathbf{q} \boldsymbol{\sigma}_2 \cdot \mathbf{q}}{q^2 + m_\pi^2} \boldsymbol{\tau}_1 \cdot \boldsymbol{\tau}_2 \,, \tag{2.11}$$

here, $g_A$ is the axial-vector coupling constant and $f_\pi$ the pion decay constant. Even though it has been experimentally determined that $g_A = 1.2723$ [93], the value used in chiral interactions is $g_A = 1.29$ to take the Goldberger-Treiman discrepance into account [103, 104]. The vector $\mathbf{q} = \mathbf{p}' - \mathbf{p}$ is the momentum transfer, difference between final and initial single-particle momenta.

At NLO, order denoted by the superscript (2), the most general contact interaction allowed by symmetry consists of 14 different terms, but, due to the fermionic nature of nucleons, only half of them are linearly independent operators . Most of the current momentum-space versions of the chiral interaction use

$$\begin{aligned} V_{\text{cont}}^{(2)} =& C_1 q^2 + C_2 q^2 \boldsymbol{\sigma}_1 \cdot \boldsymbol{\sigma}_2 + C_3 k^2 + C_4 k^2 \boldsymbol{\sigma}_1 \cdot \boldsymbol{\sigma}_2 \\ &+ C_5 (\boldsymbol{\sigma}_1 + \boldsymbol{\sigma}_2)(\mathbf{q} \times \mathbf{k}) + C_6 (\boldsymbol{\sigma}_1 \cdot \mathbf{q})(\boldsymbol{\sigma}_2 \cdot \mathbf{q}) + C_7 (\boldsymbol{\sigma}_1 \cdot \mathbf{k})(\boldsymbol{\sigma}_2 \cdot \mathbf{k}) \,, \end{aligned} \tag{2.12}$$

with $\mathbf{k} = (\mathbf{p}' + \mathbf{p})/2$ the momentum transfer in the exchange channel.

The intermediate- and long-range contributions at this order come from two-pion exchange (TPE) contributions. In general, pion-exchange contributions can be expressed in an operatorial decomposition

$$\begin{aligned} V_{\text{TPE}} =& V_C + W_C \boldsymbol{\tau}_1 \cdot \boldsymbol{\tau}_2 + (V_S + W_S \boldsymbol{\tau}_1 \cdot \boldsymbol{\tau}_2) \boldsymbol{\sigma}_1 \cdot \boldsymbol{\sigma}_2 + (V_T + W_T \boldsymbol{\tau}_1 \cdot \boldsymbol{\tau}_2) \boldsymbol{\sigma}_1 \cdot \mathbf{q} \boldsymbol{\sigma}_2 \cdot \mathbf{q} \\ & (V_{LS} + W_{LS} \boldsymbol{\tau}_1 \cdot \boldsymbol{\tau}_2)(i\boldsymbol{\sigma}_1 + \boldsymbol{\sigma}_2) \cdot \mathbf{q} \times \mathbf{k} + (V_{\sigma L} + W_{\sigma L} \boldsymbol{\tau}_1 \cdot \boldsymbol{\tau}_2) \boldsymbol{\sigma}_1 \cdot \mathbf{q} \times \mathbf{k} \boldsymbol{\sigma}_2 \cdot \mathbf{q} \times \mathbf{k} \,. \end{aligned} \tag{2.13}$$

These pion exchanges contain loops that need to be regularized. This is done in the spectral-function representation using a cutoff $\tilde{\Lambda}$.

$$W_C^{(2)}(q) = -\frac{1}{384\pi^2 f_\pi^2} L^{\tilde{\Lambda}}(q) \left( 4m_\pi^2 (5g_A^4 - 5g_A^2 - 1) + q^2 (23g_A^4 - 10g_A^2 - 1) + \frac{48 g_A^4 m_\pi^4}{4m_\pi^2 + q^2} \right) , \tag{2.14}$$

where $L^{\tilde{\Lambda}}(q)$ is the loop function given by

$$L^{\tilde{\Lambda}}(q) = \Theta(\tilde{\Lambda} - 2m_\pi) \frac{\sqrt{q^2 + 4m_\pi^2}}{2q} \ln \left( \frac{\left( \tilde{\Lambda}^2 \sqrt{q^2 + 4m_\pi^2} + q^2 \sqrt{q^2 - 4m_\pi^2} \right)^2}{(4m_\pi^2 \tilde{\Lambda}^2 + q^2)} \right) \tag{2.15}$$

with $\Theta$ the Heaviside step function.

The additional terms that contribute to the TPE at NLO read

$$V_T^{(2)}(q) = -\frac{3g_A^4}{64\pi^2 f_\pi^4} L^{\tilde{\Lambda}}(q) \,, \tag{2.16}$$

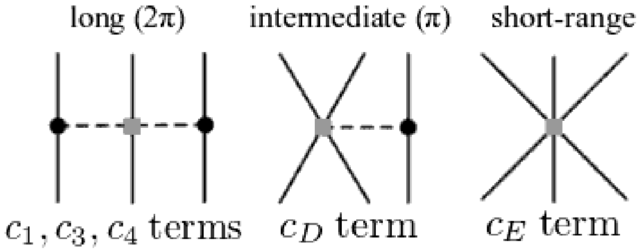

**Figure 2.3:** Three-nucleon interaction topologies at N$^2$LO. The long-range TPE depends on three LECs: $c_1$, $c_3$ and $c_4$, the intermediate-range contact-one-pion-exchange part on $c_D$, and the short-range contact interaction on $c_E$.

$$V_S^{(2)}(q) = -q^2 V_T^{(2)}(q)\,. \tag{2.17}$$

At N$^2$LO there are no additional contact interactions. Subleading TPE contributions are given by

$$V_C^{(3)}(q) = -\frac{3g_A^2}{16\pi f_\pi^4}\left(2m_\pi^2(2c_1 - c_3) - c_3 q^2\right)(2m_\pi^2 + q^2)A^{\tilde{\Lambda}}(q)\,, \tag{2.18}$$

$$W_T^{(3)}(q) = -\frac{g_A^2}{32\pi f_\pi^4} c_4 (4m_\pi^2 + q^2)A^{\tilde{\Lambda}}(q)\,, \tag{2.19}$$

$$W_S^{(3)}(q) = -q^2 W_T^{(3)}(q)\,, \tag{2.20}$$

where $c_i$ denote the LECs of pion-nucleon vertices at this order and $A^{\tilde{\Lambda}}(q)$ is the loop function defined by

$$A^{\tilde{\Lambda}}(q) = \Theta(\tilde{\Lambda} - 2m_\pi)\frac{1}{2q}\arctan\frac{q(\tilde{\Lambda} - 2m_\pi)}{2\tilde{\Lambda}m_\pi + q^2}\,. \tag{2.21}$$

### 2.3.3 Three-nucleon interactions at N$^2$LO

Three-nucleon forces in chiral EFT first contribute at N$^2$LO. As depicted in Fig. 2.2, there are three different topologies that contribute to this leading contribution: two-pion exchange, $V_C$, a contact-one-pion-exchange term, $V_D$, and a purely contact interaction, $V_E$. These topologies have associated LECs that are shown in Fig. 2.3.

The long-range term, where $c_1$, $c_3$, and $c_4$ are the same LECs that appear at two-body level in Eq. (2.18)) and (2.19), is given by

$$V_C = \frac{1}{2}\left(\frac{g_A}{2f_\pi}\right)^2 \sum_{i\neq j, j\neq k} \frac{(\boldsymbol{\sigma}_i\cdot\mathbf{q}_i)(\boldsymbol{\sigma}_j\cdot\mathbf{q}_j)}{(q_i^2 + m_\pi^2)(q_j^2 + m_\pi^2)} F_{ijk}^{\alpha\beta}\tau_i^\alpha\tau_j^\beta\,, \tag{2.22}$$

where the function $F_{ijk}^{\alpha\beta}$ is given by

$$F_{ijk}^{\alpha\beta} = \delta^{\alpha\beta}\left[-\frac{4c_1 m\pi^2}{f_\pi^2} + \frac{2c_3}{f_\pi^2}\mathbf{q}_i\cdot\mathbf{q}_j\right] + \frac{c_4}{f_\pi^2}\sum_\gamma \epsilon^{\alpha\beta\gamma}\tau_k^\gamma\boldsymbol{\sigma}_k\cdot(\mathbf{q}_i\times\mathbf{q}_j)\,. \tag{2.23}$$

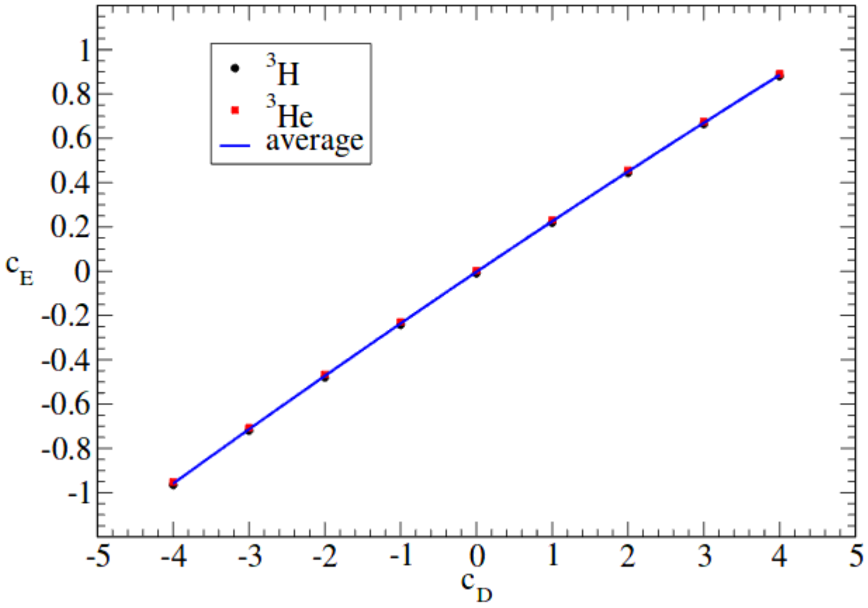

**Figure 2.4:** Trajectories of $c_D$ and $c_E$ from the fitting to $^3$H and $^3$He binding energies. Figure taken from Ref. [105].

The intermediate range, with associated LEC $c_D$, reads

$$V_D = -\frac{g_A}{8f_\pi^2}\frac{c_D}{f_\pi^2\Lambda_\chi}\sum_{i\neq j, j\neq k}\frac{\boldsymbol{\sigma}_j\cdot\mathbf{q}_j}{q_j^2+m_\pi^2}(\boldsymbol{\tau}_i\cdot\boldsymbol{\tau}_j)(\boldsymbol{\sigma}_i\cdot\mathbf{q}_j)\,, \tag{2.24}$$

with $\Lambda_\chi = 700$ MeV. Finally, the contact three-nucleon interaction is given by

$$V_E = \frac{1}{2}\frac{c_E}{f_\pi^4\Lambda_\chi}\sum_{i\neq j\neq k}\boldsymbol{\tau}_i\cdot\boldsymbol{\tau}_j\,. \tag{2.25}$$

Since $c_D$ and $c_E$ are couplings that appear only in the three-nucleon sector, these LECs have using few- or many-body observables. It is common to determine the relation between $c_D$ and $c_E$ by fits to the $^3$H or $^3$He binding energy, as can be seen in Fig. 2.4. Various possibilities to determine the values of these parameters using a second observable can be found in the literature, such as fits to $^3$H and $^4$He binding energies [37, 106], properties of light nuclei [107], $^3$H binding energy and $^3$H $\beta$-decay half-life [108], or $^3$H and $^3$He binding energies [105].

### 2.3.4 Interactions used in this work

For the study of the two-body normal ordered Hamiltonians of Sec. 7, we use three-body interactions at N$^2$LO that are constructed with the operatorial structure detailed above and decomposed in partial waves following Ref. [109]. Using this partial-wave decomposition technique, the value of the LECs for all matrix elements can be chosen freely for the different topologies.

For the comparison of nuclear binding energies and radii in Sec 8.1, we have adopted LECs of the 2.0/2.0 (EM) potential [37]. The Hamiltonian in the two-body sector has been included up to N$^3$LO, while the three-body forces are only accounted for up to N$^2$LO. The LECs used in the latter case are given in Tab. 2.5.

| Interaction | $c_1$ | $c_3$ | $c_4$ | $c_D$ | $c_E$ |
|---|---|---|---|---|---|
| 2.0/2.0 (EM) | -0.81 | -3.2 | 5.4 | 1.271 | -0.131 |

**Table 2.4:** LECs for the EM 500 2.0/2.0 interaction. $c_1$, $c_3$, and $c_4$ are given in GeV$^{-1}$. $c_D$ and $c_E$ are dimensionless, and they were fit to the $^3$H binding energy and the point charge radius of $^4$He.

Finally, for benchmarks and calculations in Sec. 8.2, we use two-body interactions of the Epelbaum, Glöckle and Meißner (EGM) family [110]. The LECs from the two-body sector are $c_1 = -0.81$, $c_3 = -3.4$, and $c_4 = 3.4$ GeV$^{-1}$ [111]. In the naming of these Hamiltonians one can find the cutoff of regulator function $\Lambda$ as the first number, while the second number denotes the spectral function cutoff $\tilde{\Lambda}$. $c_D$ and $c_E$ are determined using the $^3$H binding energy and the coherent $nd$ scattering length $b_{nd}$ [111]. Their values for the different cutoffs used in this work are given in Tab. 2.5.

| $\Lambda/\tilde{\Lambda}$ | $c_D$ | $c_E$ |
|---|---|---|
| 450/500 | 0.140 | -0.319 |
| 600/500 | -4.700 | -2.124 |
| 550/600 | -0.450 | -0.798 |
| 450/700 | 2.430 | 0.113 |

**Table 2.5:** Results for the $c_D$ and $c_E$ couplings. Values obtained using the $^3$H binding energy and the coherent $nd$ scattering length $b_{nd}$. Values from Ref. [112, 113]

# 3 Local chiral effective field theory interactions

## 3.1 Local formulation of Chiral EFT

As we saw in the previous section, the natural formulation of chiral EFT is in momentum space. Nevertheless, there are some many-body methods like Monte Carlo techniques (see, e.g., Ref. [23] for a recent review) for which it is practical to work with potentials expressed in coordinate space. Another example of applications of $r$-space potentials from chiral EFT are the nucleus-nucleus double-folding potentials presented and discussed in Sec. 5 of this thesis. In this formulation, it is easier if the potentials depend only on the distance between nucleons pairwise, denoted as $|\mathbf{r}| = |\mathbf{r}_i - \mathbf{r}_j|$.

Chiral $NN$ interactions in local form were developed initially in Refs. [114, 115], while the $3N$ expressions were first discussed in Ref. [116]. These potentials are constructed in general by Fourier transforming the interactions to obtain their coordinate-space expressions.

A possible source of nonlocality in chiral interactions is due to contact interactions that depend on the momentum transfer in the exchange channel $\mathbf{k} = (\mathbf{p}' + \mathbf{p})/2$. For this reason, dependencies on the momentum transfer $\mathbf{q} = \mathbf{p}' - \mathbf{p}$, which are local, are chosen as long as it is possible. Currently, local potentials from chiral EFT with two- and three-nucleon contributions are available up to N$^2$LO. Nevertheless, it is possible to construct maximally local N$^3$LO interactions that contain, at most, nonlocalities of second order in momentum [117].

The regularization of the potentials is another possible source of nonlocality. For this reason, these potentials are regularized directly in coordinate space. As in the momentum-space representation, a cutoff $\tilde{\Lambda}$ is used in the spectral-function regularization of the TPE, which enters first at NLO. In Refs. [114, 115] it was shown that the calculations are practically insensitive to $\tilde{\Lambda}$ for local interactions; in the present work, we will always consider $\tilde{\Lambda} = 1000$ MeV.

### 3.1.1 Real space conventions

Before discussing the expressions for $NN$ and $3N$ interactions in local form, it is useful to introduce the definitions of some functions that will be used throughout this section. As mentioned, $\mathbf{r}$ denotes the distance between two nucleons, and we introduce the following functions:

$$Y(r) = \frac{e^{-m_\pi r}}{r}\,, \tag{3.1a}$$

$$U(r) = 1 + \frac{1}{m_\pi r}\,, \tag{3.1b}$$

$$T(r) = 1 + \frac{3}{m_\pi r} + \frac{3}{(m_\pi r)^2}\,, \tag{3.1c}$$

$$S_{ij}(\mathbf{r}) = 3\frac{\boldsymbol{\sigma}_i \cdot \mathbf{r}}{r}\frac{\boldsymbol{\sigma}_j \cdot \mathbf{r}}{r} - \boldsymbol{\sigma}_i \cdot \boldsymbol{\sigma}_j\,, \tag{3.1d}$$

$$X_{ij}(\mathbf{r}) = \left(S_{ij}(\mathbf{r})T(r) + \boldsymbol{\sigma}_i \cdot \boldsymbol{\sigma}_j\right) Y(r)\,, \tag{3.1e}$$

where $S_{ij}$ is the tensor operator in coordinate space, $Y$ the standard Yukawa function and $X_{ij}$ denotes the OPE coordinate-space function.

## 3.2 Two-nucleon interactions up to N$^2$LO

In the following, we will present the expressions for local $NN$ potentials up to N$^2$LO.

In this work, the local potentials also follow Weinberg's power counting [17]. Therefore, LO contributions arise from contact interactions and OPE. We have for the short-range contribution

$$V_{\text{cont}}^{(0)}(\mathbf{r}) = (C_S + C_T \boldsymbol{\sigma}_i \cdot \boldsymbol{\sigma}_j)\delta(\mathbf{r})\,, \tag{3.2}$$

where the delta function emphasizes the contact nature of the potential. In coordinate space, pion exchanges can also be expressed as a sum of intermediate and long-range contributions to the potential. The analogue of Eq. (2.13) as a function of the distance $r$ between nucleons is given by

$$\begin{aligned} V_{\text{long}}(r) =& V_C(r) + [V_S(r) + W_S(r)\boldsymbol{\tau}_i \cdot \boldsymbol{\tau}_j]\boldsymbol{\sigma}_i \cdot \boldsymbol{\sigma}_j \\ &+ W_C(r)\boldsymbol{\tau}_i \cdot \boldsymbol{\tau}_j + [V_T(r) + W_T(r)\boldsymbol{\tau}_i \cdot \boldsymbol{\tau}_j]S_{ij}\,, \end{aligned} \tag{3.3}$$

The long- and intermediate-range contributions from the OPE are written as

$$W_S^{(0)}(r) = \frac{m_\pi^3}{12\pi}\left(\frac{g_A}{2f_\pi}\right)^2 Y(r)\,, \tag{3.4}$$

$$W_T^{(0)}(r) = \frac{m_\pi^3}{12\pi}\left(\frac{g_A}{2f_\pi}\right)^2 Y(r)T(r)\,. \tag{3.5}$$

In this case, the part of the OPE arising from the transformation of Eq. (2.11) proportional to the delta function is absorbed in the LECs of the contact interaction. It is also possible to incorporate isospin-symmetry-breaking corrections at all orders, even though they will not be used for the applications of this thesis. For details on these terms, we refer to Ref. [115].

As mentioned in Sec. 2.3, at NLO there are 14 different contributions for the contact interactions, of which only 7 are linearly independent. To construct the short-range part of local potentials, only contact operators with $q$ dependence are chosen. Since there are only 6 purely $q$ dependent possible terms, the seventh term is chosen to be proportional to the spin-orbit interaction ($\mathbf{q} \times \mathbf{k}$). Even though this term is not strictly local, the nonlocality is treatable introducing coordinate derivatives. Taking this into account, the contact interaction at NLO takes the following form

$$\begin{aligned} V_{\text{cont}}^{(2)}(\mathbf{r}) =& -(C_1 + C_2\boldsymbol{\tau}_i \cdot \boldsymbol{\tau}_j)\Delta\delta(\mathbf{r}) - (C_3 + C_4\boldsymbol{\tau}_i \cdot \boldsymbol{\tau}_j)\boldsymbol{\sigma}_i \cdot \boldsymbol{\sigma}_j \Delta\delta(\mathbf{r}) + C_5 \frac{\partial_r \delta(\mathbf{r})}{2r}\mathbf{L} \cdot \mathbf{S} \\ &+ (C_6 + C_7\boldsymbol{\tau}_i \cdot \boldsymbol{\tau}_j)\left[(\boldsymbol{\sigma}_i \cdot \hat{\mathbf{r}})(\boldsymbol{\sigma}_j \cdot \hat{\mathbf{r}})\left(\frac{\partial_r \delta(\mathbf{r})}{r} - \partial_r^2 \delta(\mathbf{r})\right) - \boldsymbol{\sigma}_i \cdot \boldsymbol{\sigma}_j \frac{\partial_r \delta(\mathbf{r})}{r}\right]\,. \end{aligned} \tag{3.6}$$

The TPE contributions are also regularized in the spectral function scheme

$$V_C^{(\nu)}(r) = \frac{1}{2\pi^2 r}\int_{2m_\pi}^{\tilde{\Lambda}} d\mu \mu e^{-\mu r} \rho_C^{(\nu)}(\mu)\,, \tag{3.7}$$

$$V_S^{(\nu)}(r) = -\frac{1}{6\pi^2 r}\int_{2m_\pi}^{\tilde{\Lambda}} d\mu \mu e^{-\mu r}\left(\mu^2\rho_T^{(\nu)}(\mu) - 3\rho_S^{(\nu)}(\mu)\right), \tag{3.8}$$

$$V_T^{(\nu)}(r) = -\frac{1}{3\pi^2 r^3}\int_{2m_\pi}^{\tilde{\Lambda}} d\mu \mu e^{-\mu r}\rho_T^{(\nu)}(\mu)\left(3 + 3\mu r + \mu^2 r^2\right), \tag{3.9}$$

with $\nu$ the index that denotes the order of the potential in Weinberg's powercounting. $\rho_C^{(\nu)}$, $\rho_S^{(\nu)}$ and $\rho_T^{(\nu)}$ are the corresponding spectral functions. The expressions for $W_C^{(\nu)}$, $W_S^{(\nu)}$ and $W_T^{(\nu)}$ are analogous to those of $V_i$ substituting the spectral functions by $\eta_C^{(\nu)}$, $\eta_S^{(\nu)}$, and $\eta_T^{(\nu)}$ respectively. The exact expressions for all the spectral functions can be found in Ref. [115].

At NLO, only $\rho_S^{(2)}$, $\rho_T^{(2)}$, and $\eta_C^{(2)}$ are non-vanishing. The expressions for the corresponding contributions to the potential are

$$V_S^{(2)}(r) = -\frac{1}{6\pi^2 r}\int_{2m_\pi}^{\tilde{\Lambda}} d\mu e^{-\mu r} 4\mu^2 \frac{3g_A^4}{128\pi F_\pi^4}\sqrt{\mu^2 - 4m_\pi^2}, \tag{3.10}$$

$$V_T^{(2)}(r) = -\frac{1}{6\pi^2 r^3}\int_{2m_\pi}^{\tilde{\Lambda}} d\mu e^{-\mu r}\left(3 + 3\mu r + \mu^2 r^2\right)\frac{3g_A^4}{128\pi F_\pi^4}\sqrt{\mu^2 - 4m_\pi^2}, \tag{3.11}$$

$$\begin{aligned} W_C^{(2)}(r) = &\frac{1}{2\pi^2 r}\int_{2m_\pi}^{\tilde{\Lambda}} d\mu e^{-\mu r}\frac{\sqrt{\mu^2 - 4m_\pi^2}}{768\pi F_\pi^4}\left(4m_\pi^2\left(5g_A^4 - 4g_A^2 - 1\right)\right. \\ &\left. -\mu^2\left(23g_A^4 - 10g_A^2 - 1\right) + \frac{48g_A^4 m_\pi^4}{4m_\pi^4 - \mu^2}\right). \end{aligned} \tag{3.12}$$

Finally, at N$^2$LO, the long-range contributions are $V_C^{(3)}$, $W_T^{(3)}$ and $W_S^{(3)}$. They have the same formal expressions as their equivalent at NLO, with corresponding spectral functions. In this case, all the integrals can be carried out analytically. Defining $x \equiv m_\pi r$ and $y \equiv \tilde{\Lambda} r$, they read

$$\begin{aligned} V_C^{(3)}(r) = &\frac{3g_A^2}{32\pi^2 f_\pi^4}\frac{e^{-2x}}{r^6}\left[2c_1 x^2(1+x)^2 + c_3(6 + 12x + 10x^2 + 4x^3 + x^4)\right] \\ &- \frac{3g_A^2}{128\pi^2 f_\pi^4}\frac{e^{-y}}{r^6}\left[4c_1 x^2\left(2 + y(2+y) - 2x^4\right) + c_3\left(24 + y(24 + 12y + 4y^2 + y^3)\right.\right. \\ &\left.\left. -4x^2(2 + 2y + y^2) + 4x^4\right)\right], \end{aligned} \tag{3.13}$$

$$\begin{aligned} W_S^{(3)}(r) = &\frac{g_A^2}{48\pi^2 f_\pi^4}\frac{e^{-2x}}{r^6}c_4(1+x)(3 + 3x + 2x^2) \\ &- \frac{g_A^2}{384\pi^2 f_\pi^4}\frac{e^{-y}}{r^6}c_4\left(24 + 24y + 12y^2 + 4y^3 + y^4 - 4x^2(2 + 2y + y^2)\right), \end{aligned} \tag{3.14}$$

$$\begin{aligned} W_S^{(3)}(r) = &\frac{g_A^2}{48\pi^2 f_\pi^4}\frac{e^{-2x}}{r^6}c_4(1+x)(3 + 3x + x^2) \\ &+ \frac{g_A^2}{768\pi^2 f_\pi^4}\frac{e^{-y}}{r^6}c_4\left(48 + 48y + 24y^2 + 7y^3 + y^4 - 4x^2(8 + 5y + y^2)\right). \end{aligned} \tag{3.15}$$

From these expressions, we can see how, as in their momentum space counterpart, they also carry the LECs dependence: $\rho_C^{(3)}$ depends on $c_1$ and $c_3$, and $\eta_T^{(3)}$ and $\eta_S^{(3)}$ depend on $c_4$.

### Fits of low-energy couplings

These local interactions are fit up to laboratory energies of 50 MeV at LO and up to 150 MeV at NLO and N$^2$LO. In particular, we consider the energies 1, 5, 10, 25, 50, 100, and 150 MeV. The LO interaction is fit to the two $S$-wave channels, while the NLO and N$^2$LO interactions are also constrained by the four $P$-waves and the $^3S_1$–$^3D_1$ mixing angle $\varepsilon_1$, where the notation for the partial waves stands for $^{(2S+1)}L_J$. The partial waves we consider at a certain order are listed below:

LO: $^1S_0$, $^3S_1$,
NLO: $^1S_0$, $^3S_1$, $^1P_1$, $^3P_0$, $^3P_1$, $^3P_2$, $\varepsilon_1$.
At N$^2$LO we use the same energy points and partial waves as at NLO.

### 3.2.1 Regularization scheme

We consider local those interactions whose only dependence is on the relative distance between the nucleons. Therefore, possible sources of nonlocalities need to be identified and avoided. One of these sources appears in the regularization scheme of the interactions. As seen in Sec. 2.3, one of the usual regulator choices is $f(p,p') = e^{-(p/\Lambda)^{2n}} e^{-(p'/\Lambda)^{2n}}$. The Fourier transformation of this function depends on both $\mathbf{r}$ and $\mathbf{r}'$, resulting in nonlocal interactions. For this reason, local interactions are regularized directly in coordinate space using separate functions for the short-range and the long-range parts of the potentials. Long-range interactions in coordinate space need to be regularized since the pion exchange contributions follow the shape of the function $1/r^3$, which diverges for short distances. This long-range regulator reads:

$$f_{\text{long}}(r) = 1 - e^{-(r/R_0)^4} . \tag{3.16}$$

Concerning the short-range interactions, the exact Dirac delta function that indicates their contact nature is replaced by a smeared-out delta function in order to keep the potential finite even for distances going to zero

$$f_{\text{short}}(r) = \frac{e^{-(r/R_0)^4}}{\pi\Gamma(3/4)R_0^3} . \tag{3.17}$$

This kind of regularization implies that every $Y$ or $X_{ij}$ function is multiplied by $f_{\text{long}}$ and any delta functions that arise must be replaced by smeared-out ones of the form $f_{\text{short}}$.

The coordinate-space cutoff $R_0$ has an approximate correspondence with the momentum-space cutoff, $\Lambda$. They are connected by an anti-proportional relation: roughly speaking, the momentum-space cutoff $\Lambda$ determines an upper limit for momenta, so, naturally, one would like to choose it as large as possible to include also high-momentum physics. This would mean the coordinate-space cutoff $R_0$ should be taken as small as possible. On the other hand, $R_0$ cannot be made arbitrarily small as one would meet difficulties related to infinity appearances. Consequently, one usually chooses $R_0$ between 1.0 and 1.6 fm (see Sec. 5.3.1). Local potentials with $R_0 = 1.0$ and 1.2 fm were determined in previous work [115], while the potentials with the cutoffs 1.4 and 1.6 fm are new from this work [118].

In the following we will also detail the local representation of $3N$ interactions at N$^2$LO. In this case, the regularization is done in the same fashion described above for two-nucleon interactions, using $R_{3N}$ as the cutoff, which is chosen consistently with the choices made in the two-body sector.

## 3.3 Three-nucleon interactions at N$^2$LO

The potentials $V_C$, $V_D$, and $V_E$ from Eq. (2.23), (2.24), and (2.25) must be Fourier transformed to coordinate space.

For the two-pion exchange term $V_C$, Fourier transformations are done with respect to momentum transfers of the first and third particle, yielding potentials depending on $\mathbf{r}_{ij}$ and $\mathbf{r}_{kj}$. The transformation to coordinate space yields 3 terms, each one of them dependent on only one LEC:

$$V^{ijk}_{C,c_1} = \frac{c_1 m_\pi^4 g_A^2}{2 f_\pi (4\pi)^2} \sum_{i<j<k} \sum_{\text{cyc}} \boldsymbol{\tau}_i \cdot \boldsymbol{\tau}_k \boldsymbol{\sigma}_i \cdot \hat{\mathbf{r}}_{ij} \boldsymbol{\sigma}_k \cdot \hat{\mathbf{r}}_{kj} \, U(r_{ij}) Y(r_{ij}) U(r_{kj}) Y(r_{kj}), \tag{3.18}$$

$$\begin{aligned} V^{ijk}_{C,c_3} = \frac{c_3 g_A^2}{36 f_\pi^4} \sum_{i<j<k} \sum_{\text{cyc}} \boldsymbol{\tau}_i \cdot \boldsymbol{\tau}_k \Bigg[ & \frac{m_\pi^4}{(4\pi)^2} X_{ij}(\mathbf{r}_{ij}) X_{kj}(\mathbf{r}_{kj}) - \frac{m_\pi^2}{4\pi} X_{ik}(\mathbf{r}_{ij}) \delta(\mathbf{r}_{kj}) \\ & - \frac{m_\pi^2}{4\pi} X_{ik}(\mathbf{r}_{kj}) \delta(\mathbf{r}_{ij}) + \boldsymbol{\sigma}_i \cdot \boldsymbol{\sigma}_k \delta(\mathbf{r}_{ij}) \delta(\mathbf{r}_{kj}) \Bigg] \end{aligned} \tag{3.19}$$

$$\begin{aligned} V^{ijk}_{C,c_4} = & \frac{c_4 g_A^2}{36 f_\pi^4} \sum_{i<j<k} \sum_{\text{cyc}} \boldsymbol{\tau}_i \cdot (\boldsymbol{\tau}_k \times \boldsymbol{\tau}_j) \Bigg\{ \frac{m_\pi^4}{2i(4\pi)^2} [X_{ij}(\mathbf{r}_{ij}), X_{kj}(\mathbf{r}_{kj})] + \boldsymbol{\sigma}_i \cdot (\boldsymbol{\sigma}_k \times \boldsymbol{\sigma}_j) \delta(\mathbf{r}_{ij}) \delta(\mathbf{r}_{kj}) \\ & - \frac{m_\pi^2}{4\pi} \left[ \boldsymbol{\sigma}_i \cdot (\boldsymbol{\sigma}_k \times \boldsymbol{\sigma}_j) Y(r_{ij}) \big(1 - T(r_{ij})\big) \delta(\mathbf{r}_{kj}) + \boldsymbol{\sigma}_k \cdot (\boldsymbol{\sigma}_j \times \boldsymbol{\sigma}_i) Y(r_{kj}) \big(1 - T(r_{kj})\big) \delta(\mathbf{r}_{ij}) \right] \\ & - \frac{3 m_\pi^2}{4\pi} \left[ \boldsymbol{\sigma}_i \cdot \hat{\mathbf{r}}_{ij} \hat{\mathbf{r}}_{ij} \cdot (\boldsymbol{\sigma}_k \times \boldsymbol{\sigma}_j) Y(r_{ij}) T(r_{ij}) \delta(\mathbf{r}_{kj}) + \boldsymbol{\sigma}_k \cdot \hat{\mathbf{r}}_{kj} \hat{\mathbf{r}}_{kj} \cdot (\boldsymbol{\sigma}_j \times \boldsymbol{\sigma}_i) Y(r_{kj}) T(r_{kj}) \delta(\mathbf{r}_{ij}) \right] \Bigg\} . \end{aligned} \tag{3.20}$$

In the case of the contact-one-pion-exchange term and the purely contact interaction, the transformation is not unique. For the Fourier transform of $V_D$, the regularization of the contact part of the potential with a smeared-out delta introduces an ambiguity: any of the two nucleons could participate in the pion exchange with the third nucleon. For this reason, the transformation can be performed with respect to the two different coordinates, yielding

$$V_{D1} = \frac{g_A c_D m_\pi^2}{96 \pi \Lambda_\chi F_\pi^4} \sum_{i<j<k} \sum_{\text{cyc}} \boldsymbol{\tau}_i \cdot \boldsymbol{\tau}_k \left[ X_{ij}(\mathbf{r}_{kj}) \delta(\mathbf{r}_{ij}) + X_{ik}(\mathbf{r}_{ij}) \delta(\mathbf{r}_{kj}) - \frac{8\pi}{m_\pi^2} \boldsymbol{\sigma}_i \cdot \boldsymbol{\sigma}_k \delta(\mathbf{r}_{ij}) \delta(\mathbf{r}_{kj}) \right]. \tag{3.21}$$

$$V_{D2} = \frac{g_A c_D m_\pi^2}{96 \pi \Lambda_\chi F_\pi^4} \sum_{i<j<k} \sum_{\text{cyc}} \boldsymbol{\tau}_i \cdot \boldsymbol{\tau}_k \left[ X_{ik}(\mathbf{r}_{ik}) - \frac{4\pi}{m_\pi^2} \boldsymbol{\sigma}_i \cdot \boldsymbol{\sigma}_k \delta(\mathbf{r}_{ik}) \right] \left[ \delta(\mathbf{r}_{ij}) + \delta(\mathbf{r}_{kj}) \right] . \tag{3.22}$$

It is interesting to note that Eqs. (3.21) and (3.22) give identical results in the limit in which $\delta$ are Dirac delta functions (or, equivalently, $R_{3N} \to 0$), as we would expect given the nature of this ambiguity. Since the fit of low-energy constants using $R_0 = R_{3N} = 1.2$ fm and $V_{D1}$ is not successful (see Fig 1(a) of Ref. [119]), this form will not be considered.

In the case of $V_E$, since local regulators violate the Fierz-rearrangement freedom (see Ref. [120] for a comprehensive analysis in the two-nucleon sector), the choice of the operatorial dependence of the potential can lead to different results. We present three possibilities that are usually explored.

$$V_{E\tau} = \frac{c_E}{2 f_\pi^4 \Lambda_\chi} \sum_{i<j<k} \sum_{\text{cyc}} \boldsymbol{\tau}_i \cdot \boldsymbol{\tau}_k \delta(\mathbf{r}_{\mathrm{ij}}) \delta(\mathbf{r}_{\mathrm{kj}}), \tag{3.23}$$

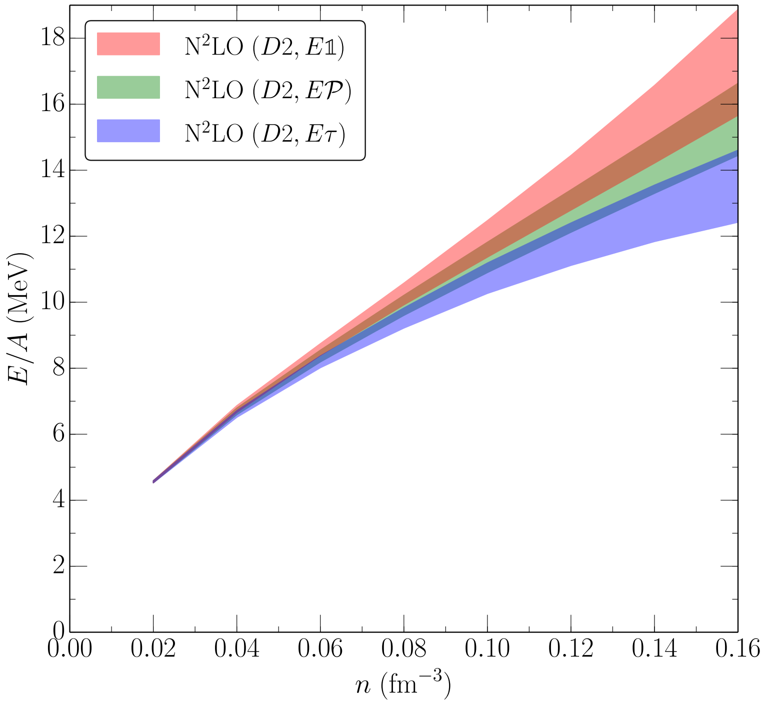

**Figure 3.1:** Energy per particle as a function of the density in neutron matter. Results obtained with the AFDMC method using $NN$ and $3N$ interactions at N$^2$LO using $V_{D2}$ and different dependencies for the contact term: $V_{E\mathbb{1}}$ (red band), $V_{E\mathscr{P}}$ (green band), $V_{E\tau}$ (blue band). The bands reflect the theoretical uncertainty. Figure taken from Ref. [121].

$$V_{E\mathbb{1}} = \frac{c_E}{2f_\pi^4\Lambda_\chi} \sum_{i<j<k} \sum_{\text{cyc}} \delta(\mathbf{r_{ij}})\delta(\mathbf{r_{kj}})\,, \tag{3.24}$$

$$V_{E\mathscr{P}} = \frac{c_E}{2f_\pi^4\Lambda_\chi} \sum_{i<j<k} \sum_{\text{cyc}} \mathscr{P}\,\delta(\mathbf{r_{ij}})\delta(\mathbf{r_{kj}})\,, \tag{3.25}$$

where $\mathscr{P}$ is a projector operator on to triples with $S = 1/2$ and $T = 1/2$, which are the only partial waves that would contribute in the case $R_{3N} \to 0$.

$$\mathscr{P} = \frac{1}{36}\left(3 - \sum_{i<j} \boldsymbol{\sigma}_i \cdot \boldsymbol{\sigma}_j\right)\left(3 - \sum_{k<l} \boldsymbol{\tau}_k \cdot \boldsymbol{\tau}_l\right) \tag{3.26}$$

On the other hand, the first two operatorial structures are chosen because they show radically different properties: $\boldsymbol{\tau}_i \cdot \boldsymbol{\tau}_k$ has negative sign for finite nuclei but is positive in the case of neutron matter, while the sign of the operator $\mathbb{1}$ does not depend on the system studied.

Fig. 3.1 shows the impact of the operator choice for $V_E$ in the AFDMC calculation of the energy per particle in neutron matter. In this study $NN$ and $3N$ interactions at N$^2$LO with $R_0 = R_{3N} = 1.0$ fm were used. Different dependencies for the contact term can be seen in the figure: $V_{E\mathbb{1}}$ (red band), $V_{E\mathscr{P}}$ (green band), $V_{E\tau}$ (blue band). The bands represent the theoretical uncertainty from the chiral

| $R_0$ [fm] | 1.2 fm | | | 1.4 fm | | | 1.6 fm | | |
|---|---|---|---|---|---|---|---|---|---|
| | LO | NLO | N$^2$LO | LO | NLO | N$^2$LO | LO | NLO | N$^2$LO |
| $C_S$ | -1.738 | 0.080 | 2.522 | -2.675 | -0.480 | 1.331 | -3.590 | -0.988 | 0.538 |
| $C_T$ | 0.159 | -0.729 | 0.179 | -0.020 | 0.723 | 0.363 | -0.188 | 0.660 | 0.495 |
| $C_1$ | | 0.212 | -0.108 | | 0.124 | -0.104 | | -0.098 | -0.206 |
| $C_2$ | | 0.209 | 0.054 | | 0.302 | 0.188 | | 0.393 | 0.368 |
| $C_3$ | | -0.156 | -0.167 | | -0.224 | -0.217 | | -0.311 | -0.278 |
| $C_4$ | | 0.092 | 0.103 | | 0.192 | 0.166 | | 0.312 | 0.267 |
| $C_5$ | | -2.112 | -1.911 | | -2.268 | -2.083 | | -2.416 | -2.282 |
| $C_6$ | | 0.343 | 0.205 | | 0.471 | 0.355 | | 0.603 | 0.536 |
| $C_7$ | | -0.376 | -0.328 | | -0.578 | -0.529 | | -0.798 | -0.790 |

**Table 3.1:** Low energy constants for the local cutoffs $R_0$=1.2, 1.4 and 1.6 fm at LO, NLO and N$^2$LO. The LO LECs $C_S$ and $C_T$ are given in fm$^2$, the rest in fm$^4$. Values published in Ref. [118].

expansion, calculated as in Ref. [19]. As it can be seen in the figure, different operatorial structures give three distinct bands that have larger uncertainties as the density increases. At nuclear density ($n = 0.16$ fm$^{-3}$), the spread of the results is significant. This spread needs to be taken into account in the estimation of the theoretical error. It is interesting to notice that the results yielded by $V_{E\mathcal{P}}$ are a good estimation of the values that would be obtained at the following order in the chiral expansion, since this operator only allows the contributions that would be present in the unregularized case (i.e., without $P$-wave mixing into the $S$-wave interaction).

### Fits of low-energy couplings

As specified in the momentum representation of the potential, $c_D$ and $c_E$ are exclusively $3N$ couplings and they are usually fitted to reproduce properties of few-body systems. In the case of $3N$ interactions in local formulation, we will concentrate on fits made to reproduce the $^4$He binding energy and the $P$-wave $n-\alpha$ scattering phase shifts. This choice is made because these two observables are not correlated, and $n-\alpha$ scattering is sensitive to spin-orbit splitting (see Ref. [119] for details on this choice).

### 3.3.1 Interactions used in this work

In order to apply these $NN$ local interactions in nucleus-nucleus potentials used for nuclear reactions (Sec. 5), in addition to the interaction of Ref. [115] with $R_0 = 1.2$ fm we construct softer interactions with cutoffs $R_0 = 1.4$ fm and 1.6 fm. We determine the LECs by fitting to the $np$ phase shifts from the Nijmegen partial wave analysis (PWA) [6]. To this end, we minimize the following $\chi^2$

$$\chi^2 = \sum_i \frac{(\delta_i^{\mathrm{PWA}} - \delta_i^{\mathrm{theo}})^2}{\Delta\delta_i^2}\,, \tag{3.27}$$

computed from the squared difference between the PWA phase shifts and the calculated ones. The uncertainty $\Delta\delta_i^2$ is obtained from the PWA, a model uncertainty, and a numerical error:

$$\Delta\delta_i^2 = (\Delta\delta_i^{\mathrm{PWA}})^2 + (\Delta\delta_i^{\mathrm{mod}})^2 + (\Delta\delta_i^{\mathrm{num}})^2\,. \tag{3.28}$$

For the model uncertainty we use a relative uncertainty multiplied with a constant value [120, 122],

$$\Delta\delta_i^{\text{model, LO}} = \left(\frac{Q}{\Lambda_b}\right)^2 C\,, \tag{3.29}$$

$$\Delta\delta_i^{\text{model, }\nu} = \left(\frac{Q}{\Lambda_b}\right)^{\nu+1} C\,, \tag{3.30}$$

where $Q = \max(m_\pi, p = \sqrt{E_i^{\text{lab}} m_N/2})$ and $C = 1^\circ$. For both cutoffs ($R_0 = 1.4$ fm and 1.6 fm), we take $\Lambda_b = 400$ MeV, which also roughly corresponds to a coordinate-space cutoff $R_0 = 1.4$ fm to get a more conservative uncertainty estimate.

The LECs and the deuteron binding energy obtained for each interaction are given in Table 3.1. All other inputs and conventions for these softer local chiral $NN$ potentials are as in Refs. [114, 115]. The phase shifts for $R_0 = 1.4$ fm are shown in Fig. 3.2; we find similar results with $R_0 = 1.6$ fm. The phase shift reproduction here is comparable to the interactions from Refs. [114, 115].

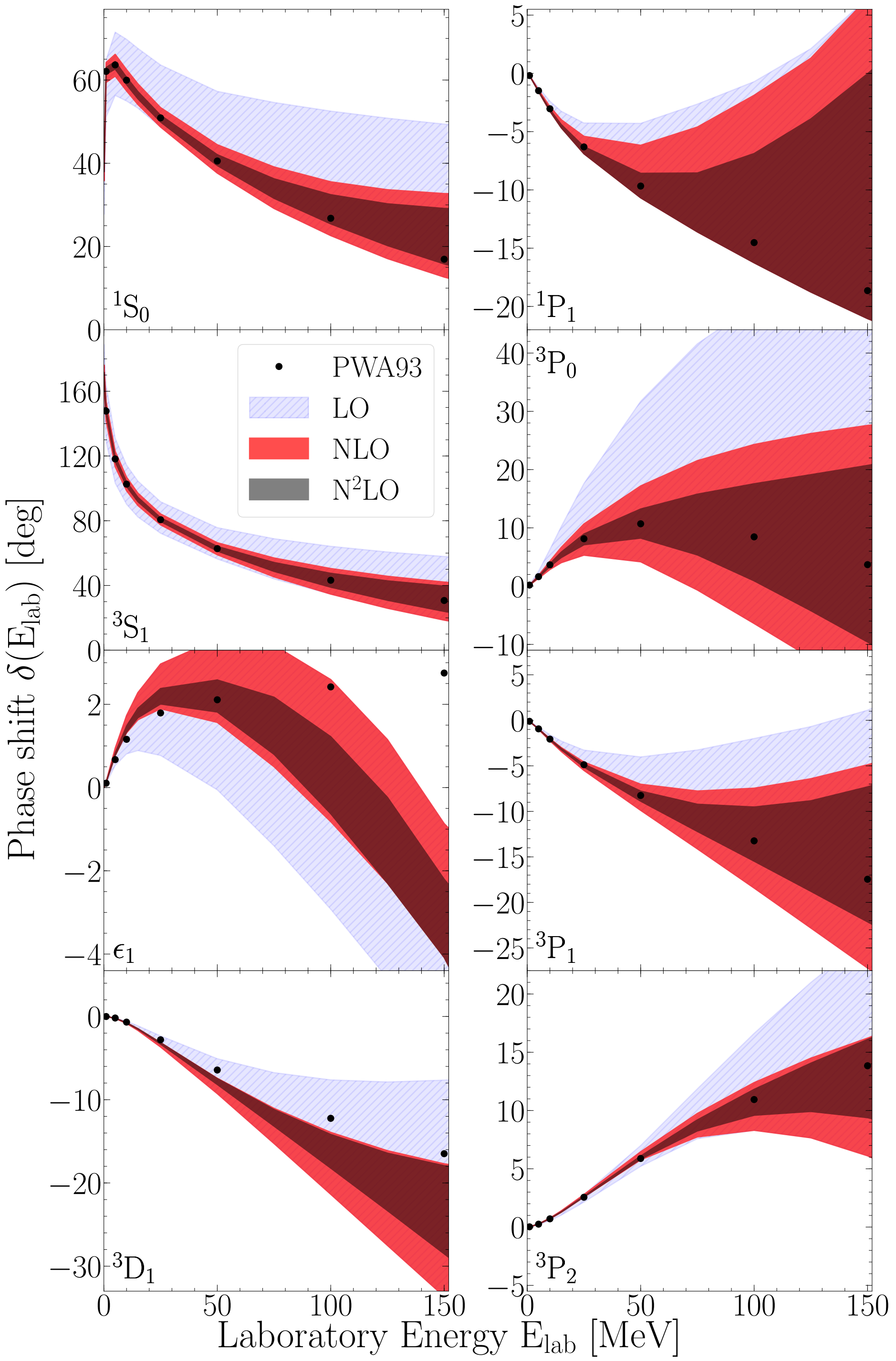

**Figure 3.2:** Phase shifts for $R_0 = 1.4$ fm in different partial waves as a function of laboratory energy. Results are shown for the LO (blue), NLO (red), and N$^2$LO (grey) interactions compared to the Nijmegen partial wave analysis (PWA) [6]. The bands at each order give the theoretical uncertainty as discussed in the text.

# 4 Nucleus-nucleus scattering and reactions

## 4.1 Basic definitions

Let us consider the collision of two nuclei, with a projectile impinging on a fixed target. In this situation, there are different possible scenarios. Schematically, we can represent the reactions between a projectile $A$ and target $B$ as

$$A+B \to C+D+\dots$$

where $C$, $D$, … are the particles resulting from the reaction process.

It is important to notice that the same $A$-$B$ system can have different possible final states. In order to classify those possibilities, we refer to them as channels. A channel is defined by all the particles involved in the collision process, indicating their corresponding energy and mass.

The different kind of reactions that can take place are:

- Elastic scattering: Projectile and target are scattered without any change in their internal structure:

$$A+B \to A+B$$

- Inelastic scattering: produced when there is exchange of energy between the projectile-target relative motion and excitation of one (or both) colliding nuclei, i.e., there is a change of channel between the incoming and the outgoing systems. In general, there are different possibilities for inelastic scattering between two particles

$$A+B \to \begin{cases} A^*+B \\ A+B^* \\ A^*+B^* \end{cases}$$

  where the superscript $^*$ denotes the excited nucleus.

- Pick-up: A part of the target is transferred to the projectile. Defining $B \equiv C+c$ and $D \equiv A+c$:

$$A+B \to C+D$$

- Stripping: A part of the projectile is transferred to the target. Defining $A \equiv C+c$ and $D \equiv B+c$:

$$A+B \to C+D$$

- Break-up: The projectile is fragmented as a result of the collision. Defining $A \equiv C+c$:

$$A+B \to C+c+B$$

- Knock-out: We understand as knock-out a break-up reaction in which $A \equiv C+c$, and neither $B$ nor $c$ are measured (which we denote by $X$):

$$A+B \to C+X$$

- Fusion: The result of the collision is a nucleus formed by the projectile and the target. Defining $F \equiv A+B$:

$$A+B \to F^*$$

### 4.1.1 Scattering Hamiltonian

In this work, we will present a general theory for elastic scattering, thereby neglecting the internal structure of the colliding nuclei and assuming that their interaction can be simulated by a potential $V$, which depends on their relative coordinate $\mathbf{r}$. We will follow Ref. [123] in this section.

We can first consider that particles $A$ and $B$ have mass and coordinate $m_A$ and $\mathbf{r}_A$, and $m_B$ and $\mathbf{r}_B$, respectively. Then, the relative coordinate between the two particles is defined as $\mathbf{r} = \mathbf{r}_A - \mathbf{r}_B$. Thus, the Hamiltonian will read

$$H = T_A + T_B + V(\mathbf{r}) = -\frac{\nabla^2_{r_A}}{2m_A} - \frac{\nabla^2_{r_B}}{2m_B} + V(\mathbf{r}) . \tag{4.1}$$

If we write $M = m_A + m_B$ as the total mass of the system, we can write the coordinate of the center-of-mass reference as

$$\mathbf{r}_{cm} = \frac{m_A \mathbf{r}_A + m_B \mathbf{r}_B}{M} . \tag{4.2}$$

Therefore we can rewrite Eq. (4.1) in terms of $\mathbf{r}$ and $\mathbf{r}_{cm}$ as

$$H = -\frac{\nabla^2_{r}}{2\mu} - \frac{\nabla^2_{r_{cm}}}{2M} + V(\mathbf{r}) , \tag{4.3}$$

where $\mu$ is the reduced mass $\mu = m_A m_B / M$. We can then write the Hamiltonian as a sum of relative and center-of-mass contributions:

$$H = H_{\text{rel}}(\mathbf{r}) + H_{cm}(\mathbf{r}_{cm}) . \tag{4.4}$$

This is an important property, because it ensures that the two-body wave function will factorize into two parts:

$$\psi(\mathbf{r}_A, \mathbf{r}_B) = \psi_{\text{rel}}(\mathbf{r}) \psi_{cm}(\mathbf{r}_{cm}) . \tag{4.5}$$

Since $H_{cm}$ is the Hamiltonian of a free particle, the center-of-mass is in a uniform translation, as we would expect from Galilean invariance. For an initial momentum of the center of mass $\mathbf{k}_{cm}$, the solution is $\psi_{cm} \propto e^{i\mathbf{k}_{cm}\mathbf{r}_{cm}}$, i.e. a plane wave. For a general reaction of the kind $A + B \to C + D + \ldots$ in which the target is fixed, the velocity of the center-of-mass system with respect to that in the laboratory frame, $\mathbf{v}_i$, is [123]

$$\mathbf{v}_{cm} = \frac{m_A}{m_A + m_B} \mathbf{v}_i . \tag{4.6}$$

A schematic representation of both velocities can be found in Fig. 4.1.

The Schrödinger equation for the Hamiltonian of the $A$-$B$ relative motion $H_{\text{rel}} = T_{\text{rel}} + V(\mathbf{r})$, that depends only on the relative coordinate, has a state $\psi_{\mathbf{k}}(\mathbf{r})$ as a solution:

$$H_{\text{rel}} \psi_{\mathbf{k}}(\mathbf{r}) = E \psi_{\mathbf{k}}(\mathbf{r}) , \tag{4.7}$$

where $E = k^2/2\mu$.

The general idea of scattering theory is to solve Eq. (4.7) with boundary conditions for the wave function that recover the experimental situation: an incident plane wave and a spherical outgoing wave, which accounts for the effect of the interaction. This defines stationary scattering states, since these states do not have the usual bound-state condition at $r \to \infty$; if we fix $z$ as the beam axis, the asymptotic behavior of such a state is described by the wave function [77]

$$\psi_{\mathbf{k}}(\mathbf{r}) \underset{r \to \infty}{\longrightarrow} A(k) \left[ e^{ikz} + f(k, \theta, \phi) \frac{e^{ikr}}{r} \right] , \tag{4.8}$$

where $f(k, \theta, \phi)$, known as scattering amplitude, is a generic function that accounts for the effect of the potential in the outgoing wave and $A(k)$ is a normalization factor that can, in general, depend on the momentum transfer $k$.

An illustration of the coordinates that will be used in this section can be found in Fig. 4.2.

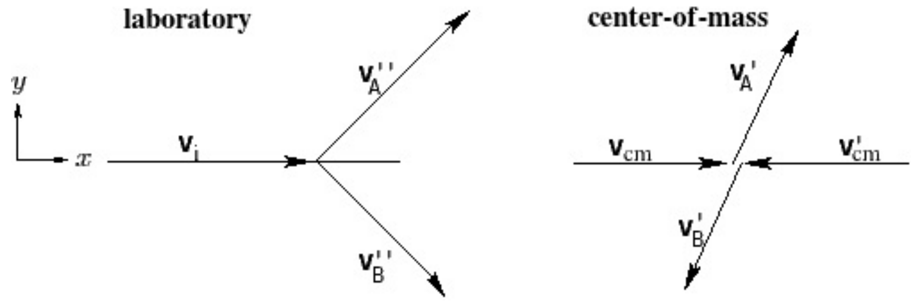

**Figure 4.1:** Schematic representation of the velocities in the laboratory (left) and center-of-mass (right) frames.

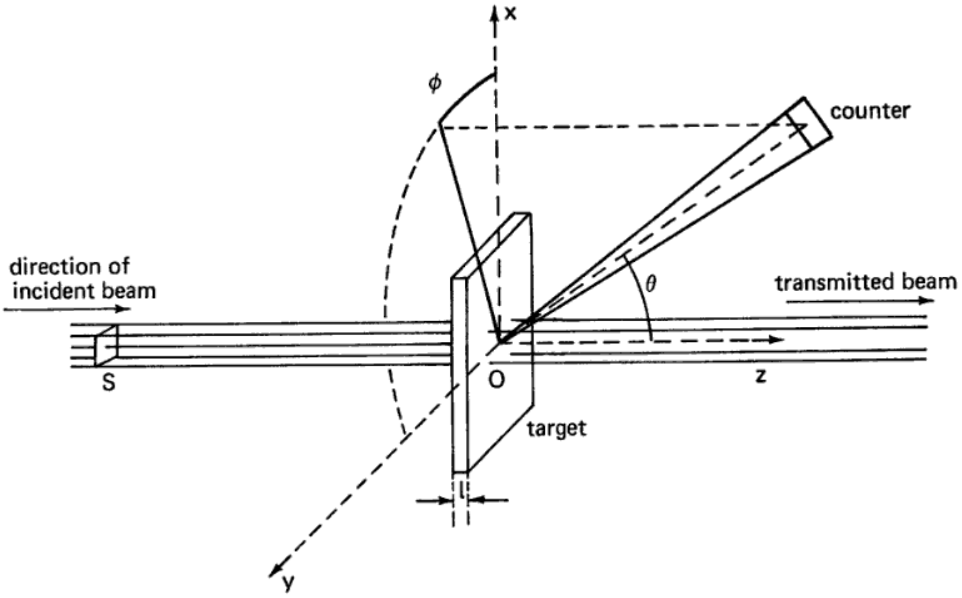

**Figure 4.2:** Illustration of various quantities used in the definition of cross sections. Figure modified from Ref. [77].

## 4.2 Scattering cross section

Cross sections are quantities used to express the results of collision experiments. The cross section of a specific kind of event (elastic, inelastic, fusion...) can be interpreted as the ratio between the probability per unit of time to detect the reaction of interest and the flux of incident particles on the target. We will assume that the experimental setup is equivalent to the one sketched in Fig. 4.2, and that particles $A$ and $B$ in the initial channel are both in well defined quantum states. As seen in the figure, we also assume that the target is a thin layer of thickness $l$ placed perpendicular to the incident beam. We denote by $n_B$ the number of particles $B$ within the target volume interacting with the incident beam of section $S$.

We can define the flux of particles $A$ crossing per unit time a unit area perpendicular to the direction of the incident beam as

$$\Phi_A = \mathcal{N}_A v_i = N_A/S \,, \tag{4.9}$$

where $\mathcal{N}_A$ is the average number of particles $A$ per unit volume in the incident beam, which has an average velocity $\mathbf{v}_i$ with respect to the target, $N_A$ is the number of particles $A$ that reach the target per unit of time, as can be seen in Fig. 4.2. The number of scattering centers in the target is

$$n_B = Sl\mathcal{N}_B\,. \tag{4.10}$$

Here, $\mathcal{N}_B$ is the average number of particles $B$ per unit volume.

Under the experimental conditions assumed here, we denote $dN$ the number of particles $A$ which have interacted per unit time with target scatterers $B$ detected within a solid angle $d\Omega$ centered around $(\theta,\phi)$. This quantity is directly proportional to the flux of particles (Eq. (4.9)) and the number of scatterers $n_B$

$$dN = \frac{d\sigma}{d\Omega}\Phi_A n_B d\Omega\,. \tag{4.11}$$

According to the definition given above, the proportionality quantity $\sigma$ has units of area and is called the cross section. $d\sigma/d\Omega$ is the differential cross section for scattering of particle $A$ by particle $B$. This definition is valid for any process of the kind $A+B \to C+D$, where $N$ would stand for the number of events detected per unit time as result of the channel of interest.

Inverting Eq. (4.11), we obtain $d\sigma/d\Omega$ as a function of $\Phi_A$ and $n_B$. Since the flux of particles, incoming and outgoing, will be, by the statistical point of view of quantum mechanics, proportional to the probability current $\mathbf{J}$, we can relate the differential cross section to probability currents as the ratio between the probability flux $|\mathbf{J}_{\text{scatt}}|$ scattered through an area $dS = r^2 d\Omega$ and the incoming probability flux $|\mathbf{J}_{\text{inc}}|$. For a single scatterer, $n_B = 1$,

$$\frac{d\sigma}{d\Omega} = \frac{dN}{d\Omega}\frac{1}{\Phi_A} = \frac{|\mathbf{J}_{\text{scatt}}|r^2}{|\mathbf{J}_{\text{inc}}|}\,, \tag{4.12}$$

with the probability current defined as $\mathbf{J} = 1/2\mu i\,(\psi^*\nabla\psi - \psi\nabla\psi^*)$ in non-relativistic Quantum Mechanics. In the outgoing spherical wave prescription presented in Eq. (4.8) there are two distinct terms: the first one corresponding to the incoming wave function, and the second to the outgoing scattered one. Computing the probability current for each of the terms of the asymptotic behavior of the wave function (4.8), we obtain

$$\mathbf{J}_{\text{inc}} = \frac{\mathbf{k}}{\mu} = \mathbf{v}_i\,, \tag{4.13}$$

$$\mathbf{J}_{\text{scatt}} = |f(k,\theta,\phi)|^2\frac{k\hat{\mathbf{r}}}{\mu r^2} + \mathcal{O}\left(\frac{1}{r^3}\right), \tag{4.14}$$

where $\hat{\mathbf{r}} = \mathbf{r}/r$ is the unit vector in radial direction. We omit terms beyond $1/r^2$ in the expansion, since in considering the factor $|\mathbf{J}_{\text{scatt}}|r^2 d\Omega$ they will quickly vanish in the asymptotic region outside the range of the potential.

We can see that $\mathbf{J}_{\text{inc}}$ is proportional to $\mathbf{v}_i$, which is what we expect from a probability current representing the incoming projectile. $\mathbf{J}_{\text{scatt}}$ is directed radially outwards, and it is proportional to the norm of the incoming velocity $v_i$, which is what we expect from an elastic scattering process, since there is no exchange of energy with the internal structure of the colliding nuclei.

Taking this into account, from Eq. (4.12) we find a simple relation between the differential cross section and the scattering amplitude $f$:

$$\frac{d\sigma}{d\Omega} = |f(k,\theta,\phi)|^2\,. \tag{4.15}$$

Therefore, the cross-section problem is reduced to the determination of $f$ for each scattering scenario. In the next section, we focus on the partial-wave expansion to compute $f$.

## 4.3 Partial-wave expansion

### 4.3.1 Partial-wave expansion of stationary scattering states

In the following, we will consider the case of short-ranged potentials ($rV \to 0$ for $r \to \infty$), such as the nuclear interaction. For a discussion on cross sections generated by Coulomb interactions, see Sec. 4.5.

If we have a central potential, the Hamiltonian presents spherical symmetry, and we can decompose the wave function into partial waves,

$$\psi_{\mathbf{k}}(\mathbf{r}) = \sum_{LM} C_{LM} u_L(r) Y_{LM}(\hat{\mathbf{r}}), \tag{4.16}$$

where $Y_{LM}$ are the spherical harmonic functions and $C_{LM}$ are expansion coefficients. Since we are working with spherically symmetric and spinless systems, we can set $\mathbf{k} = k\hat{\mathbf{z}}$, and therefore is no $\phi$ dependence. Carrying out the sum on $M$ the wave function of Eq. (4.16) can also be written in terms of Legendre polynomials,

$$\psi_{\mathbf{k}}(r,\theta) = \sum_{L} C_L (2L+1) i^L u_L(r) P_L(\cos\theta), \tag{4.17}$$

Introducing the partial-wave expansion (4.17) into the Schrödinger equation (4.7), the radial wave function $u_L$ for each orbital angular momentum $L$ is solution of

$$\left[-\frac{1}{2\mu}\frac{d^2}{dr^2} + \frac{L(L+1)}{2\mu r^2} + V(r)\right] u_L(r) = E u_L(r). \tag{4.18}$$

As a result, we have a one-dimensional problem for each $L$, and the asymptotic expansion of $u_L$ can be written as a linear combination of spherical Bessel functions as

$$u_L(r) \xrightarrow[r\to\infty]{} A_L(k) j_L(kr) + B_L(k) n_L(kr), \tag{4.19}$$

where $j_L$ and $n_L$ are spherical Bessel functions of the first and second kind, respectively. We can substitute these functions by their asymptotic behavior.

$$\begin{cases} j_L(kr) \xrightarrow[r\to\infty]{} \frac{\sin(kr - L\pi/2)}{kr}, \\ n_L(kr) \xrightarrow[r\to\infty]{} \frac{\cos(kr - L\pi/2)}{kr}. \end{cases} \tag{4.20}$$

Taking into account the relation $A\sin(x) + B\cos(x) = \sqrt{A^2+B^2}\sin(x+\delta)$, where $\delta$ is a phase shift, and renaming the expansion coefficient $C_L\sqrt{A_L^2(k)+B_L^2(k)} \equiv \tilde{C}_L(k)$, the asymptotic form of Eq. (4.17) reads

$$\psi_{\mathbf{k}}(r,\theta) \xrightarrow[r\to\infty]{} \sum_L \tilde{C}_L(k)(2L+1) i^L \sin\left(kr - \frac{L\pi}{2} + \delta_L(k)\right) P_L(\cos\theta). \tag{4.21}$$

To determine $\tilde{C}_L$, the wave function can also be written as the combination of incoming plane wave and outgoing spherical wave (Eq. (4.8))

$$\psi_{\mathbf{k}}(r,\theta) \xrightarrow[r\to\infty]{} A(k)\left[e^{ikz} + f(k,\theta)\frac{e^{ikr}}{r}\right]. \tag{4.22}$$

Using Raileigh's formula [124], $e^{ikz}$ can be expanded in Legendre polynomials,

$$e^{ikz} = \sum_L (2L+1) i^L j_L(kr) P_L(\cos\theta), \tag{4.23}$$

where $j_L$ are spherical Bessel functions of the first kind. The scattering amplitude can also be expanded in partial waves as a function of $P_L$

$$f(k,\theta) = \sum_L (2L+1) f_L(k) P_L(\cos\theta). \tag{4.24}$$

Inserting (4.23) and (4.24) into Eq. (4.22) leads to

$$\psi_k(r,\theta) \underset{r\to\infty}{\longrightarrow} A(k) \left[ \sum_L (2L+1) \left[ i^L \frac{\sin(kr - L\pi/2)}{kr} + f_L(k) \frac{e^{ikr}}{r} \right] P_L(\cos\theta) \right]. \tag{4.25}$$

To determine $f_L$, we can compare Eqs. (4.25) and (4.21). Expressing the sin functions in its exponential form, we get that

$$1 + 2ikf_L(k) = e^{2i\delta_L(k)}, \tag{4.26}$$

where $\delta_L(k)$ are the phase shifts of the wave function in $L$ wave (which are measured in radians or degrees). Alternatively, we can also define the $S$-matrix elements,

$$S_L(k) = e^{2i\delta_L(k)}. \tag{4.27}$$

Therefore, in terms of the $S$-matrix we can differentiate two terms in the asymptotic behavior of the wave function:

$$\begin{aligned} \psi_k(r,\theta) \underset{r\to\infty}{\longrightarrow} & -\frac{e^{-ikr}}{r}\frac{1}{2ik}\sum_L (2L+1)(-1)^L P_L(\cos\theta) \\ & \frac{e^{ikr}}{r}\frac{1}{2ik}\sum_L (2L+1) S_L P_L(\cos\theta). \end{aligned} \tag{4.28}$$

Eq. (4.28) is the sum of an incoming spherical wave and an outgoing spherical wave. The latter is modified from the former one just by $S_L$, hence it is phaseshifted.

### 4.3.2 Cross section

We can now derive the differential cross section:

$$\frac{d\sigma}{d\Omega} = |f(k,\theta)|^2 = \left| \frac{1}{2ik} \sum_L (2L+1) P_L(\cos\theta)(S_L - 1) \right|^2. \tag{4.29}$$

And the integrated cross section can be simply defined as

$$\sigma = 2\pi \int d(\cos\theta) \left| \frac{1}{2ik} \sum_L (2L+1) P_L(\cos\theta)(S_L - 1) L \right|^2. \tag{4.30}$$

This integral can be performed thanks to the orthogonality relation of the Legendre polynomials

$$\int_{-1}^{1} P_L(x) P_{L'}(x) dx = \delta_{LL'} \frac{2}{2L+1}, \tag{4.31}$$

leading to the integrated cross section as a function of the momentum $k$, the angular momentum $L$ and the S-matrix elements

$$\sigma = \frac{\pi}{k^2} \sum_L (2L+1) |S_L - 1|^2 \tag{4.32}$$

We concentrate now on the forward direction of the scattering flux ($\theta = 0$). Since $f$ is complex, we can interpret what its imaginary part means. The optical theorem states that the imaginary part of the scattering amplitude is related to the "shadow" casted by the potential. From Eq. (4.29):

$$\mathrm{Im}(f(k,\theta)) = \mathrm{Im}\left(\sum_L (2L+1)\frac{e^{i\delta_L(k)}\sin\delta_L(k)}{k}P_L(\cos\theta)\right) = k\sum_L (2L+1)\frac{\sin^2\delta_L(k)}{k^2}P_L(\cos\theta)\,. \tag{4.33}$$

Comparing Eqs. (4.32) and (4.33) and considering that $P_L(1) = 1$, we can identify

$$\mathrm{Im}(f(k,\theta=0)) = \frac{k}{4\pi}\sigma(k)\,. \tag{4.34}$$

This is the optical theorem [125], and it is a direct consequence of the conservation of the probability flux. This means that the imaginary part of $f$ gives a contribution to the total cross section that comes from destructive interference between the incoming wave and the outgoing wave. This is why it is said that the potential "casts a shadow".

## 4.4 Optical potential method

Analogously to the method applied in Optics to analyze the propagation of light through a refractive medium, where a complex refractive index is used to account for the absorption of light in the medium, a complex potential can be used to simulate absorption from the elastic channel in nuclear reactions. Usually, at sufficiently large energy, other channels are open, and some probability flux can populate these channels instead of the elastic one. The optical potential approach enables us to model the particles that leave the elastic channel by an absorption channel instead of describing these reactions explicitly in the reaction models.

A first application of this idea to study $\alpha$-decay was made by Ostrofsky, Breit and Johnson in 1936 [126], and was continued by H. A. Bethe in 1940 [127] who applied an optical potential for compound nuclei scattering at low energy. In 1947, this approach was generalized by R. Serber [128] to describe high energy elastic nucleon-nucleus scattering in terms of nucleon-nucleon collisions using their known cross sections.

The introduction of an optical potential to describe elastic scattering is based on the fact that it can be formally considered as the potential scattering of two particles without structure, since no internal degrees of freedom are considered. The main idea of this method is to reduce the complex process of scattering to a one-body problem by substituting the interactions between composed projectile and target by a suitable optical potential. In general, optical potentials are non-local, complicated operators with complex values difficult to determine from first principles. Nevertheless, phenomenological potentials of this kind are widely used to study elastic scattering, traditionally fitted to Woods-Saxon form factors [78], parametrized to reproduce elastic-scattering data, or obtained from inversion of electron scattering data [129], amongst other techniques.

We consider now the case in which particles can be removed from the incident elastic channel. Therefore, the amplitude of the outgoing wave has to be either left unchanged (case that corresponds to purely elastic scattering), or reduced (if there are non-elastic processes involved).

Considering that the total cross section will be composed of the sum of all elastic and all non-elastic processes, we can write

$$\sigma_{\mathrm{tot}} = \sigma^{\mathrm{el}}_{\mathrm{tot}} + \sigma^{\text{non-el}}_{\mathrm{tot}}\,. \tag{4.35}$$

where we identify the cross section derived in Eq. (4.32) as the total elastic cross section.

If we assume that there is a dispersive center that removes particles form the elastic channel, for $\sigma_{\text{tot}}^{\text{non-el}}$ to be non-vanishing, there must be a difference between the current density that enters the dispersive center $|\mathbf{J}_{\text{ent}}|$ and the current density that leaves it $|\mathbf{J}_{\text{out}}|$. We can then write

$$\frac{d\sigma_{\text{tot}}^{\text{non-el}}}{d\Omega} = \frac{\frac{|\mathbf{J}_{\text{ent}}|-|\mathbf{J}_{\text{out}}|}{d\Omega} r^2 d\Omega}{|\mathbf{J}_{\text{inc}}|} . \tag{4.36}$$

We can divide Eq. (4.28) into two contributions to the wave function. The first one corresponds to the system before interacting with the dispersive center

$$\psi_{\text{ent}} \xrightarrow[r\to\infty]{} \frac{e^{-ikr}}{r} \frac{1}{2ik} \sum_L (2L+1)(-1)^L P_L(\cos\theta) , \tag{4.37}$$

while the second part of the wave function describes the system after the scattering

$$\psi_{\text{out}} \xrightarrow[r\to\infty]{} \frac{e^{ikr}}{r} \frac{1}{2ik} \sum_L (2L+1) S_L P_L(\cos\theta) . \tag{4.38}$$

Therefore, the difference in current densities reads

$$|\mathbf{J}_{\text{ent}}| - |\mathbf{J}_{\text{out}}| = \frac{1}{4\mu k r^2} \sum_L \sum_{L'} (2L+1)(2L'+1) \left[ (-1)^{L+L'} - S_L S_{L'}^* \right] P_L(\cos\theta) P_{L'}(\cos\theta) . \tag{4.39}$$

Leading to the differential cross section for non-elastic processes (or absorption)

$$\frac{d\sigma_{\text{tot}}^{\text{non-el}}}{d\Omega} = \frac{1}{4k^2} \sum_{LL'} (2L+1)(2L'+1) \left[ (-1)^{L+L'} - S_L S_{L'}^* \right] P_L(\cos\theta) P_{L'}(\cos\theta) . \tag{4.40}$$

And we can calculate the intergated absorption cross section applying again the orthogonality of $P_L$,

$$\sigma_{\text{tot}}^{\text{non-el}} = \frac{\pi}{k^2} \sum_L (2L+1)(1-|S_L|^2) . \tag{4.41}$$

It is clear from this expression that in order for $\sigma_{\text{tot}}^{\text{non-el}}$ to be nonzero, $|S_L|^2 \neq 1$. This means that $|e^{2i\delta_L(k)}|^2 \neq 1$, and this condition can only be fulfilled if $\delta_L(k)$ is a complex quantity.

As a consequence, for the non-elastic channels to be open, the interaction has to necessarily be complex (and non-Hermitian). This reflects the fact that the system can leave the elastic channel, or, in other words, probability conservation only in the elastic channel is not required. In this model, the optical potential is expressed as

$$U(r) = V(r) + iW(r) . \tag{4.42}$$

## 4.5 Scattering by a Coulomb potential

As mentioned above, the results derived up to now are only applicable to finite-ranged potentials, and therefore they are not suitable for particles affected by a Coulomb potential.

### 4.5.1 Elastic scattering of two point charges

We can approach the problem of scattering by a Coulomb potential by first considering the collision of two point-charges. In this case, the Coulomb potential between two nuclei of atomic numbers $Z_1$ and $Z_2$ can be expressed as

$$V_C(r) = \frac{Z_1 Z_2 e^2}{r}\,. \tag{4.43}$$

Therefore, the Schrödinger equation for two particles scattered by a Coulomb potential reads

$$\left(\frac{\nabla_r^2}{2\mu} + V_C(r) - \frac{k^2}{2\mu}\right)\psi_C(\mathbf{r}) = 0\,. \tag{4.44}$$

The Coulomb wave function solution of this Schrödinger equation can be written as (see Ref. [123] for details on the derivation shown in this section)

$$\psi_{\mathbf{k}}^C = C_c e^{kz} F\left(-i\eta, 1, ik(r-z)\right), \tag{4.45}$$

where $C_c$ is a normalization constant, $F$ is the confluent hypergeometric function, and

$$\eta = \frac{\mu Z_1 Z_2 e^2}{k} = \frac{Z_1 Z_2 e^2}{v}\,. \tag{4.46}$$

The asymptotic behavior of the Coulomb wave function can be determined solving the hypergeometric equation, leading to

$$\psi_{\mathbf{k}}^C \underset{r\to\infty}{\longrightarrow} C_c \frac{e^{\eta\pi/2}}{\Gamma(1+i\eta)}\left[e^{i(kz+\eta\ln(r-z)k)} + \frac{e^{i(kr-\eta\ln 2kr)}}{r} f_C(k,\theta)\right], \tag{4.47}$$

with $\Gamma$ the Euler Gamma function, and the Coulomb scattering amplitude defined as

$$f_C(k,\theta) = -\frac{\eta}{2k\sin(\theta/2)} e^{2i[\sigma_0 - \eta\ln(\sin(\theta/2))]}\,. \tag{4.48}$$

where $\sigma_0 = \arg\Gamma(1+i\eta)$.

The differential scattering cross section for a purely Coulomb interaction resulting from the solution of the quantum mechanical Schrödinger equation has the well-known form

$$\frac{d\sigma_C}{d\Omega} = |f_C(k,\theta)|^2 = \left[\frac{Z_1 Z_2 e^2}{4E\sin^2(\theta/2)}\right]^2 = \frac{\eta^2}{4k^2\sin^4(\theta/2)}\,. \tag{4.49}$$

It is interesting to notice that this quantum mechanically derived result is *identical* to the formula derived by Ernest Rutherford in 1911 [1] for alpha and beta particles using classical mechanics.

Despite of the fact that a pure Coulomb field is an idealization, the solution of this type of collision is of great importance and can be later-on modified to accommodate more realistic scenarios. In our calculations for elastic scattering, a proton-proton point-like Coulomb potential is used as input to calculate a more realistic double-folding Coulomb interaction (see Ch. 5 for more details).

This purely electromagnetical cross section diverges for $\theta = 0$ and it is not applicable to reproduce real experimental situations. Nevertheless, for these realistic cases, the Coulomb field is modified by, e.g., the strong interaction at short distances. Therefore, the Schrödinger equation has to be solved using the full Hamiltonian, including all the contributions to the potential.

### 4.5.2 Scattering by a modified Coulomb field

To approach this scenario, it is useful to go back to the partial-wave expansion, taking into account the long-range distortion due to the Coulomb interaction. The partial-wave expansion of the Coulomb wave function is in general a linear combination of the regular and irregular Coulomb functions, $F_L$ and $G_L$ [124]. For a purely Coulomb interaction, the part proportional to $G_L$, diverges at $r = 0$. Therefore, it is not considered in the wave function. Writing $\psi_{\mathbf{k}}^C$ in terms of the asymptotics of $F_L$:

$$\psi_{\mathbf{k}}^C \xrightarrow[r\to\infty]{} \sum_L (2L+1) i^L e^{i\sigma_L} \frac{1}{kr} \sin\left(kr - \frac{L\pi}{2} - \eta \ln 2kr + \sigma_L\right), \tag{4.50}$$

where $\sigma_L = \arg\Gamma(L+1+i\eta)$ is known as Coulomb phaseshift.

In contrast, for the case of nuclear reactions both the strong and the Coulomb interactions act between the two nuclei. Therefore, we work with a system that interacts through a potential $V = V_C + V_N$, where $V_N$ corresponds to the nuclear interaction. The asymptotic limit of the corresponding wave function can also have contribution from the irregular Coulomb function, since the short-range nature of the problem is modified by the nuclear iteraction,

$$\psi_{C+N}(r) \xrightarrow[r\to\infty]{} A_C F_L(\eta, kr) + B_C G_L(\eta, kr), \tag{4.51}$$

This problem is formally equivalent to what was seen in Sec. 4.3, substituting the spherical Bessel functions by the Coulomb functions. Using the asymptotic form of $F_L$ and $G_L$, Eq. (4.51) can be rewritten as [77]

$$\psi_{C+N}(r) \xrightarrow[r\to\infty]{} \sum_L \tilde{A}_L(k) \left[ e^{-i(kr - L\pi/2 - \eta \ln 2kr)} - e^{2i(\sigma_L + \hat{\delta}_L)} e^{i(kr - L\pi/2 - \eta \ln 2kr)} \right], \tag{4.52}$$

where $\hat{\delta}_L$, called additional phase shift, contains all the information of the modified electromagnetic potential by the nuclear interaction. Taking into account Eq. (4.21),

$$\psi_{C+N}(r) \xrightarrow[r\to\infty]{} \psi_C(r) + \frac{1}{2ik} \sum_L (2L+1) e^{2i\sigma_L} (e^{2i\hat{\delta}_L(k)} - 1) P_L \cos(\theta) \frac{e^{i(kr - \eta \ln(kr))}}{r}, \tag{4.53}$$

and we can define

$$\hat{f}(\theta) = \frac{1}{2ik} \sum_L (2L+1) e^{2i\sigma_L} (e^{2i\hat{\delta}_L(k)} - 1) P_L \cos(\theta). \tag{4.54}$$

This is the additional scattering amplitude that accounts for the short-range part of the potential, in which the Coulomb potential will be modified by the nuclear interaction. Since the scattering amplitude of this process will then be the sum of $\hat{f}$ and the Coulomb scattering amplitude $f_C$, we can write

$$\frac{d\sigma}{d\Omega} = |f_C(\theta) + \hat{f}(\theta)|^2 \tag{4.55}$$

## 4.6 Scattering of identical particles

In chapter 5 we will discuss the scattering of two $^{16}$O nuclei as the main system to benchmark our theory. Since these nuclei are identical spinless bosons, we need to consider this quantum mechanical property, i.e., the wave function for their relative motion needs to be symmetrical with respect to their exchange. To account for the totally symmetric nature of the process, we can define the relative part of a general symmetrized wave function

$$\psi_b(\mathbf{r}) = \frac{1}{\sqrt{2}}\left[\psi(\mathbf{r}) + \psi(-\mathbf{r})\right], \tag{4.56}$$

Since the corresponding angles of the vector $-\mathbf{r}$ in polar coordinates are $\pi - \theta$ and $\phi + \pi$, we can derive the symmetrized scattering amplitude as

$$f^{\text{symm}}(\theta, \phi) = \frac{1}{\sqrt{2}}\left[f(\theta, \phi) + f(\pi - \theta, \phi + \pi)\right], \tag{4.57}$$

It is important to notice that, since the detector in the experimental situation is not able to distinguish between particles 1 and 2, each particle emitted towards the direction $\mathbf{r}$ will have an identical counterpart emitted towards $-\mathbf{r}$. For this reason, the differential cross section is defined as

$$\frac{d\sigma^{\text{symm}}}{d\Omega} = 2\left|f^{\text{symm}}(\theta, \phi)\right|^2 . \tag{4.58}$$

Therefore, in the case of study in which $f$ is independent of $\phi$

$$\frac{d\sigma^{\text{symm}}}{d\Omega} = |f(\theta)|^2 + |f(\pi - \theta)|^2 + 2\text{Re}\left[f(\theta) f^*(\pi - \theta)\right] . \tag{4.59}$$

A direct consequence of this expression is that the symmetrized scattering amplitude only involves partial waves with even angular momenta, since $P_L\left[\cos(\pi - \theta)\right] = (-1)^L P_L\left[\cos\theta\right]$.

This interference effect will also affect purely Coulomb scattering between the bosons, leading to what is known as the Mott formula, after the derivation done by Sir Nevill Mott in 1930 [130].

$$\frac{d\sigma^{\text{Mott}}}{d\Omega} = \left(\frac{\eta}{2k}\right)^2 \left| \frac{\exp\left(-2i\eta \log\left[\sin(\theta/2)\right]\right)}{\sin^2(\theta/2)} + \frac{\exp\left(-2i\eta \log\left[\cos(\theta/2)\right]\right)}{\cos^2(\theta/2)} \right|^2 . \tag{4.60}$$

## 4.7 Fusion cross section

In the case of nuclear fusion involving collisions of light or medium-mass nuclei at energies in a range that goes from below to slightly above Coulomb barrier, one can usually assume that the imaginary part of the optical potential is confined inside it. This barrier is created as a consequence of the cancellation between the attractive nature of the nuclear interaction and the repulsive nature of the Coulomb potential. In this context, we will have an effective potential $V_{\text{eff}}$, formed by the real part of the optical potential that comes from the nuclear interaction $V_{\text{nuc}}$, the Coulomb potential between the nuclei $V_{\text{Coul}}$ and a centrifugal barrier depending on $L$:

$$V_{\text{eff}}(r, L, E) = \text{Re}[V_{\text{nuc}}(r, E)] + V_{\text{Coul}}(r) + \frac{L(L+1)}{2\mu r^2} . \tag{4.61}$$

A representation of this barrier for $L = 0$ can be seen in Fig. 5.10. It is clear from the figure that the nuclear interaction dominates at short distances, while the Coulomb potential dictates the behavior

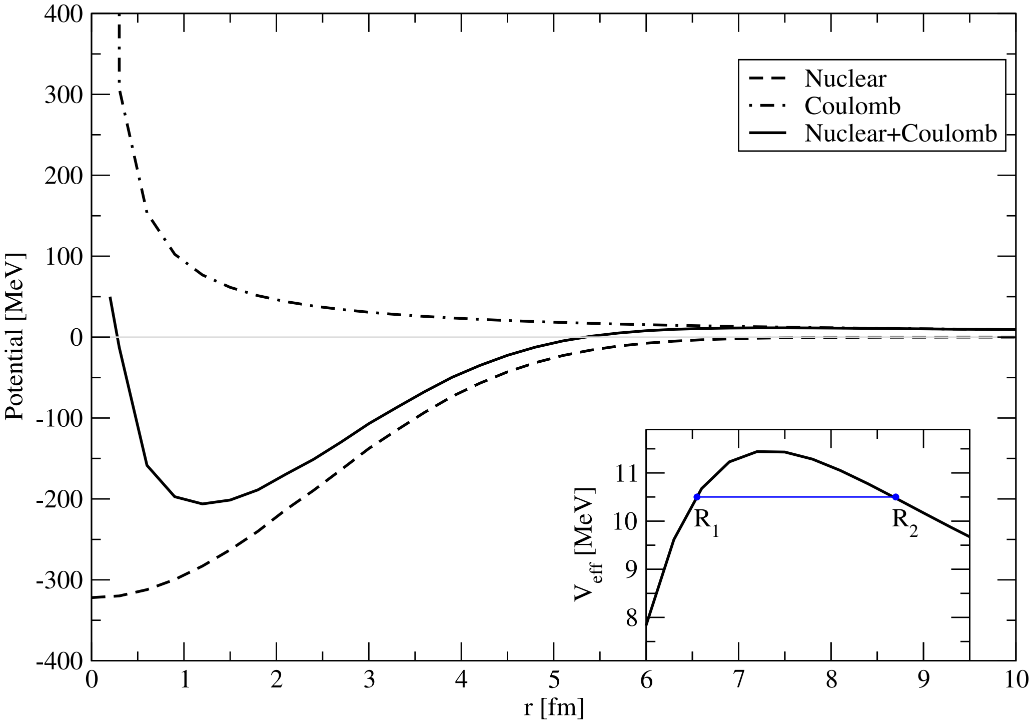

**Figure 4.3:** Nuclear (dashed line) and Coulomb (dash-dotted line) contributions to the full potential (solid line). The sum of both (forming the Coulomb barrier) can be seen as a solid line. The nuclear contribution is given by the two-body folding potential of Ch. 5 at N$^2$LO for $R_0 = 1.4$ fm. In the inset, the Coulomb barrier is zoomed in and the classical turning points for a given energy (blue line) are shown as blue dots.

of the total interaction at large distances. The inner and outer turning points $R_1$ and $R_2$, which satify $V_{\text{eff}}(R_1, L, E) = V_{\text{eff}}(R_2, L, E) = E$, are also depicted for an arbitrary collision energy.

Since the imaginary part of the potential is supposed to be well inside the range of the effective potential, it does not take part in $V_{\text{eff}}$, and the fusion cross section can be regarded as the total absorption cross section [131]. At low energy, due to Coulomb and centrifugal barriers, the projectile and target do not come close to one another. However, thanks to the quantum-mechanical tunnel effect, they can get through those barriers and merge, i.e., fuse. Once the nucleus is inside the barrier, its probability to get out is so low that it can be neglected. This situation is described by the incoming-wave boundary condition (IWBC) [132], under which Eq. (4.41) can be written in terms of the barrier penetrability $P_L$ as

$$\sigma_{\text{fus}}(E) = \frac{\pi}{k^2} \sum_L (2L+1) P_L(E)\,. \tag{4.62}$$

In terms of the transmission coefficient the wave function under the IWBC has the form

$$u_L(r) = \sqrt{\frac{k}{k_L(r)}} \mathcal{T}_L(E) \exp\left(-i \int_{r_{\text{abs}}}^{r} k_L(r') dr'\right), \quad r \leq r_{\text{abs}}\,, \tag{4.63}$$

where $P_L = |\mathcal{T}_L|^2$, $r_{\text{abs}}$ stands for the absorption radius, which is taken to be inside the Coulomb barrier, and $k_L(r)$ is the local wave number for the $L$th partial wave

$$k_L(r) = \sqrt{2\mu\left[E - V_{\text{eff}}(r, L, E)\right]}\,. \tag{4.64}$$

The probability of crossing the barrier can be calculated in the WKB approximation [123], named after Wentzel, Kramers, and Brillouin, with the incoming-wave boundary condition, which leads to

$$P_L(E) = \left[1 + \exp\left(\int_{R_1}^{R_2} \sqrt{8\mu(V_{\text{eff}}(r,L,E) - E)}dr\right)\right]^{-1} . \tag{4.65}$$

Since in Sec. 5.3.4 we will consider the fusion of two $^{16}$O, we need to explicitly take into account their bosonic nature. As seen in Sec. 4.6, in a collision between two identical bosons only partial waves with even $L$ contribute to the cross section, and therefore we need to rewrite Eq. (4.62) as

$$\sigma_{\text{fus}}(E) = \frac{\pi}{k^2} \sum_L (1 + (-1)^L)(2L+1)P_L(E) . \tag{4.66}$$

# 5 Double-folding potentials and applications

## 5.1 Double-folding potential: Formalism

We consider the potential between nucleus 1 (with atomic and mass numbers $Z_1$ and $A_1$) and nucleus 2 (with $Z_2$ and $A_2$). In the double-folding formalism, the nuclear part of the nucleus-nucleus potential can be constructed from a given $NN$ interaction $v$ by double folding over the densities in the direct (D) channel and the density matrices in the exchange (Ex) channel. The review of the formalism for the double-folding potential in this section follows Ref. [84]. The results with $NN$ interactions shown here are published in Ref. [118, 133]. A preliminary study of the impact of three-body interactions is presented in Sec. 5.4, and was carried on in collaboration with Sulamith Weber [134].

In general, the microscopic nucleus-nucleus potential can be written as a Hartree-Fock type potential:

$$V_F = \sum_{i\in A_1, j\in A_2} \left[\langle ij|v_{\mathrm{D}}|ij\rangle + \langle ij|v_{\mathrm{Ex}}|ji\rangle\right] = V_{\mathrm{D}} + V_{\mathrm{Ex}} \,. \tag{5.1}$$

In the direct channel, the double-folding potential is calculated by integrating the $NN$ interaction over the neutron ($n$) and proton ($p$) density distributions $\rho_1^{n,p}$ and $\rho_2^{n,p}$ of the colliding nuclei,

$$V_{\mathrm{D}}(\mathbf{r}) = \sum_{i,j=n,p} \int\int \rho_1^i(\mathbf{r}_1)\, v_{\mathrm{D}}^{ij}(\mathbf{s})\, \rho_2^j(\mathbf{r}_2)\, d^3\mathbf{r}_1 d^3\mathbf{r}_2 \,, \tag{5.2}$$

where $\mathbf{r}$ is the relative coordinate between the center of mass of the nuclei, $\mathbf{r}_1$ and $\mathbf{r}_2$ are the coordinates from the center of mass of each nucleus, $\mathbf{s} = \mathbf{r} - \mathbf{r}_1 + \mathbf{r}_2$ (the geometry is shown in Fig. 5.1), and the sum $i, j$ is over neutrons and protons with their respective densities.

To account for the antisymmetrization between nucleons, the double-folding potential receives contributions also from the exchange channel. In this context, non-local terms appear for $v_{\mathrm{Ex}}$. Nevertheless, the final potential can be written in local form by using the density matrix expansion as introduced in Ref. [135].

We start from the formal identity

$$\begin{aligned}\rho(\mathbf{r}+\mathbf{s}/2, \mathbf{r}-\mathbf{s}/2) &= \sum_a \phi_a^*(\mathbf{r}+\mathbf{s}/2)\phi_a(\mathbf{r}-\mathbf{s}/2) \\ &= \exp\left[\mathbf{s}(\boldsymbol{\nabla}_1 - \boldsymbol{\nabla}_2)/2\right] \sum_a \phi_a^*(\mathbf{r}_1)\phi_a(\mathbf{r}_2) \,,\end{aligned} \tag{5.3}$$

where $\phi_a$ are Kohn-Sham orbitals [136]. From Eq. (5.3), we can see that the densities used in Eq. (5.2) are the diagonal elements of the density matrices, corresponding to the case $\mathbf{s} = 0$.

Since $\rho$ depends only on radial degrees of freedom, this expression can be averaged over the angular direction of $\mathbf{s}$ (with angle $\theta_s$ with respect to $\mathbf{r}$),

$$\rho(\mathbf{r}+\mathbf{s}/2, \mathbf{r}-\mathbf{s}/2) = \frac{1}{2}\int d(\cos\theta_s) \exp\left[\mathbf{s}(\boldsymbol{\nabla}_1 - \boldsymbol{\nabla}_2)/2\right] \sum_a \phi_a^*(\mathbf{r}_1)\phi_a(\mathbf{r}_2) \,. \tag{5.4}$$

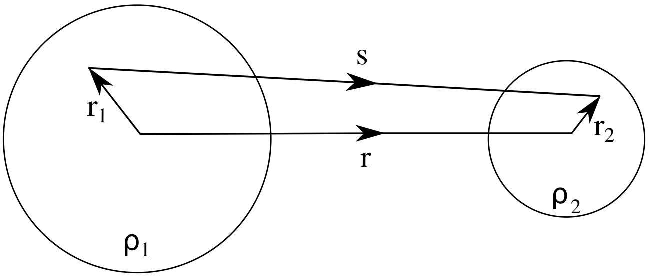

**Figure 5.1:** Coordinates of the nuclei involved in the double-folding calculation.

The quantity $[(\nabla_1 - \nabla_2)/2]^2$ can be related to the relative momentum of the colliding system. Since the momentum is negative inside the nucleus, $[(\nabla_1 - \nabla_2)/2]^2 = -\mathbf{k}^2$. Then, Eq. (5.4) reads

$$\rho(\mathbf{r}+\mathbf{s}/2, \mathbf{r}-\mathbf{s}/2) = \int d(\cos\phi) \exp\left[\frac{i\mathbf{k}(\mathbf{r})\cdot\mathbf{s}}{\mu/m_N}\right] \rho(\mathbf{r_1}, \mathbf{r_2}) \,. \tag{5.5}$$

We can write the momentum for the nucleus-nucleus relative motion $\mathbf{k}$ as

$$k^2(\mathbf{r}) = 2\mu\left[E_{\text{cm}} - V_{\text{F}}(\mathbf{r}, E_{\text{cm}}) - V_{\text{Coul}}(\mathbf{r})\right], \tag{5.6}$$

where $E_{\text{cm}}$ is the center-of-mass energy, $V_{\text{F}}$ the nuclear part of the double-folding potential, $V_{\text{Coul}}$ the double-folding Coulomb potential, and $\mu = m_N A_1 A_2/(A_1 + A_2)$.

Taking this into account, the exchange part of the double-folding potential can be written in a local form as

$$V_{\text{Ex}}(\mathbf{r}, E_{\text{cm}}) = \sum_{i,j=n,p} \int\int \rho_1^i(\mathbf{r}_1, \mathbf{r}_1 + \mathbf{s})\, v_{\text{Ex}}^{ij}(\mathbf{s}) \rho_2^j(\mathbf{r}_2, \mathbf{r}_2 - \mathbf{s}) \exp\left[\frac{i\mathbf{k}(\mathbf{r})\cdot\mathbf{s}}{\mu/m_N}\right] d^3\mathbf{r}_1 d^3\mathbf{r}_2 \,, \tag{5.7}$$

As a consequence of Eq. (5.6), the double-folding potential depends on the energy $E_{\text{cm}}$. Therefore, $V_{\text{Ex}}$ has to be determined self-consistently. Note that at our level of calculation the double-folding potential, $V_{\text{F}}$, is real. The density matrices entering in Eq. (5.7) are approximated using the density matrix expansion [135] restricted to its leading term,

$$\rho^i(\mathbf{r}, \mathbf{r} \pm \mathbf{s}) = \frac{3}{s\, k_{\text{F}}^i(\mathbf{R})}\, j_1\big(s\, k_{\text{F}}^i(\mathbf{R})\big)\, \rho^i(\mathbf{R}) \,, \tag{5.8}$$

where $\mathbf{R} = \mathbf{r} \pm \mathbf{s}/2$, $j_1$ is a spherical Bessel function of the first kind, and we take the effective local Fermi momentum, which is an arbitrary scale in the density-matrix expansion, as in Ref. [84]:

$$k_{\text{F}}^i = \left[(3\pi^2\rho^i)^{2/3} + \frac{5(\nabla\rho^i)^2}{12(\rho^i)^2} + \frac{5\nabla^2\rho^i}{36\rho^i}\right]^{1/2} . \tag{5.9}$$

In the case of spherical nuclei, the densities and the effective local Fermi momenta depend only on the distance from the center of mass of the nucleus ($r_i$ or $R$).

For doubly closed-shell nuclei, only the central parts of the $NN$ interaction contributes to the double-folding potential in the direct and exchange channels, $v_{\text{D}}$ and $v_{\text{Ex}}$, respectively. Then also the $NN$ interaction and the double-folding potentials depend only on the relative distance ($s$ or $r$).

Considering that a general antisymmetrized interaction can be written in terms of the permutation operator, $P_{ij}$, as

$$v = v_{\mathrm{D}} + v_{\mathrm{Ex}} = (1 - P_{ij})v\,. \tag{5.10}$$

Writing the $NN$ interaction in terms of their two-body spin-isospin matrix elements, and summing over spin singlet and triplet states, $v_{\mathrm{D}}$ reads

$$v_{\mathrm{D}}^{TM_T}(s) = \frac{1}{4}\sum_{S,M_S} \langle s; SM_S TM_T | v | s; SM_S TM_T \rangle\,, \tag{5.11}$$

Therefore, we find that, since central potentials are independent of $M_S$, the direct part reads

$$v_D^{M_T}(s) = \begin{cases} \frac{1}{4}\left(v^{01} + 3v^{11}\right) & \text{if } T = 1\,, \\ \frac{1}{4}\left(v^{00} + 3v^{10}\right) & \text{if } T = 0\,. \end{cases} \tag{5.12}$$

For the exchange part $v_{\mathrm{Ex}}$, it holds that

$$v_{\mathrm{Ex}}^{TM_T}(s) = \frac{1}{4}\sum_{S,M_S} \langle s; SM_S TM_T | (-P_{12}) v | s; SM_S TM_T \rangle\,. \tag{5.13}$$

For a local interaction, $P_{ij} = P^{\sigma}P^{\tau}$ with $P^{\sigma} = \frac{1}{2}(1 + \boldsymbol{\sigma}_i \cdot \boldsymbol{\sigma}_j)$ and $P^{\tau} = \frac{1}{2}(1 + \boldsymbol{\tau}_i \cdot \boldsymbol{\tau}_j)$. Since $P^{\sigma} = (-1)^{S+1}$ and $P^{\tau} = (-1)^{T+1}$,

$$v_{\mathrm{Ex}}^{TM_T} = \begin{cases} \frac{1}{4}\left(v^{01}(-P^{\sigma}_{S=0}P^{\tau}_{T=1}) + 3v^{11}(-P^{\sigma}_{S=1}P^{\tau}_{T=1})\right) = \frac{1}{4}\left(v^{01} - 3v^{11}\right) & \text{if } T = 1\,, \\ \frac{1}{4}\left(v^{00}(-P^{\sigma}_{S=0}P^{\tau}_{T=0}) + 3v^{10}(-P^{\sigma}_{S=1}P^{\tau}_{T=0})\right) = \frac{1}{4}\left(-v^{00} + 3v^{10}\right) & \text{if } T = 0\,. \end{cases} \tag{5.14}$$

Distinguishing between the different $M_T$ projections, we can write proton-proton ($pp$), proton-neutron ($pn, np$), and neutron-neutron ($nn$) interactions in a compact form as

$$v_{\mathrm{D,Ex}}^{pp,nn}(s) = \frac{1}{4}\Big[v^{01}(s) \pm 3v^{11}(s)\Big], \tag{5.15}$$

$$v_{\mathrm{D,Ex}}^{pn,np}(s) = \frac{1}{8}\Big[\pm v^{00}(s) + v^{01}(s) + 3v^{10}(s) \pm 3v^{11}(s)\Big], \tag{5.16}$$

where the upper (lower) signs refer to the direct (exchange) term and we have neglected the small isospin-symmetry-breaking corrections to $v$.

For completeness, we also present the derivation for tensor interactions, which depend on the spin projection $M_S$. The expected values of the tensor operator in $SM_S$ basis are

$$\langle SM_S | S_{12} | SM_S \rangle = \begin{cases} 2 - 6\cos^2\theta_{Sr} & \text{if } S = 1, M_S = 0\,, \\ 3\cos^2\theta_{Sr} - 1 & \text{if } S = 1, M_S = \pm 1\,, \\ 0 & \text{if } S = 0\,. \end{cases} \tag{5.17}$$

where $\theta_{Sr}$ is the angle between the spin vector and the radial coordinate between nucleons. Therefore, the direct and exchange contributions of the tensor interaction to $v$ read

$$\begin{cases} v_{D,EX}^{(pp,nn)} = \frac{1}{4}\left[\pm 3\left(v_{S_{12}}^{T=1M_S=-1} + v_{S_{12}}^{T=1M_S=0} + v_{S_{12}}^{T=1M_S=1}\right)\right] \\ v_{D,EX}^{(pn,np)} = \frac{1}{8}\left[v_{S_{12}}^{T=0M_S=-1} + v_{S_{12}}^{T=0M_S=0} + v_{S_{12}}^{T=0M_S=1} \pm 3\left(v_{S_{12}}^{T=1M_S=-1} + v_{S_{12}}^{T=1M_S=0} + v_{S_{12}}^{T=1M_S=1}\right)\right], \end{cases} \tag{5.18}$$

which means that, taking into account Eq. (5.17), the tensor interaction does not play a role in the double-folding potential for doubly closed nuclei at the simple Hartree-Fock level considered here, as was mentioned before.

## 5.2 Nuclear density profiles

The densities of the colliding nuclei are an important input for the calculation of the double-folding potential. In this first study based on chiral EFT interactions, we adopt the two-parameter Fermi distributions provided by the São Paulo group [82] for the proton and neutron densities, whose parameters were fitted to Dirac-Hartree-Bogoliubov calculations on a large range of nuclei throughout the whole nuclear chart

$$\rho^{p,n}(r) = \frac{\rho_0}{1+\exp\left(\frac{r-R_{p,n}}{a_{p,n}}\right)}\,, \tag{5.19}$$

where $\rho_0 = 0.091\ \text{fm}^{-3}$ for $^{16}$O and the radii $R_{p,n}$ and diffusenesses $a_{p,n}$ depend on the proton and neutron numbers of the nucleus. Expressed in fm, they are given by

$$R_p = 1.81\,Z^{1/3} - 1.12\,, \quad a_p = 0.47 - 0.00083\,Z\,, \tag{5.20}$$

$$R_n = 1.49\,N^{1/3} - 0.79\,, \quad a_n = 0.47 + 0.00046\,N\,. \tag{5.21}$$

It is important to note that the double-folding potential is calculated at the Hartree-Fock level, but using phenomenological densities (which would otherwise be deficient when taking them from a Hartree-Fock calculation based on $NN$ interactions). From now on, we will refer to our calculations as Hartree-Fock, for which this point is implicitly understood.

The impact of different density profiles using densities obtained from electron scattering will be discussed in Sec. 5.3.3

## 5.3 Results with local chiral interactions

This section contains calculations of double-folding potentials based on chiral EFT $NN$ interactions in coordinate space, as presented in chapter 3 (developed in Ref. [114,115]). We expect that the reliable estimate of $NN$ interaction in the systematic order-by-order expansion of chiral EFT will provide also an order-by-order behavior in the double-folding potentials.

### 5.3.1 Double-folding potentials

To apply the double-folding method using local chiral $NN$ interactions, we consider the $^{16}$O–$^{16}$O system, where there are ample sets of data to which we can compare our calculations. To this purpose, we use local chiral EFT interactions because their coordinate space expressions simplify the double-folding calculation. Elastic scattering has been accurately measured at various energies [79,137–143] and these data sets have been precisely analyzed with phenomenological optical potentials [79,144]. This enables us to compare our results with state-of-the-art phenomenological calculations. At lower energy, the fusion of two $^{16}$O nuclei [145–149] is another observable with which we can test our double-folding potential. In this section, we present results for the double-folding potential computed at different energies and we illustrate its order-by-order behavior and the sensitivity to the cutoff scale. As it turns out, the available local interactions from Refs. [114,115] with $R_0 = 1.0$ fm and 1.1 fm are too hard (see also Ref. [150]) and, thus, not suitable for calculations of a nucleus-nucleus potential at the simple Hartree-Fock level considered here, because the resulting double-folding potentials are repulsive. For this reason, we use the softer potentials constructed as explained in Ch. 3.

Figure 5.2 shows the direct (upper panel) and exchange (lower panel) contributions to the double-folding potential based on the local chiral N$^2$LO potential with $NN$ cutoff $R_0 = 1.4$ fm. Since the $NN$ interaction is energy independent, the direct contribution of the double-folding potential is also energy independent [see Eq. (5.2)]. The exchange contribution given by Eq. (5.7), however, includes

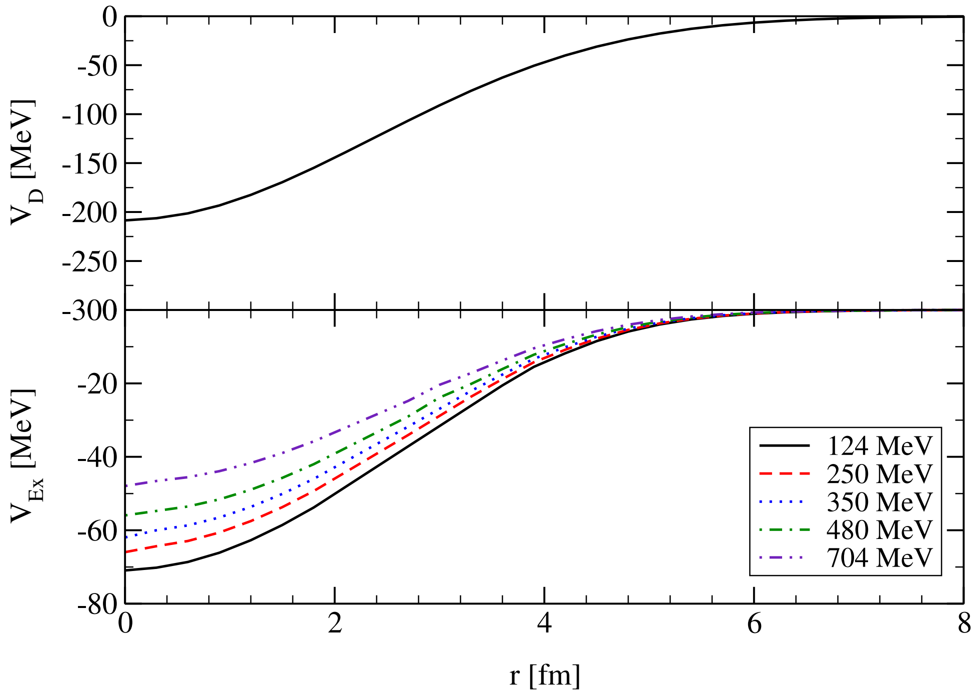

**Figure 5.2:** Direct (upper panel) and exchange (lower panel) contributions to the double-folding potential for the $^{16}$O–$^{16}$O system based on the local chiral EFT interaction at N$^2$LO with $R_0 = 1.4$ fm. The direct contribution (Eq. (5.2)) is energy independent and we show results for different laboratory energies, $E_{\text{lab}}$, in the exchange channel.

an energy dependence through the relative momentum $\mathbf{k}$ in the exponential factor [see Eq. (5.6)]. The shape of this exchange contribution does not vary significantly with energy, but its attractive strength decreases with increasing energy, which can be understood by the increasing variation of the exponential factor.

The final double-folding potential computed at different orders and with different cutoffs $R_0$ is displayed for $E_{\text{lab}} = 350$ MeV in Fig. 5.3. The order-by-order behavior is similar to what is observed in Fig. 3.2. As explained before, lower cutoffs ($R_0 \lesssim 1.2$ fm) provide harder $NN$ interactions, which lead to repulsive double-folding potentials at LO and NLO. These interactions require the additional attraction expected to come from many-body contributions beyond the simple Hartree-Fock level considered here. At N$^2$LO, the calculations have been performed with three different cutoffs: $R_0 =$ 1.2 fm (dotted line), 1.4 fm (solid line), and 1.6 fm (dashed line); the lowest cutoff providing the less attractive potential. Interestingly, the potentials computed with the other two cutoffs are close to one another. The range of $R_0$, highlighted by the shaded band in Fig. 5.3, will allow us to gauge the level of details needed in $NN$ interactions to reproduce the physical observables in nucleus-nucleus reactions.

### 5.3.2 Elastic scattering

The elastic scattering of medium-mass to heavy nuclei can be described within the optical model (for details see Sec. 4.4.). In that model, the nuclear part of the interaction between the colliding nuclei is described by a complex potential. Roughly speaking, the real part corresponds to the attractive interaction between the nuclei, whereas the imaginary part simulates the absorption of the incoming channel to other open channels, such as inelastic scattering or transfer. Double-folding potentials are

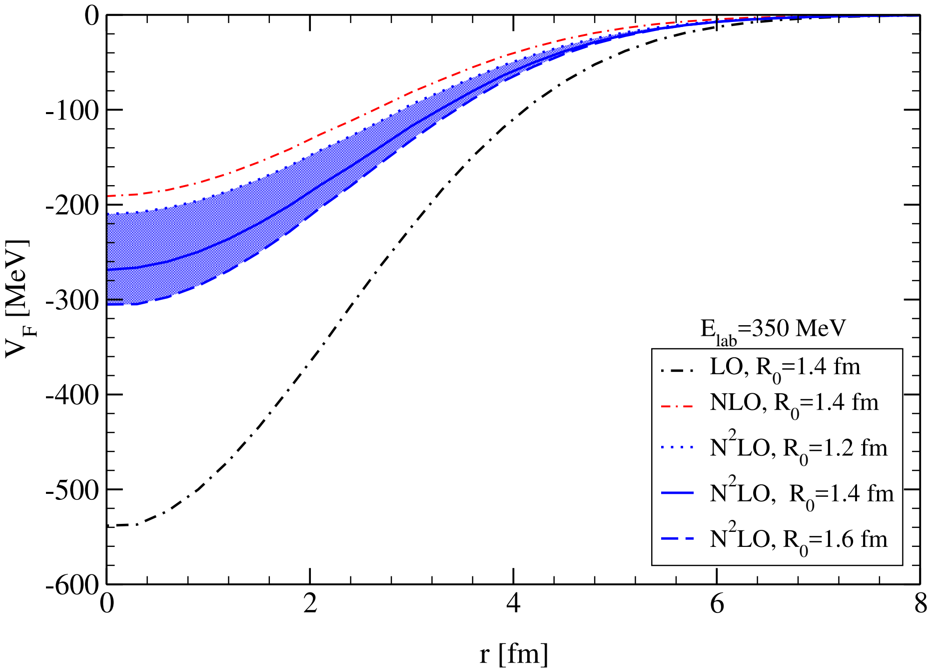

**Figure 5.3:** Double-folding potential for the $^{16}$O–$^{16}$O system at $E_{\text{lab}} = 350$ MeV. The results obtained at LO, NLO, and N$^2$LO (for $R_0 = 1.4$ fm) illustrate the order-by-order behavior, while the calculations performed at N$^2$LO with $R_0 = 1.2$, 1.4, and 1.6 fm show the sensitivity to the cutoff scale.

often used for the real part of the optical potential. In this first study, we follow the São Paulo group and assume the imaginary part of the optical potential $U_{\text{F}}$ to be proportional to its real part [83]

$$U_{\text{F}}(r, E_{\text{cm}}) = (1 + i\,N_W)\,V_{\text{F}}(r, E_{\text{cm}})\,, \tag{5.22}$$

where $V_{\text{F}}$ is our double-folding potential and $N_W$ is a real coefficient taken in the range 0.6–0.8. Additionally, the Coulomb potential is generated by folding two uniform charge distributions of radius $R_C = 3.54$ fm.

Note that since $^{16}$O is a spinless boson, the wave function for the $^{16}$O–$^{16}$O relative motion needs to be properly symmetrized. For details on how this changes the cross section calculation, see Sec. 4.6. The cross section for $^{16}$O–$^{16}$O elastic scattering for laboratory energy $E_{\text{lab}} = 350$ MeV is shown in Fig. 5.4 as a ratio to the Mott cross section (Eq. (4.60)). In these calculations, we take for the imaginary part $N_W = 0.8$. We study the sensitivity to $N_W$ later.

As in Figs. 3.2 and 5.3, we observe a systematic order-by-order behavior. The uncertainty related to the cutoff choice at N$^2$LO (shaded area) is similar to that observed in the double-folding potential itself (see Fig. 5.3). At forward angles, i.e., up to 10°, the agreement of our calculations with experiment is excellent, knowing in particular that there are no parameters fitted to reproduce the data. At larger angles this agreement deteriorates. Since the spread observed in the $NN$ cutoff band remains small even at larger angles, this discrepancy cannot be fully explained by the detail of the $NN$ interactions considered. It is likely due to the simple Hartree-Fock level of the many-body calculation or to the choice of the $^{16}$O density, which could be improved. In addition, it could also reflect the simple description of the imaginary part. To compare the calculations performed at different energies, it is

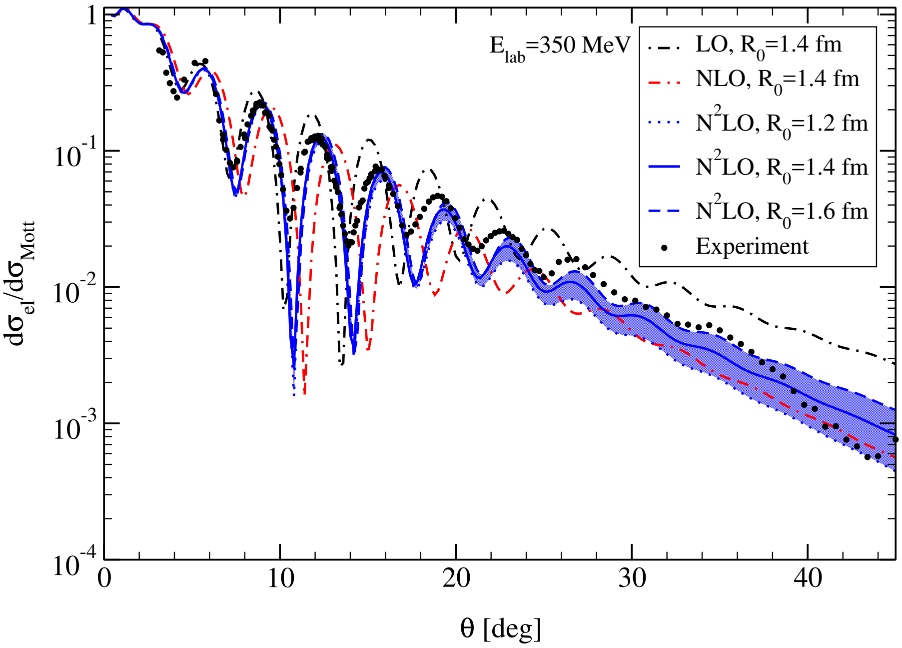

**Figure 5.4:** Ratio of the cross section for elastic $^{16}$O–$^{16}$O scattering to the Mott cross section for laboratory energy $E_{\text{lab}} = 350$ MeV. Results are shown at LO, NLO, and N$^2$LO for $R_0 = 1.4$ fm, and the sensitivity to $R_0 = 1.2$–$1.6$ fm is illustrated at N$^2$LO by the shaded area. In all cases, we take for the imaginary part $N_W = 0.8$ [see Eq. (5.22)]. The results are compared to experimental data from Ref. [138].

useful to present the cross section as a function of the momentum transfer $q$, that depends on both the laboratory energy and the scattering angle

$$q = 2k \sin\left(\frac{\theta}{2}\right) = \sqrt{2mE_{\text{lab}}}\sin\left(\frac{\theta}{2}\right). \tag{5.23}$$

The elastic scattering cross sections computed at various laboratory energies between 124 and 704 MeV are displayed in Fig. 5.5 as a ratio to the Mott cross section. The bands are delimited by results for the range $N_W = 0.6 - 0.8$. Results generated by the cutoffs $R_0 = 1.2$ fm, 1.4 fm, and 1.6 fm are displayed in red, blue, and green, respectively. We find that the cutoff variation is less relevant than the impact of the imaginary part coefficient $N_W$. As in Fig. 5.4, we observe a general agreement between our calculations and the data, especially at forward angles. At larger momentum transfer, the agreement is less good, although the experimental points remain close to the spread obtained for the $N_W$ range. This confirms that going beyond the simple description of the imaginary part could improve our calculations.

For comparison, we also show the cross sections computed with the phenomenological optical potential developed by Khoa *et al.* [79] (dotted line in Fig. 5.5), which provides a near-perfect reproduction of the data. This potential follows a standard optical potential prescription combining squared Woods-Saxon (WS) form factors to describe the volume terms and an additional surface term. In this case, the Coulomb potential is also generated by folding two uniform charge distributions of radius $R_C = 3.54$ fm. The resulting potential has the form

$$U(r) = V_C(r) - V_n f_n(r) - iW_v f_v(r) - iW_d g_d(r), \tag{5.24}$$

where

$$f_x(r) = \frac{1}{[1 + e^{(r-R_x)/a_x}]^2}, \tag{5.25}$$

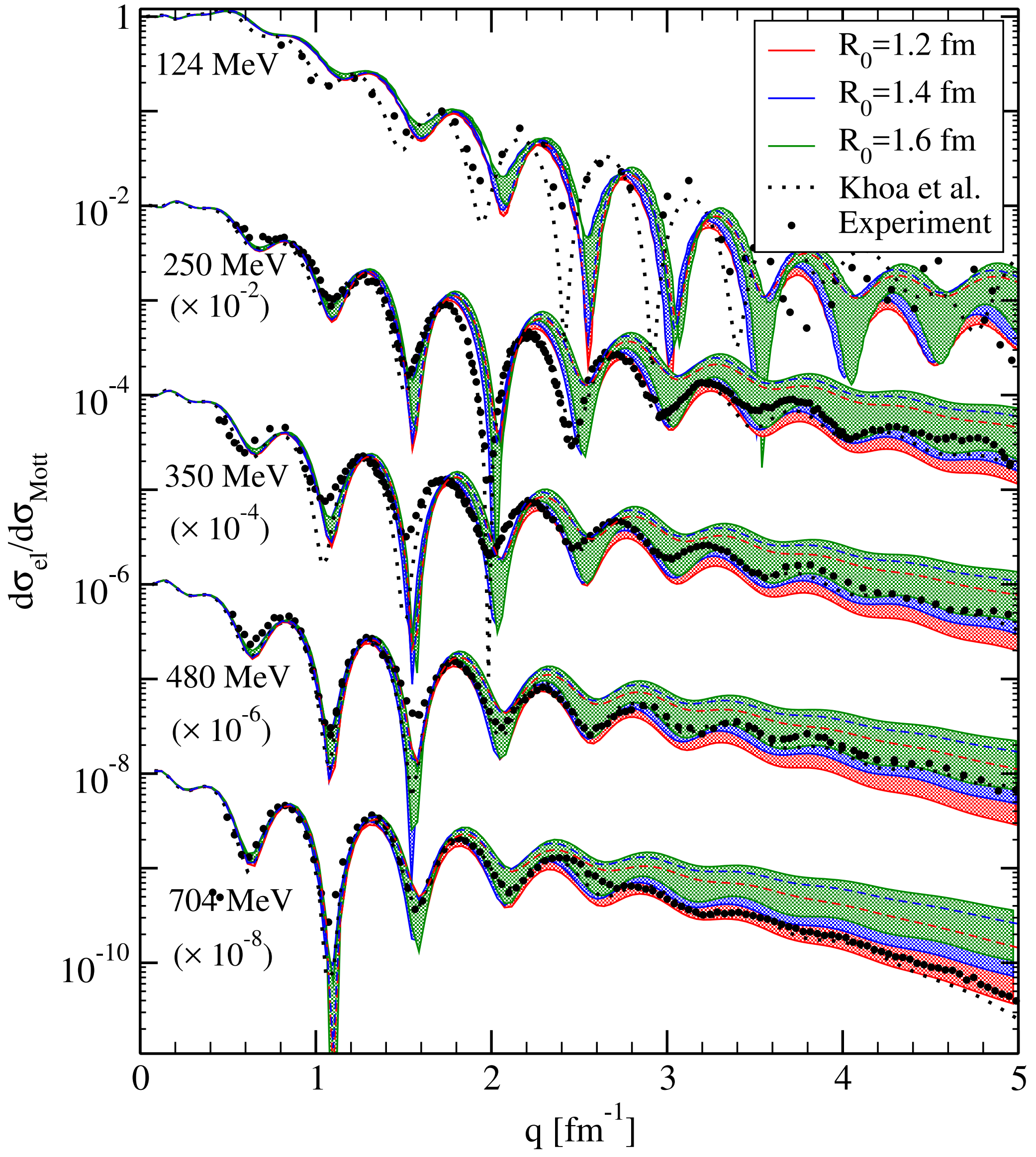

**Figure 5.5:** Ratio of the cross section for elastic $^{16}$O–$^{16}$O scattering to the Mott cross section as a function of momentum transfer $q$ for various laboratory energies (the different energy results are offset by a factor as indicated). Results are shown at N$^2$LO for $R_0 = 1.2$ fm (red), 1.4 fm (blue), and 1.6 fm (green). For these cutoffs, the region between the results with $N_W = 0.6$ (upper limit) and $N_W = 0.8$ (lower limit) is shaded. In the case of $R_0 = 1.2$ fm and 1.4 fm, the upper line is shown as a dashed line. For comparison, we also show the optical-potential results of Khoa *et al.* [79] and the experimental data from Refs. [79, 138, 140–143].

| $E_{\text{lab}}$ | $V_n$ | $R_n$ | $a_n$ | $W_v$ | $R_v$ | $a_v$ | $W_d$ | $R_d$ | $a_d$ |
|---|---|---|---|---|---|---|---|---|---|
| 124 | 452.9 | 3.720 | 1.608 | 14.85 | 5.550 | 0.296 | 5.049 | 6.479 | 0.539 |
| 250 | 311.0 | 4.337 | 1.336 | 34.86 | 5.148 | 0.887 | 9.250 | 5.356 | 0.737 |
| 350 | 367.1 | 3.967 | 1.528 | 28.16 | 6.315 | 0.978 | 8.426 | 4.641 | 0.344 |
| 480 | 282.0 | 4.297 | 1.363 | 40.45 | 5.900 | 1.100 | 3.745 | 4.911 | 0.257 |
| 704 | 294.8 | 4.128 | 1.468 | 41.99 | 5.937 | 0.990 | 2.481 | 4.643 | 0.222 |

**Table 5.1:** Optical potential parameters used in Eq. (5.24), (5.25) and (5.26). $E_{\text{lab}}$, $V_n$, $W_v$ and $W_d$ are given in MeV, while the parameters $R_x$ and $a_x$ are in fm. Values taken from Ref. [79]

and

$$g_d(r) = \frac{4e^{(r-R_d)/a_d}}{\left[1+e^{(r-R_d)/a_d}\right]^2}. \tag{5.26}$$

In these expressions $V_n$ and $W_x$ are the depth of the potentials and $R_x$ and $a_x$ the radius and diffuseness, respectively. All nine are adjustable parameters that are fitted at each energy and for each target-projectile combination. The values of these parameters for $^{16}$O-$^{16}$O scattering at the different energies shown in Fig. 5.5 can be found in Table 5.1.

The imaginary part of these potentials is shown in Fig. 5.6 for $E = 124$, 350, and 704 MeV. Comparing these shapes with those of Fig. 5.2, the difference between the imaginary potentials used in this work and those obtained by fitted optical potentials becomes evident: especially for low energies, the surface term of Eq. (5.24) plays a crucial role in determining the shape of the imaginary part. We therefore expect that the inclusion of a more realistic imaginary potential in our calculations will bring an important improvement of the comparison with experimental data.

Given that we do not include any adjustable parameter to fit the data, our results with the double-folding potential based on chiral EFT interactions are therefore very encouraging.

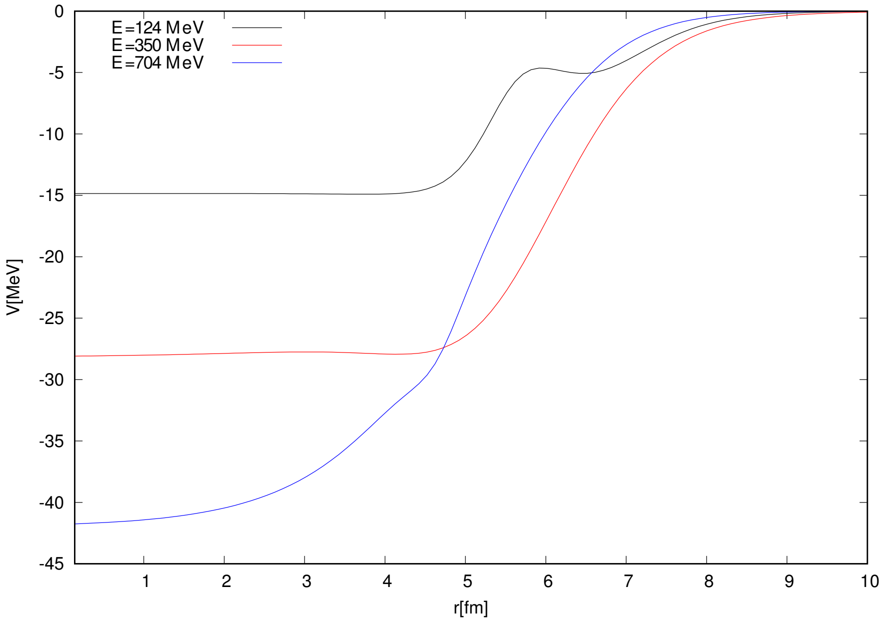

**Figure 5.6:** Imaginary part of the optical potentials from Ref. [79] for laboratory energies of 124 (black), 350 (red) and 704 (blue) MeV.

### 5.3.3 Impact of density profile

A technique to experimentally determine charge density profiles of nuclei consists on performing a parametrization of them using results of electron-scattering experiments. For the case at hand, we take Ref. [151] that contains functional forms and the corresponding parameters of different fittings to charge distributions of various nuclei. Since $^{16}$O is a relatively light nucleus, we take $\rho_p = \rho_n$. For this case, Ref. [151] presents two possibilities, the first one being a Fourier-Bessel expansion

$$\rho_p^{\mathrm{FB}}(r) = \begin{cases} \sum_\nu a_\nu j_0(\frac{\nu\pi r}{R_{\mathrm{FB}}}) & \text{if } r \leq R_{\mathrm{FB}} \\ 0 & \text{if } r > R_{\mathrm{FB}} \end{cases}, \tag{5.27}$$

where $R_{\mathrm{FB}}$ and $a_\nu$ are parameters that can be found in Table 5.2.

| $a_1$ | $a_2$ | $a_3$ | $a_4$ | $a_5$ | $a_6$ | $a_7$ |
|---|---|---|---|---|---|---|
| $2.024{\cdot}10^{-2}$ | $4.479{\cdot}10^{-2}$ | $3.353{\cdot}10^{-2}$ | $3.503{\cdot}10^{-3}$ | $-1.229{\cdot}10^{-2}$ | $-1.3033{\cdot}10^{-2}$ | $-3.404{\cdot}10^{-3}$ |
| $a_8$ | $a_9$ | $a_{10}$ | $a_{11}$ | $a_{12}$ | $a_{13}$ | $R_{\mathrm{FB}}$ |
| $-4.163{\cdot}10^{-4}$ | $-9.444{\cdot}10^{-4}$ | $-2.577{\cdot}10^{-4}$ | $2.538{\cdot}10^{-4}$ | $-1.060{\cdot}10^{-4}$ | $4.148{\cdot}10^{-5}$ | 8.0 |

**Table 5.2:** Coefficients of the Fourier-Bessel parametrization of Eq. (5.27). The values describe the density of $^{16}$O and taken from Ref. [151]. $R_{\mathrm{FB}}$ is given in fm, while the coefficients $a_\nu$ have units of fm$^{-3}$.

The second parametrization is a sum of Gaussians

$$\rho_p^{\mathrm{G}}(r) = \sum_i A_i \left( \exp\left[ -\left( \frac{r - R_i}{\gamma} \right)^2 \right] + \exp\left[ -\left( \frac{r + R_i}{\gamma} \right)^2 \right] \right). \tag{5.28}$$

where $\gamma$ is the width of the Gaussians at the smallest width of the peaks in the nuclear radial wave functions, and the coefficients $A_i$ are given by

$$A_i = \frac{ZeQ_i}{2\pi^{3/2}\gamma^3(1 + 2R_i^2/\gamma^2)}. \tag{5.29}$$

All parameters $Q_i$ and $R_i$ as well as the value for $\gamma$ are listed in Table 5.3.

| $\gamma$ | 1.06 | | | | | |
|---|---|---|---|---|---|---|
| $i$ | 1 | 2 | 3 | 4 | 5 | 6 |
| $R_i$ | 0.4 | 1.1 | 1.9 | 2.2 | 2.7 | 3.3 |
| $Q_i$ | $5.706{\cdot}10^{-2}$ | $1.957{\cdot}10^{-1}$ | $3.112{\cdot}10^{-1}$ | $2.243{\cdot}10^{-1}$ | $5.995{\cdot}10^{-2}$ | $1.357{\cdot}10^{-1}$ |
| $i$ | 7 | 8 | 9 | 10 | 11 | 12 |
| $R_i$ | 4.1 | 4.6 | 5.3 | 5.6 | 5.9 | 6.4 |
| $Q_i$ | $2.4{\cdot}10^{-5}$ | $1.396{\cdot}10^{-2}$ | $7.0{\cdot}10^{-6}$ | $2.0{\cdot}10^{-6}$ | $2.0969{\cdot}10^{-3}$ | $2.0{\cdot}10^{-6}$ |

**Table 5.3:** Parameters of sum-of-Gaussians parametrization of Eq. (5.28). The values describe the density of $^{16}$O and taken from Ref. [151]. $Q_i$ are dimensionless, $R_i$ and $\gamma$ are given in fm.

As it can be seen in Fig. 5.7, these two parameterizations give very similar results for the elastic scattering cross sections at different energies. The agreement with results yielded by the original

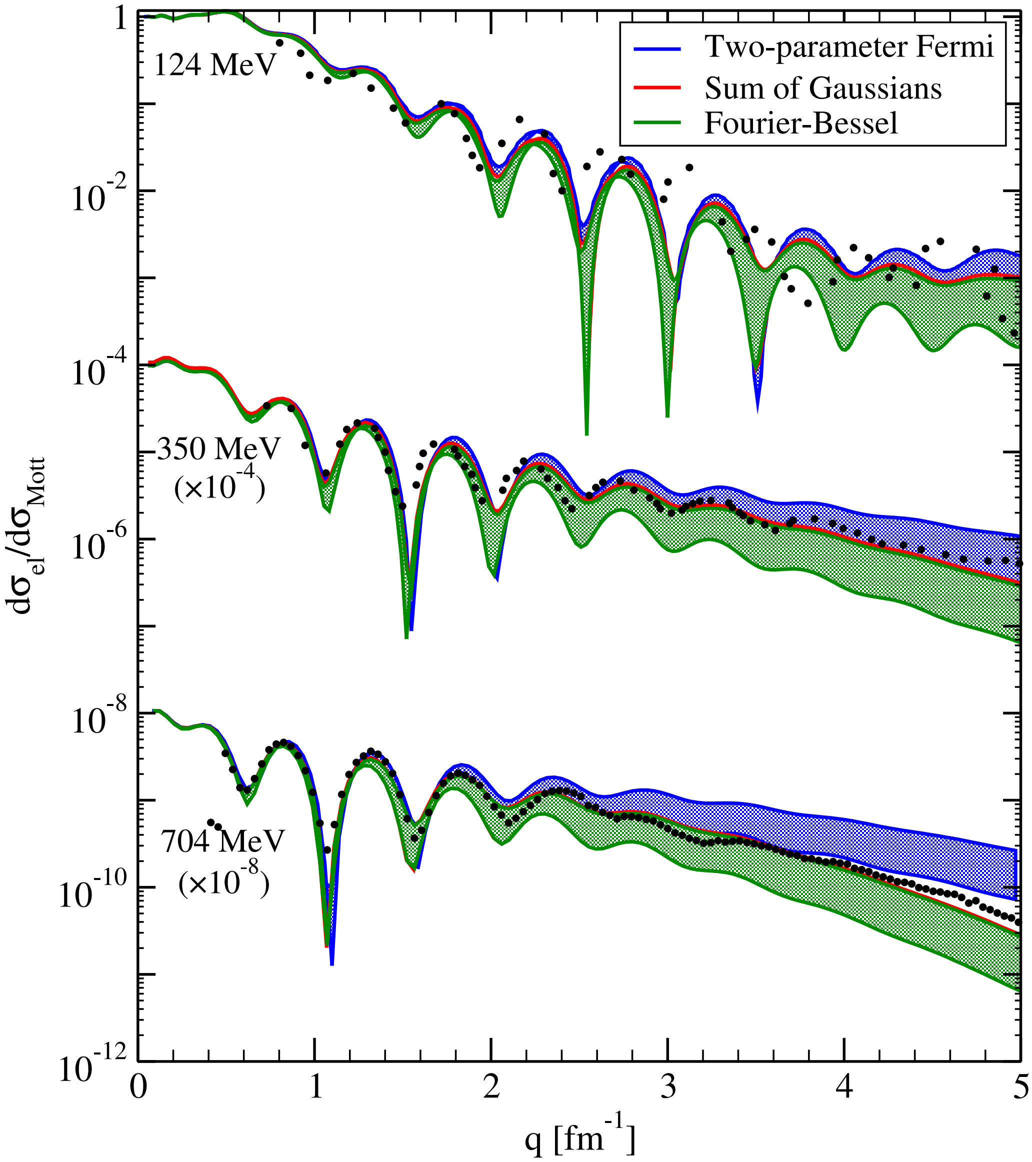

**Figure 5.7:** Ratio of the cross section for elastic $^{16}$O–$^{16}$O scattering to the Mott cross section as a function of momentum transfer $q$ for various laboratory energies (the different energy results are offset by a factor as indicated). Results are show at N$^2$LO for $R_0 = 1.4$ fm using different density profiles for the proton distribution: two-parameter Fermi (blue), sum of Gaussians (red), and Fourier Bessel (green) . For these cutoffs, the region between the results with $N_W = 0.6$ (upper limit) and $N_W = 0.8$ (lower limit) is shaded. For comparison, we also show experimental data from Refs. [79, 138, 140–143].

São Paulo density profile deteriorates for large momenta and energies, not overlapping for results at $E_{\text{lab}} = 704$ MeV and $q > 3$ fm$^{-1}$. For the other energies, the difference between cross sections calculated using the different density profiles is smaller than the impact of the imaginary part, which makes the latter a more urgent issue to address.

### 5.3.4 Fusion reactions

The $^{16}$O+$^{16}$O fusion reaction is another test for our double-folding potential. This cross section $\sigma_{\text{fus}}$ has been measured at low energies to study the role of intermediate resonances during fusion [145, 146] and because this reaction takes place in medium- to heavy-mass stars [146–149]. Oxygen fusion is crucial in medium-mass nuclei burning chains, which provide the seeds to the synthesis of heavy elements. At low energy, the reaction takes place through quantum tunneling of the effective potential barrier that results from the combination of the attractive strong interaction, the repulsive Coulomb interaction, and the centrifugal term of the kinetic energy (see Eq. (4.61)).

Since the fusion reaction takes place at very low energies and involves light spherical nuclei, we take the (real) double-folding potential as the nuclear interaction for this reaction [152]. For light systems like $^{16}$O+$^{16}$O, the fusion barrier is at around 9 fm, well before the neck formation, which justifies the use of the double-folding procedure.

In scenarios of nuclear fusion, where the impact parameter of the collision is small, the scattering nuclei cannot be considered as point-like objects. In this case, the nuclei can be approximated as two homogeneously charged spheres. For identical nuclei, both radii are equal ($R_1 = R_2 = R$), as well as the charges ($Z_1 = Z_2 = Z$), and we can write the sphere-sphere Coulomb potential [153] as

$$V_C(r) = \begin{cases} \frac{Z^2e^2}{R_C}\left(\frac{12}{5} - 4\frac{R^2}{R_C^2} + 3\frac{R^3}{R_C^3} - \frac{2}{5}\frac{R^5}{R_C^5}\right) & \text{if } R \leq R_C\,, \\ \frac{Z^2e^2}{r} & \text{if } R \geq R_C\,. \end{cases} \tag{5.30}$$

where $R_C = 2r_C A^{1/3}$ depends on the nuclei under consideration. In the calculations of this work, we consider $r_C = 1.79$ fm following Ref. [153]. $R_C$ represents the distance at which the two nuclei are touching each other, and can be interpreted as twice the radius of each nucleus.

We do not expect this approximation to change from the double-folding Coulomb term used in Eq. (5.6) to affect significantly our results.

The fusion cross section of $^{16}$O+$^{16}$O can be obtained from the probability $P_L$ to tunnel through the barrier in each of the partial waves using Eq. (4.66),

$$\sigma_{\text{fus}}(E_{\text{cm}}) = \frac{\pi}{k^2}\sum_L (1 + (-1)^L)(2L+1)P_L(E_{\text{cm}})\,. \tag{5.31}$$

The probabilities $P_L$ are determined using the incoming-wave boundary condition detailed in Ref. [152] and implemented in the code CCFULL [154], in which we have included the effects of the symmetrization of the wave function for the fusing nuclei being identical spinless bosons.

At low energy, the fusion process is strongly hindered by the Coulomb repulsion, which makes the cross sections drop rapidly when $E_{\text{cm}}$ decreases, as can be seen in the upper panel of Fig. 5.8. This effect is well accounted for by the Gamow factor, which provides a good first-order estimate of the hindrance of the fusion process by the Coulomb barrier and thus removes most of the dependence of the cross section on the energy. Therefore, it is usually factorized out of the cross section to define the astrophysical $S$ factor

$$S(E_{\text{cm}}) = E_{\text{cm}}\, e^{2\pi\eta}\, \sigma_{\text{fus}}(E_{\text{cm}})\,, \tag{5.32}$$

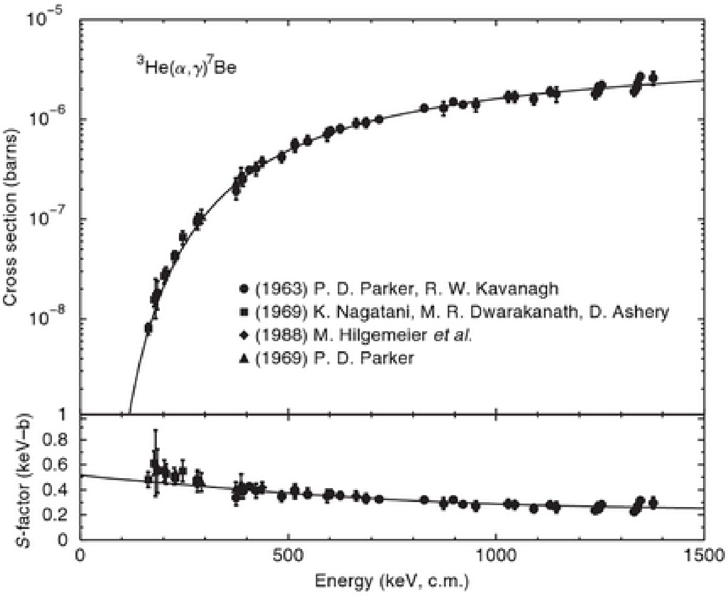

**Figure 5.8:** Illustrative comparison between the energy dependence of the cross section (upper panel) and the astrophysical $S$-factor (lower panel) for the fusion of $^3$He+$\alpha$. Figure taken from Ref. [155].

where the Sommerfeld parameter is given by $\eta = Z_1 Z_2 e^2/v$, with $v$ the relative velocity between the two nuclei. It can be appreciated in Fig. 5.8 how it does not vary as strongly as $\sigma_{\text{fus}}(E_{\text{cm}})$: while the cross section (upper panel) has values in a range larger than 3 orders of magnitude, the $S$ factor (in the lower panel) has a small variation for all the energy values.

The $S$ factor obtained at LO, NLO, and N$^2$LO for $R_0 = 1.4$ fm and with different cutoffs $R_0$ at N$^2$LO is displayed in Fig. 5.9. Given the very weak energy dependence of the double-folding potential observed at the relevant energies, $V_{\text{Ex}}$ is taken at the center of the energy range, $E_{\text{cm}} = 12$ MeV. We have tested that taking a different energy in this range leads to indistinguishable results from those in Fig. 5.9. It is interesting to note that, due to the nearly cutoff-independent asymptotic behavior of the nuclear folding potential (Fig. 5.3), the spread between the results obtained with different values of $R_0$ is small below the Coulomb barrier. This leads to results at N$^2$LO in Fig. 5.9 that are closer than what Fig. 5.3 would suggest. To have an intuitive idea of the impact of the potential in $\sigma_{\text{fus}}$, it is useful to consider that, for low energies, the results can be approximated by the Wong cross section [156]. Assuming that the effective potential can be fitted by a parabola, then $\sigma_{\text{fus}}$ is given by

$$\sigma^{Wong}(E) = \frac{R_{B_0}^2 \hbar\omega_0}{2E} \ln\left(1 + \exp\left[\frac{2\pi(E - V_B)}{\hbar\omega_0}\right]\right), \tag{5.33}$$

where $R_{B_0}$ and $V_B$ are the position and height of the maximum of the parabola for $L = 0$, and $\hbar\omega_0$ is the corresponding curvature.

It can be seen in Fig. 5.10, how the dispersion of $R_{B0}$ and $V_B$ for $V_{\text{eff}}$ obtained with $V_F$ at N$^2$LO is small for the different cutoffs, explaining qualitatively the results seen in Fig. 5.9. This is especially true for low energies, where the small differences in $R_{B_0}$, $V_B$ and $\omega_0$ would become unnoticeable.

Note also that the less attractive potentials (at NLO with $R_0 = 1.4$ fm, and N$^2$LO with $R_0 = 1.2$ fm) naturally lead to the lowest fusion cross sections. The general agreement with the data is good, recalling that there is no fitting parameter. As for elastic scattering, we observe that the sensitivity to the details in the $NN$ interaction shown by the shaded area can only partially explain the discrepancy with experiment. In future work, we will explore how a better many-body calculation of the double-folding potential and more realistic densities of the fusing nuclei may improve this agreement.

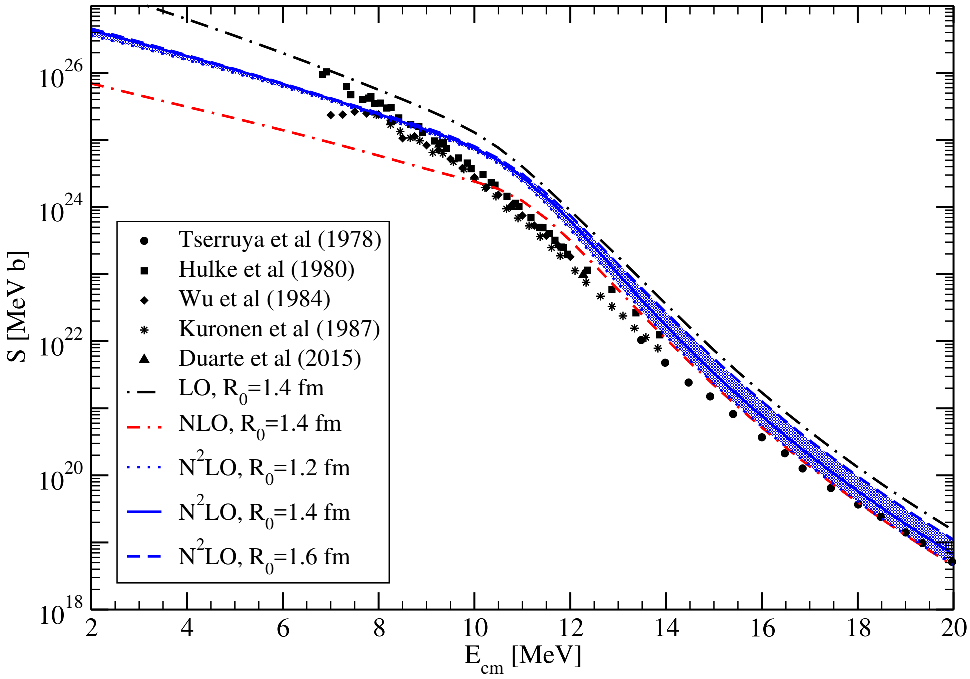

**Figure 5.9:** Astrophysical $S$-factor for the fusion of $^{16}$O+$^{16}$O as a function of the energy $E_{\text{cm}}$ in the center-of-mass system. Results are shown at LO, NLO, and N$^2$LO for $R_0 = 1.4$ fm, and the sensitivity to $R_0 = 1.2$–$1.6$ fm at N$^2$LO is illustrated by the shaded area. The results are compared to experimental data from Refs. [145–149].

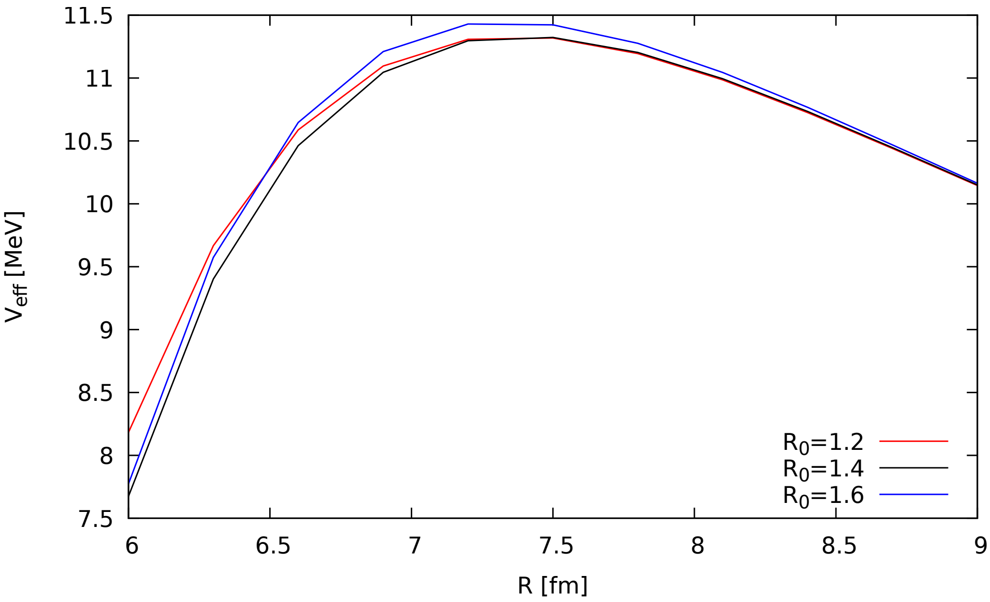

**Figure 5.10:** $V_{\text{eff}}$ with contributions of $V_F$ at N$^2$LO for $R_0$=1.2 (red), $R_0$=1.4 (black) and 1.6 fm (blue).

## 5.4 Perspectives for $3N$ interactions

This section presents first results for the inclusion of $3N$ interactions in this formalism, introducing the triple-folding potential approach. In this case, there is an integral over the density for the coordinate of each of the three-particles, analogous to the $NN$ case. This work was carried out in collaboration with Sulamith Weber [134].

### 5.4.1 Geometry

For the $3N$ case, the geometric situation is more complex than in the $NN$ case. There are two possible distributions of three nucleons in two nuclei. These are shown in Figs. 5.11 and 5.12. Furthermore, the integration now has to run not only over $\mathbf{r}_1$ and $\mathbf{r}_2$ but also over $\mathbf{r}_3$ for the third nucleon.

Also here, the potential between the two nuclei is expressed as a function of $|\mathbf{r}|$. But in comparison to the $NN$ case, one needs not only one ($\mathbf{s}$ for $NN$), but three nucleon-nucleon distances. For this purpose, new labels $d_{ij}$ are introduced. The coordinates corresponding to Fig. 5.11 read

$$d_{12} = |\mathbf{r} - \mathbf{r}_1 + \mathbf{r}_2| = \sqrt{r^2 + r_1^2 + r_2^2 + 2r_2 r\cos(\theta_2) - 2r_1 r\cos(\theta_1) - 2r_1 r_2\cos(\theta_{12})}\,, \tag{5.34a}$$

$$d_{31} = |\mathbf{r} - \mathbf{r}_1 + \mathbf{r}_3| = \sqrt{r^2 + r_1^2 + r_3^2 + 2r_3 r\cos(\theta_3) - 2r_1 r\cos(\theta_1) - 2r_1 r_3\cos(\theta_{13})}\,, \tag{5.34b}$$

$$d_{32} = |\mathbf{r}_2 - \mathbf{r}_3| = \sqrt{r_2^2 + r_3^2 - 2r_2 r_3\cos(\theta_{23})}\,. \tag{5.34c}$$

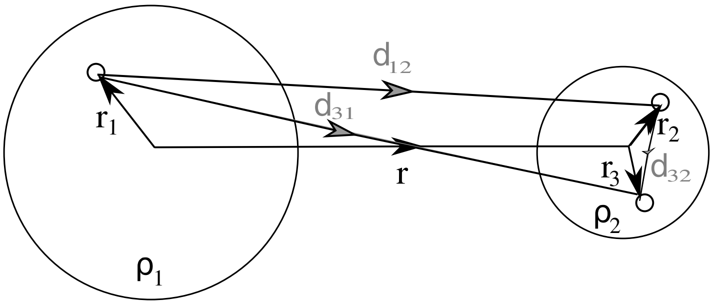

**Figure 5.11:** First of the possible distributions for the folding geometry from 3N interactions. Nucleons are represented by small circles. $\mathbf{r}$ labels the distance between the nuclei, while $\mathbf{r}_1$, $\mathbf{r}_2$, and $\mathbf{r}_3$ mark the position of the nucleons. In addition, the distances $d_{ij}$ between nucleon pairs are shown in gray.

And the second set of coordinates, corresponding to the situation depicted in Fig. 5.12, is written as

$$d'_{12} = |\mathbf{r} - \mathbf{r}_1 + \mathbf{r}_2| = \sqrt{r^2 + r_1^2 + r_2^2 + 2r_2 r\cos(\theta_2) - 2r_1 r\cos(\theta_1) - 2r_1 r_2\cos(\theta_{12})}\,, \tag{5.35a}$$

$$d'_{31} = |\mathbf{r}_1 - \mathbf{r}_3| = \sqrt{r_1^2 + r_3^2 - 2r_1 r_3\cos(\theta_{13})}\,, \tag{5.35b}$$

$$d'_{32} = |\mathbf{r} - \mathbf{r}_2 + \mathbf{r}_3| = \sqrt{r^2 + r_2^2 + r_3^2 + 2r_3 r\cos(\theta_3) - 2r_2 r\cos(\theta_1) - 2r_2 r_3\cos(\theta_{23})}\,. \tag{5.35c}$$

In both cases, $\cos(\theta_{ij})$ is understood as

$$\cos(\theta_{ij}) = \cos(\theta_i)\cos(\theta_j) + \sin(\theta_i)\sin(\theta_j)\cos(\phi_i - \phi_j)\,. \tag{5.36}$$

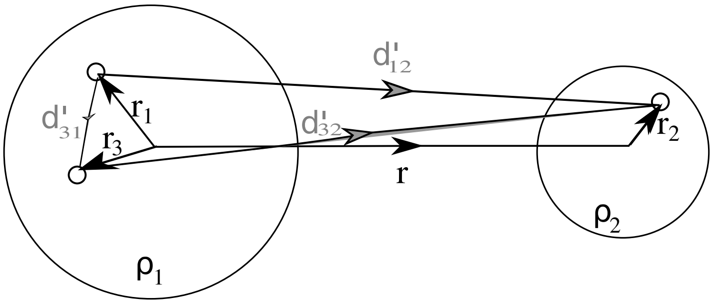

**Figure 5.12:** Second of the possible distributions for the folding geometry from $3N$ interactions. For further explanations see Fig. 5.11.

### 5.4.2 Folding integral: direct part

Analogous to the double-folding case, the direct part of a triple-folding potential can be written as

$$V_F^D(r) = \frac{1}{3!}\int d\mathbf{r}_1 \int d\mathbf{r}_2 \int d\mathbf{r}_3 \sum_{i=1,2,3}\sum_{\sigma_i,\tau_i} \rho(r_1)\rho(r_2)\rho(r_3)\langle 123|v_{3N}(\mathbf{r}_1,\mathbf{r}_2,\mathbf{r}_3)|123\rangle\,, \tag{5.37}$$

where we use the compact notation $|1\rangle \equiv |\mathbf{r}_1 s_1 t_1\rangle$. Eq. (5.37) can, again analogous to the $NN$ case, be rewritten as

$$\begin{aligned} V_F^D(r) = \frac{1}{3!}\int d\mathbf{r}_1 \int d\mathbf{r}_2 \int d\mathbf{r}_3\,[\, & v^{ppp}\rho^p(r_1)\rho^p(r_2)\rho^p(r_3) + v^{ppn}\rho^p(r_1)\rho^p(r_2)\rho^n(r_3) \\ & + v^{pnp}\rho^p(r_1)\rho^n(r_2)\rho^p(r_3) + v^{npp}\rho^n(r_1)\rho^p(r_2)\rho^p(r_3) \\ & + v^{pnn}\rho^p(r_1)\rho^n(r_2)\rho^n(r_3) + v^{npn}\rho^n(r_1)\rho^p(r_2)\rho^n(r_3) \\ & + v^{nnp}\rho^n(r_1)\rho^n(r_2)\rho^p(r_3) + v^{nnn}\rho^n(r_1)\rho^n(r_2)\rho^n(r_3)]\,. \end{aligned} \tag{5.38}$$

### Input three-body potential

In the case of the direct part of the nucleus-nucleus interaction for closed-nuclei, only contributions that depend on the isospin operators without having dependence on the spin will lead to non-vanishing $V_F^D$. In the case of three-nucleon interactions at N$^2$LO, only the potential from Eq. (3.23) fulfills this requirement. Therefore, for the direct part of the triple-folding potential we have that

$$v^{ppp} = v^{nnn} = \frac{c_E}{2f_\pi^4\Lambda_\chi}\left[\delta(d_{32})\delta(d_{12}) + \delta(d_{32})\delta(d_{12}) + \delta(d_{32})\delta(d_{12})\right], \tag{5.39a}$$

$$v^{ppn} = v^{nnp} = \frac{c_E}{2f_\pi^4\Lambda_\chi}\left[\delta(d_{32})\delta(d_{12}) - \delta(d_{32})\delta(d_{12}) - \delta(d_{32})\delta(d_{12})\right], \tag{5.39b}$$

$$v^{npn} = v^{pnp} = \frac{c_E}{2f_\pi^4\Lambda_\chi}\left[-\delta(d_{32})\delta(d_{12}) - \delta(d_{32})\delta(d_{12}) + \delta(d_{32})\delta(d_{12})\right], \tag{5.39c}$$

$$v^{pnn} = v^{npp} = \frac{c_E}{2f_\pi^4\Lambda_\chi}\left[-\delta(d_{32})\delta(d_{12}) + \delta(d_{32})\delta(d_{12}) - \delta(d_{32})\delta(d_{12})\right]. \tag{5.39d}$$

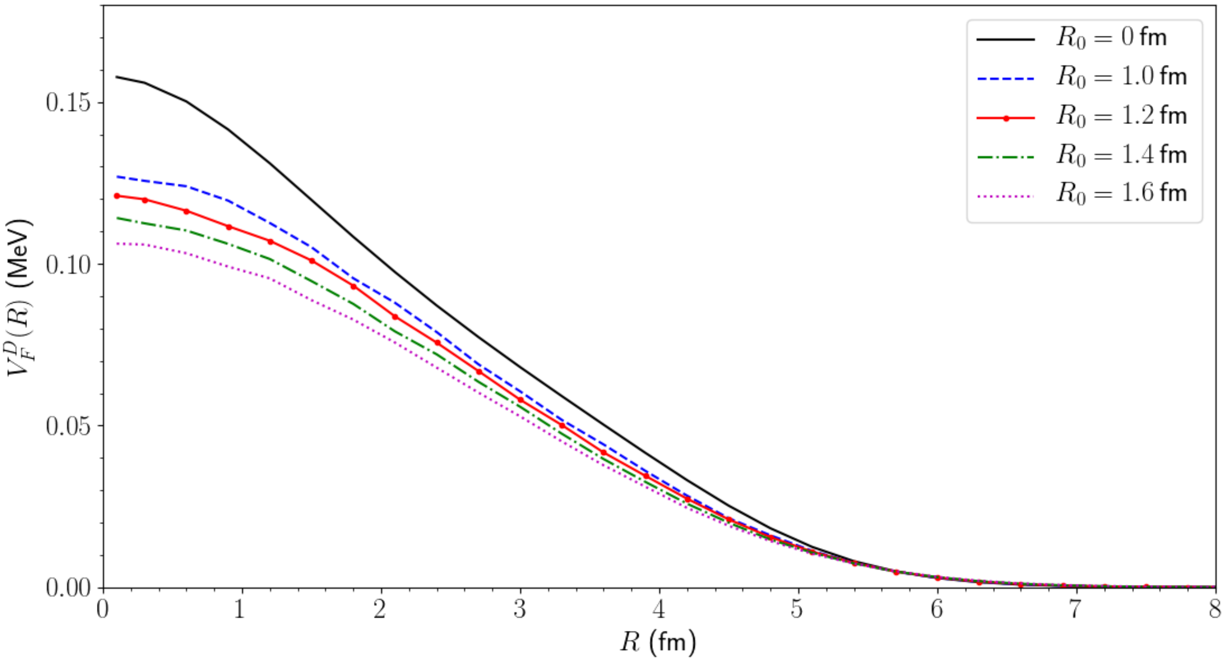

**Figure 5.13:** Triple-folding direct potential $V_F^D(R)$ at N$^2$LO for $R_{3N}$ = 1.0 fm, 1.2 fm, 1.4 fm , 1.6 fm and for the Dirac delta function. The plot shows the convergence of the full folding potential towards $V_F^\delta$ with decreasing values for the coordinate-space cutoff $R_{3N}$. Taken from [134].

### Results

Fig. 5.13 shows the direct part of the nucleus-nucleus potential resulting from the eight-dimensional triple-folding integral. The simplified case $R_{3N}=0$ equivalent to the case in which the potential is proportional to Dirac delta functions can be seen as a reference. To illustrate the convergence of $V_F^D$ towards an unregularized interaction, different cutoffs from 1.0 to 1.6 fm are used in the evaluation of the $NN$ interaction. However, the LEC $c_E$ has not been determined yet for cutoffs other than $R_{3N} =$ 1.2 fm. Consequently, we do not see the proper potentials for these cutoffs. Nevertheless, in order to see the intended behavior of the potential for decreasing values of $R_{3N}$ , we keep $c_E = 0.09$ as it has been fitted for the case $R_{3N} = 1.2$ fm. In all cases, we see that the contribution of the three-body interaction is repulsive, but the order of magnitude of the direct part of the triple-folding potential is too small to be of significance when compared to the double-folding potential of Fig. 5.3. For this reason, it is important to study the exchange term resulting of a $3N$ interaction.

### 5.4.3 Estimation of the exchange triple-folding integral

To get an idea of the size of the impact that the consideration of the exchange potential might have on the triple-folding potential, we do a relatively simple estimation. This is to compute the exchange integral for the summand $W_S(\mathbf{r})\boldsymbol{\tau_1} \cdot \boldsymbol{\tau_2}\boldsymbol{\sigma_1} \cdot \boldsymbol{\sigma_2}$ of the long-range potential for $NN$ forces at N$^2$LO. The particular structure of this summand includes both the spin-spin operator and the isospin-isospin operator, which resembles the structure of the other $3N$ potentials from chiral EFT that vanish in the calculation of the direct part (see Eq. (3.18) to (3.25)). In particular, this operatorial structure is the predominant one in the contact-OPE contribution, which is proportional to $c_D$ (see Eqs. (3.21) and (3.22)). Unlike $c_E$, which is rather small for the case studied here ($c_E = 0.09$), this constant is rather

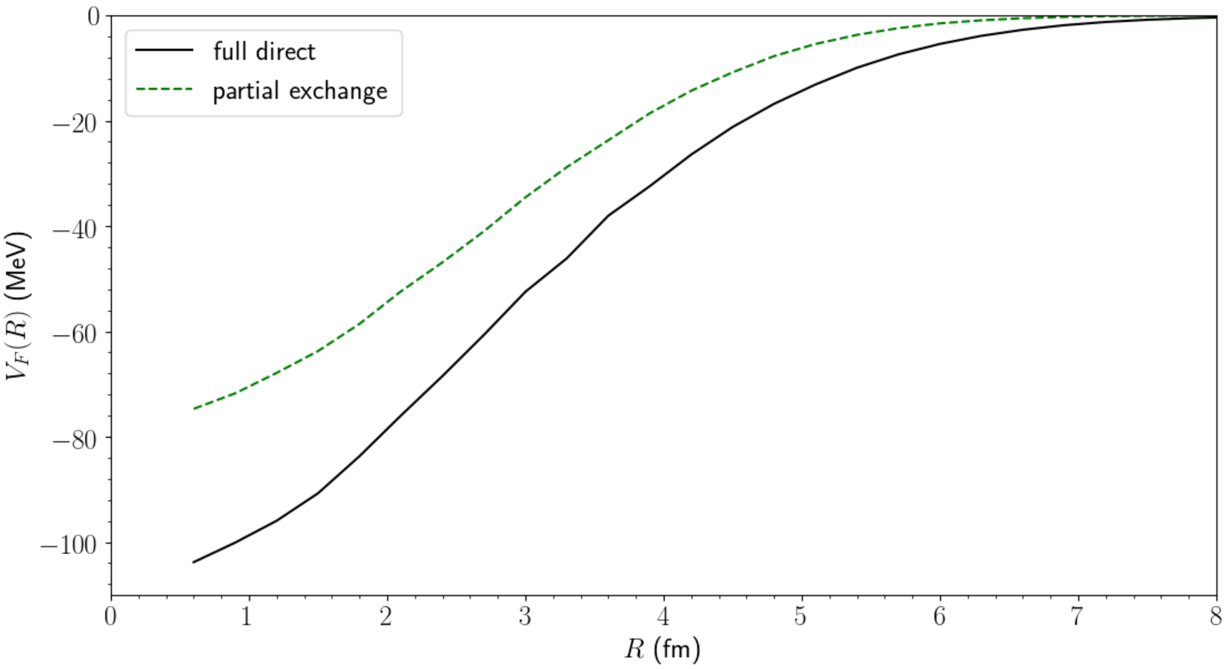

**Figure 5.14:** Exchange part of the double-folding potential at N$^2$LO using only the $W_S$ summand, $V_F^{\mathrm{EX}}(R)$ compared to the full direct folding potential $V_F^{\mathrm{D}}(R)$ at the same order. Results shown for $R_0$= 1.2 fm and $E_{\mathrm{cm}}$ = 175 MeV. Taken from [134].

large ($c_D = 3.5$). Therefore, we would expect that the contribution from this topology to the exchange part of the triple folding potential is enhanced.

Fig. 5.14 shows the double-folding potential for the summand $W_S(\mathbf{r})\boldsymbol{\tau_1} \cdot \boldsymbol{\tau_2}\boldsymbol{\sigma_1} \cdot \boldsymbol{\sigma_2}$ of the $NN$ potential (called partial exchange) compared to the curve for the full direct double-folding potential. One can see that this partial exchange contribution makes up nearly 3/4 of the direct part and is also attractive. Since in the case of the $3N$ potential, the direct potential has found to be repulsive, the exchange part to the 3N forces will probably be repulsive as well.

However, the exchange term in the three-body case differs in the complexity of its structure from the two-body case. There is not only the permutation of two particles to be taken into account, but all possible permutations of three particles, which leads to the following formula for the total antisymmetrized potential:

$$V_{3N}^{\mathrm{antisym}} = (1 - P_{ij} - P_{jk} - P_{ki} + P_{ij}P_{ki} + P_{jk}P_{ij})V_{3N} \,. \tag{5.40}$$

From this relation, we see that there are five instead of, as in the case of the two-body potentials, one additional term that yield the total antisymmetrized potential. Consequently, the exchange contributions for the three-body potentials might make up a larger percentage of the direct potential than those of the $NN$ case, especially since the potentials for the TPE interaction (see Eqs. (3.18) to (3.20)) do not generally vanish as they did in the direct part. This reaffirms the supposition that the exchange contribution for the triple-folding potential would have an impact significantly larger than what seen in Fig. 5.14. To summarize, we would expect, based on this first estimation, the exact computation of the exchange correction for the $3N$ forces at N$^2$LO to be a promising task for future work.

# 6 Three-body interactions and normal ordering

Two- and three-body interactions from chiral EFT are used as a starting point for many *ab initio* aplications to finite nuclei. While there are many-body methods that use an operatorial representation of the interaction, there is a large set of different methods that use a basis expansion as the starting point. In the second case, the basic input are matrix elements of the Hamiltonian, which are, in many cases such as NCSM, MBPT or SM, expressed in a basis of harmonic oscillator (HO) eigenvalues. These matrix elements have to be then decomposed in partial waves in order to be used in calculations of nuclear properties applying the method of preference. Performing the partial wave decomposition calculations, and being able to store and include these matrix elements as exactly and consistently as possible is one of the main challenges of Nuclear Physics nowadays.

Many of the aforementioned many-body methods are developed and optimized only at a two-body level, making the inclusion of higher-body matrix elements a challenge. A standard technique to treat many-body interactions is transforming the original Hamiltonian into an effective interaction with respect to a chosen reference state by means of the normal-ordering technique. While normal ordering is a well-known method to include dominant $3N$ contributions as effective two-body interactions in many-body techniques, it also presents some challenges. The most important of those nowadays are the time needed to perform these calculations and the computational memory required to store the matrix elements at all the steps of the process, that grows quickly with the model space.

In this chapter, we will expand on the description of the treatment of three-body normal-ordered interactions. We will also give technical details, such as the description of the different two- and three-body bases involved in the inclusion of these interactions in many-body calculations. Finally, we will outline the usual normal-ordering procedure and discuss the challenges involved in this approach.

## 6.1 Normal-ordered Hamiltonian

In general, the second-quantization representation of a nuclear Hamiltonian with up to three-nucleon interactions reads:

$$H = \sum_{12} T_{12} a_1^\dagger a_2 + \frac{1}{(2!)^2} \sum_{1234} \langle 12 | V_{NN} | 34 \rangle \, a_1^\dagger a_2^\dagger a_4 a_3 + \frac{1}{(3!)^2} \sum_{123456} \langle 123 | V_{3N} | 456 \rangle \, a_1^\dagger a_2^\dagger a_3^\dagger a_6 a_5 a_4 \,. \quad (6.1)$$

Here, the fermionic creation and annihilation operators satisfy the anticommutation relations

$$\{a_i^\dagger, a_j\} = \delta_{ij} \,, \; \{a_i, a_j\} = \{a_i^\dagger, a_j^\dagger\} = 0 \,. \quad (6.2)$$

At the same time, the representation of the Hamiltonian in a chosen basis implies that these operators also fulfill

$$a_i |\phi_0\rangle = 0 \,, \quad (6.3)$$

where $|\phi_0\rangle$ is the ground state wave function.

Applying Wick's theorem [157], we can evaluate the normal ordering of the operators of the Hamiltonian with respect to the chosen reference state. In order to do so, the contraction of two operators will be represented with the symbol $\sqcap$.

Starting with the one-body piece

$$a_1^\dagger a_2 = \wick{\c a_1^\dagger \c a_2} + \{a_1^\dagger a_2\}\,,$$

leads to

$$\sum_{12} T_{12} a_1^\dagger a_2 = T_{11} n_1 + \sum_{12} T_{12} \{a_1^\dagger a_2\} n_1 n_2\,,$$

where $n_i$ represents the occupation function corresponding to the chosen basis.

Applying the same procedure to the two-body contribution

$$\begin{aligned} a_1^\dagger a_2^\dagger a_4 a_3 &= \{a_1^\dagger a_2^\dagger a_4 a_3\} + \wick{\c a_1^\dagger a_2^\dagger \c a_4 a_3} + \wick{\c a_1^\dagger a_2^\dagger a_4 \c a_3} + \wick{a_1^\dagger \c a_2^\dagger \c a_4 a_3} + \wick{a_1^\dagger \c a_2^\dagger a_4 \c a_3} + \wick{\c1 \c3 a_1^\dagger \c2 \c4 a_2^\dagger \c1 \c4 a_4 \c2 \c3 a_3} \\ &= \{a_1^\dagger a_2^\dagger a_4 a_3\} - \{a_2^\dagger a_3\}\delta_{14} + \{a_2^\dagger a_4\}\delta_{13} + \{a_1^\dagger a_3\}\delta_{24} - \{a_1^\dagger a_4\}\delta_{23} + \delta_{13}\delta_{24} - \delta_{14}\delta_{23}\,, \end{aligned}$$

$$\begin{aligned} \sum_{1234} \langle 12|V_{NN}|34\rangle\, a_1^\dagger a_2^\dagger a_4 a_3 = &\sum_{1234} \langle 12|V_{NN}|34\rangle\, \{a_1^\dagger a_2^\dagger a_4 a_3\} \\ &+ 4 \sum_{12} \sum_i \langle 1i|V_{NN}|2i\rangle\, n_i \{a_1^\dagger a_2\} \\ &+ 2 \sum_{12} \langle 12|V_{NN}|12\rangle\, n_1 n_2\,, \end{aligned} \tag{6.4}$$

and the three-body piece

$$\begin{aligned} a_1^\dagger a_2^\dagger a_3^\dagger a_6 a_5 a_4 = \{a_1^\dagger a_2^\dagger a_3^\dagger a_6 a_5 a_4\} &+ \wick{\c a_1^\dagger a_2^\dagger a_3^\dagger a_6 a_5 \c a_4} + \overset{\text{(1 contraction)}}{\cdots} \\ &+ \wick{\c1 a_1^\dagger \c2 a_2^\dagger a_3^\dagger a_6 \c2 a_5 \c1 a_4} + \wick{\c1 a_1^\dagger \c2 a_2^\dagger a_3^\dagger \c2 a_6 a_5 \c1 a_4} + \wick{\c1 a_1^\dagger a_2^\dagger \c2 a_3^\dagger a_6 \c2 a_5 \c1 a_4} + \wick{\c1 a_1^\dagger a_2^\dagger \c2 a_3^\dagger \c2 a_6 a_5 \c1 a_4} \\ &+ \wick{\c1 a_1^\dagger \c2 a_2^\dagger a_3^\dagger a_6 \c1 a_5 \c2 a_4} + \wick{\c1 a_1^\dagger \c2 a_2^\dagger a_3^\dagger \c2 a_6 \c1 a_5 a_4} + \wick{\c1 a_1^\dagger a_2^\dagger \c2 a_3^\dagger a_6 \c1 a_5 \c2 a_4} + \wick{\c1 a_1^\dagger a_2^\dagger \c2 a_3^\dagger \c2 a_6 \c1 a_5 a_4} \\ &+ \wick{\c1 a_1^\dagger \c2 a_2^\dagger a_3^\dagger \c1 a_6 \c2 a_5 a_4} + \wick{\c1 a_1^\dagger \c2 a_2^\dagger a_3^\dagger \c1 a_6 a_5 \c2 a_4} + \wick{\c1 a_1^\dagger a_2^\dagger \c2 a_3^\dagger \c1 a_6 \c2 a_5 a_4} + \wick{\c1 a_1^\dagger a_2^\dagger \c2 a_3^\dagger \c1 a_6 a_5 \c2 a_4} \\ &+ \wick{\c1 \c4 a_1^\dagger \c2 \c5 a_2^\dagger \c3 \c6 a_3^\dagger \c1 \c6 a_6 \c2 \c5 a_5 \c3 \c4 a_4} + \wick{\c1 \c4 a_1^\dagger \c2 \c5 a_2^\dagger \c3 \c6 a_3^\dagger \c1 \c5 a_6 \c3 \c6 a_5 \c2 \c4 a_4} + \wick{\c1 \c4 a_1^\dagger \c2 \c5 a_2^\dagger \c3 \c6 a_3^\dagger \c1 \c5 a_6 \c3 \c4 a_5 \c2 \c6 a_4}\,, \end{aligned}$$

$$\begin{aligned} \sum_{123456} \langle 123|V_{3N}|456\rangle\, a_1^\dagger a_2^\dagger a_3^\dagger a_6 a_5 a_4 = &\sum_{123456} \langle 123|V_{3N}|456\rangle\, \{a_1^\dagger a_2^\dagger a_3^\dagger a_6 a_5 a_4\} \\ &+ 9 \sum_{1234} \sum_i \langle 12i|V_{3N}|34i\rangle\, n_i \{a_1^\dagger a_2^\dagger a_4 a_3\} \\ &+ 12 \sum_{12} \sum_{ij} \langle 1ij|V_{3N}|2ij\rangle\, n_i n_j \{a_1^\dagger a_2\} \\ &+ 6 \sum_{123} \langle 123|V_{3N}|123\rangle\, n_1 n_2 n_3\,, \end{aligned} \tag{6.5}$$

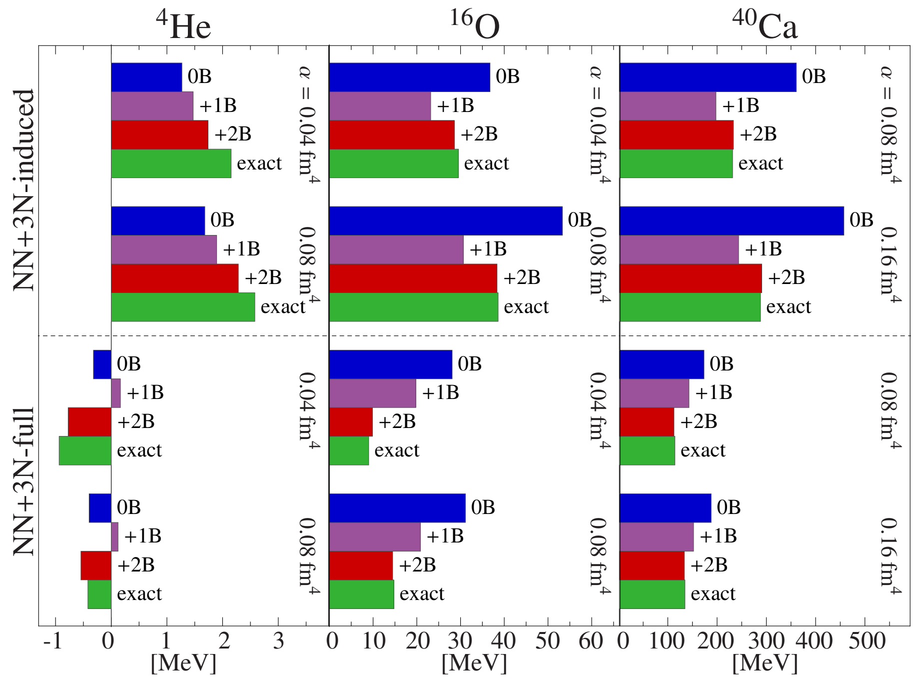

**Figure 6.1:** *Anatomy of the NO$n$B approximation of the ground-state energies of $^4$He, $^{16}$O, and $^{40}$Ca*: Figure shows the expectation values of the $3N$ interaction computed at different levels of the normal-ordering approximation. The eigenstates correspond to the ground states of the different nuclei obtained in an IT-NCSM calculation. The interaction is normal-ordered regarding the unperturbed HO Slater determinant. Figure taken from Ref. [158].

the Hamiltonian of Eq. (6.1) can be exactly written as

$$\begin{aligned} H =& T_{11}n_1 + \frac{1}{2}\sum_{12}\langle 12|V_{NN}|12\rangle\, n_1n_2 + \frac{1}{6}\sum_{123}\langle 123|V_{3N}|123\rangle\, n_1n_2n_3 \\ &+ \sum_{12}\left( T_{12}n_1n_2 + \sum_i \langle 1i|V_{NN}|2i\rangle\, n_i + \frac{1}{2}\sum_{ij}\langle 1ij|V_{3N}|2ij\rangle\, n_in_j \right)\{a_1^\dagger a_2\} \\ &+ \frac{1}{(2!)^2}\sum_{1234}\left( \langle 12|V_{NN}|34\rangle + \sum_i \langle 12i|V_{3N}|34i\rangle\, n_i \right)\{a_1^\dagger a_2^\dagger a_4 a_3\} \\ &+ \frac{1}{(6!)^2}\sum_{123456} \langle 123|V_{3N}|456\rangle\, \{a_1^\dagger a_2^\dagger a_3^\dagger a_6 a_5 a_4\} \end{aligned} \tag{6.6}$$

where we can see line-by-line the 0-, 1-, 2- and 3-body components of the interaction. The term $\sum_i \langle 12i|V_{3N}|34i\rangle\, n_i$ is known as the two-body normal ordered (2BNO) contribution. As it can be seen in Fig. 6.1, the inclusion of this term is necessary to reproduce properties of medium- and heavy-mass nuclei, while the contribution of the residual 3-body interaction ($\langle 123|V_{3N}|456\rangle$) can be regarded as negligible, especially for heavier systems.

## 6.2 Bases for matrix elements

In this section, we will give a description of the bases that will be used in the rest of this work.

All relevant momentum coordinates involved in the following of this work are represented schematically in Fig. 6.2.

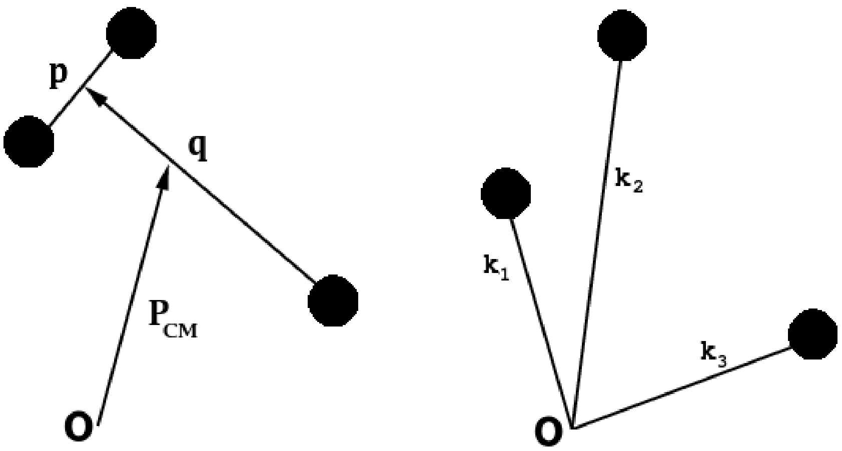

**Figure 6.2:** Graphical representation of three-body momentum coordinate bases: Jacobi $\mathbf{p}$, $\mathbf{q}$, and $\mathbf{P}_{cm}$ (left) and single-particle momenta $\mathbf{k}_1$, $\mathbf{k}_2$, and $\mathbf{k}_3$ (right). The letter O indicates the coordinate origin in both cases.

### 6.2.1 Jacobi momentum basis

A general translationally invariant three-body force can be written as a function of the relative Jacobi momenta, defined in terms of single-particle momenta $\mathbf{k}_i$ as

$$\mathbf{p} = \frac{1}{2}(\mathbf{k}_1 - \mathbf{k}_2), \tag{6.7a}$$

$$\mathbf{q} = \frac{2}{3}\left(\mathbf{k}_3 - \frac{1}{2}(\mathbf{k}_1 + \mathbf{k}_2)\right), \tag{6.7b}$$

$$\mathbf{X} = \mathbf{k}_1 + \mathbf{k}_2 + \mathbf{k}_3, \tag{6.7c}$$

where $\mathbf{X}$ is the conserved total momentum.

Since the normal-ordering procedure is performed with respect to a given reference state, Galilean invariance is broken and therefore a normal-ordered interaction depends, in the most general case, also on the two-body center-of-mass coordinate. We also introduce the definition of such

$$\mathbf{P} = \mathbf{k}_1 + \mathbf{k}_2 . \tag{6.8}$$

Hence, the single-particle momenta in terms of the Jacobi coordinates can be written as

$$\mathbf{k}_1 = \mathbf{p} + \frac{\mathbf{P}}{2}, \tag{6.9a}$$

$$\mathbf{k}_2 = -\mathbf{p} + \frac{\mathbf{P}}{2}, \tag{6.9b}$$

$$\mathbf{k}_3 = \frac{3}{2}\mathbf{q} + \frac{\mathbf{P}}{2}, \tag{6.9c}$$

whereas the total three-body momentum is given by:

$$\mathbf{X} = \mathbf{k}_1 + \mathbf{k}_2 + \mathbf{k}_3 = \frac{3}{2}\mathbf{P} + \frac{3}{2}\mathbf{q} = \frac{3}{2}\mathbf{P}' + \frac{3}{2}\mathbf{q}' = \mathbf{k}_1' + \mathbf{k}_2' + \mathbf{k}_3' . \tag{6.10}$$

Here and in the following, $\mathbf{p}$ and $\mathbf{q}$ denote the three-body Jacobi momenta and $\mathbf{P}$ the two-body center-of-mass coordinate of the initial state, while their primed counterparts denote the coordinates for the final state.

### 6.2.2 Partial-wave decomposed relative-momentum basis

In order to determine the quantum numbers corresponding to two-body matrix elements dependent on $\mathbf{p}$, these can be decomposed into partial waves with defined total relative angular momentum, $L$ and angular momentum projection $M_L$. This is achieved by collapsing the state with the spherical harmonics function $Y_{LM_L}(\hat{\mathbf{p}})$, where $\hat{\mathbf{p}}$ denotes the angular part of the vector $\mathbf{p}$, and integrating over all possible angular contributions. The same holds for the primed variables, leading to

$$\langle pLM_L|V_{NN}|p'L'M_L'\rangle = \int d\hat{\mathbf{p}} Y^*_{LM_L}(\hat{\mathbf{p}}) \int d\hat{\mathbf{p}}' Y_{L'M_L'}(\hat{\mathbf{p}'})\langle \mathbf{p}|V_{NN}|\mathbf{p}'\rangle \,. \tag{6.11}$$

Three-body interactions can also be decomposed in partial waves in an analogous manner. The relative angular momentum and projection of the first nucleon pair is also denoted by $L$ and $M_L$, while $l_3$ is the angular momentum associated to the third particle with coordinate $\mathbf{q}$, and $m_3$ its projection. Therefore, taking into account intial and final states

$$\begin{aligned}\langle pqLMl_3m_3|V_{3N}|p'q'L'M'l_3'm_3'\rangle = &\int d\hat{\mathbf{p}} Y^*_{LM}(\hat{\mathbf{p}}) \int d\hat{\mathbf{p}}' Y_{L'M'}(\hat{\mathbf{p}'}) \\ &\times \int d\hat{\mathbf{q}} Y^*_{l_3m_3}(\hat{\mathbf{q}}) \int d\hat{\mathbf{q}}' Y_{l_3{}'m_3{}'}(\hat{\mathbf{q}'})\langle \mathbf{pq}|V_{3N}|\mathbf{p}'\mathbf{q}'\rangle\end{aligned} \tag{6.12}$$

### 6.2.3 Harmonic-oscillator basis

The HO basis presents a complete and discrete basis with localized wave functions and it is widely used in various many-body methods due to its many advantages. Since it is based on the nuclear symmetries, those are easy to exploit, as is the treatment of angular momentum degrees of freedom, which are well defined. On the other hand, its localized nature well-describes self-bound systems, which makes it a suitable basis to study nuclei.

In the case of a problem in which the Hamiltonian can be written as a sum of an intrinsic and a center-of-mass (cm) contributions ($H = H_{\text{int}} + H_{\text{cm}}$), working in HO basis ensures that the wave function of the system factorizes as $\psi = \psi_{\text{int}}\psi_{\text{cm}}$, leading to eigenenergies of physical states that are independent of cm excitations, hence spurious effects of center-of-mass motion can be isolated and removed. These spurious states appear due to the fact that a single particle basis composed of eigenstates of both linear and angular momentum does not exist. For this reason, one normally considers a basis that conserves angular momentum and breaks translational invariance, which leads to a mixing of intrinsic and cm excitations. The real solution of a many-body problem uses a truncated basis instead of working with an ideal infinite space, and therefore said mixing of cm degrees of freedom cannot be removed. A way of shifting cm excitations to high energies, which are in general less relevant for the problem, is the Lawson method [159]. Nevertheless, it is necessary to point out that in cases in which states of high energy or states in the continuum are important, such as, e.g., halo nuclei, the incorrect asymptotic behavior of the matrix elements in HO basis has a noticeable impact and needs to be addressed.

The states in this basis are defined by the HO well frequency $\hbar\omega$ and the quantum numbers $N$ and $L$ both in relative and center-of-mass coordinates. Schematically, we write a general state as

$$V_{HO} = \langle NLN_{\text{cm}}L_{\text{cm}}|V|N'L'N_{\text{cm}}'L_{\text{cm}}'\rangle \,, \tag{6.13}$$

Notice that there can also be single-particle harmonic oscillator representations, in which $N$, $L$, $N_{\text{cm}}$ and $L_{\text{cm}}$ are substituted by $n_i$ and $l_i$, where $i$ indicates a generic index that accounts for the different particles of the problem. These two representations are related by the Talmi-Moshinsky transformation. For more details on this topic, see Sec. 7.6.3.

Harmonic oscillator radial wave functions

Working in spherical coordinates, the harmonic oscillator two-body relative radial wave function can be written as [160]

$$\tilde{R}_{nl}\left(r_{12}\right)=\tilde{N}_{nl}\left(\frac{r_{12}}{b}\right)^{l}e^{-\left(\frac{r_{12}}{b}\right)^{2}/2}L_{n}^{l+1/2}\left[\left(\frac{r_{12}}{b}\right)^{2}\right], \tag{6.14}$$

where $b=\sqrt{\frac{\hbar}{m\omega}}$ is the harmonic oscillator length. The normalization constant is given by

$$\tilde{N}_{nl}=\frac{1}{b^{3/2}}\sqrt{\frac{2n!}{\Gamma\left(n+l+3/2\right)}}, \tag{6.15}$$

and the Laguerre polynomials are defined as

$$L_{n}^{k}=\frac{e^{x}x^{-k}}{n!}\frac{d^{n}}{dx^{n}}\left(e^{-x}x^{n+k}\right). \tag{6.16}$$

The Fourier transform of Eq. (6.14) gives that in momentum space

$$R_{nl}(p)=N_{nl}\left(pb\right)^{l}e^{-(pb)^{2}/2}L_{n}^{l+1/2}\left[(pb)^{2}\right], \tag{6.17}$$

with

$$N_{nl}=b^{3/2}\sqrt{\frac{2n!}{\Gamma\left(n+l+3/2\right)}}. \tag{6.18}$$

It is important to point out that in our definition, the two-body harmonic oscillator Hamiltonian with relative distance **x** and center-of-mass coordinate **X** reads

$$H=\frac{\mathbf{P}^{2}}{2M}+\frac{1}{2}M\omega^{2}\mathbf{X}^{2}+\frac{\mathbf{k}^{2}}{2\mu}+\frac{1}{2}\mu\omega^{2}\mathbf{x}^{2}, \tag{6.19}$$

where $M=m_1+m_2=2m$ is the total mass and $\mu=m/2$ the reduced mass of the problem. Therefore the HO lengths associated to the relative and center-of-mass parts

$$\begin{aligned} b_{\text{rel}}&=\sqrt{\frac{\hbar}{\mu\omega}}, \\ b_{\text{cm}}&=\sqrt{\frac{\hbar}{M\omega}}, \end{aligned} \tag{6.20}$$

are related by a factor 2, being $b_{\text{cm}}=b_{\text{rel}}/2$. In order to perform a symmetric treatment of the radial wave functions, they need to be related to $b$ taking into account these factors. In consequence, we will always consider

$$\begin{aligned} b_{\text{rel}}&=\sqrt{2}b, \\ b_{\text{cm}}&=\frac{b}{\sqrt{2}}. \end{aligned} \tag{6.21}$$

### 6.2.4 $JT$-coupled single-particle basis

Given the nature of the interaction, the nuclear Hamiltonian is, in almost all cases, rotationally invariant. This implies that $[H, \boldsymbol{J}] = [H, \boldsymbol{J}_z] = 0$, leading to eigenstates with good $J$ and $M_J$ quantum numbers, where $J$ stands for the two-body coupled total angular momentum and $M_J$ is its projection along the $z$-axis.

Since this symmetry holds also for isospin degrees of freedom, a good basis to work with this Hamiltonian is one that has fixed $J$ and $T$, or $JT$-coupled basis.

The quantum numbers are defined with respect to single-particle coordinates coupling their individual angular momenta $j_i$ to $J$ and the single-particle isospins $t_i$ to $T$,

$$|n_a l_a; n_b l_b; (j_a j_b) J; (t_a t_b) T\rangle , \tag{6.22}$$

The main advantage of working in this basis is the reduced number of elements that it englobes. This makes it an ideal candidate to store final two-body matrix elements to be used as input for many-body calculations.

### 6.2.5 $m$-scheme single-particle basis

Alternatively to the $JT$-coupled basis, we can choose to construct a basis that has the projection of angular momenta fixed, since the eigenstates of the Hamiltonian do not depend on the orientation $M$.

The $m$-scheme is an antisymmetrized many-body basis that arises from $A$-body Slater determinants of single-particle HO states. The quantum numbers are defined with respect to single particle coordinates coupling the orbital angular momentum $l_i$ and the spin $s_i$ of each particle to its total angular momentum $j_i$

$$|n_a j_a m_{j_a} m_{t_a}; n_b j_b m_{j_b} m_{t_b}; n_c j_c m_{j_c} m_{t_c}\rangle . \tag{6.23}$$

One of the main advantages of this representation is that the quantum numbers of each particle are well defined and known, being an excellent basis to, e.g, perform the normal-ordering of the Hamiltonian.

On the other hand, given its construction, one of the disadvantages is that angular momentum is not a well-defined quantum number. Another drawback of this representation is that the complete basis is large, even though it contains a significant number of states that are zero, which makes computational storage a challenge.

## 6.3 Usual approach to the calculation of two-body normal ordered matrix elements

In the following, we will concentrate on the two-body part of a normal-ordered three-body Hamiltonian. Even though the determination of observables including three-body interactions elements requires also one- and zero-body matrix elements arising from $V_{3N}$, the calculation of these is much less involved once the two-body matrix elements are known. Therefore, we will not explicitly mention them, but they are included in all results shown, unless stated otherwise.

In this section we will outline the main components needed to calculate NO2B matrix elements to be included in many-body calculations, as done in the conventional manner: starting from three-body matrix elements in Jacobi basis that will be transformed to single-particle basis. Once in this form the normal-ordering procedure can be carried out to finalize with a transformation to change the basis at two-body level, if needed.

### 6.3.1 Nomenclature

Before dealing with the expressions involved in the normal-ordering procedure, it is useful and necessary to detail the quantum numbers that will be used in this section:

- Lower case letters with latin letters as subindices, such as $n_a$, $l_a$ ..., are the single-particle quantum numbers in HO basis.
- $L_{ab}$, $S_{ab}$, $J_{ab}$... are the result of coupling single-particle quantum numbers of particles $a$ and $b$.
- $L_3$, $S_3$, $J_3$... (upper case letters) are the coupled quantum numbers of the three-body system $(ab)c$.
- $\mathscr{N}_{12}$, $\mathscr{L}_{12}$... are the center-of-mass two-body quantum numbers of the particles in Jacobi basis.
- $N_{12}$, $L_{12}$, $J_{12}$... are the relative two-body quantum numbers of the particles in Jacobi basis.
- Lower case letters with numbers as subindices, such as $n_1$, $l_1$ ... are the quantum numbers corresponding to each particle in Jacobi basis.
- $\mathscr{L}$, $\mathscr{S}$, $\mathscr{J}$, $\mathscr{T}$... are the $3N$ quantum numbers result of coupling the system (12)3 in Jacobi basis.
- $\mathscr{J}_{\text{tot}}$ is the total angular momentum coupling of $\mathscr{L}$ and $\mathscr{S}$.
- $N_{\text{cm}}$, $L_{\text{cm}}$... are the two-body center-of-mass in the three-body frame.
- $\Lambda$ is the angular momentum coupling of $\mathscr{L}_{12}$ and $l_c$.

We also introduce a compact notation that englobes the three-body coupled bases as

$$|\alpha\rangle = |[(N_{12}L_{12}, S_{12})J_{12}, (n_3 l_3, s_3)j_3]\mathscr{J}\mathscr{M}_{\mathscr{J}}\rangle|(T_{12}t_3)\mathscr{T}\mathscr{M}_{\mathscr{T}}\rangle \tag{6.24}$$

### 6.3.2 Normal-ordering in single-particle basis

The two-body normal ordered interaction is schematically defined as

$$\left\langle ab|V_{\text{eff}}|a'b'\right\rangle = \sum_{\text{c}} \left\langle abc|V_{3N}|a'b'c\right\rangle \tag{6.25}$$

whereas $V_{3N}$ is an antisymmetrized 3N interaction and $a, b, c, a', b'$ are quantum numbers in a single-particle basis. The sum over $c$ runs over occupied orbitals in a reference state for a given core. Also, in this equation the states in bra and ket are defined as

$$\langle ab|V_{\text{eff}}|a'b'\rangle = \langle n_a l_a n_b l_b (j_a j_b) J_{ab} T_{ab}|V_{\text{eff}}|n'_a l'_a n'_b l'_b (j'_a j'_b) J'_{ab} T'_{ab}\rangle \tag{6.26}$$

Since the matrix elements from chiral EFT are computed and stored in Jacobi basis, the first step is to transform them into $JT$-coupled scheme:

$$\begin{aligned}
\langle abcJ_{ab}J_3T_{ab}J_3|V_{3N}|a'b'c'J'_{ab}J_3T'_{ab}J_3\rangle = \sum_{\substack{N_1N_2\alpha \\ N'_1N'_2\alpha}} \sum_{i,i'} \sum_{N_{\text{cm}}L_{\text{cm}}} & \delta_{T_{ab},T_1}\delta_{T'_{ab},T'_1}\delta_{T,T_{12}}\delta_{T,T'_{12}} \\
& \times \langle N_{cm}L_{cm};\alpha;n_1n_2;J_3|(abc)J_{ab}J_3;T_{ab}T_3\rangle \\
& \times \langle N_{cm}L_{cm};\alpha';n'_1n'_2;J_3|(a'b'c')J'_{ab}J_3;T'_{ab}T_3\rangle \\
& \times C^i_\alpha C^{i'}_{\alpha'}\langle\alpha|V_{3N}|\alpha'\rangle\,,
\end{aligned} \tag{6.27}$$

where $C^i_\alpha$ are the coefficients of fractional parentage (CFPs) [161, 162]. CFPs are used to obtain the completely antisymmetric three-body states with respect to the exchange of any particle pair. With help of these coefficients, we can write states defined using the energy quantum number $E$ ($E = 2N_{12} + L_{12} + n_3 + l_3 = 2N'_{12} + L'_{12} + n'_3 + l'_3$), and the total angular momentum and isospin $\mathscr{J}\mathscr{T}$. Since the subspace within each $E\mathscr{J}\mathscr{T}$ block is degenerate, there is the additional label $i$ that defines these coefficients. Therefore, we have the relation

$$|E\mathscr{J}\mathscr{T}\rangle = \sum_{\alpha} \langle \alpha | E\mathscr{J}\mathscr{T}\rangle |\alpha\rangle = C^i_\alpha |\alpha\rangle\,. \tag{6.28}$$

The overlaps of the single-particle states with the Jacobi states are known as $T$-coefficients

$$T^{n_a l_a j_a n_b l_b j_b n_c l_c j_c J_{ab} J_3}_{n_1 l_1 j_1 n_2 l_2 j_2 J_{12} N_{cm} L_{cm}} \equiv \langle N_{cm} L_{cm}; \alpha; n_1 n_2; J_3 | (abc) J_{ab} J_3; T_{ab} T_3\rangle\,, \tag{6.29}$$

and they are calculated as follows (for details on this derivation, see Ref. [106, 163])

$$\begin{aligned}
T^{n_a l_a j_a n_b l_b j_b n_c l_c j_c J_{ab} J}_{N_{cm} L_{cm}} = & \sum_{\substack{L_{ab} N_{ab} L_{ab} \mathscr{L} \\ L_3 \Lambda S_3}} (-1)^{l_c + \Lambda + L_{ab} + L_{12} + \mathscr{L} + S_3 + J_3} \hat{j}_a \hat{j}_b \hat{j}_c \hat{S}_{ab} \hat{J}_{ab} \hat{J}_{12} \hat{L}^2_{ab} \hat{\mathscr{L}}^2 \hat{S}^2_3 \hat{L}^2_3 \hat{J}_3 \hat{\Lambda}^2 \\
& \times \langle \mathscr{N}_{12} \mathscr{L}_{12} N_{12} L_{12} | n_a l_a n_b l_b L_{ab}\rangle_{d=1} \, \langle N_{cm} L_{cm} n_3 l_3 | \mathscr{N}_{12} \mathscr{L}_{12} n_c l_c \Lambda\rangle_{d=2} \\
& \times \begin{Bmatrix} l_a & 1/2 & j_a \\ l_b & 1/2 & j_b \\ L_{ab} & S_{ab} & J_{ab} \end{Bmatrix} \begin{Bmatrix} L_{ab} & S_{ab} & J_{ab} \\ l_c & 1/2 & j_c \\ L_3 & S_3 & J_3 \end{Bmatrix} \begin{Bmatrix} L_{12} & l_3 & \mathscr{L} \\ S_{ab} & 1/2 & S_3 \\ J_{12} & j_3 & \mathscr{J}_{\text{tot}} \end{Bmatrix} \\
& \times \begin{Bmatrix} l_c & \mathscr{L}_{12} & \Lambda \\ L_{12} & L_3 & L_{ab} \end{Bmatrix} \begin{Bmatrix} L_{cm} & l_3 & \Lambda \\ L_{12} & L_3 & \mathscr{L} \end{Bmatrix} \begin{Bmatrix} L_{cm} & \mathscr{L} & L_3 \\ S_3 & J_3 & \mathscr{J}_{\text{tot}} \end{Bmatrix}
\end{aligned} \tag{6.30}$$

Once the Jacobi matrix elements are expressed in single-particle (carrying out the sums indicated in Eq. (6.27)), the sum over the states of third particle, and hence the normal-ordering procedure, is conceptually straightforward to perform,

$$\begin{aligned}
\langle ab | V_{\text{eff}} | a'b'\rangle = & \sum_{c, m_c, m_{t_c}} \langle (ab) J M T M_T | \langle c m_c 1/2 m_{t_c} | V_{3N} | (a'b') J' M' T' M'_T\rangle | c m_c 1/2 m_{t_c}\rangle \\
= & \sum_{c} \sum_{J_3 T_3} \frac{(2J_3+1)(2T_3+1)}{(2J+1)(2+1)} \delta_{JJ'} \delta_{MM'} \delta_{TT'} \delta_{M_T M'_T} \\
& \times \langle [(ab) J T c 1/2] J_3 T_3 | V_{3N} | [(a'b') J' T' c 1/2] J_3 T_3\rangle
\end{aligned} \tag{6.31}$$

### 6.3.3 Challenges of this approach

As detailed in the previous section, the conventional way of calculating these matrix elements is done in single-particle basis.

Fig. 6.3 reflects the memory needs to store matrix elements in different representations: Jacobi (purple squares), $JT$-coupled (red triangles), and $m$-scheme (blue circles) bases as a function of the maximal three-body energy of the states, $E_{3N}$, which is given by $2N_{12} + L_{12} + 2n_3 + l_3$ in the relative basis and $\sum_{i=1}^{3} 2n_i + l_i$ in the single-particle representations.

As it can be seen in the plot, the memory required depends on the symmetries that the three-body basis incorporates. The antisymmetrized Jacobi basis requires the least memory because it exploits all symmetries of the interaction: hermicity, rotational invariance, antisymmetry, and translational invariance. On the other hand, the $JT$-coupled scheme does include coupling between relative and

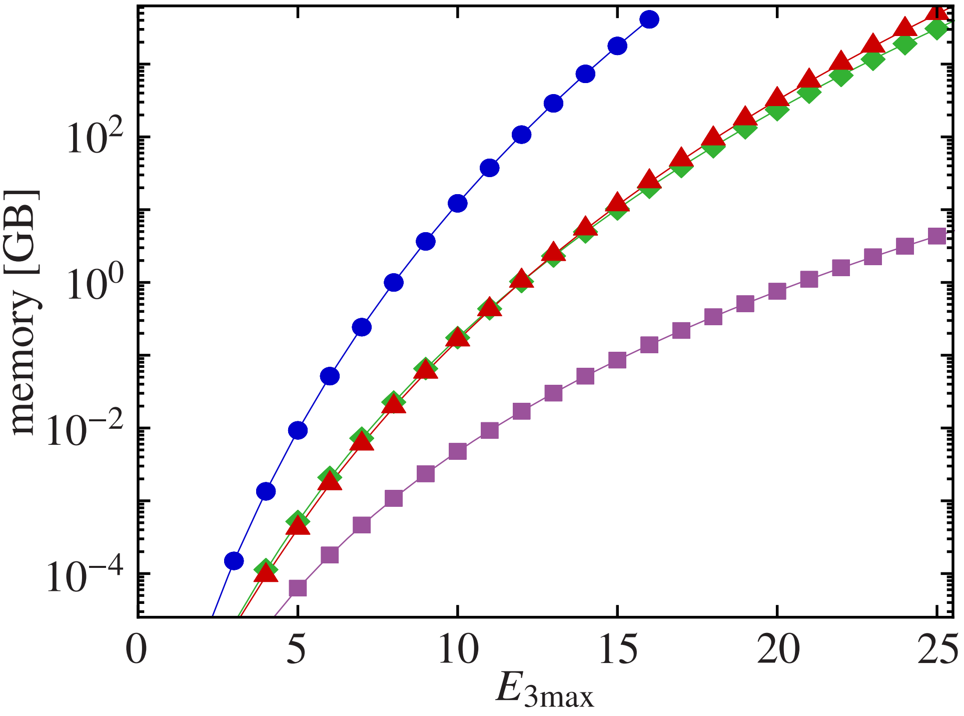

**Figure 6.3:** Memory usage as function of the three-body maximum energy $E_{3\max}$. In ascending order, the plot shows the memory required to store three-body matrix elements in antisymmetrized Jacobi basis (purple squares), $JT$-coupled basis (red triangles), and $m$-scheme basis (blue circles). The memory requirements of the $T$-coefficients for the three-body Talmi-Moshinsky transformation are shown as green diamonds. Image taken from Ref. [46]

center-of-mass degrees of freedom, which translates into the need of two more orders of magnitude of memory to store the matrix elements. Finally, in the case of the $m$-scheme, the storage needed is further increased because this basis includes center-of-mass degrees of freedom but does not include rotational symmetry.

While there are normal-ordering strategies that approach these memory limitations in a clever manner, by introducing the $JT$-coupled matrix element scheme in the many-body method, and computing the normal-ordering without prestoring the matrix elements in $m$-scheme (see, e.g., Ref. [59]), calculations for heavy nuclei still remain a challenge. One of the bottlenecks of this kind of approach is the calculation of the $T$-coefficients (Eq. (6.30)), that also need to be stored. The memory required to store them is also shown in Fig. 6.3 as green diamonds.

In Fig. 6.4, we can see results for the error in ground state energies with different $E_3^{\max}$ trunctations. In this context, $\Delta E_3$ stands for

$$\Delta E_3 = \frac{\Delta(E_3^{\max}=14) - \Delta(E_3^{\max}=12)}{\Delta(E_3^{\max}=14) + \Delta(E_3^{\max}=12)}, \tag{6.32}$$

where $\Delta(E_3^{\max}) = E(E_3^{\max}) - E_{\text{exp}}$. The results are obtained with the CCSD formalism for different SRG flow parameters $\alpha$: 0.02 (red), 0.04 (green), and 0.08 fm$^4$ (blue) and an energy cut $e_{\max} = 2n+l = 12$, see Ref. [58] for details on the calculation. In the context of the SRG, the larger the flow parameter, the softer the potential resulting from the evolution. It is clear from the figure that for nuclei heavier than $^{48}$Ca the difference in energies starts to be significant even for the softest potential ($\alpha = 0.08$ fm$^4$). This is an effect known to be enhanced for heavier nuclei (see, e.g. Ref. [59, 164]). Therefore,

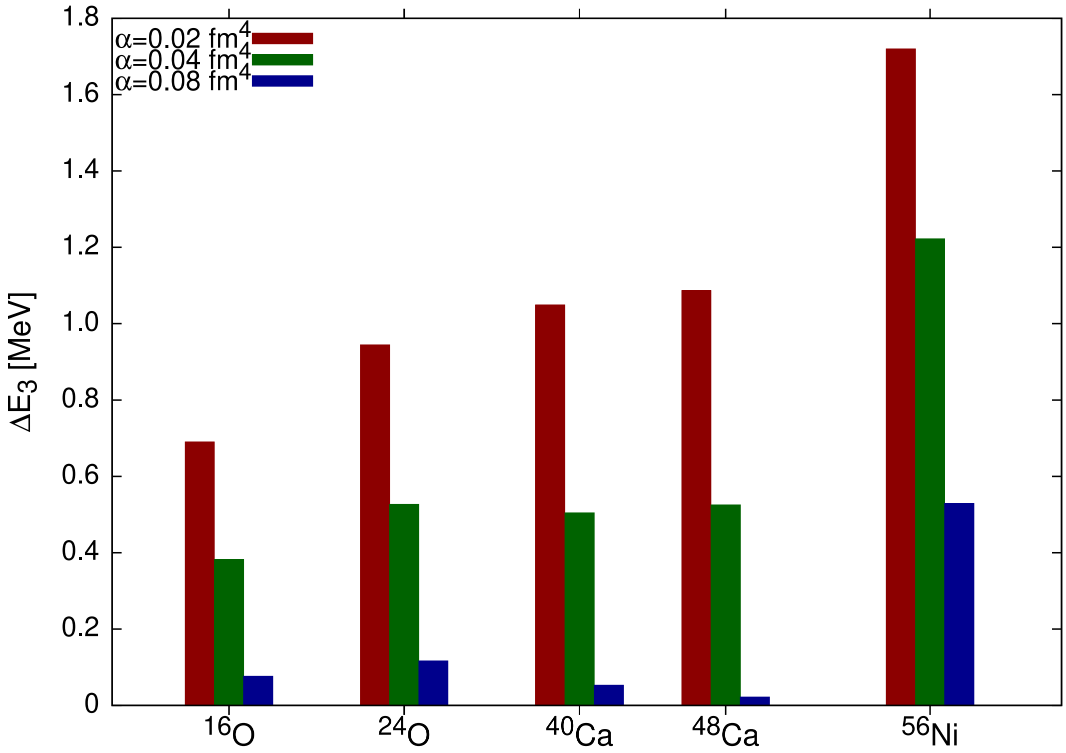

**Figure 6.4:** Difference of the relative errors of CCSD ground-sate energies for Hamiltonian with $E_3^{\text{max}}$ cuts 12 and 14 MeV in the $3N$ Hamiltonian [see Eq. (6.32)]. Results are computed at optimum oscillator frequency for the different isotopes, shown for different SRG flow parameters $\alpha$: 0.02 (red), 0.04 (green), and 0.08 fm$^4$ (blue). Data taken from Ref. [58].

it is not enough to use soft potentials for calculations involving heavier nuclei ($A \approx 100$), since the convergence with respect to the cut in three-body energy becomes challenging. We consider that this is a problem that needs to be addressed, and will present a novel NO technique developed with the aim of expanding the model space in which three-body interactions can be included in the many-body methods.

# 7 Two-body normal ordering in Jacobi basis

In this section, we will focus on the calculation of three-body matrix elements in their two-body normal-ordered form using a novel technique that will allow us to expand the model space in which these effective interaction can be applied.

We will present the derivation of two-body normal-ordered matrix elements obtained directly in Jacobi basis. Before detailing all the steps, it is useful to summarize the key points of the derivation: to be able to perform a sum over its quantum numbers, we start formulating matrix elements whose 3rd particle is represented in single particle basis. To work in momentum space, we will then relate this to an expression involving $\left\langle \mathbf{k}_1\mathbf{k}_2\mathbf{k}_3|V_{3N}|\mathbf{k}_1'\mathbf{k}_2'\mathbf{k}_3'\right\rangle$. Since the initial representation of the 3N interaction is made in Jacobi momentum space, the matrix elements will then be transformed to this basis. From this expression, we will perform a partial-wave decomposition. To be able to write the final matrix elements in $JT$-coupled single-particle basis, we will apply a transformation to harmonic oscillator basis using a Talmi-Moshinsky transformation.

## 7.1 Nomenclature

Before dealing with details on partial-wave decomposition and further steps of the derivation, we list here for clarity the notation for the quantum numbers that appear in the following sections

- $\bar{N}$, $\bar{L}$, $\bar{S}$, $\bar{J}$, $\bar{T}$... are the relative two-body quantum numbers of the final effective two-body interaction.
- $\bar{N}_{\mathrm{cm}}$, $\bar{L}_{\mathrm{cm}}$... are the center-of-mass two-body quantum numbers of the final effective two-body interaction.
- $n_c$, $l_c$... are the single-particle quantum numbers of the third particle in the reference state.
- $L$, $S$, $J$ $T$... are the two-body Jacobi quantum numbers of the subsystem composed by nucleons 1 and 2 in a three-body configuration.
- $l_3$, $s_3$, $j_3$... are the quantum numbers of the third nucleon in Jacobi basis.
- $\mathscr{L}$, $\mathscr{S}$, $\mathscr{J}$, $\mathscr{T}$... are the total $3N$ quantum numbers.
- Lower case letters with latin letters as subindices, such as $n_a$, $l_a$ ..., are the single-particle quantum numbers in two-body HO basis.
- $\bar{\Lambda}$ is the angular momentum coupling of $\bar{L}$ and $\bar{L}_{\mathrm{cm}}$.

We also introduce a compact notation that encodes the 2- and 3-body coupled bases as

$$|pP\beta\rangle \equiv \left|pP\left[(\bar{L}\bar{S})\bar{j}_{rel}\bar{L}_{cm}\right]\bar{J}\right\rangle \tag{7.1}$$

$$|pq\alpha\rangle \equiv \left|pq(LS)J\left(l_3\frac{1}{2}\right)j_3(Jj_3)\mathscr{J}\mathscr{M}_{\mathscr{J}}\right\rangle \tag{7.2}$$

where $p$, $q$, and $P$ are the moduli of the vectors presented in Eqs. (6.7a), (6.7b), and (6.8), respectively.

## 7.2 Initial momentum representation

### 7.2.1 Two- and three-body matrix elements in momentum basis

We start from a momentum representation of the two particles in NO2B, while keeping the third particle in a basis that will allow us to sum over its single-particle quantum numbers. Ignoring spin and isospin quantum numbers for brevity

$$\left\langle \mathbf{k}_1\mathbf{k}_2|V_{\text{eff}}|\mathbf{k}_1'\mathbf{k}_2'\right\rangle = \sum_{\text{c}} \left\langle \mathbf{k}_1\mathbf{k}_2 c|V_{3N}|\mathbf{k}_1'\mathbf{k}_2' c\right\rangle , \tag{7.3}$$

where the label $c$ denotes a generic representation of the quantum numbers of the third particle. In order to work with an expression that involves matrix elements in momentum basis, we introduce the identity in $\mathbf{k}_3$ and $\mathbf{k}_3'$,

$$\left\langle \mathbf{k}_1\mathbf{k}_2|V_{\text{eff}}|\mathbf{k}_1'\mathbf{k}_2'\right\rangle = \int d\mathbf{k}_3 \int d\mathbf{k}_3' \left\langle \mathbf{k}_1\mathbf{k}_2\mathbf{k}_3|V_{3N}|\mathbf{k}_1'\mathbf{k}_2'\mathbf{k}_3'\right\rangle \sum_{\text{c}} \langle c|\mathbf{k}_3\rangle \left\langle \mathbf{k}_3'|c\right\rangle . \tag{7.4}$$

As mentioned before, for a large group of many-body techniques the reference state is given in a HO basis. It is therefore convenient to assume single-particle HO quantum numbers for $c$

$$\langle c|\mathbf{k}_3\rangle = \langle n_c l_c|\mathbf{k}_3\rangle = R_{n_c l_c}(k_3) Y^*_{l_c m_c}(\hat{\mathbf{k}}_3), \tag{7.5}$$

hence:

$$\langle \mathbf{k}_3|c\rangle \left\langle c|\mathbf{k}_3'\right\rangle = R_{n_c l_c}(k_3) R_{n_c l_c}(k_3') Y_{l_c m_c}(\hat{\mathbf{k}}_3') Y^*_{l_c m_c}(\hat{\mathbf{k}}_3) \tag{7.6}$$

In order to establish a relation between $\left\langle \mathbf{k}_1\mathbf{k}_2\mathbf{k}_3|V_{3N}|\mathbf{k}_1'\mathbf{k}_2'\mathbf{k}_3'\right\rangle$ and $\langle \mathbf{pq}|V_{3N}|\mathbf{p}'\mathbf{q}'\rangle$, we insert complete sets of states in Jacobi basis on the left and right hand side of Eq. (7.4). It is important to note that, in general, the single-particle momenta, $\mathbf{k}_i$, are related to relative and center-of-mass momentum coordinates ($\mathbf{p}$, $\mathbf{q}$ and $\mathbf{P}$), even though the three-body interaction only depends on the relative coordinates $\mathbf{p}$ and $\mathbf{q}$.

The left-hand side of Eq. (7.4) can then be written as

$$\int d\mathbf{p} \int d\mathbf{P} \int d\mathbf{p}' \int d\mathbf{P}' \, \langle \mathbf{k}_1\mathbf{k}_2|\mathbf{pP}\rangle \left\langle \mathbf{pP}|V_{\text{eff}}|\mathbf{p}'\mathbf{P}'\right\rangle \left\langle \mathbf{p}'\mathbf{P}'|\mathbf{k}_1'\mathbf{k}_2'\right\rangle \tag{7.7}$$

with

$$\langle \mathbf{k}_1\mathbf{k}_2|\mathbf{pP}\rangle = (2\pi)^6 \delta^3\left(\mathbf{p} - \frac{\mathbf{k}_1 - \mathbf{k}_2}{2}\right) \delta^3\left(\mathbf{P} - (\mathbf{k}_1 + \mathbf{k}_2)\right) . \tag{7.8}$$

Similarly, the right-hand side reads

$$\begin{aligned} &\int d\mathbf{p} \int d\mathbf{q} \int d\mathbf{P} \int d\mathbf{p}' \int d\mathbf{q}' \int d\mathbf{P}' \int d\mathbf{k}_3 \int d\mathbf{k}_3' \sum_{n_c, l_c, m_c} \langle c|\mathbf{k}_3\rangle \left\langle \mathbf{k}_3'|c\right\rangle \\ &\times \langle \mathbf{k}_1\mathbf{k}_2\mathbf{k}_3|\mathbf{pqP}\rangle \left\langle \mathbf{pq}|V_{3N}|\mathbf{p}'\mathbf{q}'\right\rangle \left\langle \mathbf{p}'\mathbf{q}'\mathbf{P}'|\mathbf{k}_1'\mathbf{k}_2'\mathbf{k}_3'\right\rangle , \end{aligned} \tag{7.9}$$

where

$$\langle \mathbf{k}_1\mathbf{k}_2\mathbf{k}_3|\mathbf{pqP}\rangle = (2\pi)^9 \delta^3\left(\mathbf{p} - \frac{\mathbf{k}_1 - \mathbf{k}_2}{2}\right) \delta^3\left(\mathbf{q} - \frac{2}{3}\left[\mathbf{k}_3 - \frac{1}{2}(\mathbf{k}_1 + \mathbf{k}_2)\right]\right) \delta^3\left(\mathbf{P} - (\mathbf{k}_1 + \mathbf{k}_2)\right) . \tag{7.10}$$

In addition, we used that $V_{3N}$ only depends on the two Jacobi momenta and conserves the total momentum $\mathbf{X}$ defined in Eq. (6.10).

Evaluating the delta functions in Eq. (7.8) and (7.10) we obtain the equation

$$\left\langle \mathbf{pP}|V_{\text{eff}}|\mathbf{p'P'}\right\rangle = \int d\mathbf{k}_3 \int d\mathbf{k}'_3 \sum_{n_c,l_c,m_c} \left\langle \mathbf{pq}|V_{3N}|\mathbf{p'q'}\right\rangle \delta^3(\mathbf{P}+\mathbf{k}_3-\mathbf{P}'-\mathbf{k}'_3)\left\langle c|\mathbf{k}_3\right\rangle \left\langle \mathbf{k}'_3|c\right\rangle . \tag{7.11}$$

And performing the sum over $m_c$

$$\begin{aligned} \left\langle \mathbf{pP}|V_{\text{eff}}|\mathbf{p'P'}\right\rangle = \int d\mathbf{k}_3 \int d\mathbf{k}'_3 \sum_{n_c,l_c} \left\langle \mathbf{pq}|V_{3N}|\mathbf{p'q'}\right\rangle \delta^3(\mathbf{P}+\mathbf{k}_3-\mathbf{P}'-\mathbf{k}'_3) \\ \times R_{n_c l_c}(k_3) R_{n_c l_c}(k'_3)\frac{2l_c+1}{4\pi} P_{l_c}(\cos(\mathbf{k}_3\cdot\mathbf{k}'_3)) , \end{aligned} \tag{7.12}$$

where we have used the spherical harmonics sum rule,

$$\sum_{m_c} Y_{l_c m_c}(\hat{\mathbf{k}}'_3) Y^*_{l_c m_c}(\hat{\mathbf{k}}_3) = \frac{2l_c+1}{4\pi} P_{l_c}(\mathbf{k}_3\cdot\mathbf{k}'_3) . \tag{7.13}$$

## 7.3 Approximation for the center-of-mass momenta

As a first approximation to approach this idea, the treatment of the dependence in $\mathbf{P}$ and $\mathbf{P}'$ of Eq. (7.12) can be eliminated assuming that $\mathbf{P}$ vanishes. This approximation has been tested to give reasonable results for neutron matter in Ref. [165] and its validity has been benchmarked against more sophisticated approximations, such as angle averages for $\hat{\mathbf{P}}$, in Ref. [166] for different asymmetries of nuclear matter. Imposing the condition $\mathbf{P}=\mathbf{k}_1+\mathbf{k}_2=0$ it follows:

$$\begin{cases} \mathbf{p}=\mathbf{k}_1 , \\ \mathbf{q}=\frac{2}{3}\mathbf{k}_3 . \end{cases} \tag{7.14}$$

This approximation implies that for the left-hand side of Eq. (7.4)

$$\begin{aligned} \left\langle \mathbf{k}_1\mathbf{k}_2|V_{\text{eff}}|\mathbf{k}'_1\mathbf{k}'_2\right\rangle &= \int d\mathbf{P}' \int d\mathbf{P}\delta(\mathbf{P})\left\langle \mathbf{p}|V_{\text{eff}}|\mathbf{p}'\right\rangle \delta(\mathbf{P}-\mathbf{P}') \\ &= \int d\mathbf{P}'\delta(\mathbf{P}')\left\langle \mathbf{p}|V_{\text{eff}}|\mathbf{p}'\right\rangle = \left\langle \mathbf{p}|V_{eff}^{\mathbf{P}=\mathbf{P}'=0}|\mathbf{p}'\right\rangle . \end{aligned} \tag{7.15}$$

Making the same assumption about its the right-hand side, we have that within this approximation Eq. (7.4) can be expressed as

$$\begin{aligned} \left\langle \mathbf{p}|V_{\text{eff}}^{\mathbf{P}=\mathbf{P}'=0}|\mathbf{p}'\right\rangle = \sum_{n_c,l_c}\int d\mathbf{P}\delta(\mathbf{P})\int d\mathbf{P}'\int \frac{d\mathbf{k}_3}{(2\pi)^3}\int \frac{d\mathbf{k}'_3}{(2\pi)^3} \\ \times \frac{2l_c+1}{4\pi} P_{l_c}\left(\cos(\hat{\mathbf{k}}_3\cdot\hat{\mathbf{k}}'_3)\right) R_{n_c l_c}(k_3) R_{n_c l_c}(k'_3)\left\langle \mathbf{k}_1\mathbf{k}_2\mathbf{k}_3|V_{3N}|\mathbf{k}'_1\mathbf{k}'_2\mathbf{k}'_3\right\rangle . \end{aligned} \tag{7.16}$$

Taking also into account that $\left\langle \mathbf{k}_1\mathbf{k}_2\mathbf{k}_3|V_{3N}|\mathbf{k}'_1\mathbf{k}'_2\mathbf{k}'_3\right\rangle = (2\pi)^3\delta(\mathbf{k}_1+\mathbf{k}_2+\mathbf{k}_3-\mathbf{k}'_1-\mathbf{k}'_2-\mathbf{k}'_3)\left\langle \mathbf{pq}|V_{3N}|\mathbf{p'q'}\right\rangle$, this implies that $\mathbf{P}'=\mathbf{k}'_3-\mathbf{k}_3$ Eq.(7.16) reads:

$$\left\langle \mathbf{p}|V_{\text{eff}}^{\mathbf{P}=\mathbf{P}'=0}|\mathbf{p}'\right\rangle = \frac{1}{(2\pi)^3}\sum_{n_c,l_c}\int d\mathbf{k}_3\int d\mathbf{k}'_3 \frac{2l_c+1}{4\pi} P_{l_c}\left(\cos(\hat{\mathbf{k}}_3\cdot\hat{\mathbf{k}}'_3)\right) R_{n_c l_c}(k_3) R_{n_c l_c}(k'_3)\left\langle \mathbf{pq}|V_{3N}|\mathbf{p'q'}\right\rangle . \tag{7.17}$$

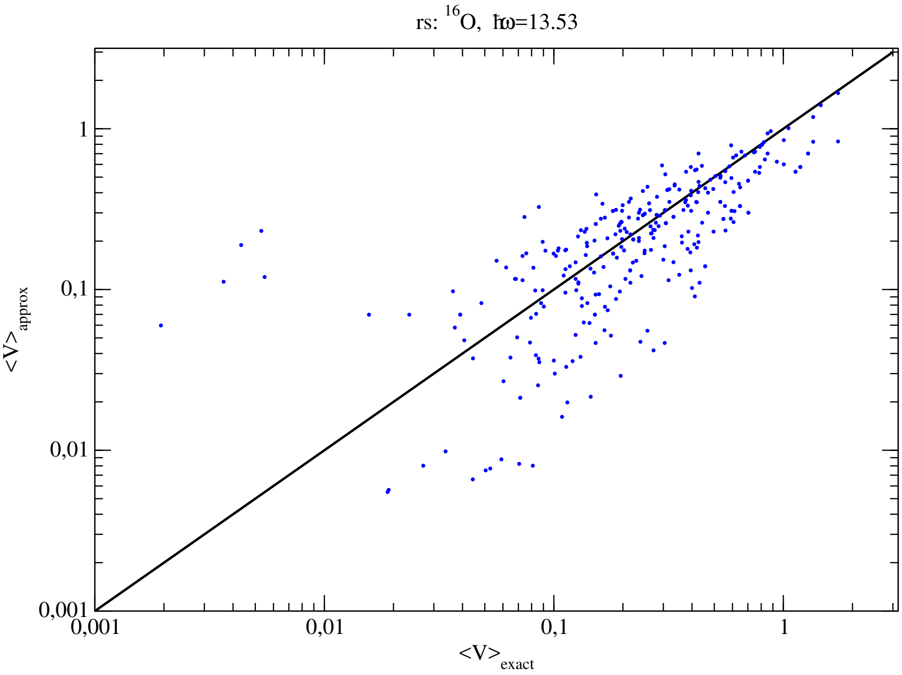

**Figure 7.1:** Comparison between exact NO2B matrix elements ($\langle V_{\text{exact}}\rangle$) and matrix elements calculated within this approximation ($\left(\left\langle V_{\text{approx}}\right\rangle\right)$) for a $^{16}$O reference state. The Hamiltonian considered has $c_E = 1$, while the remaining LECs are set to zero. The solid line $x = y$ is shown to guide the eye.

### 7.3.1 Partial-wave decomposition

In order to obtain an expression that uses matrix elements in a partial-wave decomposed relative-momentum basis, we need to project both sides on partial waves as presented in Sec. 6.2.2. Including explicitly the spin and isospin degrees of freedom consistent with the coupling scheme, we come to the final expression for the effective two-body potential,

$$\begin{aligned}\left\langle p\left(\bar{L}\bar{S}\right)\bar{J}\bar{T}\bar{M}_T\right| V_{\text{eff}}\left|p'\left(\bar{L}'\bar{S}'\right)\bar{J}\bar{T}\bar{M}'_T\right\rangle = &\frac{1}{(4\pi)^2(2\pi)^3}\sum_{\mathcal{J},\mathcal{T}}\frac{2\mathcal{J}+1}{2J_{12}+1}\,\frac{2\mathcal{T}+1}{2T_{12}+1}\sum_{n_c,l_c}\frac{2l_c+1}{4\pi}\\ &\times\int d\mathbf{k}_3\int d\mathbf{k}'_3 P_{l_c}\left(\cos(\hat{\mathbf{k}}_3\cdot\hat{\mathbf{k}}'_3)\right)R_{n_c l_c}(k_3)R_{n_c l_c}(k'_3)\\ &\times\left\langle pq\alpha\right| V_{3N}\left|p'q'\alpha'\right\rangle .\end{aligned} \tag{7.18}$$

In this equation, it is important to have in mind that

$$\begin{cases} q = \frac{2}{3}k_3\,, \\ q' = \left|\frac{2}{3}\mathbf{k}'_3 - \frac{1}{3}\mathbf{P}'\right| = \left|\frac{1}{3}(\mathbf{k}_3 + \mathbf{k}'_3)\right|\,, \end{cases} \tag{7.19}$$

which means that the dependence on $q'$ is actually a dependence on $k'_3$, $k_3$, and the angle between the two vectors.

### 7.3.2 Benchmarks

In order to compare these matrix elements with existing results obtained in the manner outlined in Sec. 6.3, they can be transformed to $JT$-coupled basis performing an intermediate transformation to relative HO basis.

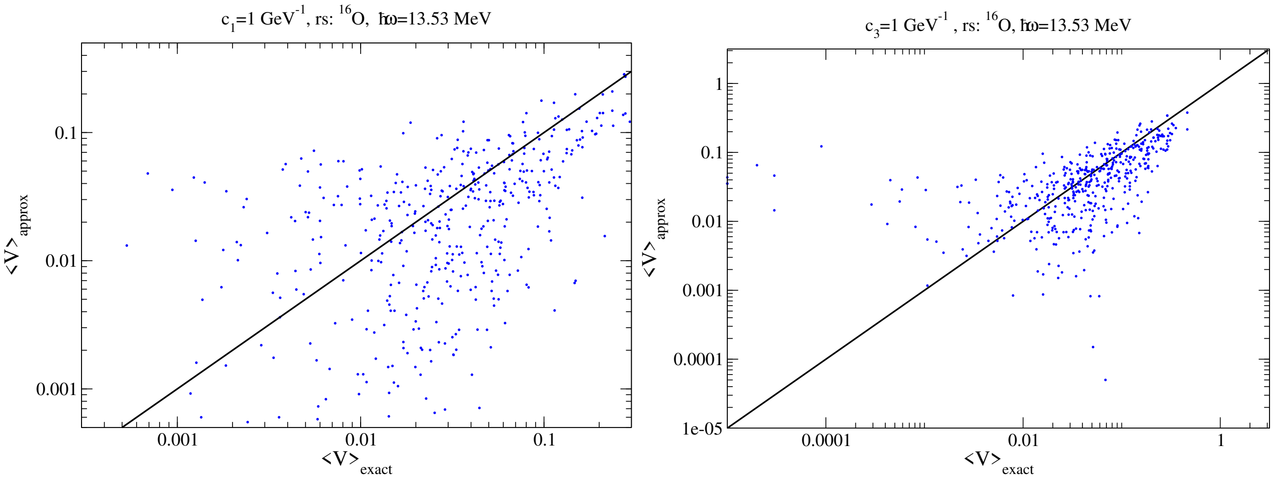

**Figure 7.2:** Comparison as in Fig. 7.1 for $c_1$=1 GeV$^{-1}$ (left panel) and $c_3$=1 GeV$^{-1}$ (right panel).

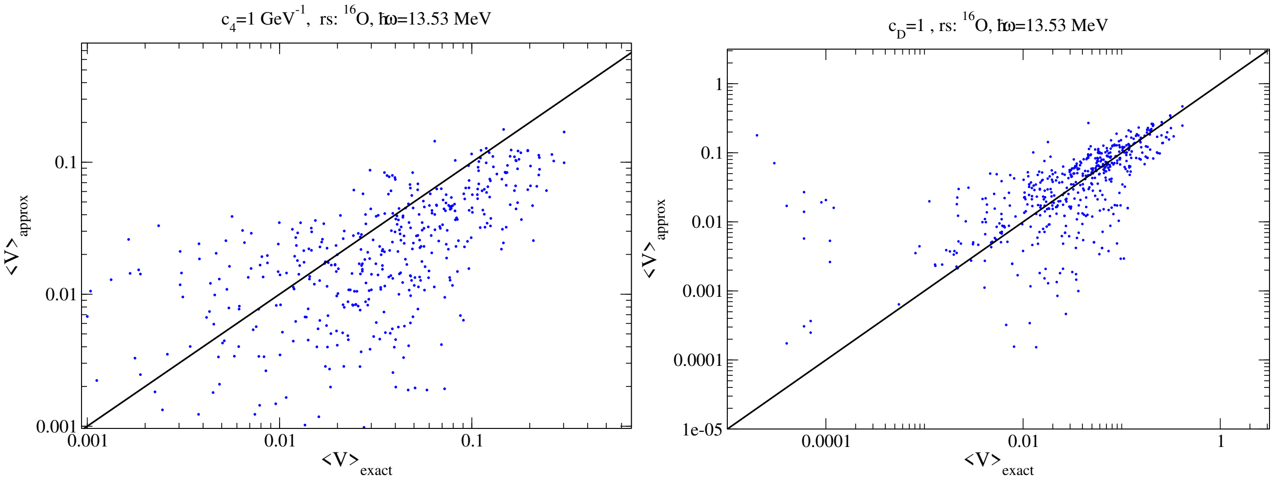

**Figure 7.3:** Comparison as in Fig. 7.1 for $c_4$=1 GeV$^{-1}$ (left panel) and $c_D$=1 (right panel).

Figure 7.1 shows the result of this comparison assuming only a $3N$ contact interaction, i.e., the only contributing term of the Hamiltonian is the one in Eq. (2.25). Furthermore, we set $c_E = 1$. Each dot corresponds to the exact value for the single-particle matrix element ($\langle V_{\text{exact}} \rangle$) versus the value obtained performing the normal ordering using Eq. (7.18) $\left(\langle V_{\text{approx}} \rangle\right)$. Therefore, a line $x = y$ would denote perfect agreement. The reference state considered is $^{16}$O with a HO frequency $\hbar\omega$=13.53 MeV (which is used in shell model calculations to approximate the HO reference state close to the physical radius).

As it can be seen, even though the general trend seems to follow a diagonal line with a certain width, there are matrix elements for which the comparison lies far away from this trend, making the use of this approximation not valid for applications in finite nuclei calculations. For completeness, we also include the results of this comparison only taking into account Hamiltonians with $c_1$=1 GeV$^{-1}$, $c_3$=1 GeV$^{-1}$ (both in Fig. 7.2), $c_4$=1 GeV$^{-1}$, and $c_D$=1 (in Fig. 7.3)

## 7.4 Exact treatment of the center-of-mass momenta

As we can see from the results in the previous section, the center-of-mass degrees of freedom have to be explicitely included in the calculation of matrix elements for applications in finite nuclei. This is the most general case and, as such, it will be presented with full detail in the following.

### 7.4.1 Partial-wave decomposition

We start by projecting the matrix elements $\langle \mathbf{p}\mathbf{P}|V_{\text{eff}}|\mathbf{p}'\mathbf{P}'\rangle$ into partial waves,

$$\begin{aligned}\left\langle p\bar{L}\bar{M}P\bar{L}_{\text{cm}}\bar{M}_{\text{cm}}|V_{\text{eff}}|p'\bar{L}'\bar{M}'P'\bar{L}'_{\text{cm}}\bar{M}'_{\text{cm}}\right\rangle = \int d\hat{\mathbf{p}}d\hat{\mathbf{P}}d\hat{\mathbf{p}}'d\hat{\mathbf{P}}'Y^*_{\bar{L}\bar{M}}(\hat{\mathbf{p}})Y^*_{\bar{L}_{\text{cm}}\bar{M}_{\text{cm}}}(\hat{\mathbf{P}})Y_{\bar{L}'\bar{M}'}(\hat{\mathbf{p}}')Y_{\bar{L}'_{\text{cm}}\bar{M}'_{\text{cm}}}(\hat{\mathbf{P}}') \\ \times \left\langle \mathbf{p}\mathbf{P}|V_{\text{eff}}|\mathbf{p}'\mathbf{P}'\right\rangle .\end{aligned} \tag{7.20}$$

Inserting in this expression the right-hand side of Eq. (7.12) also projected into partial waves, we get

$$\begin{aligned}\left\langle p\bar{L}\bar{M}P\bar{L}_{\text{cm}}\bar{M}_{\text{cm}}|V_{\text{eff}}|p'\bar{L}'\bar{M}'P'\bar{L}'_{\text{cm}}\bar{M}'_{\text{cm}}\right\rangle = &\int d\hat{\mathbf{P}}\int d\hat{\mathbf{P}}'Y^*_{\bar{L}_{\text{cm}}\bar{M}_{\text{cm}}}(\hat{\mathbf{P}})Y_{\bar{L}'_{\text{cm}}\bar{M}'_{\text{cm}}}(\hat{\mathbf{P}}')\int d\hat{\mathbf{p}}\int d\hat{\mathbf{p}}'Y^*_{\bar{L}\bar{M}}(\hat{\mathbf{p}})Y_{\bar{L}'\bar{M}'}(\hat{\mathbf{p}}') \\ &\times \sum_{\substack{L,l_3\\L',l'_3}}\sum_{\substack{M_L,m_{l_3}\\M'_L,m'_{l_3}}}\sum_{n_c,l_c}\int\frac{d\mathbf{k}_3}{(2\pi)^3}\int\frac{d\mathbf{k}'_3}{(2\pi)^3}R_{n_cl_c}(k_3)R_{n_cl_c}(k'_3)P_{l_c}(\hat{\mathbf{k}}_3\cdot\hat{\mathbf{k}}'_3) \\ &\times Y^*_{LM}(\hat{\mathbf{p}})Y^*_{l_3m_3}\left(\widehat{\mathbf{k}_3-\frac{\mathbf{P}}{2}}\right)Y_{L'M'}(\hat{\mathbf{p}}')Y_{l'_3m'_3}\left(\widehat{\mathbf{k}'_3-\frac{\mathbf{P}'}{2}}\right) \\ &\times (2\pi)^3\delta^3(\mathbf{P}+\mathbf{k}_3-\mathbf{P}'-\mathbf{k}'_3) \\ &\times \left\langle pLMql_3m_{l_3}|V_{3N}|p'L'M'q'l'_3m'_{l_3}\right\rangle .\end{aligned} \tag{7.21}$$

### Inclusion of spin quantum numbers

We now expand the three-body force in partial waves while including the spin degrees of freedom to work in the coupled basis introduced in Eq. (7.2):

$$\begin{aligned}\left\langle \mathbf{p}\mathbf{q}|V_{3N}|\mathbf{p}'\mathbf{q}'\right\rangle = &\sum_{\mathscr{J},M_{\mathscr{J}}}\sum_{\substack{L,l_3\\L',l'_3}}\sum_{\substack{J,j_3\\J',j'_3}}\sum_{\substack{M_L,m_{l_3}\\M'_L,m'_{l_3}}}\sum_{\substack{M_J,m_{j_3}\\M'_J,m'_{j_3}}}\mathscr{C}^{\mathscr{J}M_{\mathscr{J}}}_{JM_Jj_3m_{j_3}}\mathscr{C}^{j_3m_{j_3}}_{l_3m_{l_3}1/2m_s}\mathscr{C}^{JM_J}_{LM_LSm_S}\mathscr{C}^{\mathscr{J}M_{\mathscr{J}}}_{J'M'_Jj'_3m'_{j_3}}\mathscr{C}^{j'_3m'_{j_3}}_{l'_3m'_{l_3}1/2m'_s}\mathscr{C}^{JM_J}_{L'M'_LS'M'_S} \\ &\times Y_{LM_L}(\hat{\mathbf{p}})Y_{l_3m_{l_3}}(\hat{\mathbf{q}})Y^*_{L'M'_L}(\hat{\mathbf{p}}')Y^*_{l'_3m'_{l_3}}(\hat{\mathbf{q}}')\left\langle pq\alpha|V_{3N}|p'q'\alpha'\right\rangle\end{aligned} \tag{7.22}$$

We can do the same for the effective two-body interaction. Including all necessary Clebsch-Gordan coefficients $\mathscr{C}$ to account for the corresponding spin couplings:

$$\begin{aligned}\langle pP\beta|\,V_{\text{eff}}\left|p'P'\beta'\right\rangle = &\sum_{\substack{\bar{M}_L,\bar{M}_{cm},\bar{M}_j,\bar{M}_S\\ \bar{M}_{L'},\bar{M}'_{cm},\bar{M}'_j,\bar{M}'_S}} \mathscr{C}^{\bar{j}_{rel}\bar{M}_j}_{\bar{L}M_L\bar{S}\bar{M}_S}\mathscr{C}^{\bar{j}'_{rel}\bar{M}'_j}_{\bar{L}'\bar{M}'_L\bar{S}'\bar{M}'_S}\mathscr{C}^{\bar{J}\bar{M}_J}_{\bar{j}_{rel}\bar{M}_j\bar{L}_{cm}\bar{M}_{cm}}\mathscr{C}^{\bar{J}\bar{M}_J}_{\bar{j}'_{rel}\bar{M}'_j\bar{L}'_{cm}\bar{M}'_{cm}}\\ &\times\int d\hat{\mathbf{p}}\int d\hat{\mathbf{p}}'\int d\hat{\mathbf{P}}\int d\hat{\mathbf{P}}' Y^*_{\bar{L}\bar{M}_L}(\hat{\mathbf{p}})Y^*_{\bar{L}_{cm}\bar{M}_{cm}}(\hat{\mathbf{P}})Y_{\bar{L}'\bar{M}_{L'}}(\hat{\mathbf{p}}')Y_{\bar{L}'_{cm}\bar{M}'_{cm}}(\hat{\mathbf{P}}')\\ &\times\sum_{\text{c}}\int\frac{d\mathbf{k}_3}{(2\pi)^3}\frac{d\mathbf{k}'_3}{(2\pi)^3}\left\langle\mathbf{pq}|V_{3N}|\mathbf{p}'\mathbf{q}'\right\rangle(2\pi)^3\delta^3(\mathbf{P}+\mathbf{k}_3-\mathbf{P}'-\mathbf{k}'_3)R_{n_cl_c}(k_3)R_{n_cl_c}(k'_3)\end{aligned} \tag{7.23}$$

Because the normal-ordering procedure does not alter the two-body coupled spin degrees of freedom, the conditions $S=\bar{S}$ and $M_S=\bar{M}_S$ have to be fulfilled (and analogous for the primed quantum numbers). Additionally, $m_s=m'_s=m_{s_c}$ holds for the third particle.

It is also more convenient to write all the expressions in terms of $\mathbf{k}_3$. From now on, it is understood that $\hat{\mathbf{q}}=\widehat{\mathbf{k}'_3-\frac{\mathbf{P}'}{2}}$.

Taking into account these conditions, we insert (7.22) into (7.23),

$$\begin{aligned}\langle pP\beta|\,V_{\text{eff}}\left|p'P'\beta'\right\rangle = &\sum_{\substack{\bar{M}_L,\bar{M}_{cm},\bar{M}_j,\bar{M}_S\\ \bar{M}_{L'},\bar{M}'_{cm},\bar{M}'_j,\bar{M}'_S}} \mathscr{C}^{\bar{j}_{rel}\bar{M}_j}_{\bar{L}\bar{M}_L\bar{S}\bar{M}_S}\mathscr{C}^{\bar{j}'_{rel}\bar{M}'_j}_{\bar{L}'\bar{M}'_L\bar{S}'\bar{M}'_S}\mathscr{C}^{\bar{J}\bar{M}_J}_{\bar{j}_{rel}\bar{M}_j\bar{L}_{cm}\bar{M}_{cm}}\mathscr{C}^{\bar{J}\bar{M}_J}_{\bar{j}'_{rel}\bar{M}'_j\bar{L}'{}_{cm}\bar{M}'_{cm}}\\ &\times\int d\hat{\mathbf{p}}\int d\hat{\mathbf{p}}'\int d\hat{\mathbf{P}}\int d\hat{\mathbf{P}}' Y^*_{\bar{L}\bar{M}_L}(\hat{\mathbf{p}})Y^*_{\bar{L}_{cm}\bar{M}_{cm}}(\hat{\mathbf{P}})Y_{\bar{L}'\bar{M}_{L'}}(\hat{\mathbf{p}}')Y_{\bar{L}'_{cm}\bar{M}'_{cm}}(\hat{\mathbf{P}}')\\ &\times\int\frac{d\mathbf{k}_3}{(2\pi)^3}\frac{d\mathbf{k}'_3}{(2\pi)^3}\sum_{\text{c}}(2\pi)^3\delta^3(\mathbf{P}+\mathbf{k}_3-\mathbf{P}'-\mathbf{k}'_3)R_{n_cl_c}(k_3)R_{n_cl_c}(k'_3)\\ &\times\sum_{\mathscr{J},M_{\mathscr{J}}}\sum_{\substack{L,l_3\\ L',l'_3}}\sum_{\substack{J,j_3\\ J',j'_3}}\sum_{\substack{M_L,m_{l_3}\\ M'_L,m'_{l_3}}}\sum_{\substack{M_J,m_{j_3}\\ M'_J,m'_{j_3}}} Y_{LM_L}(\hat{\mathbf{p}})Y_{l_3m_{l_3}}(\hat{\mathbf{q}})Y^*_{L'M'_L}(\hat{\mathbf{p}}')Y^*_{l'_3m'_{l_3}}(\hat{\mathbf{q}}')\\ &\times\mathscr{C}^{\mathscr{J}M_{\mathscr{J}}}_{JM_Jjm_j}\mathscr{C}^{j_3m_{j_3}}_{l_3m_{l_3}1/2m_s}\mathscr{C}^{JM_J}_{LM_L\bar{S}\bar{M}_S}\mathscr{C}^{\mathscr{J}M_{\mathscr{J}}}_{J'M'_Jj'_3m'_{j_3}}\mathscr{C}^{j'_3m'_{j_3}}_{l'_3m'_{l_3}1/2m'_s}\mathscr{C}^{JM_J}_{L'M'_L\bar{S}'\bar{M}'_S}\\ &\times\left\langle pq\alpha|V_{3N}|p'q'\alpha'\right\rangle\end{aligned} \tag{7.24}$$

Performing the integrals in $\hat{\mathbf{p}}$ and $\hat{\mathbf{p}}'$, we find that $\delta_{\bar{L},L}\delta_{\bar{M}_L,M_L}$, $\delta_{\bar{L}',L'}\delta_{\bar{M}'_L,M'_L}$. Also, since $\bar{S}=S$,

$$\sum_{\substack{\bar{M}_L,\bar{M}_S\\ \bar{M}_{L'},\bar{M}'_S}}\mathscr{C}^{JM_J}_{\bar{L}\bar{M}_L\bar{S}\bar{M}_S}\mathscr{C}^{J'M'_J}_{\bar{L}'\bar{M}'_L\bar{S}'\bar{M}'_S}\mathscr{C}^{\bar{j}_{rel}\bar{M}_j}_{\bar{L}\bar{M}_L\bar{S}\bar{M}_S}\mathscr{C}^{\bar{j}'_{rel}\bar{M}'_j}_{\bar{L}'\bar{M}'_L\bar{S}'\bar{M}'_S}=\delta_{\bar{j}_{rel},J}\delta_{\bar{j}'_{rel},J'}\delta_{M_j,M_J}\delta_{M'_j,M'_J}\,, \tag{7.25}$$

which implies

$$\begin{aligned}\langle pP\beta|\,V_{\text{eff}}\left|p'P'\beta'\right\rangle = &\sum_{\substack{\bar{M}_{cm},\bar{M}_j\\ \bar{M}'_{cm},\bar{M}'_j}} \mathscr{C}^{\bar{J}\bar{M}_J}_{\bar{j}_{rel}\bar{M}_j\bar{L}_{cm}\bar{M}_{cm}} \mathscr{C}^{\bar{J}\bar{M}_J}_{\bar{j}'_{rel}\bar{M}'_j\bar{L}'{}_{cm}\bar{M}'_{cm}} \\ &\times \int d\hat{\mathbf{P}} \int d\hat{\mathbf{P}}' Y^*_{\bar{L}_{cm}\bar{M}_{cm}}(\hat{\mathbf{P}}) Y_{\bar{L}'_{cm}\bar{M}'_{cm}}(\hat{\mathbf{P}}') \\ &\times \int \frac{d\mathbf{k}_3}{(2\pi)^3} \sum_{n_c,l_c,m_{s_c}} R_{n_c l_c}(k_3) R_{n_c l_c}(k'_3) \frac{2l_c+1}{4\pi} P_{l_c}(\mathbf{k}_3\cdot\mathbf{k}'_3) \\ &\times \sum_{\alpha,\alpha'} \sum_{\mathscr{J},M_{\mathscr{J}}} \sum_{m_{l_3},m'_{l_3}} \sum_{m_{j_3},m'_{j_3}} Y^*_{l_3 m_{l_3}}(\hat{\mathbf{q}}) Y_{l'_3 m'_{l_3}}(\hat{\mathbf{q}}') \\ &\times \mathscr{C}^{\mathscr{J}M_{\mathscr{J}}}_{\bar{j}_{rel}\bar{M}_j j_3 m_{j_3}} \mathscr{C}^{j_3 m_{j_3}}_{l_3 m_{l_3} 1/2 m_{s_c}} \mathscr{C}^{\mathscr{J}M_{\mathscr{J}}}_{\bar{j}'_{rel}\bar{M}'_j j'_3 m'_{j_3}} \mathscr{C}^{j'_3 m'_{j_3}}_{l'_3 m'_{l_3} 1/2 m_{s_c}} \left\langle pq\alpha|V_{3N}|p'q'\alpha'\right\rangle ,\end{aligned} \tag{7.26}$$

Up to this point, this expression is valid for any kind of interaction or topology. Before considering different kinds of three-body interactions, it is useful to determine the behavior of isospin degrees of freedom in this case.

## Inclusion of isospin quantum numbers

Because the isospin quantum numbers can be factorized from the angular part, this dependence can be derived independently from the previous discussion.

Starting from an isospin uncoupled basis

$$\begin{aligned}\left\langle \bar{T}\bar{M}_T|V^{3N}|\bar{T}'\bar{M}'_T\right\rangle = &\sum_{\substack{\mathscr{T},\mathscr{M}'_{\mathscr{T}}\\ \mathscr{T}'\mathscr{M}_{\mathscr{T}'}}} \sum_{m_{t_3}} \mathscr{C}^{\mathscr{T}\mathscr{M}_{\mathscr{T}}}_{\bar{T}\bar{M}_T\frac{1}{2}m_{t_3}} \mathscr{C}^{\mathscr{T}\mathscr{M}_{\mathscr{T}}{}'}_{\bar{T}'M'_{\bar{T}}\frac{1}{2}m_{t_3}} \delta_{\bar{M}_T+m_{t_3},\mathscr{M}_{\mathscr{T}}} \delta_{\bar{M}'_T+m_{t_3},\mathscr{M}_{\mathscr{T}}{}'} \\ &\times \left\langle \left(\bar{T}\frac{1}{2}\right)\mathscr{T}\left(\bar{M}_T\frac{1}{2}\right)\mathscr{M}_{\mathscr{T}}\left|V^{3N}\right|\left(\bar{T}'\frac{1}{2}\right)\mathscr{T}'\left(\bar{M}'_T\frac{1}{2}\right)\mathscr{M}_{\mathscr{T}}{}'\right\rangle .\end{aligned} \tag{7.27}$$

Considering that the interaction is diagonal in $\bar{T}$ (case for a $Z=N$ reference state), we can write

$$\begin{aligned}\left\langle \bar{T}\bar{M}_T|V_{\text{eff}}|\bar{T}'\bar{M}'_T\right\rangle = &\sum_{\mathscr{T},\mathscr{M}_{\mathscr{T}}} \sum_{m_{t_3}} \mathscr{C}^{\mathscr{T}\mathscr{M}_{\mathscr{T}}}_{\bar{T}\bar{M}_T\frac{1}{2}m_{t_3}} \mathscr{C}^{\mathscr{T}\mathscr{M}_{\mathscr{T}}{}'}_{\bar{T}'M'_{\bar{T}}\frac{1}{2}m_{t_3}} \delta_{\bar{M}_T+m_{t_3},\mathscr{M}_{\mathscr{T}}} \delta_{\bar{M}'_T+m_{t_3},\mathscr{M}_{\mathscr{T}}{}'} \\ &\times \left\langle \left(\bar{T}\frac{1}{2}\right)\mathscr{T}\left(\bar{M}_T\frac{1}{2}\right)\mathscr{M}_{\mathscr{T}}\left|V_{3N}\right|\left(\bar{T}'\frac{1}{2}\right)\mathscr{T}\left(\bar{M}'_T\frac{1}{2}\right)\mathscr{M}_{\mathscr{T}}{}'\right\rangle .\end{aligned} \tag{7.28}$$

Applying the conditions given by the deltas and rearranging the indices for the Clebsch-Gordan coefficients:

$$\begin{aligned}\left\langle \bar{T}\bar{M}_T|V_{\text{eff}}|\bar{T}'\bar{M}'_T\right\rangle = &\sum_{\mathscr{T},\mathscr{M}_{\mathscr{T}}} \sum_{m_{t_3}} \mathscr{C}^{\mathscr{T}\mathscr{M}_{\mathscr{T}}}_{\bar{T}(\mathscr{M}_{\mathscr{T}}-m_{t_3})\frac{1}{2}m_{t_3}} \mathscr{C}^{\mathscr{T},\mathscr{M}_{\mathscr{T}}}_{\bar{T}'(\mathscr{M}_{\mathscr{T}}{}'-m_{t_3})\frac{1}{2}m_{t_3}} \delta_{\mathscr{M}_{\mathscr{T}}\mathscr{M}_{\mathscr{T}}{}'} \delta_{\bar{T}\bar{T}'} \\ &\times \left\langle \left(\bar{T}\frac{1}{2}\right)\mathscr{T}\left(\bar{M}_T\frac{1}{2}\right)\mathscr{M}_{\mathscr{T}}\left|V_{3N}\right|\left(\bar{T}'\frac{1}{2}\right)\mathscr{T}\left(\bar{M}'_T\frac{1}{2}\right)\mathscr{M}_{\mathscr{T}}{}'\right\rangle \\ = &\sum_{\mathscr{T}} (-1)^{(1+2m_{t_3})} \frac{(2\mathscr{T}+1)}{(2\bar{T}+1)} \\ &\times \left\langle \left(\bar{T}\frac{1}{2}\right)\mathscr{T}\left(\bar{M}_T\frac{1}{2}\right)\mathscr{M}_{\mathscr{T}}\left|V_{3N}\right|\left(\bar{T}'\frac{1}{2}\right)\mathscr{T}\left(\bar{M}_T\frac{1}{2}\right)\mathscr{M}_{\mathscr{T}}\right\rangle ,\end{aligned} \tag{7.29}$$

and since $2m_{j_3}$ is always an odd number, the phase $(-1)^{(1+2m_{t_3})}$ vanishes.

## 7.5 Simplified expression for a short-range three-body interaction

Given the complex structure of Eq. (7.26), it is useful to test the validity of this approach considering the simplest interaction. As a first case of study, we assume that only the contact interaction, $c_E$, contributes to the potential. In this scenario, only partial waves with $\bar{L} = \bar{L}' = l_3 = l_3' = 0$ contribute, and hence $\bar{j}_{rel} = \bar{S}$. Furthermore, only one three-body channel with $\mathscr{J} = 1/2$ is non vanishing and we have $M_J = M_S = \bar{M}_S$ and $m_{j_3} = m_s = m_{s_c}$.

Taking into account these considerations, Eq. (7.26) can be written as

$$\begin{aligned}\left\langle pP\left(\bar{L}_{cm}\bar{S}\right)\bar{J}\right| V_{\text{eff}}\left|p'P'\left(\bar{L}'_{cm}\bar{S}'\right)\bar{J}\right\rangle = &\sum_{\substack{\bar{M}_{cm},\bar{M}_S\\ \bar{M}'_{cm},\bar{M}'_S}} \mathscr{C}^{\bar{J}\bar{M}_J}_{\bar{L}_{cm}\bar{M}_{cm}\bar{S}\bar{M}_S}\mathscr{C}^{\bar{J}\bar{M}_J}_{\bar{L}'_{cm}\bar{M}'_{cm}\bar{S}'\bar{M}'_S}\\ &\times\int d\hat{\mathbf{P}}\int d\hat{\mathbf{P}}' Y^*_{\bar{L}_{cm}\bar{M}_{cm}}(\hat{\mathbf{P}})Y_{\bar{L}'_{cm}\bar{M}'_{cm}}(\hat{\mathbf{P}}')\\ &\times\int\frac{d\mathbf{k}_3}{(2\pi)^3}\sum_{n_c,l_c,m_{s_c}} R_{n_cl_c}(k_3)R_{n_cl_c}(k_3')\frac{2l_c+1}{4\pi}P_{l_c}(\mathbf{k}_3\cdot\mathbf{k}_3')\\ &\times\sum_{\alpha,\alpha'}\sum_{M_\mathscr{J}}\frac{\delta_{L0}\delta_{L'0}\delta_{l_30}\delta_{l_3'0}}{4\pi}\mathscr{C}^{\mathscr{J}M_\mathscr{J}}_{\bar{S}\bar{M}_S1/2m_{s_c}}\mathscr{C}^{\mathscr{J}M_\mathscr{J}}_{\bar{S}'\bar{M}'_S1/2m_{s_c}}\\ &\times\left\langle pq\alpha|V_{3N}|p'q'\alpha'\right\rangle .\end{aligned}\tag{7.30}$$

The sum over $m_{s_c}$ and $M_\mathscr{J}$ can be performed by using:

$$\sum_{m_{s_c},M_\mathscr{J}}\mathscr{C}^{\mathscr{J}M_\mathscr{J}}_{\bar{S}\bar{M}_S1/2m_{s_c}}\mathscr{C}^{\mathscr{J}M_\mathscr{J}}_{\bar{S}'\bar{M}'_S1/2m_{s_c}} = \frac{2\mathscr{J}+1}{2\bar{S}+1}\delta_{\bar{M}_S\bar{M}'_S}\delta_{\bar{S}\bar{S}'}\,,\tag{7.31}$$

and since the three-body interaction is rotationally invariant, the total result does not depend on the projection of the total angular momentum. If we average the remaining expression over $\bar{M}_J$ using the factor $1/(2\bar{J}+1)$, we can also perform the sum over $M_S$:

$$\frac{1}{2\bar{J}+1}\sum_{\bar{M}_J,\bar{M}_S}\mathscr{C}^{\bar{J}\bar{M}_J}_{\bar{L}_{cm}\bar{M}_{cm}\bar{S}\bar{M}_S}\mathscr{C}^{\bar{J}\bar{M}_J}_{\bar{L}'_{cm}\bar{M}'_{cm}\bar{S}\bar{M}_S} = \frac{1}{2\bar{L}_{cm}+1}\delta_{\bar{L}_{cm}\bar{L}'_{cm}}\delta_{\bar{M}_{cm}\bar{M}'_{cm}}\,.\tag{7.32}$$

Owing to these delta functions, we can transform the remaining spherical harmonics into a Legendre polynomial:

$$\sum_{\bar{M}_{cm}}\int d\hat{\mathbf{P}}\int d\hat{\mathbf{P}}' Y^*_{\bar{L}_{cm}\bar{M}_{cm}}(\hat{\mathbf{P}})Y_{\bar{L}_{cm}\bar{M}_{cm}}(\hat{\mathbf{P}}') = 8\pi^2\int d\cos\theta_{\mathbf{PP}'}\frac{2\bar{L}_{cm}+1}{4\pi}P_{\bar{L}_{cm}}(\hat{\mathbf{P}}\cdot\hat{\mathbf{P}}')\,.\tag{7.33}$$

Hence in the end we obtain

$$\begin{aligned}&\left\langle pP\left(\bar{L}_{cm}\bar{S}\right)\bar{J}\bar{T}\right| V_{\text{eff}}\left|p'P'\left(\bar{L}_{cm}\bar{S}\right)\bar{J}\bar{T}\right\rangle =\\ &\times\frac{2\mathscr{J}+1}{2\bar{S}+1}\frac{2\mathscr{T}+1}{2\bar{T}+1}\frac{8\pi^2}{4\pi}\int d\cos\theta_{\mathbf{PP}'}P_{\bar{L}_{cm}}(\hat{\mathbf{P}}\cdot\hat{\mathbf{P}}')\\ &\times\int\frac{d\mathbf{k}_3}{(2\pi)^3}\sum_{n_c,l_c}R_{n_cl_c}(k_3)R_{n_cl_c}(k_3')\frac{2l_c+1}{4\pi}P_{l_c}(\mathbf{k}_3\cdot\mathbf{k}_3')\\ &\times\sum_{\alpha,\alpha'}\frac{\delta_{L0}\delta_{L'0}\delta_{l0}\delta_{l'0}}{4\pi}\left\langle pq\alpha|V_{3N}|p'q'\alpha'\right\rangle .\end{aligned}\tag{7.34}$$

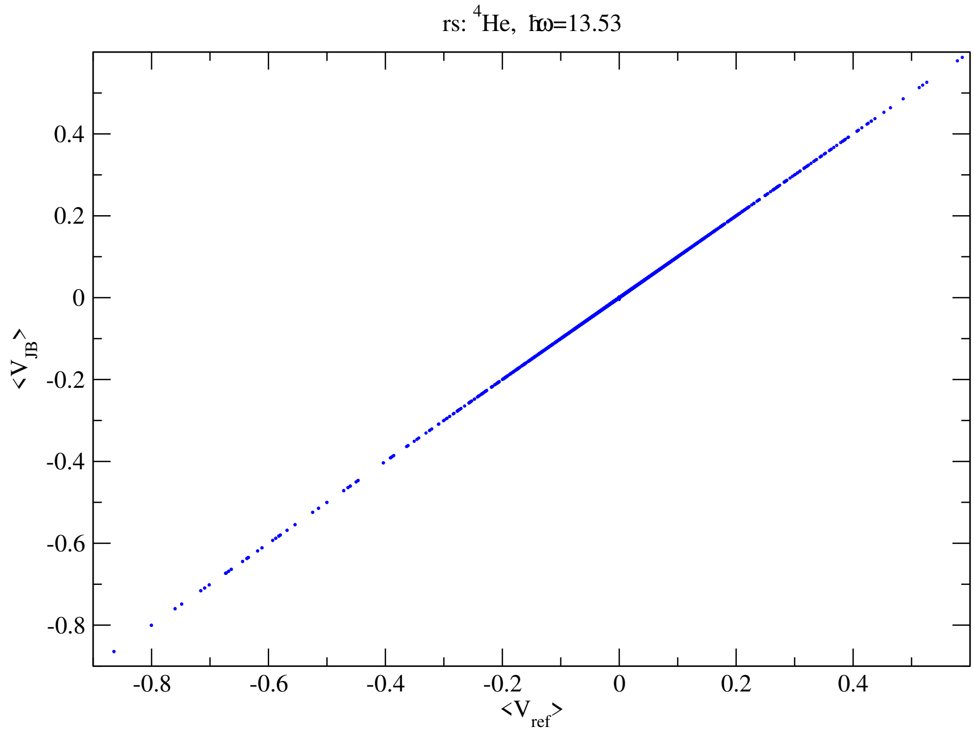

**Figure 7.4:** Comparison between single-particle normal-ordered matrix ($\langle V_{\text{ref}} \rangle$) elements and this work ($\langle V_{\text{JB}} \rangle$) for $^4$He reference state.

### 7.5.1 Benchmarks

#### Benchmark for a $^4$He reference state

To benchmark our approach, the NO2B matrix elements in Jacobi basis obtained from Eq. (7.34) have to be transformed to two-body matrix elements in single-particle basis, $\langle ab|V_{\text{eff}}|a'b'\rangle$. In order to do so, first a transformation to harmonic oscillator takes place (see Sec. 7.6.2), to then apply a Talmi-Moshinsky transformation (see Sec. 7.6.3). It is important to remark that since our original NO2B matrix elements depend on the center-of-mass degrees of freedom, both transformations have to explicitly account for those.

In Fig. 7.4, we can see how the results for a $^4$He reference state agree perfectly with the single-particle normal ordered matrix elements, for matrix elements with two-body energy $E_{2N} = 2n_i + l_i + 2n_j + l_j \leq 12$ and including partial waves up to $\bar{J} = 9$.

#### Benchmark for a $^{16}$O reference state

In contrast to the previous case, when normal ordering with respect to $^{16}$O, Fig. 7.5 shows some matrix elements that do not match the reference results (highlighted in red). This mismatch is due to the energy cut in the calculation for the NO2B taken as reference, where the condition $E_{3N} = e_a + e_b + e_c \leq 12$ is applied. In the case of oxygen, the particle $c$ can have $e_c = 1$ if it occupies the $p$ orbital, and therefore $E_{3N} = e_a + e_b + 1$, causing a discrepancy in the comparison for matrix elements with $e_a + e_b \geq 12$, as can be seen in the red dots in the figure.

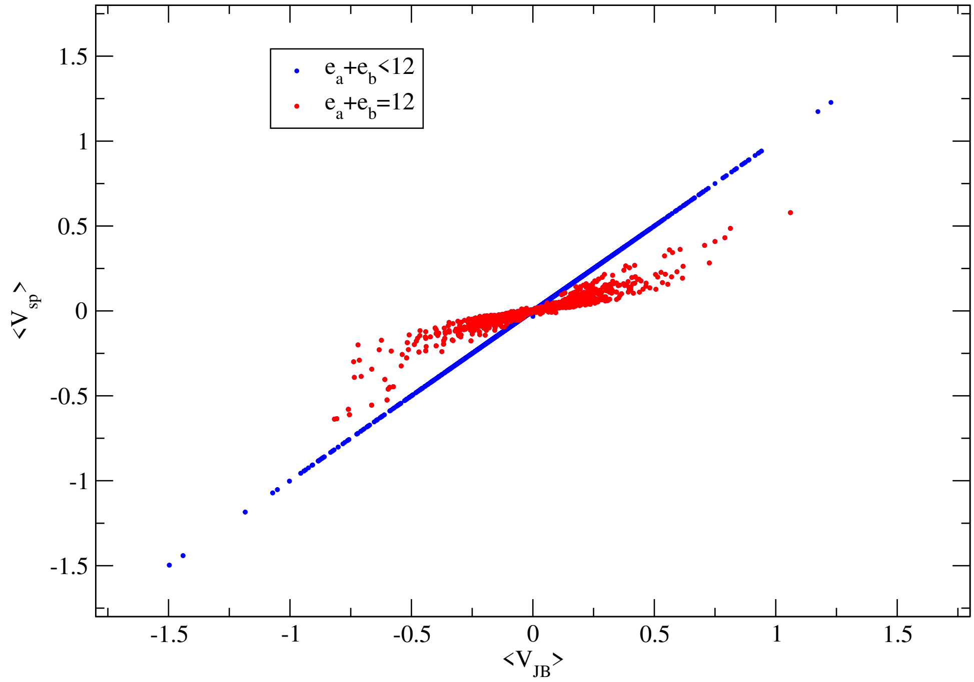

**Figure 7.5:** Comparison between single-particle normal-ordered matrix ($\langle V_{\text{ref}} \rangle$) elements and this work ($\langle V_{\text{JB}} \rangle$) for $^{16}$O reference state. Matrix elements with two-body energy $e_a + e_b$ equal to 12 are highlighted in red due to the cutoff $E_{3N} \leq 12$ used in the calculation of $\langle V_{\text{ref}} \rangle$ (see text for details).

## 7.6 General expression

Looking back at Eq. (7.26), we can now consider the general case for which all partial waves are susceptible to contribute to the Hamiltonian. The Clebsch-Gordan coefficients introduce constraints that reduce the number of sums. In this case,

$$\begin{aligned} \bar{M}_{cm} &= \bar{M}_J - \bar{M}_j\,, \\ \bar{M}_j &= M_{\mathscr{J}} - m_{j_3}\,. \end{aligned} \tag{7.35}$$

From these two equations follows that

$$\mathscr{C}^{\bar{J}\bar{M}_J}_{\bar{j}_{rel}\bar{M}_j\bar{L}_{cm}\bar{M}_{cm}} = \mathscr{C}^{\bar{J}\bar{M}_J}_{\bar{j}_{rel}(M_{\mathscr{J}}-m_{j_3})\bar{L}_{cm}(\bar{M}_J+m_{j_3}-M_{\mathscr{J}})}\,. \tag{7.36}$$

Another condition that needs to be fulfilled is given by the coupling of the quantum numbers of the third particle: $m_{l_3} = m_{j_3} - m_{s_c}$. All constraints presented have to be also fulfilled by the primed projections.

Therefore, we can write that:

$$\begin{aligned}
\left\langle pP\beta\right| V_{\mathrm{eff}} \left|p'P'\beta'\right\rangle = & \sum_{\mathscr{J},M_{\mathscr{J}}} \mathscr{C}^{\bar{J}\bar{M}_J}_{\bar{j}_{rel}(M_{\mathscr{J}}-m_j)\bar{L}_{cm}(\bar{M}_J+m_j-M_{\mathscr{J}})} \mathscr{C}^{\bar{J}\bar{M}_J}_{\bar{j}'_{rel}(M_{\mathscr{J}}-m'_j)\bar{L'}_{cm}(\bar{M}_J+m'_j-M_{\mathscr{J}})} \\
& \times \int d\hat{\mathbf{P}} \int d\hat{\mathbf{P}}' Y^{*}_{\bar{L}_{cm}(\bar{M}_J+m_j-M_{\mathscr{J}})}(\hat{\mathbf{P}}) Y_{\bar{L'}_{cm}(\bar{M}_J+m'_j-M_{\mathscr{J}})}(\hat{\mathbf{P}}') \\
& \times \int \frac{d\mathbf{k}_3}{(2\pi)^3} \sum_{n_c,l_c,m_{s_c}} R_{n_c l_c}(k_3) R_{n_c l_c}(k'_3) \frac{2l_c+1}{4\pi} P_{l_c}(\mathbf{k}_3\cdot\mathbf{k}'_3) \\
& \times \sum_{\alpha,\alpha'} \sum_{m_j,m'_j} Y^{*}_{l(m_j-m_{s_c})}(\hat{\mathbf{q}}) Y_{l'(m'_j-m_{s_c})}(\hat{\mathbf{q}}') \\
& \times \mathscr{C}^{\mathscr{J}M_{\mathscr{J}}}_{\bar{j}_{rel}(M_{\mathscr{J}}-m_j)jm_j} \mathscr{C}^{jm_j}_{l(m_j-m_{s_c})1/2m_{s_c}} \mathscr{C}^{\mathscr{J}M_{\mathscr{J}}}_{\bar{j}'_{rel}(M_{\mathscr{J}}-m'_j)j'm'_j} \mathscr{C}^{j'm'_j}_{l'_3(m'_j-m_{s_c})1/2m_{s_c}} \\
& \times \left\langle pq\alpha|V_{3N}|p'q'\alpha'\right\rangle .
\end{aligned} \tag{7.37}$$

In this general case, the Hamiltonian is also independent of the projection of the total angular momentum. Averaging over all the values of $\bar{M}_J$:

$$\begin{aligned}
\left\langle pP\beta\right| V_{\mathrm{eff}} \left|p'P'\beta'\right\rangle = & \frac{1}{2\bar{J}+1} \sum_{\bar{M}_J} \sum_{\mathscr{J},M_{\mathscr{J}}} \sum_{m_j,m'_j} \\
& \times \mathscr{C}^{\bar{J}\bar{M}_J}_{\bar{j}_{rel}(M_{\mathscr{J}}-m_j)\bar{L}_{cm}(\bar{M}_J+m_j-M_{\mathscr{J}})} \mathscr{C}^{\bar{J}\bar{M}_J}_{\bar{j}'_{rel}(M_{\mathscr{J}}-m'_j)\bar{L'}_{cm}(\bar{M}_J+m'_j-M_{\mathscr{J}})} \\
& \times \int d\hat{\mathbf{P}} \int d\hat{\mathbf{P}}' Y^{*}_{\bar{L}_{cm}(\bar{M}_J+m_j-M_{\mathscr{J}})}(\hat{\mathbf{P}}) Y_{\bar{L'}_{cm}(\bar{M}_J+m'_j-M_{\mathscr{J}})}(\hat{\mathbf{P}}') \\
& \times \int \frac{d\mathbf{k}_3}{(2\pi)^3} \sum_{n_c,l_c,m_{s_c}} R_{n_c l_c}(k_3) R_{n_c l_c}(k'_3) \frac{2l_c+1}{4\pi} P_{l_c}(\mathbf{k}_3\cdot\mathbf{k}'_3) \\
& \times \sum_{\alpha,\alpha'} Y^{*}_{l(m_j-m_{s_c})}(\hat{\mathbf{q}}) Y_{l'(m'_j-m_{s_c})}(\hat{\mathbf{q}}') \\
& \times \mathscr{C}^{\mathscr{J}M_{\mathscr{J}}}_{\bar{j}_{rel}(M_{\mathscr{J}}-m_j)jm_j} \mathscr{C}^{jm_j}_{l(m_j-m_{s_c})1/2m_{s_c}} \mathscr{C}^{\mathscr{J}M_{\mathscr{J}}}_{\bar{j}'_{rel}(M_{\mathscr{J}}-m'_j)j'm'_j} \mathscr{C}^{j'm'_j}_{l'(m'_j-m_{s_c})1/2m_{s_c}} \\
& \times \left\langle pq\alpha|V_{3N}|p'q'\alpha'\right\rangle .
\end{aligned} \tag{7.38}$$

For this reason, this quantity will not depend on all the directions of the momenta, and there is freedom to choose a direction and an angle. For the numerical calculations, we choose $\theta_P = 0$, $\phi_P = 0$, and $\phi_{P'} = 0$.

### Final result

Implementing Eq. (7.38) together with (7.29), we obtain the final expression for the effective two-body potential:

$$
\begin{aligned}
\left\langle pP\beta\bar{T}\bar{M}_T\right| V_{\text{eff}}\left|p'P'\beta'\bar{T}\bar{M}_T\right\rangle = & \frac{1}{2\bar{J}+1}\sum_{\bar{M}'_{cm},\bar{M}'_j,\bar{M}_J}\sum_{\alpha,\alpha'}\sum_{\mathcal{T}}\sum_{\mathcal{J},M_{\mathcal{J}}}\sum_{m_j,m'_j}\sum_{m_{s_c}}\frac{2\mathcal{T}+1}{2\bar{T}+1} \\
& \times \mathcal{C}^{\bar{J}\bar{M}_J}_{\bar{j}_{rel}\bar{M}_j\bar{L}_{cm}\bar{M}_{cm}}\,\mathcal{C}^{\bar{J}\bar{M}_J}_{\bar{j}'_{rel}\bar{M}'_j\bar{L}'{}_{cm}\bar{M}'_{cm}}\,\mathcal{C}^{\mathcal{J}M_{\mathcal{J}}}_{\bar{j}_{rel}\bar{M}_j jm_j}\,\mathcal{C}^{jm_j}_{lm_l1/2m_{s_c}}\,\mathcal{C}^{\mathcal{J}M_{\mathcal{J}}}_{\bar{j}'_{rel}\bar{M}'_j j'm'_j}\,\mathcal{C}^{j'm'_j}_{l'm'_l1/2m_{s_c}} \\
& \times 8\pi^2\sqrt{\frac{1+2\bar{L}_{cm}}{4\pi}}\int d\theta_{P'}\sin\theta_{P'}Y_{\bar{L}'_{cm}\bar{M}'_{cm}}(\theta_{P'},0)Y^*_{lm_l}(\hat{\mathbf{q}})Y_{l'm'_l}(\hat{\mathbf{q}}') \\
& \times \int\frac{d\mathbf{k}_3}{(2\pi)^3}\sum_{n_c,l_c}R_{n_cl_c}(k_3)R_{n_cl_c}(k'_3)\frac{2l_c+1}{4\pi}P_{l_c}(\mathbf{k}_3\cdot\mathbf{k}'_3) \\
& \times \left\langle pq\alpha\mathcal{T}\mathcal{M}_{\mathcal{T}}|V_{3N}|p'q'\alpha'\mathcal{T}\mathcal{M}_{\mathcal{T}}\right\rangle .
\end{aligned}
\tag{7.39}
$$

It is important to note that in this expression all angular and spin quantum numbers, except $\bar{J}$, are in general off-diagonal.

### 7.6.1 Calculational strategy

Since the transformation from three- to two-body matrix elements does not mix two-body coupled total angular momentum states, Eq. (7.39) can be calculated independently for each value of $\bar{J}$.

Table 7.1 shows the number of partial waves involved in the calculation for different values of $\bar{J}$ and two different cutoffs in $\bar{L}$: 3 and 4. Partial waves with higher $\bar{L}$ yield small three-body matrix elements and do not contribute significantly to the normal-ordered results. The lists of partial waves include 10 quantum numbers: $\bar{L}$, $\bar{S}$, $\bar{j}_{rel}$, $\bar{L}_{cm}$, $\bar{L}'$, $\bar{S}'$, $\bar{j}'_{rel}$, $\bar{L}'_{cm}$, $\bar{J}$, and $\bar{T}$. Given that at the level considered here there is no isospin breaking, $\bar{M}_T$ is not a relevant quantum number.

| $\bar{J}$ | $\bar{L}^{\max}$ | $\bar{L}^{\max}_{\text{cm}}$ | partial waves |
|---|---|---|---|
| 0 | 3 | 4 | 64 |
| | 4 | 5 | 81 |
| 1 | 3 | 5 | 400 |
| | 4 | 6 | 259 |
| 2 | 3 | 6 | 900 |
| | 4 | 7 | 1225 |
| 3 | 3 | 7 | 1156 |
| | 4 | 8 | 1681 |

**Table 7.1:** Number of partial waves involved in the calculation for each value of $\bar{J}$. The quantum numbers that define each partial wave are $\bar{L}$, $\bar{S}$, $\bar{j}_{rel}$, $\bar{L}_{cm}$, $\bar{L}'$, $\bar{S}'$, $\bar{j}'_{rel}$, $\bar{L}'_{cm}$, $\bar{J}$, and $\bar{T}$.

Given that $\langle V_{3N}\rangle$ and $\langle V_{\text{eff}}\rangle$ are independent of the projections of angular and spin quantum numbers, it is also possible to perform the calculation of all these sums separately, and we can define

$$\begin{aligned}\mathscr{M}^{\bar{J}}_{\bar{j}_{rel},\bar{L}_{cm},\bar{j}'_{rel},\bar{L}'{}_{cm}}(\theta_{P'},\hat{\mathbf{q}},\hat{\mathbf{q}}') = &\sum_{\bar{M}'_{cm},\bar{M}'_j,\bar{M}_J}\sum_{M_{\mathscr{J}}}\sum_{m_l,m'_l}\sum_{m_j,m'_j}\mathscr{C}^{\bar{J}\bar{M}_J}_{\bar{j}_{rel}\bar{M}_J\bar{L}_{cm}0}\mathscr{C}^{\bar{J}\bar{M}_J}_{\bar{j}'_{rel}\bar{M}'_j\bar{L}'_{cm}\bar{M}'_{cm}}\\ &\times\mathscr{C}^{\mathscr{J}M_{\mathscr{J}}}_{\bar{j}_{rel}\bar{M}_J jm_j}\mathscr{C}^{jm_j}_{lm_l1/2m_{s_c}}\mathscr{C}^{\mathscr{J}M_{\mathscr{J}}}_{\bar{j}'_{rel}\bar{M}'_j j'm'_j}\mathscr{C}^{j'm'_j}_{l'm'_l1/2m_{s_c}}\\ &\times Y^*_{\bar{L}_{cm}\bar{M}_{cm}}(0,0)Y_{\bar{L}'_{cm}\bar{M}'_{cm}}(\theta_{P'},0)Y^*_{lm_l}(\hat{\mathbf{q}})Y_{l'm'_l}(\hat{\mathbf{q}}')\,.\end{aligned}\tag{7.40}$$

This part of the final result is independent of the chosen interaction. To optimize the calculations, it can be prestored and read afterwards to compute $\langle V_{\text{eff}}\rangle$. As it can be seen, this quantity does not depend on the isospin or the relative $\bar{L}$, $\bar{S}$, nor their primed counterparts. For this reason, its calculation can be performed using only a subset of partial waves involving $\bar{j}_{rel}$, $\bar{L}_{cm}$, $\bar{j}'_{rel}$, and $\bar{L}'_{cm}$. The storage of these files does not represent a severe challenge, even though it is worth mentioning that the largest file that we have in storage is that with $\mathscr{J}^{\max}=5/2$, $\bar{J}=3$ and $\bar{L}^{\max}=\bar{L}^{\max}_{cm}=4$, which occupies 59 gigabytes.

We can reduce the number of integrals in Eq. (7.39) from 4 to 3 by using the Lebedev quadrature [167] to perform the angular integral $\Omega_{k_3}$ in both spherical angles at the same time. We found that the minimum size of this mesh to obtain converged results in this dimension is 86 points. For the two remaining integrals, we use a standard Gauss-Legendre quadrature [124] with 15 points for each of them.

Our calculations were performed in the strongint cluster: Intel Xeon E5-4620 with 40 Cores and 2.1 GHz. With these settings, the normal-ordering procedure for $\bar{J}=3$ and $\bar{L}^{\max}=\bar{L}^{\max}_{cm}=4$ takes approximately 32h, making it the most time-consuming step of the transformation from three-body Jacobi basis to two-body single-particle basis (Sec. 7.6.2 and 7.6.3 describe the following steps).

### 7.6.2 Transformation to harmonic oscillator relative basis

A transformation from a partial-wave decomposed Jacobi scheme to HO relative basis does not alter the coupling of the isospin degrees of freedom. Therefore, they can be factorized from the orbital part:

$$\langle Pp\beta|V|P'p'\beta'\rangle = \left\langle\bar{T}\bar{M}_T\right|\left\langle Pp[(\bar{L}\bar{S})\bar{j}_{rel}\bar{L}_{cm}]\bar{J}|V_{\text{eff}}|P'p'[(\bar{L}'\bar{S}')\bar{j}'_{rel}\bar{L}'_{cm}]\bar{J}'\right\rangle\left|\bar{T}\bar{M}_T\right\rangle\,.\tag{7.41}$$

Ignoring the isospin part, the transformation is done collapsing the interaction with the harmonic oscillator radial wave functions,

$$\begin{aligned}\left\langle\bar{N}_{cm}\bar{N}\beta|V_{\text{eff}}|\bar{N}'_{cm}\bar{N}'\beta'\right\rangle = &\int dPP^2R_{\bar{N}_{cm}\bar{L}_{cm}}(P)\int dP'P'^2R_{\bar{N}'_{cm}\bar{L}'_{cm}}(P')\\ &\times\int dpp^2R_{\bar{N}\bar{L}}(p)\int dp'p'^2R_{\bar{N}'\bar{L}'}(p')\left\langle Pp\beta|V_{\text{eff}}|P'p'\beta'\right\rangle\,.\end{aligned}\tag{7.42}$$

### 7.6.3 Transformation to single-particle basis

The transformation from the relative HO basis to a single-particle $jj$-coupled HO basis for free-space interactions is done through a Talmi-Moshinsky transformation [168, 169]. In this case the process can schematically be represented as

$$\begin{gathered}\left\langle\bar{N}(\bar{L}\bar{S})\bar{J}\middle|V_{NN}\middle|\bar{N}'(\bar{L}'\bar{S})\bar{J}\right\rangle\\ \downarrow\\ \left\langle n_an_b\left[\left(l_a\frac{1}{2}\right)j_a\left(l_b\frac{1}{2}\right)j_b\right]\bar{J}\middle|V_{NN}\middle|n'_an'_b\left[\left(l'_a\frac{1}{2}\right)j'_a\left(l'_b\frac{1}{2}\right)j'_b\right]\bar{J}\right\rangle\end{gathered}\tag{7.43}$$

and it is implicitly considered that the center-of-mass dependence in the harmonic oscillator basis can be factored from the relative coordinates.

In contrast, in the case discussed in this chapter we need to transform the matrix elements obtained from Eq. (7.39). Thus, we deal with a non-translationally invariant interaction in which the interaction depends on the center-of-mass degrees of freedom. Hence, we need to perform the transformation

$$\begin{gathered}\left\langle \bar{N}_{cm}\bar{N}\left[(\bar{L}_{cm}\bar{L})\bar{\Lambda}\bar{S}\right]\bar{J}\middle|V_{NN}\middle|\bar{N}'_{cm}\bar{N}'\left[(\bar{L}'_{cm}\bar{L}')\bar{\Lambda}'\bar{S}'\right]\bar{J}\right\rangle \\ \downarrow \\ \left\langle n_a n_b\left[\left(l_a\frac{1}{2}\right)j_a\left(l_b\frac{1}{2}\right)j_b\right]\bar{J}\middle|V_{NN}\middle|n'_a n'_b\left[\left(l'_a\frac{1}{2}\right)j'_a\left(l'_b\frac{1}{2}\right)j'_b\right]\bar{J}\right\rangle\end{gathered} \tag{7.44}$$

We recouple the single-particle basis in order to factor the spin part:

$$\left|n_a n_b\left[\left(l_a\frac{1}{2}\right)j_a\left(l_b\frac{1}{2}\right)j_b\right]\bar{J}\right\rangle = \sum_{\bar{\Lambda}\bar{S}}\hat{\bar{\Lambda}}\hat{\bar{S}}\hat{j}_a\hat{j}_b\begin{Bmatrix} l_a & l_b & \bar{\Lambda} \\ \frac{1}{2} & \frac{1}{2} & \bar{S} \\ j_a & j_b & \bar{J}\end{Bmatrix}\left|n_a n_b\left[(l_a l_b)\bar{\Lambda}\left(\frac{1}{2}\frac{1}{2}\right)\bar{S}\right]\bar{J}\right\rangle . \tag{7.45}$$

where $\hat{x} = \sqrt{2x+1}$. Expressing this equation in terms of relative coupled HO states,

$$\begin{aligned}\left|n_a n_b\left[\left(l_a\frac{1}{2}\right)j_a\left(l_b\frac{1}{2}\right)j_b\right]\bar{J}\right\rangle = &\sum_{\substack{\bar{N}\bar{L}\\ N_{cm}\bar{L}_{cm}}}\sum_{\bar{\Lambda}\bar{S}}\hat{\bar{\Lambda}}\hat{\bar{S}}\hat{j}_a\hat{j}_b\begin{Bmatrix} l_a & l_b & \bar{\Lambda} \\ \frac{1}{2} & \frac{1}{2} & \bar{S} \\ j_a & j_b & \bar{J}\end{Bmatrix} \\ &\times\left\langle \bar{N}_{cm}\bar{N}(\bar{L}_{cm}\bar{L})\bar{\Lambda}|n_a n_b(l_a l_b)\bar{\Lambda}\right\rangle_{d=1}\left|\bar{N}_{cm}\bar{N}\left[(\bar{L}_{cm}\bar{L})\bar{\Lambda}\bar{S}\right]\bar{J}\right\rangle .\end{aligned} \tag{7.46}$$

Here, $\langle N_{cm}N_{rel}(L_{cm}L)\Lambda|n_a n_b(l_a l_b)\Lambda\rangle_{d=1}$ is the Talmi-Moshinsky bracket for two particles of the same mass. These brackets are calculated following the prescription of Ref. [170].

In order to work with $\bar{j}_{rel}$ as a quantum number of our basis, coupling of $\bar{L}$ and $\bar{S}$, we perform a change in the coupling scheme for the matrix elements to get rid of the explicit dependence on $\bar{\Lambda}$,

$$\begin{aligned}\left|n_a n_b\left[\left(l_a\frac{1}{2}\right)j_a\left(l_b\frac{1}{2}\right)j_b\right]\bar{J}\right\rangle = &\sum_{\substack{\bar{N}\bar{L}\\ N_{cm}\bar{L}_{cm}}}\sum_{\bar{\Lambda}\bar{S}}\hat{\bar{\Lambda}}\hat{\bar{S}}\hat{j}_a\hat{j}_b\begin{Bmatrix} l_a & l_b & \bar{\Lambda} \\ \frac{1}{2} & \frac{1}{2} & \bar{S} \\ j_a & j_b & \bar{J}\end{Bmatrix}\left\langle \bar{N}_{cm}\bar{N}(\bar{L}_{cm}\bar{L})\bar{\Lambda}|n_a n_b(l_a l_b)\bar{\Lambda}\right\rangle_{d=1} \\ &\times\left\langle \bar{N}_{cm}\bar{N}\left[(\bar{L}\bar{S})\bar{j}_{rel}\bar{L}_{cm}\right]\bar{J}|\bar{N}_{cm}\bar{N}\left[(\bar{L}_{cm}\bar{L})\bar{\Lambda}\bar{S}\right]\bar{J}\right\rangle\left|\bar{N}_{cm}\bar{N}\left[(\bar{L}\bar{S})\bar{j}_{rel}\bar{L}_{cm}\right]\bar{J}\right\rangle .\end{aligned} \tag{7.47}$$

Finally, we can write the Talmi-Moshinsky transformation with explicit dependence on the center-of-mass degrees of freedom as

$$\begin{aligned}\left|n_a n_b\left[\left(l_a\frac{1}{2}\right)j_a\left(l_b\frac{1}{2}\right)j_b\right]\bar{J}\right\rangle = &\sum_{\substack{\bar{N}\bar{L}\\ N_{cm}\bar{L}_{cm}}}\sum_{\bar{\Lambda}\bar{S}}\hat{\bar{\Lambda}}\hat{\bar{S}}\hat{j}_a\hat{j}_b\begin{Bmatrix} l_a & l_b & \bar{\Lambda} \\ \frac{1}{2} & \frac{1}{2} & \bar{S} \\ j_a & j_b & \bar{J}\end{Bmatrix}\left\langle \bar{N}_{cm}\bar{N}(\bar{L}_{cm}\bar{L})\bar{\Lambda}|n_a n_b(l_a l_b)\bar{\Lambda}\right\rangle_{d=1} \\ &\times\sum_{\bar{j}_{rel}}(-1)^{\bar{L}+\bar{S}+\bar{j}_{rel}}\hat{\bar{\Lambda}}\hat{\bar{j}}_{rel}\begin{Bmatrix} \bar{L}_{cm} & \bar{L} & \bar{\Lambda} \\ \bar{S} & \bar{J} & \bar{j}_{rel}\end{Bmatrix}\left|\bar{N}_{cm}\bar{N}\left[(\bar{L}\bar{S})\bar{j}_{rel}\bar{L}_{cm}\right]\bar{J}\right\rangle .\end{aligned} \tag{7.48}$$

### Comment on the Talmi-Moshinsky brackets

The subindex $d$ in the bracket notation is the one defining the relation between single-particle and relative+center-of-mass coordinates, in the fashion,

$$\begin{pmatrix} \mathbf{R}_{cm} \\ \mathbf{r}_{rel} \end{pmatrix} = \begin{pmatrix} \sqrt{\frac{d}{1+d}} & \sqrt{\frac{1}{1+d}} \\ \sqrt{\frac{1}{1+d}} & -\sqrt{\frac{d}{1+d}} \end{pmatrix} \begin{pmatrix} \mathbf{r}_1 \\ \mathbf{r}_2 \end{pmatrix} \tag{7.49}$$

In the case of a two-body interaction between particles of the same mass,

$$\begin{cases} \mathbf{r}_{rel} = \sqrt{\frac{1}{2}}\mathbf{r}_1 - \sqrt{\frac{1}{2}}\mathbf{r}_2 \\ \mathbf{R}_{cm} = \sqrt{\frac{1}{2}}\mathbf{r}_1 + \sqrt{\frac{1}{2}}\mathbf{r}_2 \end{cases} , \tag{7.50}$$

and, therefore, $d = 1$.

### 7.6.4 Benchmarks

Fig. 7.7 shows the convergence of this approach in $\bar{L}$ and $\bar{L}_{cm}$ comparing the matrix elements with single-particle normal-ordered ones ($\langle V_{\text{ref}} \rangle$). In this case, we consider that only the first term of Eq. (2.23) contributes to the Hamiltonian with $c_1$=1 GeV$^{-1}$. Calculations are made for $^{16}$O as the reference state and $\hbar\omega = 13.53$ MeV. The states have total two-body energy $E_2 = e_i + e_j < 12$ and include partial waves up to $\bar{J} = 3$ (in the plot $\bar{J} = 0$ is shown by blue diamonds, $\bar{J} = 1$ by green triangles, $\bar{J} = 2$ by blue squares, and $\bar{J} = 3$ by black circles). Three-body partial waves are included up to $\mathscr{J} = 5/2$ to optimize the run time, since it was seen in our calculations that increasing $\mathscr{J}$ to 7/2 did not improve the comparison significantly. There are two possible $\bar{L}$ and $\bar{L}_{cm}$ cuts considered: 3 and 4. The panels of this figure show from left to right and top to bottom: $\bar{L} = 3$ and $\bar{L}_{cm} = 4$, $\bar{L} = 3$ and $\bar{L}_{cm} = 4$, $\bar{L} = 3$ and $\bar{L}_{cm} = 4$, and $\bar{L} = 4$ and $\bar{L}_{cm} = 4$. As it can be seen, the results for $\bar{J} = 0$ are converged in all cases, the same being true for $\bar{J} = 1$. In the other two cases, $\bar{J} = 2$ converges for $\bar{L}^{\max} = 4$, being the increase in $\bar{L}_{cm}$ of almost no impact, while for $\bar{J} = 3$ an increase in both quantum numbers is necessary to see convergence towards the line $x = y$, even though there are still some outliers corresponding to large matrix elements.

A second example of convergence on $\bar{L}$ and $\bar{L}_{cm}$ is given in Fig. 7.8, where we can see the same four panels shown in Fig. 7.7 for a Hamiltonian with only $c_3 = 1$ GeV$^{-1}$ and all the rest of LECs set to zero. It is evident from the comparison of both figures that, even though the general features are shared between both topologies, matrix elements corresponding to the $c_1$ Hamiltonian have a slower convergence pattern than those for $c_3$. In our calculations for the remaining LECs, we see that $c_1$ is indeed the least converged of the topologies. The results for a Hamiltonian with $c_4 = 1$ GeV$^{-1}$ show a behaviour equivalent to that seen in Fig. 7.8, while if the only topology contributing are $c_D$ the matrix elements converge visibly towards the reference value already at $\bar{L}_{cm} = \bar{L} = 3$. The case for the contact interaction ($c_E$) is as well converged as the case shown in Fig. 7.4, already at $\bar{L}_{cm} = 3$ (partial waves with $\bar{L} > 0$ do not contribute to this topology).

The slow convergence for the $c_1$ part of the two-pion exchange has already been observed for chiral EFT Hamiltonians, e.g., in the convergence of the two-body normal-ordered matrix elements for infinite matter. Fig. 7.6 shows the accumulated contributions up to a given three-body partial-wave for the $^1S_0$ channel, including all the lower partial-waves for each case, in the case of normal-ordered two-body matrix elements for symmetric nuclear matter as a function of $p$ (only matrix elements diagonal in momentum are shown). The normal-ordering procedure is performed as explained in Ref. [166] at nuclear saturation density ($k_F^n = k_F^p = 1.35$ fm$^{-1}$). For plotting purposes, we use the

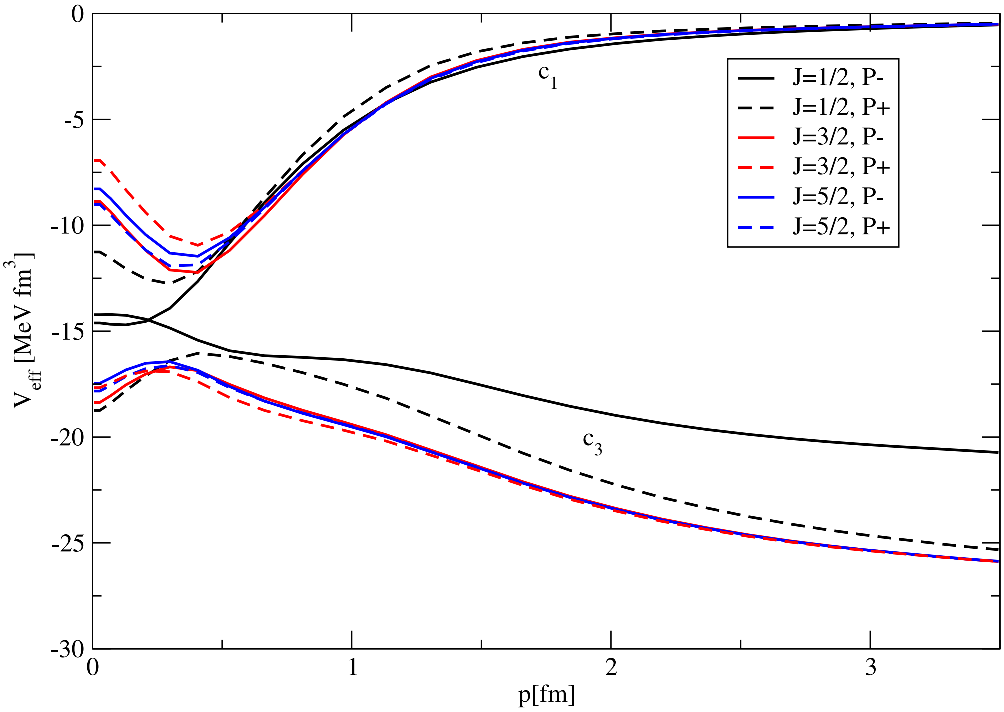

**Figure 7.6:** Partial-wave contributions to the normal-ordered two-body matrix elements in symmetric nuclear matter at nuclear saturation density, as a function of the two-body momentum transfer $p$. We only show contributions diagonal in momentum for the $^1S_0$ channel. For the matrix elements shown, we use the coupling constants $c_1 = 1$ GeV$^{-1}$ and $c_3 = 2$ GeV$^{-1}$. All results show accumulated contributions up to the given partial-wave channel including both three-body isospins.

coupling constants $c_1 = 1$ GeV$^{-1}$ and $c_3 = 2$ GeV$^{-1}$. The curves corresponding to each LEC are indicated in the plot. We can see how for both LECs going from $\mathscr{J} = 1/2$ (black lines) to $\mathscr{J} = 3/2$ (red lines) and finally to $\mathscr{J} = 5/2$ (blue lines) leads to clear convergence towards the same value $V_{\text{eff}}$. It is also clear from the plot that, especially for low momenta, matrix elements for $c_1$ converge slower. See also Ref. [109] for an analysis of the convergence for three-body energies with respect to different parts of the Hamiltonian.

Even though the convergence towards the reference values is relatively slow for the TPE case, these benchmarks at matrix element level already indicate that results for nuclear observables will give reasonable values in comparison to existing calculations performed with interactions normal-ordered in three-body single-particle basis. In the following chapter (Sec. 8.1), we will show results for the ground-state energy and charge radius of $^{16}$O.

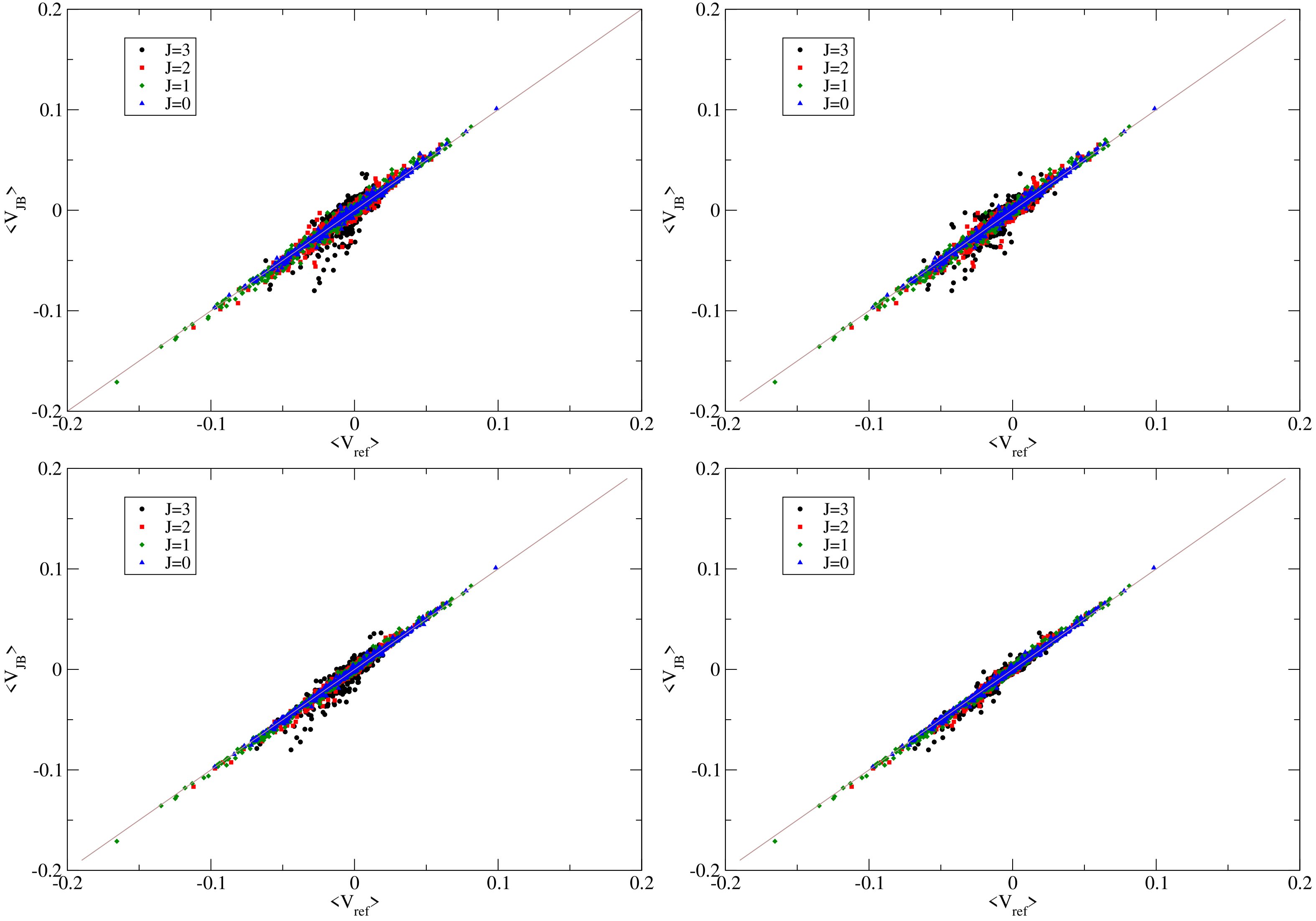

**Figure 7.7:** Study of the convergence in $\bar{L}$ and $\bar{L}_{cm}$ for the comparison between single-particle normal-ordered matrix ($\langle V_{\text{ref}} \rangle$) elements and this work ($\langle V_{\text{JB}} \rangle$). Calculations are made for $^{16}$O reference state and $\hbar\omega = 13.53$ MeV. The Hamiltonian considered has $c_1 = 1$ GeV$^{-1}$, while the rest of LECs are set to zero. The solid line $x = y$ is shown to guide the eye. The panels show in clockwise direction: $\bar{L} = 3$ and $\bar{L}_{cm} = 3$, $\bar{L} = 3$ and $\bar{L}_{cm} = 4$, $L = 4$ and $\bar{L}_{cm} = 4$, and $\bar{L} = 4$ and $\bar{L}_{cm} = 3$.

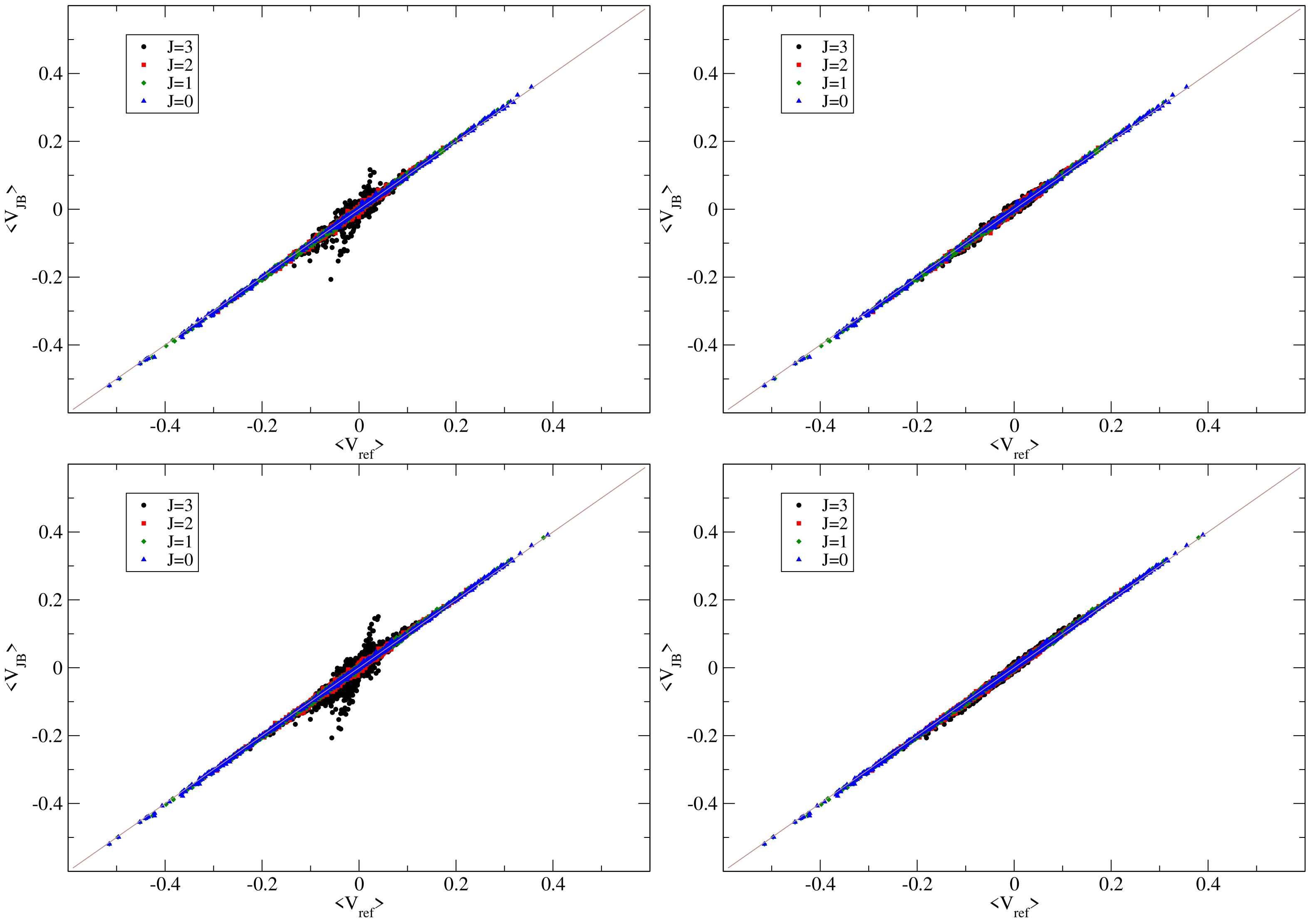

**Figure 7.8:** Study of the convergence in $\bar{L}$ and $\bar{L}_{cm}$ for the comparison between single-particle normal-ordered matrix ($\langle V_{\text{ref}} \rangle$) elements and this work ($\langle V_{\text{JB}} \rangle$). Calculations are made for $^{16}$O reference state and $\hbar\omega = 13.53$ MeV. The Hamiltonian considered has $c_3 = 1$ GeV$^{-1}$, while the rest of LECs are set to zero. The solid line $x = y$ is shown to guide the eye. The panels show in clockwise direction: $\bar{L} = 3$ and $\bar{L}_{cm} = 3$, $\bar{L} = 3$ and $\bar{L}_{cm} = 4$, $L = 4$ and $\bar{L}_{cm} = 4$, and $\bar{L} = 4$ and $\bar{L}_{cm} = 3$.

# 8 Applications to nuclei

## 8.1 Calculations with novel normal-ordering scheme

In this section, we apply the IM-SRG method [61, 63], which solves the many-body problem in terms of the flow equation by decoupling particle-hole excitations from the ground-state. The prefix *in-medium* refers to the normal ordering with respect to a chosen reference state. In this case, following what was done in Chapter 7, the reference state is expressed in HO basis. All the results presented here are obtained using the Magnus expansion [171–173], truncating all operators and commutators at the normal-ordered two-body level (Magnus(2) approach). This work is done in collaboration with Jan Hoppe.

Table 8.1 shows the ground-state energy $E_{\text{gs}}$ and charge radius $R_{\text{ch}}$ for $^{16}$O using a HO basis as reference state. The results are obtained using $NN$ interactions at N$^3$LO plus NO2B $3N$ interactions at N$^2$LO for the EM 500 $\lambda_{NN}/\Lambda_{3N} = 2.0/2.0$ potential (see Table 2.5). For both observables, different combinations of $\bar{L}^{\text{max}} = 3, 4$ and $\bar{L}_{cm}^{\text{max}} = 3, 4$ were applied in the NO2B matrix elements using the novel NO technique presented in Sec. 7. Furthermore, the results were obtained with $\bar{J}^{\text{max}} = 3$ and $e_{\text{max}} = 6$, where $e = 2n + l$. The reference values are obtained from the calculation with the conventional NO technique (presented in Sec. 6.3) including all partial-waves up to $\bar{J} = 8$ for three-body partial waves with $\mathcal{J}$ up to 5/2 and the cut $\bar{J} = 7$ and $\bar{J} = 6$ for $\mathcal{J} = 7/2$ and $\mathcal{J} = 9/2$, respectively. The energy cuts are $e_{\text{max}}/E_{3\text{max}} = 6/14$ for all cases, and the HO frequency was set to $\hbar\omega = 13.53$ MeV.

| cut $\bar{L}/\bar{L}_{cm}$ | 3/3 | 3/4 | 4/3 | 4/4 | reference |
|---|---|---|---|---|---|
| $E_{\text{gs}}$ [MeV] | -115.537 | -115.888 | -116.168 | -116.674 | -116.949 |
| $R_{\text{ch}}$ [fm] | 2.691 | 2.680 | 2.677 | 2.673 | 2.668 |

**Table 8.1:** Values of $E_{\text{gs}}$ and $R_{\text{ch}}$ for $^{16}$O, calculated with the $NN$+NO2B $3N$ 2.0/2.0 (EM) interaction of Ref. [37] for different $\bar{L}/\bar{L}_{cm}$ cuts in the NO2B matrix elements using the novel NO technique presented in Sec. 7. The last row ("reference") shows the results obtained with the usual NO technique for the NO2B matrix elements and no $\bar{L}/\bar{L}_{cm}$ cut. For all cuts in the novel normal ordering technique, the truncations $\bar{J}^{\text{max}} = 3$ and $e_{\text{max}} = 6$ were applied. The HO frequency was set to $\hbar\omega = 13.53$ MeV and the IM-SRG calculations were done with $e_{\text{max}}/E_{3\text{max}}$ =6/14.

The charge radius is obtained from the intrinsic point proton mean-square radius $R_p^2$ evolved with the Magnus formalism, taking into account the proton and neutron mean-square charge radii, $r_p$ and $r_n$, and the relativistic Darwin-Foldy [174, 175], as well as the spin-orbit corrections $r_{so}$:

$$R_{\text{ch}} = \sqrt{R_p^2 + \left\langle r_p^2 \right\rangle + \frac{N}{Z}\left\langle r_n^2 \right\rangle + \frac{3}{4m_p^2 c^4} + \left\langle r_{so}^2 \right\rangle} \tag{8.1}$$

Fig. 8.1 shows the ground state energy, while the charge radius can be seen in Fig. 8.2. In the figures, we take into account only the $3N$ contribution, by subtracting the $NN$-only contributions from the total result. The orange circles depict the calculations obtained with the novel NO technique (NO Jacobi basis) using the different $\bar{L}/\bar{L}_{cm}$ truncations as specified on the $x$-axis. The dashed line

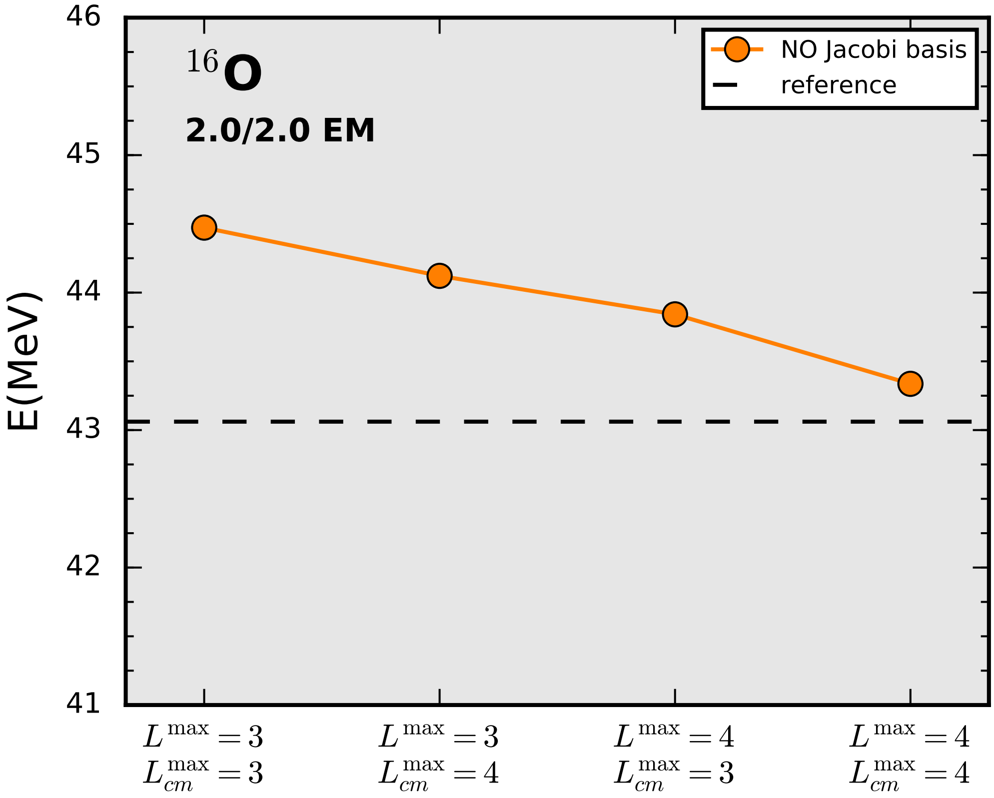

**Figure 8.1:** Ground-state energy of $^{16}$O, reflecting only the impact of $3N$ interactions for the EM 500 2.0/2.0 potential. The orange circles depict the calculations obtained with the novel NO technique using the different $\bar{L}/\bar{L}_{cm}$ truncations specified on the $x$-axis, $\bar{J}^{\max} = 3$, and $e_{\max} = 6$. The dashed line represents the result obtained using reference NO matrix elements, with $e_{\max}/E_{3\max} = 6/14$. The harmonic oscillator frequency was set to $\hbar\omega = 13.53$ MeV.

represents the calculation with the conventional NO technique (reference). All other parameters are the same as those used for Table 8.1. It can be clearly seen how as $\bar{L}$ and $\bar{L}_{cm}$ grow, the results for the energy and the charge radius converge rapidly to the reference value, with errors of 0.6% and 0.12% in the energy, and 0.43% and 0.28% in the radius for $\bar{L}^{\max}/\bar{L}^{\max}_{cm} = 3/3$ and $\bar{L}^{\max}/\bar{L}^{\max}_{cm} = 4/4$, respectively.

Since the new NO method allows to increase the cut in $E_{3\max}$ by increasing the quantum numbers $\bar{N}$ and $\bar{N}_{cm}$, the trend of the results of Fig. 8.1 makes it clear that this is a promising approach to implement in calculations for heavier nuclei. Additionally, not having to read in $3N$ matrix elements and normal-order them inside the IM-SRG algorithm speeds up the calculations of observables, which further reinforces the motivation to implement this novel technique to include normal-ordered matrix elements in IM-SRG calculations.

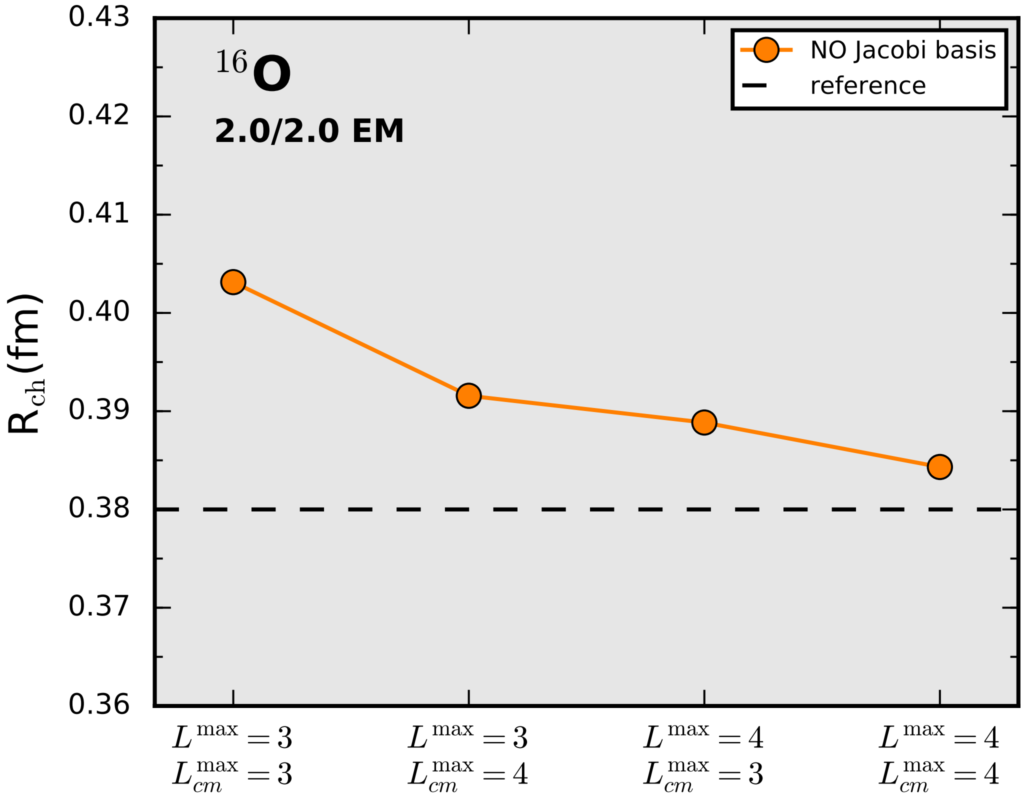

**Figure 8.2:** Charge radius of $^{16}$O, reflecting only the impact of $3N$ interactions for the EM 500 2.0/2.0 potential. See caption of Fig. 8.1 for details.

## 8.2 Harmonic-oscillator radial wave functions and spherical Bessel functions

In this section we will present another approximation for the calculation of HO wave functions. We will assess the validity of this approximation performing benchmarks of three-body matrix elements and triton binding energy.

### 8.2.1 Two-body case

Given the mathematical nature of the radial wave functions in Eq. (6.14), it is possible to establish a very accurate relation between $R_{nl}$ and the spherical Bessel functions of the first kind, $j_l$. This relation has been proven to be useful for calculations of scattering $T$-matrix elements in infinite matter as well as finite nuclei [176]. In this work we establish their validity for further calculations of matrix elements and finite nuclei properties.

Mathematically, for $n \to \infty$ and $x \to 0$, Laguerre polynomials can be expressed as [177]

$$e^{-\frac{1}{2}x} x^{\frac{1}{2}a} L_n^a(x) = \frac{\Gamma(n+a+1)}{\left(\frac{1}{4}\nu\right)^{\frac{1}{2}a} n!} J_a\left[(\nu x)^{\frac{1}{2}}\right] + \mathcal{O}\left(n^{\frac{1}{2}a-\frac{3}{4}}\right), \tag{8.2}$$

where $\nu = 4n + 2a + 2$ and $J_a$ are the Bessel functions of the first kind. Comparing this asymptotic behavior with the function $R_{nl}$, we can identify

$$x = \left(\frac{r_{12}}{\sqrt{2}b}\right)^2, \qquad a = l + 1/2 \tag{8.3}$$

which leads to

$$e^{-\frac{1}{2}\left(\frac{r_{12}}{\sqrt{2}b}\right)^2}\left(\frac{r_{12}}{\sqrt{2}b}\right)^l L_n^{l+1/2}\left[\left(\frac{r_{12}}{\sqrt{2}b}\right)^2\right]=\left(\frac{\sqrt{2}b}{r_{12}}\right)^{\frac{1}{2}}\frac{\Gamma(n+1+3/2)}{\left(\frac{1}{4}\nu\right)^{\frac{l}{4}+\frac{1}{2}}n!}J_{l+\frac{1}{2}}\left[\nu^{\frac{1}{2}}\frac{r_{12}}{\sqrt{2}b}\right]. \tag{8.4}$$

Taking into account that in general Bessel functions of the first kind can be written as

$$J_{l+\frac{1}{2}}(x)=\sqrt{\frac{2x}{\pi}}j_l(x), \tag{8.5}$$

with $j_l$ the spherical Bessel function of the first kind, the final form of the radial part of the harmonic oscillator wave function in terms of the functions $j_l$ reads

$$R_{nl}(r_{12})=\frac{1}{b^{\frac{3}{2}}}\sqrt{\frac{2\Gamma(n+l+3/2)}{\pi n!\,\nu^l}}2^{l+1}j_l(k_{nl}r_{12}), \tag{8.6}$$

where

$$k_{nl}=\frac{\sqrt{2n+l+3/2}}{b}. \tag{8.7}$$

Therefore, we have an approximated wave function depending on the radial coordinate and the new momentum-like variable $k_{nl}$ defined for every level $(n,l)$ of the harmonic oscillator basis. A graphical representation of the agreement between this approximation and the exact wave functions can be found in Fig. 8.3. As it can be seen, the wave approximation is better for small distances and improves for increasing $n$ with constant orbital wave number $l$.

## Fourier transform of the radial wave functions

We determine the radial wave function $\tilde{R}_{nl}(k_{12})$ as the Fourier-bessel transform of $R_{nl}(r_{12})$

$$\tilde{R}_{nl}(k_{12})=\sqrt{\frac{2}{\pi}}\int_0^\infty drr^2 j_l(k_{12}r_{12})R_{nl}(r_{12}). \tag{8.8}$$

Then, applying Eq. (8.6), the radial wave function in momentum space will be determined by an integral of the form

$$\tilde{R}_{nl}(k_{12})=\sqrt{\frac{2}{\pi}}\sqrt{\frac{2\Gamma(n+l+\frac{3}{2})}{\pi n!\,\nu^l}}\frac{2^{l+1}}{b^{\frac{3}{2}}}\int_0^\infty drr^2 j_l(k_{12}r_{12})j_l(k_{nl}r_{12}), \tag{8.9}$$

which can be easily evaluated taking into account the completeness relation of the functions $j_l(r)$

$$\frac{2r^2}{\pi}\int_0^\infty dpp^2 j_l(pa)j_l(pr)=\delta(r-a), \tag{8.10}$$

leading to,

$$\tilde{R}_{nl}(k_{12})=\sqrt{\frac{\Gamma(n+l+\frac{3}{2})}{n!\,\nu^l}}\frac{2^{l+1}}{b^{\frac{3}{2}}}\frac{\delta(k_{nl}-k_{12})}{k_{12}^2}. \tag{8.11}$$

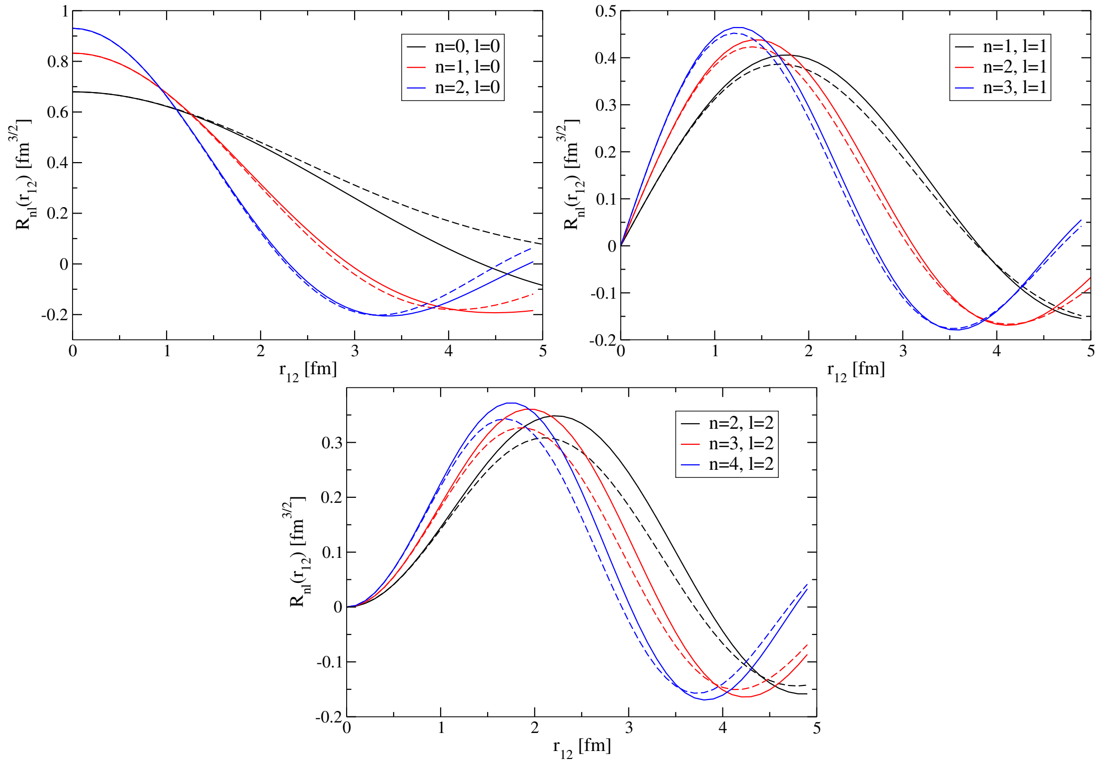

**Figure 8.3:** Comparison between exact (solid lines) and approximated (dashed lines) radial wave functions for different $l$ and $n$ values. Each panel shows different $n$ values for constant $l$, with $l$=0, 1 and 2.

This result indicates that, thanks to the Dirac delta function, the matrix elements of the potential in this basis will depend on specific values of $k$ and $k'$ corresponding to $k_{nl}$ and $k_{n'l'}$. Therefore, following the prescription given in Sec. 7.6.2, the transformation of a generic matrix element in momentum space will have the form

$$\begin{aligned}\langle nl|V_{NN}|n'l'\rangle &= \int_0^{k_{\max}} k_{12}^2 dk_{12} \int_0^{k_{\max}} k_{12}'^2 dk_{12}' R_{nl}(k_{12}) \langle k_{12} l|V_{NN}|k_{12}' l'\rangle R_{n'l'}(k_{12}') \\ &= \sqrt{\frac{\Gamma(n'+l'+3/2)}{n'!\,\nu^{l'}}} \sqrt{\frac{\Gamma(n+l+3/2)}{n!\,\nu^{l}}} \frac{2^{l'+l+2}}{b^3} \\ &\times \int_0^{k_{\max}} dk_{12} \int_0^{k_{\max}} dk_{12}' \delta(k_n - k_{12}) \langle k_{12} l|V_{NN}|k_{12}' l'\rangle \delta(k_{n'} - k_{12}') \,. \end{aligned} \tag{8.12}$$

The result of the integrals in Eq. (8.12) is

$$\begin{aligned}\langle nl|V_{NN}|n'l'\rangle =& C_{nn'}^{ll'} \left(2\theta(k_{\max})-1\right) \theta\left(k_{nl} - k_{\max}\theta(-k_{\max})\right) \left(k_{\max}\theta(k_{\max}) - k_{nl}\right) \\ & \times \left(2\theta(k_{\max})-1\right) \theta\left(k_{n'l'} - k_{\max}\theta(-k_{\max})\right) \left(k_{\max}\theta(k_{\max}) - k_{n'l'}\right) \\ & \times \langle k_{nl}|V_{NN}|k_{n'l'}\rangle \,, \end{aligned} \tag{8.13}$$

where $\theta$ denotes the Heaviside step function and the constants are defined as

$$C_{nn'}^{ll'} \equiv \sqrt{\frac{\Gamma(n'+l'+3/2)}{n'!\,\nu^{l'}}} \sqrt{\frac{\Gamma(n+l+3/2)}{n!\,\nu^{l}}} \frac{2^{l'+l+2}}{b^3} \,, \tag{8.14}$$

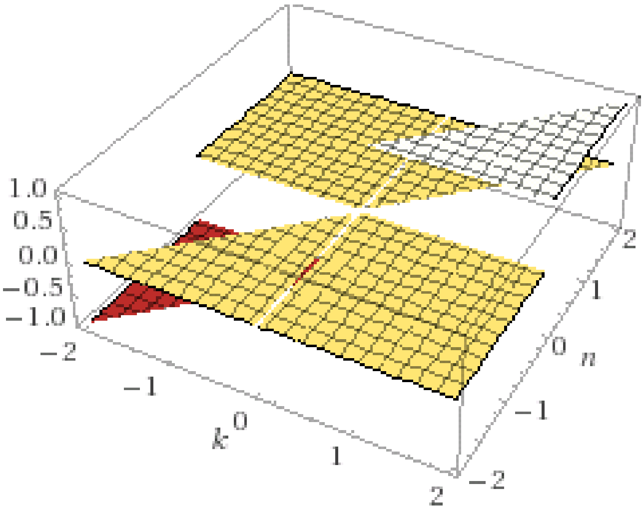

**Figure 8.4:** Graphical behavior of the function $(2\theta(k_{\text{max}})-1)\,\theta\,(k_n - k_{\text{max}}\theta(-k_{\text{max}}))\,(k_{\text{max}}\theta(k_{\text{max}})-k_n)$.

As anticipated, we can clearly see from Eq. (8.13) that the matrix elements do not depend on all possible momenta, but only on specific values of $k$ determined by the condition $\sqrt{2n+l+3/2}\sqrt{\frac{\hbar}{m\omega}} = k_{nl}$ (the same is true for the primed counterparts).

Since $k_{nl}$ and $k_{\text{max}}$ are both positive quantities, we can evaluate the step functions:

$$(2\theta(k_{\text{max}})-1)\,\theta\,(k_{nl} - k_{\text{max}}\theta(-k_{\text{max}}))\,(k_{\text{max}}\theta(k_{\text{max}})-k_{nl}) = \begin{cases} 1 \text{ if } k_{nl} < k_{\text{max}} \\ 0 \text{ otherwise} \end{cases}, \tag{8.15}$$

as can be seen graphically in Fig. 8.4. Therefore, in the case $k_{nl} < k_{\text{max}}$ and $k_{n'l'} < k_{\text{max}}$, the matrix elements will be determined by the simple expression

$$\langle nl|V_{NN}|n'l'\rangle = C_{nn'}^{ll'}\langle k_{nl}|V_{NN}|k_{n'l'}\rangle\,. \tag{8.16}$$

### 8.2.2 Three-body case

For the three-body case, the relative distances are defined by the Jacobi coordinates, analogous to the momentum case. The coordinate counterpart of $\mathbf{p}$ and $\mathbf{q}$ in Eq. (6.7) read

$$\boldsymbol{\rho} = \frac{1}{\sqrt{2}}(\mathbf{r}_1 - \mathbf{r}_2)\,, \tag{8.17a}$$

$$\boldsymbol{\lambda} = \frac{1}{\sqrt{3}}(\mathbf{r}_1 + \mathbf{r}_2 - 2\mathbf{r}_3)\,. \tag{8.17b}$$

Therefore, analogously to Eq. (8.6), the radial part of the harmonic oscillator wave functions in coordinate space will be approximated as

$$R_{nl}(\rho) \approx \frac{2^{L_{12}+1}}{b_1^{3/2}}\sqrt{\frac{2\Gamma(N_{12}+L_{12}+3/2)}{\pi N_{12}!\,\nu_{12}^{L_{12}}}}\,j_{L_{12}}(p_{nl}\rho)\,, \tag{8.18}$$

$$R_{nl}(\lambda) \approx \frac{2^{l_3+1}}{b_2^{3/2}} \sqrt{\frac{2\Gamma(n_3+l_3+3/2)}{\pi n_3! \nu_3^{l_3}}} j_{l_3}(q_{nl}\lambda) , \tag{8.19}$$

with the normalized HO lenghts $b_1$ and $b_2$

$$b_1 = \sqrt{2}\sqrt{\frac{\hbar}{m\omega}} , \tag{8.20a}$$

$$b_2 = \sqrt{\frac{3}{2}}\sqrt{\frac{\hbar}{m\omega}} , \tag{8.20b}$$

and the momenta $p_{nl}$ and $q_{nl}$ defined as

$$p_{nl} = \frac{\sqrt{2N_{12}+L_{12}+3/2}}{b_1} , \tag{8.21a}$$

$$q_{nl} = \frac{\sqrt{2n_3+l_3+3/2}}{b_2} . \tag{8.21b}$$

With these definitions, the wave functions of Eqs. (8.18) and (8.19) can also be Fourier transformed to obtain their expressions in momentum space, as done in the two-body sector.

## Three-body matrix elements

The radial part of the matrix elements can be calculated in a simpler way using this approximation. The final result of the transformation from momentum space three-body matrix elements is given by

$$\begin{aligned} \langle N_{12}L_{12}n_3l_3|V_{3N}|N'_{12}L'_{12}n'_3l'_3\rangle = & \int p^2dp \int q^2dq \int p^{'2}dp' \int p^{'2}dp' \\ & \times R_{NL}(p)R_{nl}(q)\langle pq|V_{3N}|p'q'\rangle R_{N'L'}(p')R_{n'l'}(q') . \end{aligned} \tag{8.22}$$

Resulting in

$$\begin{aligned} \langle N_{12}L_{12}n_3l_3|V_{3N}|N'_{12}L'_{12}n'_3l'_3\rangle = & \sqrt{\frac{\Gamma(N_{12}+L_{12}+3/2)}{N_{12}!\nu_{12}^{L_{12}}}}\sqrt{\frac{\Gamma(n_3+l_3+3/2)}{n_3!\nu_3^{l_3}}} \\ & \times \sqrt{\frac{\Gamma(N'_{12}+L'_{12}+3/2)}{N'_{12}!\nu_{12}^{'L'_{12}}}}\sqrt{\frac{\Gamma(n'_3+l'_3+3/2)}{n'_3!\nu_3^{'l'_3}}} \\ & \times \frac{2^{L_{12}+l_3+L'_{12}l'_3+2}}{b_1^3b_2^3}\langle p_{nl}q_{nl}|V_{3N}|p_{n'l'}q_{n'l'}\rangle . \end{aligned} \tag{8.23}$$

Calculationally, this approximation implies that we can substitute the four integrals that affect the product between HO radial wave functions and the matrix elements in Jacobi basis by interpolating those matrix elements to their values at discrete momenta given by $N_{12}$, $n_3$, $L_{12}$, $l_3$, $N'_{12}$, $n'_3$, $L'_{12}$, and $l'_3$.

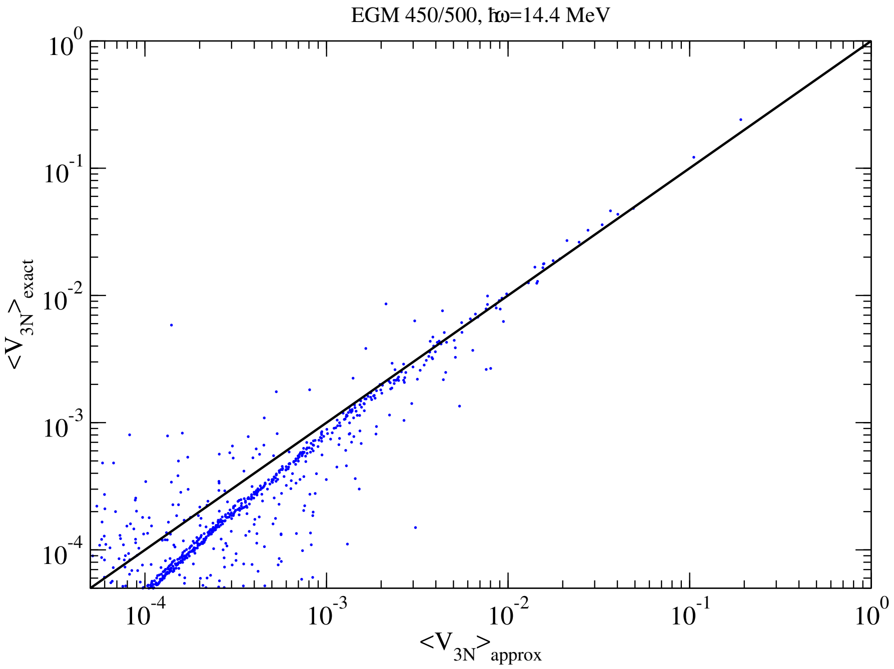

**Figure 8.5:** Comparison between exact HO three-body matrix elements ($\langle V_{3N}\rangle_{\text{exact}}$) and matrix elements calculated within this approximation ($\langle V_{3N}\rangle_{\text{approx}}$). Only the largest matrix elements are shown. The solid line x = y is shown to guide the eye.

### 8.2.3 Benchmarks of matrix elements

Fig. 8.5 shows an example of the comparison between the diagonal eigenvalues of the matrix elements calculated using the exact form of the harmonic oscillator radial wave function ($\langle V_{3N}\rangle_{\text{exact}}$) and those calculated with help of the approximation discussed above ($\langle V_{3N}\rangle_{\text{approx}}$) for the 450/500 Hamiltonian (see Sec. 2.3.4). In the following, we will just refer to them as $\Lambda/\tilde{\Lambda}$ Hamiltonians. In this comparison we show matrix elements with total three-body angular momentum $\mathscr{J}$ up to 7/2, three-body isospin $\mathscr{T} = 1/2$ and positive parity, using an arbitrary HO frequency $\hbar\omega = 14.4$ MeV.

As it can be seen in the plot, there is good agreement between these two approaches, specially for the largest (and most relevant) matrix elements. This behavior is also seen for different Hamiltonians and different HO frequencies, even if they are not explicitly shown in this work. Although the dots start to systematically deviate from the $x = y$ line as they become smaller, we will estimate in the following section the validity of this approximation for the calculation of physical observables, such as binding energies.

### 8.2.4 Triton binding energy

To test this approximation, it is possible to perform calculations for the ground state energy of triton using matrix elements calculated as in Eq. (8.23) and compare them with exact calculations. In this context, "exact" means that the results are obtained using the exact form of the harmonic oscillator wave function. All energies are obtained solving the Faddeev equations [38]. For more information on the Hamiltonians used here, see Sec. 2.3.4.

Figures 8.6 and 8.7 show results for the energy performed keeping the exact matrix elements for the low lying states of the system and using approximated matrix elements beyond a certain cut $\tilde{N} = 2N + L + 2n_3 + l_3$. Each figure contains two panels with different Hamiltonians: 450/500 and

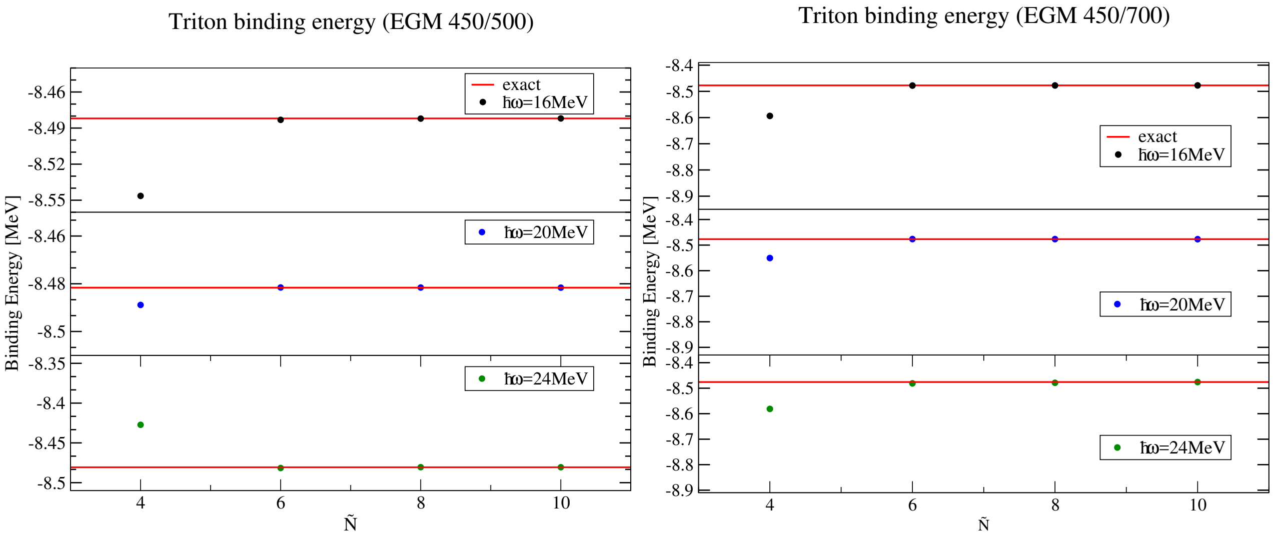

**Figure 8.6:** Triton binding energy as a function of $\tilde{N} = 2N_{12} + L_{12} + 2n_3 + l_3$ for 450/500 (left) and 450/700 (right) Hamiltonians. All states with $\tilde{N}$ higher than the corresponding in the plot use the approximation for the HO wave function. Each panel shows three subplots for different values of $\hbar\omega$: 16 (top), 20 (middle), and 24 MeV (bottom). In all cases the red horizontal line represents the exact calculation.

450/700 in Fig. 8.6, and 550/600 and 600/500 in Fig. 8.7. At the same time, each panel is divided in three subplots that explore the dependence in $\hbar\omega$ for 16, 20, and 24 MeV.

It can be seen in all cases that the convergence pattern towards the exact value of the energy (depicted by a red line) depends weakly on $\hbar\omega$. Also, the errors of the approximation decreases fast for increasing $\tilde{N}$: we obtain errors that are smaller than 4% for a cut $\tilde{N} = 4$ and 1% for a cut $\tilde{N} = 6$ for all the Hamiltonians explored. Therefore, this benchmark opens the possibility of working with a more general problem maintaining exact matrix elements for the lower states and approximating the rest of them. Varying the cut $\tilde{N}$ will enable us to work within the desired accuracy margin in each occasion.

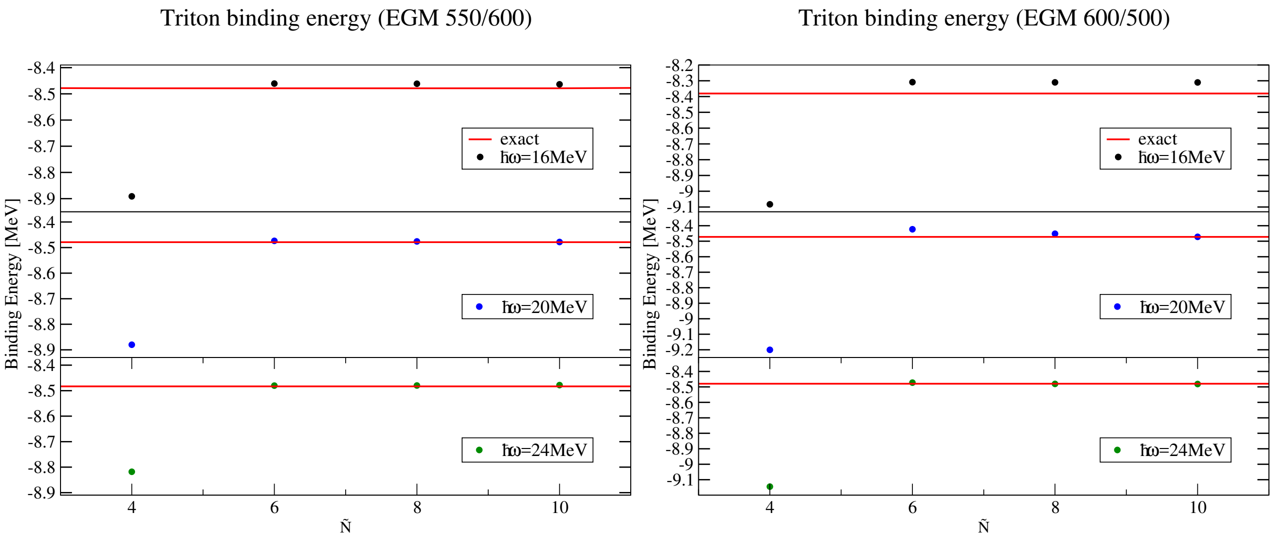

**Figure 8.7:** Caption as in Fig. 8.6 for 550/600 (left) and 600/500 (right) Hamiltonians.

Having confirmed the validity of this approximation for calculations of observables, this approach can be incorporated in Eq. (7.39) to estimate the functions $R_{n_c l_c}$. We expect that the impact of this substitution will be minimal in the case normal-ordered two-matrix elements with heavier nuclei as reference states (like, e.g., $^{100}$Sn), and that it will render a convergence towards the exact value of observables similar as the behavior seen for the binding energy of triton.

## 8.3 Applications to chiral shell-model interactions

Results presented in this section are an application of the transformation introduced in Sec. 7.6.3. This study was published in Ref. [29].

In order to perform calculations in the nuclear shell model [178–180], one requires an effective Hamiltonian that describes the interactions among nucleons in the valence space under consideration.

Valence-space Hamiltonians are developed mainly using two approaches, which typically consist of single-particle energies (SPEs) and two-body matrix elements (TBMEs): one can either use phenomenological approaches, where an effective interaction is constructed in a specific valence space by fitting free parameters. Alternatively one can use the TBMEs and SPEs directly as fit parameters starting from realistic few-body interactions. A prominent example of the second approach are the universal *sd*-shell (USD) interactions of Ref. [181]. These approaches (see, e.g., Refs. [178, 179] for reviews) typically lead to shell-model interactions that reproduce the experimental data with a root-mean-square (RMS) deviation of only a few hundred keV.

Second, valence-space Hamiltonians can be derived using modern *ab initio* methods, which can then be used in shell-model calculations. These methods do not achieve the same overall accuracy as the phenomenological fits, but they can provide uncertainty estimates.

Because the pion-exchange interactions describe long-range physics, which is not renormalized in the medium, we take the long-range pion-exchange contributions directly as in free-space nuclear forces [182,183]. The short-range contact interactions encode physics beyond the degrees of freedom resolved in the EFT and therefore, for chiral shell-model interactions these are fitted directly to data in the *sd* shell. Since in the valence space, the presence of the core breaks Galilean invariance, novel short-range operators that depend on the two-body center-of-mass degrees of freedom will arise. They enter at NLO in Weinberg counting, and we explore them for the first time in shell-model interactions.

In this Section, we will show the applications of valence-space Hamiltonians in the *sd* shell based on chiral EFT operators up to NLO (published in [29]). LECs are fitted to 441 ground- and excited-state energies in this model space. The LECs absorb in-medium effects due to the truncation of the model space. We will show the significance of the novel CM-dependent operators through the construction of a full valence-space (vs) interactions. We also compare our chiral shell-model interactions with the USD interactions from Ref. [181]. Moreover, we explore order-by-order uncertainty estimates and show promising predictions for neutron-rich isotopes beyond the fitted data set.

### Operators from chiral EFT

As seen in Sec. 2.3.2, there are two LECs at LO and seven new LECs at NLO: $C_S$ and $C_T$, and $C_1$–$C_7$, respectively. All of the corresponding operatorial structures in momentum space depend on $\mathbf{p}$ and/or $\mathbf{k}$.

The additional operators in the valence space, due to broken Galilean invariance by the presence of the core, depend explicitly on the two-body CM momentum $\mathbf{P} = \mathbf{p}_1 + \mathbf{p}_2$. We count powers of $\mathbf{P}$ as powers of $Q$, as they are set by the same scale (the inverse oscillator length) in a shell-model basis. Thus, the first contributions from these operators arise at NLO. We label the CM-dependent part of

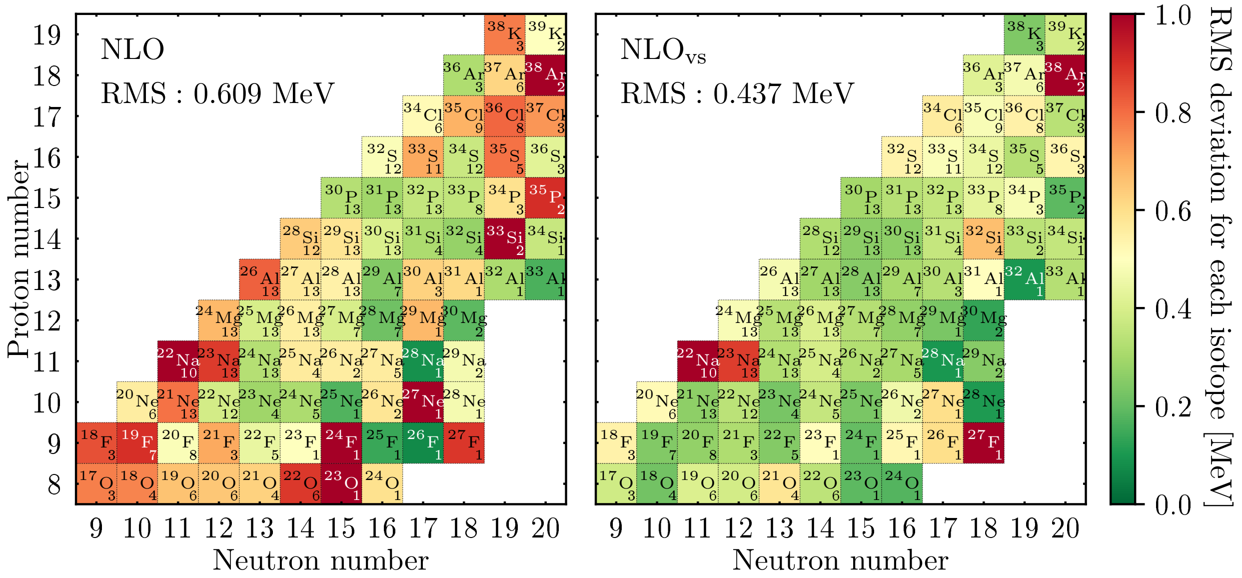

**Figure 8.8:** Graphical representation of the RMS deviation from experiment for each fitted nucleus in the *sd* shell. The figure shows the results for the charge-dependent (CD) chiral shell-model interactions NLO (left) and $\mathrm{NLO}_{vs}$ (right). The color coding of the RMS deviation is given in the bar on the right. Isotopes with a small RMS deviation are colored green, while those with a large deviation are colored red. Each square shows the isotope label and the number of fitted states in the bottom right corner. The total RMS deviation is given on the upper left side of each panel. The text color changes from black to white for RMS deviations larger than 0.7 MeV. Figure adapted from Ref. [29].

the contact interactions as $\mathrm{NLO_{vs}}$, where vs is short for valence space. These take the following form in momentum space:

$$\begin{aligned}\langle \mathbf{p},\mathbf{P}|V_{\text{cont}}^{(\mathrm{NLO_{vs}})}|\mathbf{p}',\mathbf{P}\rangle &= P_1\mathbf{P}^2 + P_2\mathbf{P}^2\sigma_1\cdot\sigma_2 \\ &\quad + P_3\,\mathrm{i}(\sigma_1-\sigma_2)\cdot(\mathbf{q}\times\mathbf{P}) \\ &\quad + P_4(\sigma_1\times\sigma_2)\cdot(\mathbf{k}\times\mathbf{P}) \\ &\quad + P_5(\sigma_1\cdot\mathbf{P})(\sigma_2\cdot\mathbf{P})\,. \end{aligned} \tag{8.24}$$

The CM-dependent interactions include central parts, given by the LECs $P_1$ and $P_2$, the difference- and cross-vector operators determined by $P_3$ and $P_4$, and a CM tensor operator, given by $P_5$. The latter three have been introduced and discussed in the context of noncentral interactions in Fermi liquid theory [184]. The central and tensor parts are diagonal in two-body spin $S$, relative orbital angular momentum $L$, and total angular momentum $J$. Moreover, the central parts are diagonal in CM angular momentum $L_{cm}$.

The difference- and cross-vector operators are spin-violating [184] and mix spin-singlet ${}^1S_0$ (${}^1P_1$) with spin-triplet ${}^3P_j$ (${}^3S_1$) relative partial waves. At $\mathrm{NLO_{vs}}$, they do not contribute to higher $L$ waves. As a result of the $S$-$P$ mixing and parity conservation, the spin-violating interactions also change the CM angular momentum $L_{cm}, L'_{cm}$ and are not necessarily diagonal in $J, J'$. In the shell-model context, their structure is similar to the anti-symmetric spin-orbit interaction (see, e.g., Ref. [185]).

A detailed explanation of the fit of these new LECs and the determination of the interactions can be found in chapters 7 and 8 of Ref. [186].

The influence of the center-of-mass operators at NLO can be seen in Fig. 8.8, where the RMS deviation from experiment for each fitted nucleus in the $sd$ shell for the chiral shell-model interactions at NLO (left), and $\mathrm{NLO}_{\mathrm{vs}}$ (right) is shown. The RMS deviation is given by a color coding that ranges from 0 MeV (green) to 1 MeV (red) and is calculated as

$$\mathrm{RMS} = \sqrt{\frac{1}{N}\sum_{i=1}^{N}\left(E_i^{\mathrm{exp}} - E_i^{\mathrm{th}}\right)^2}\,. \tag{8.25}$$

The results show a striking improvement when the valence space operators are included. At $\mathrm{NLO}_{\mathrm{vs}}$, there are only a few outliers with large RMS deviations. This demonstrates the large impact of the new operators.

In Ref. [29] we also studied predictions for excited states of neutron-rich nuclei beyond the fitted data set. Fig. 8.9 shows the spectra of neutron-rich oxygen, fluorine, and neon isotopes. Only the first excited state in $^{26}$Ne was included in the fit. All remaining states are predictions of the chiral shell-model interactions. Because our calculations do not include the continuum, we emphasize this by showing the neutron separation energy $S_n$. For states close to or above $S_n$, the explicit inclusion of the continuum will lead to changes, which are often of the order of few hundred keV unless this is further resonantly enhanced.

In comparison to measured states, the chiral shell-model interactions at $\mathrm{NLO}_{\mathrm{vs}}$ again lead to the best overall agreement, and there is generally an improvement in going from LO to NLO to $\mathrm{NLO}_{\mathrm{vs}}$. For the oxygen isotopes this is especially visible in $^{23,24}$O. Moreover, all our interactions reproduce the first $2^+$ energy in $^{26}$O recently measured at RIKEN [187]. This state is especially impressive, since neither the ground-state energy, nor the excitation energy was used in our dataset, and the order-by-order behavior is very stable. The agreement of our chiral shell-model interaction predictions at $\mathrm{NLO}_{\mathrm{vs}}$ is also very good for the fluorine isotopes, especially for the low-lying states known, and for all neon isotopes shown.

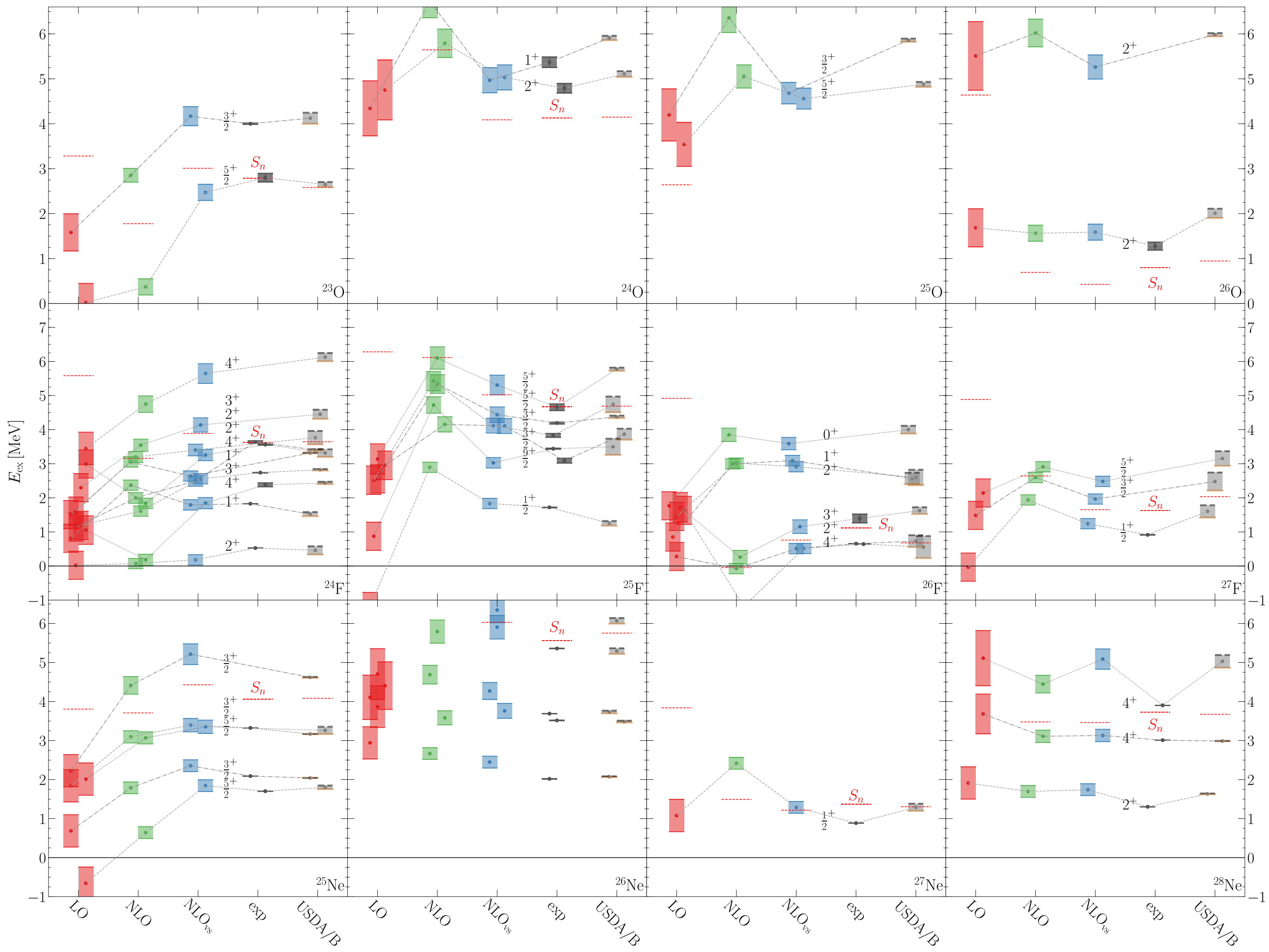

**Figure 8.9:** Predictions of excited states in oxygen, fluorine, and neon isotopes. In addition to the ENSDF [188] spectra, we compare our results to experimental data in $^{23}$O [189, 190], $^{26}$O [187], $^{24}$F [191], and $^{25,26}$F [192, 193]. Moreover, to emphasize the effects of the continuum, not included in our calculation, we give the calculated and experimental neutron separation energy $S_n$ as horizontal dashed line.

# 9 Summary and outlook

In the first part of this thesis, we have presented a first study of constructing nucleus-nucleus potentials from local chiral $NN$ interactions [114, 115] using the double-folding method applied to the $^{16}$O–$^{16}$O system. Our results show that for soft cutoffs, $R_0 \gtrsim 1.4$ fm, the resulting double-folding potential exhibits a systematic order-by-order behavior expected in EFT and a weak cutoff dependence on the details of the $NN$ interactions used, which suggests that the scattering observables do not depend strongly on the short-range physics. These features carry through to the elastic scattering cross section and the $S$-factor for the fusion reaction. In order to solve the elastic scattering problem through the optical model, we assumed the imaginary part of the potential to be proportional to its real part, obtained through the double-folding procedure [83]. The sensitivity of the cross sections to the imaginary part is large, providing the most uncertainty in our results. We also evaluated the influence of the nucleon density of the colliding nuclei in elastic scattering by using more realistic density profiles obtained from electron-scattering measurements [151]. The results indicate that the density choice has a larger impact at large angles and colliding energies, even though the impact of the imaginary part is larger in most of the cases.

We have focused on the $^{16}$O–$^{16}$O reactions, because these have been accurately measured and are well studied theoretically [79, 137–149]. In all cases, a good agreement with the data has been obtained without any fitting parameter. Our results thus suggest that the idea to derive nucleus-nucleus potentials using the double-folding method based on local chiral EFT interactions is very promising.

Aside from double-folding potentials from $NN$ interactions, we have also presented first steps on the exploration of the impact of $3N$ forces on nucleus-nucleus interactions. To that end, we have calculated the direct part of the triple-folding potential, and made an estimation of the impact of the exchange part. Even though the contribution of the direct part is small, the determination of the exact impact of the exchange part of the potential is crucial to assess the role of $3N$ forces from chiral EFT, and this investigation should be pursued in the future.

We consider this a first step in a more fundamental description of nucleus-nucleus potentials, but there are several directions how the calculations can be improved, both at the level of the input interactions and the many-body folding method. First, we need to refine the imaginary part of the potential, since this provides the largest uncertainty observed in our tests. Assuming it to be proportional to the double-folding potential provides a first estimate, but it is clear that this can be improved. Comparisons with phenomenological potentials [79] can also provide tests towards more realistic prescriptions, such as, e.g., the introduction of a surface-like term. The imaginary part of the potential can also be obtained from its real part using dispersion relations [194]. In a calculation beyond Hartree-Fock, an imaginary part as well as nonlocal contributions would arise (see, e.g., Refs. [195, 196]). Moreover, going beyond the level of the density-matrix expansion considered here, there will be gradient corrections [135] (i.e., surface terms) to the double-folding potential. At the same time, it is necessary to estimate the impact of three-body forces, performing the computation of the exchange correction at N$^2$LO.

Parallel to these improvements, it is also necessary and interesting to study different systems that involve open-shell and heavier nuclei.

In conclusion, coupling chiral EFT interactions with the double-folding method provides nucleus-nucleus potentials that lead to very encouraging agreement with elastic-scattering and fusion data in a broad range of energies. This idea is thus a promising first step towards the construction of microscopic optical potentials from first principles with control over uncertainty estimates. Through the above future developments, we hope to improve this new method to obtain a systematic way to build efficient optical potentials for nuclear reactions.

In the second part of this thesis, we have presented a novel approach to calculate effective two-body matrix elements from $3N$ interactions in momentum representation [102, 109]. Since three-body matrix elements are stored in Jacobi basis, we take advantage of this fact by performing the normal ordering directly in this representation. In order to do so, we choose a harmonic-oscillator representation for the particle in the reference state. In contrast to the usual normal ordering, where the center-of-mass is not coupled in the relative bases, this approach takes into account both degrees of freedom explicitly in all the steps of the procedure. For this reason, the subsequent transformations of the effective matrix elements harmonic-oscillator single-particle basis (Talmi-Moshinsky transformation [168, 169]) have to account for center-of-mass quantum numbers as well.

We have presented results for matrix elements with partial waves that include up to $\bar{L}^{\max} = \bar{L}^{\max}_{cm} = 4$ and $\bar{J}^{\max} = 3$, with three-body angular momentum $\mathscr{J}^{\max} = 5/2$. The benchmarks of these were performed for all different topologies of $3N$ interactions at N$^2$LO separately. They show clear convergence towards the reference value (obtained in the conventional normal ordering manner in single-particle basis) when $\bar{L}^{\max}$ and $\bar{L}^{\max}_{cm}$ are increased. Furthermore, benchmarks for the ground-state energy and the charge radius of $^{16}$O from IM-SRG show that including these matrix elements gives values that differ from the reference calculations by less than 0.3% when considering energy cuts of $e_{\max}/E_{3\max} = 6/14$ in all cases. The reference values include normal ordering matrix elements obtained in single-particle basis, without applying any cut to the orbital angular momenta of the partial waves involved in the calculation, and using $\bar{J}^{\max} = 8$ for partial waves with $\mathscr{J}^{\max} = 5/2$ (partial waves up to $\mathscr{J}^{\max} = 9/2$ are included, with different $\bar{J}^{\max}$ cuts).

One of the main advantages of this novel normal ordering method is that it allows to increase the cut in $E_{3\max}$ by increasing the harmonic-oscillator energy quantum numbers ($\bar{N}$, $\bar{N}_{cm}$) with very little computational cost, thus increasing the model space beyond the energies that are currently feasible to achieve with normal ordering in single-particle basis. This would make this approach especially promising for calculations involving heavy nuclei. However, due to the large number of partial waves that a combination of relative and center-of-mass quantum numbers generates, increasing the orbital quantum numbers is not so trivial in terms of memory needs and run time. This is a limitation that needs to be studied and circumvented, but that does not diminish the validity of this proof-of-principle.

We have also presented an approximation for harmonic-oscillator radial wave functions testing the agreement of such with exact calculations at three-body matrix-element level and against values of the triton-binding energy for different Hamiltonians. These benchmarks confirm the validity of this approximation for large $n$, and make it a candidate to be included in calculations of normal-ordered matrix-elements with heavy nuclei as reference states.

Finally, since they benefit from the transformation we have used for this novel normal ordering approach, results for $sd$-shell Hamiltonians constructed from chiral EFT have also been presented. These Hamiltonians are determined by fitting low-energy constants to include the effect of valence space-contributions, and hence they account for Galilean invariance breaking by the core present in the shell-model framework. For this reason, the valence-space operators depend explicitly on the two-body center-of-mass momentum. In order to account for these effects, the LECs were fitted to 441 ground- and excited-state energies in this model space. We presented the root mean square (RMS) deviation from experiment for fitted nuclei in the $sd$-shell for Hamiltonians at NLO with and without valence-space operators (which we call $\mathrm{NLO_{vs}}$), which clearly exemplifies the importance of the latter. Spectra containing excited states for neutron-rich isotopes beyond the fitted data set are also shown. We compare predicted excitation energies of oxygen, fluorine, and neon isotopes obtained with chiral potentials at LO, NLO, and $\mathrm{NLO_{vs}}$ against those calculated with USDA/B interactions [181] and experimental data from ENSDF [188]. In comparison to measured states, the chiral shell-model interactions at $\mathrm{NLO_{vs}}$ lead to the best overall agreement for those cases, being able to also reproduce the correct order of the excited states.

Now that the validity of this approach to the calculation of normal-ordered matrix elements has been tested, there are several paths to follow for its implementation in calculations of heavy nuclei observables: on one hand, it is necessary to study the impact of a larger model space obtained by increasing $\bar{N}$ and $\bar{N}_{cm}$, to determine the importance of $\bar{L}$ and $\bar{L}_{cm}$ in future implementations. Another step towards the calculation of heavy nuclei observables is the implementation of a more realistic reference state, such as Hatree-Fock. From Eq. (7.39) it can be seen that replacing the functions $R_{n_c l_c}$ by Hartree-Fock occupation states would achieve this goal.

On the other hand, one of the most urgent aspects is the optimization of the run time needed to compute the normal ordering matrix elements, in order to include partial waves with higher $\bar{J}$, and use heavier nuclei as the reference state. This bottleneck could be circumvented by implementing additional prestorage of the functions involved int he calculation, as well as exploring different integration methods, such as an adaptive Monte-Carlo integrator (e.g., Vegas) following the idea of what was done in Ref. [197]. In conclusion, we have presented a first approach that opens the door towards calculations of heavy nuclei properties in large model spaces, which is necessary for comparison with experiment.

# Bibliography

[1] E. Rutherford, The scattering of alpha and beta particles by matter and the structure of the atom, Phil. Mag. 21 (1911) 669.

[2] J. Chadwick, Possible Existence of a Neutron, Nature 129 (1932) 312.

[3] C. F. von Weizsäcker, Zur Theorie der Kernmassen, Z. Phys. 96 (1935) 431.

[4] H. A. Bethe, R. F. Bacher, Nuclear Physics A. Stationary States of Nuclei, Rev. Mod. Phys. 8 (1936) 82.

[5] H. Yukawa, On the Interaction of Elementary Particles I, Proc. Phys. Math. Soc. Jap. 17 (1935) 48, [Prog. Theor. Phys. Suppl.1,1(1935)].

[6] V. G. J. Stoks, R. A. M. Klomp, M. C. M. Rentmeester, J. J. de Swart, Partial wave analaysis of all nucleon-nucleon scattering data below 350 MeV, Phys. Rev. C 48 (1993) 792.

[7] V. G. J. Stoks, R. A. M. Klomp, C. P. F. Terheggen, J. J. de Swart, Construction of high quality $NN$ potential models, Phys. Rev. C 49 (1994) 2950.

[8] R. B. Wiringa, V. G. J. Stoks, R. Schiavilla, Accurate nucleon-nucleon potential with charge independence breaking, Phys. Rev. C 51 (1995) 38.

[9] R. Machleidt, High precision, charge dependent Bonn nucleon-nucleon potential, Phys. Rev. C 63 (2001) 024001.

[10] R. Machleidt, Q. MacPherson, E. Marji, R. Winzer, C. Zeoli, D. R. Entem, Recent Progress in the Theory of Nuclear Forces, Few Body Syst. 54 (2013) 821.

[11] S. K. Bogner, A. Schwenk, R. J. Furnstahl, A. Nogga, Is nuclear matter perturbative with low-momentum interactions?, Nucl. Phys. A 763 (2005) 59.

[12] H.-W. Hammer, A. Nogga, A. Schwenk, Three-body forces: From cold atoms to nuclei, Rev. Mod. Phys. 85 (2013) 197.

[13] J. W. Holt, N. Kaiser, W. Weise, Nuclear chiral dynamics and thermodynamics, Prog. Part. Nucl. Phys. 73 (2013) 35.

[14] J. Fujita, H. Miyazawa, Pion Theory of Three-Body Forces, Prog. Theor. Phys. 17 (1957) 360.

[15] S. Weinberg, Phenomenological Lagrangians, Physica A 96 (1979) 327.

[16] S. Weinberg, Nuclear forces from chiral Lagrangians, Phys. Lett. B 251 (1990) 288.

[17] S. Weinberg, Effective chiral Lagrangians for nucleon-pion interactions and nuclear forces, Nucl. Phys. B 363 (1991) 3.

[18] E. Epelbaum, H. Krebs, U.-G. Meißner, Improved chiral nucleon-nucleon potential up to next-to-next-to-next-to-leading order, Eur. Phys. J. A 51 (2015) 53.

[19] S. Binder, A. Calci, R. J. Furnstahl, J. Golak, K. Hebeler, H. Kamada, H. Krebs, J. Langhammer, S. Liebig, P. Maris, et al., Few-nucleon systems with state-of-the-art chiral nucleon-nucleon forces, Phys. Rev. C 93 (2016) 044002.

[20] J. Erler, N. Birge, M. Kortelainen, W. Nazarewicz, E. Olsen, A. M. Perhac, M. Stoitsov, The limits of the nuclear landscape, Nature 486 (2012) 509.

[21] S. R. Beane, E. Chang, S. D. Cohen, W. Detmold, H. W. Lin, T. C. Luu, K. Orginos, A. Parreño, M. J. Savage, A. Walker-Loud, Light Nuclei and Hypernuclei from Quantum Chromodynamics in the Limit of SU(3) Flavor Symmetry, Phys. Rev. D 87 (3) (2013) 034506.

[22] A. Parreño, Lattice QCD calculations for nuclear physics, AIP Conf. Proc. 1606 (2014) 226.

[23] J. Carlson, S. Gandolfi, F. Pederiva, S. C. Pieper, R. Schiavilla, K. E. Schmidt, R. B. Wiringa, Quantum Monte Carlo methods for nuclear physics, Rev. Mod. Phys. 87 (2015) 1067.

[24] T. T. S. Kuo, G. E. Brown, Structure of finite nuclei and the free nucleon-nucleon interaction: An application to $^{18}$O and $^{18}$F, Nucl. Phys. 85 (1) (1966) 40.

[25] L. Coraggio, A. Covello, A. Gargano, N. Itaco, T. T. S. Kuo, D. R. Entem, R. Machleidt, Microscopic nuclear structure based upon a chiral NN potential, Phys. Rev. C 66 (2002) 021303.

[26] M. Bender, P.-H. Heenen, P.-G. Reinhard, Self-consistent mean-field models for nuclear structure, Rev. Mod. Phys. 75 (2003) 121.

[27] K. Hebeler, J. D. Holt, J. Menéndez, A. Schwenk, Nuclear forces and their impact on neutron-rich nuclei and neutron-rich matter, Ann. Rev. Nucl. Part. Sci. 65 (2015) 457.

[28] T. Abe, P. Maris, T. Otsuka, N. Shimizu, Y. Utsuno, J. P. Vary, Monte Carlo Shell Model for ab initio nuclear structure, EPJ Web Conf. 66 (2014) 02001.

[29] L. Huth, V. Durant, J. Simonis, A. Schwenk, Shell-model interactions from chiral effective field theory, Phys. Rev. C 98 (2018) 044301.

[30] J. Bonnard, M. Grasso, D. Lacroix, Energy-density functionals inspired by effective-field theories: Applications to neutron drops, Phys. Rev. C 98 (3) (2018) 034319.

[31] G. Hagen, A. Ekström, C. Forssén, G. R. Jansen, W. Nazarewicz, T. Papenbrock, K. A. Wendt, S. Bacca, N. Barnea, B. Carlsson, et al., Neutron and weak-charge distributions of the $^{48}$Ca nucleus, Nature Phys. 12 (2) (2016) 186.

[32] T. Otsuka, T. Suzuki, J. D. Holt, A. Schwenk, Y. Akaishi, Three-Body Forces and the Limit of Oxygen Isotopes, Phys. Rev. Lett. 105 (2010) 032501.

[33] H. A. Bethe, B. H. Brandow, A. G. Petschek, Reference Spectrum Method for Nuclear Matter, Phys. Rev. 129 (1) (1963) 225.

[34] J. D. Holt, T. Otsuka, A. Schwenk, T. Suzuki, Three-body forces and shell structure in calcium isotopes, J. Phys. G: Nucl. Part. Phys. 39 (2012) 085111.

[35] F. Wienholtz, D. Beck, K. Blaum, C. Borgmann, M. Breitenfeldt, S. Cakirli, S. George, F. Herfurth, J. D. Holt, M. Kowalska, et al., Masses of exotic calcium isotopes pin down nuclear forces, Nature 498 (2013) 346.

[36] V. Somà, A. Cipollone, C. Barbieri, P. Navrátil, T. Duguet, Chiral two- and three-nucleon forces along medium-mass isotope chains, Phys. Rev. C 89 (2014) 061301(R).

[37] K. Hebeler, S. K. Bogner, R. J. Furnstahl, A. Nogga, A. Schwenk, Improved nuclear matter calculations from chiral low-momentum interactions, Phys. Rev. C 83 (2011) 031301(R).

[38] H. Witała, W. Glockle, A New form of three-body Faddeev equations in the continuum, Eur. Phys. J. A 37 (2008) 87.

[39] N. Barnea, W. Leidemann, G. Orlandini, State dependent effective interaction for the hyperspherical formalism, Phys. Rev. C 61 (2000) 054001.

[40] S. K. Bogner, T. T. S. Kuo, A. Schwenk, Model-independent low momentum nucleon interaction from phase shift equivalence, Phys. Rep. 386 (2003) 1.

[41] H. Feldmeier, T. Neff, R. Roth, J. Schnack, A Unitary correlation operator method, Nucl. Phys. A 632 (1998) 61.

[42] F. Wegner, Flow-equations for Hamiltonians, Annalen der Physik 506 (2) (1994) 77.

[43] F. J. Wegner, Flow equations for Hamiltonians, Nucl. Phys. Proc. Suppl. 90 (2000) 141.

[44] S. K. Bogner, R. J. Furnstahl, R. J. Perry, Similarity Renormalization Group for Nucleon-Nucleon Interactions, Phys. Rev. C 75 (2007) 061001(R).

[45] R. Roth, J. Langhammer, A. Calci, S. Binder, P. Navrátil, Similarity-Transformed Chiral $NN+3N$ Interactions for the Ab Initio Description of $^{12}$C and $^{16}$O, Phys. Rev. Lett. 107 (2011) 072501.

[46] R. Roth, A. Calci, J. Langhammer, S. Binder, Evolved Chiral $NN+3N$ Hamiltonians for Ab Initio Nuclear Structure Calculations, Phys. Rev. C 90 (2014) 024325.

[47] C. Drischler, A. Carbone, K. Hebeler, A. Schwenk, Neutron matter from chiral two- and three-nucleon calculations up to N$^3$LO, Phys. Rev. C 94 (2016) 054307.

[48] S. K. Bogner, R. J. Furnstahl, H. Hergert, M. Kortelainen, P. Maris, M. Stoitsov, J. P. Vary, Testing the density matrix expansion against ab initio calculations of trapped neutron drops, Phys. Rev. C 84 (2011) 044306.

[49] H. D. Potter, S. Fischer, P. Maris, J. P. Vary, S. Binder, A. Calci, J. Langhammer, R. Roth, Ab Initio study of neutron drops with chiral Hamiltonians, Phys. Lett.B 739 (2014) 445.

[50] P. Maris, J. P. Vary, A. Calci, J. Langhammer, S. Binder, R. Roth, $^{12}$C properties with evolved chiral three-nucleon interactions, Phys. Rev. C 90 (1) (2014) 014314.

[51] S. K. Bogner, H. Hergert, J. D. Holt, A. Schwenk, S. Binder, A. Calci, J. Langhammer, R. Roth, Nonperturbative shell-model interactions from the in-medium similarity renormalization group, Phys. Rev. Lett. 113 (2014) 142501.

[52] R. Wirth, D. Gazda, P. Navrátil, A. Calci, J. Langhammer, R. Roth, Ab Initio Description of p-Shell Hypernuclei, Phys. Rev. Lett. 113 (19) (2014) 192502.

[53] R. Wirth, D. Gazda, P. Navrátil, R. Roth, Hypernuclear No-Core Shell Model, Phys. Rev. C 97 (6) (2018) 064315.

[54] C. Stumpf, J. Braun, R. Roth, Importance-Truncated Large-Scale Shell Model, Phys. Rev. C 93 (2) (2016) 021301.

[55] G. Hagen, T. Papenbrock, D. J. Dean, M. Hjorth-Jensen, Medium-mass nuclei from chiral nucleon-nucleon interactions, Phys. Rev. Lett. 101 (2008) 092502.

[56] G. Hagen, M. Hjorth-Jensen, G. R. Jansen, R. Machleidt, T. Papenbrock, Continuum effects and three-nucleon forces in neutron-rich oxygen isotopes, Phys. Rev. Lett. 108 (2012) 242501.

[57] S. Binder, P. Piecuch, A. Calci, J. Langhammer, P. Navrátil, R. Roth, Extension of coupled-cluster theory with a noniterative treatment of connected triply excited clusters to three-body Hamiltonians, Phys. Rev. C 88 (5) (2013) 054319.

[58] S. Binder, J. Langhammer, A. Calci, P. Navrátil, R. Roth, Ab Initio calculations of medium-mass nuclei with explicit chiral 3N interactions, Phys. Rev. C 87 (2) (2013) 021303(R).

[59] S. Binder, J. Langhammer, A. Calci, R. Roth, Ab initio path to heavy nuclei, Phys. Lett. B 736 (2014) 119.

[60] K. Tsukiyama, S. K. Bogner, A. Schwenk, In-medium Similarity Renormalization Group for Nuclei, Phys. Rev. Lett. 106 (2011) 222502.

[61] H. Hergert, S. K. Bogner, S. Binder, A. Calci, J. Langhammer, et al., In-Medium Similarity Renormalization Group with Chiral Two- Plus Three-Nucleon Interactions, Phys. Rev. C 87 (2013) 034307.

[62] H. Hergert, S. K. Bogner, T. D. Morris, A. Schwenk, K. Tsukiyama, The In-Medium Similarity Renormalization Group: A Novel Ab Initio Method for Nuclei, Phys. Rept. 621 (2016) 165.

[63] H. Hergert, S. K. Bogner, T. D. Morris, A. Schwenk, K. Tsukiyama, The In-Medium Similarity Renormalization Group: A Novel Ab Initio Method for Nuclei, Phys. Rept. 621 (2016) 165.

[64] J. D. Holt, J. Menéndez, A. Schwenk, Chiral three-nucleon forces and bound excited states in neutron-rich oxygen isotopes, Eur. Phys. J. A 49 (2013) 39.

[65] J. D. Holt, J. Menéndez, J. Simonis, A. Schwenk, Three-nucleon forces and spectroscopy of neutron-rich calcium isotopes, Phys. Rev. C 90 (90) (2014) 024312.

[66] V. Somà, T. Duguet, C. Barbieri, Ab initio self-consistent Gorkov-Green's function calculations of semi-magic nuclei: Formalism at second order with a two-nucleon interaction, Phys. Rev. C 84 (2011) 064317.

[67] A. Cipollone, C. Barbieri, P. Navrátil, Isotopic chains around oxygen from evolved chiral two- and three-nucleon interactions, Phys. Rev. Lett. 111 (2013) 062501.

[68] T. Duguet, V. Somà, S. Lecluse, C. Barbieri, P. Navrátil, Ab initio calculation of the potential bubble nucleus $^{34}$Si, Phys. Rev. C 95 (3) (2017) 034319.

[69] E. Gebrerufael, A. Calci, R. Roth, Open-shell nuclei and excited states from multireference normal-ordered Hamiltonians, Phys. Rev. C 93 (3) (2016) 031301(R).

[70] E. Gebrerufael, K. Vobig, H. Hergert, R. Roth, Ab Initio Description of Open-Shell Nuclei: Merging No-Core Shell Model and In-Medium Similarity Renormalization Group, Phys. Rev. Lett. 118 (2017) 152503.

[71] H. Hergert, In-Medium Similarity Renormalization Group for Closed and Open-Shell Nuclei, Phys. Scripta 92 (2) (2017) 023002.

[72] A. Tichai, J. Langhammer, S. Binder, R. Roth, Hartree-Fock many-body perturbation theory for nuclear ground-states, Phys. Lett. B 756 (2016) 283.

[73] T. D. Morris, J. Simonis, S. R. Stroberg, C. Stumpf, G. Hagen, J. D. Holt, G. R. Jansen, T. Papenbrock, R. Roth, A. Schwenk, Structure of the lightest tin isotopes, Phys. Rev. Lett. 120 (15) (2018) 152503.

[74] P. Navrátil, S. Quaglioni, G. Hupin, C. Romero-Redondo, A. Calci, Unified ab initio approaches to nuclear structure and reactions, Phys. Scripta 91 (5) (2016) 053002.

[75] J. P. Vary, P. Maris, P. J. Fasano, M. A. Caprio, Perspectives on Nuclear Structure and Scattering with the Ab Initio No-Core Shell Model (2018). `arXiv:1804.10995`.

[76] M. Brandan, G. Satchler, The interaction between light heavy-ions and what it tells us, Phys. Rep. 285 (4) (1997) 143.

[77] C. J. Joachain, Quantum Collision Theory, North-Holland, Amsterdam, 1983.

[78] R. D. Woods, D. S. Saxon, Diffuse Surface Optical Model for Nucleon-Nuclei Scattering, Phys. Rev. 95 (1954) 577.

[79] D. T. Khoa, W. von Oertzen, H. G. Bohlen, F. Nuoffer, Study of diffractive and refractive structure in the elastic $^{16}$O+$^{16}$O scattering at incident energies ranging from 124 to 1120 MeV , Nucl. Phys. A 672 (2000) 387.

[80] G. Satchler, W. Love, Folding model potentials from realistic interactions for heavy-ion scattering, Phys. Rep. 55 (3) (1979) 183.

[81] C. Mahaux, R. Sartor, Families of strictly equivalent potentials for the elastic wavefunction, Nucl. Phys. A 530 (1991) 303.

[82] L. C. Chamon, B. V. Carlson, L. R. Gasques, D. Pereira, C. De Conti, M. A. G. Alvarez, M. S. Hussein, M. A. Candido Ribeiro, E. S. Rossi, Jr., C. P. Silva, Toward a global description of the nucleus-nucleus interaction, Phys. Rev. C 66 (2002) 014610.

[83] D. Pereira, J. Lubian, J. R. B. Oliveira, D. P. de Sousa, L. C. Chamon, An imaginary potential with universal normalization for dissipative processes in heavy-ion reactions, Phys. Lett. B 670 (2009) 330.

[84] T. Furumoto, W. Horiuchi, M. Takashina, Y. Yamamoto, Y. Sakuragi, Global optical potential for nucleus-nucleus systems from 50 MeV/u to 400 MeV/u, Phys. Rev. C 85 (2012) 044607.

[85] K. Minomo, M. Kohno, K. Ogata, Microscopic coupled-channels calculations of nucleus-nucleus scattering including chiral three-nucleon-force effects, Phys. Rev. C 93 (1) (2016) 014607.

[86] J. W. Holt, N. Kaiser, G. A. Miller, W. Weise, Microscopic optical potential from chiral nuclear forces, Phys. Rev. C 88 (2013) 024614.

[87] M. Vorabbi, P. Finelli, C. Giusti, Theoretical Optical Potential Derived From Nucleon-Nucleon Chiral Potentials, Phys. Rev. C 93 (3) (2016) 034619.

[88] J. Rotureau, P. Danielewicz, G. Hagen, F. M. Nunes, T. Papenbrock, Optical potential from first principles, Phys. Rev. C 95 (2017) 024315.

[89] A. Idini, C. Barbieri, P. Navrátil, Ab initio optical potentials and nucleon scattering on medium mass nuclei, Acta Phys. Pol. B 48 (2017) 273.

[90] M. Gell-Mann, A Schematic Model of Baryons and Mesons, Phys. Lett. 8 (1964) 214–215.

[91] G. Zweig, An SU(3) model for strong interaction symmetry and its breaking. Version 1.

[92] O. W. Greenberg, Spin and unitary-spin independence in a paraquark model of baryons and mesons, Phys. Rev. Lett. 13 (1964) 598.

[93] C. Patrignani, et al., Review of Particle Physics, Chin. Phys. C 40 (2016) 100001.

[94] K. G. Wilson, Confinement of quarks, Phys. Rev. D 10 (1974) 2445.

[95] C. Vafa, E. Witten, Parity Conservation in QCD, Phys. Rev. Lett. 53 (1984) 535.

[96] E. Klempt, Do parity doublets in the baryon spectrum reflect restoration of chiral symmetry?, Phys. Lett. B 559 (2003) 144.

[97] J. Goldstone, A. Salam, S. Weinberg, Broken Symmetries, Phys. Rev. 127 (3) (1962) 965.

[98] V. R. Pandharipande, D. R. Phillips, U. van Kolck, Delta effects in pion-nucleon scattering and the strength of the two-pion-exchange three-nucleon interaction, Phys. Rev. C 71 (2005) 064002.

[99] E. Epelbaum, Delta-Resonance Contributions To The Nuclear Force, eConf C 070910 (2007) 137.

[100] H. Krebs, E. Epelbaum, U.-G. Meißner, Nuclear forces with $\Delta$-excitations up to next-to-next-to-leading order. I. Peripheral nucleon-nucleon waves, Eur. Phys. J. A 32 (2007) 127.

[101] B. A. Lippmann, J. Schwinger, Variational Principles for Scattering Processes. I, Phys. Rev. 79 (1950) 469.

[102] E. Epelbaum, Nuclear Forces from Chiral Effective Field Theory: A Primer (2010).

[103] S. A. Coon, M. D. Scadron, Goldberger-Treiman discrepancy and the momentum variation of the pion-nucleon form factor and pion decay constant, Phys. Rev. C 23 (1981) 1150.

[104] R. Machleidt, F. Sammarruca, Chiral EFT based nuclear forces: Achievements and challenges, Phys. Scripta 91 (8) (2016) 083007.

[105] F. Sammarruca, L. E. Marcucci, L. Coraggio, J. W. Holt, N. Itaco, R. Machleidt, Nuclear and neutron matter equations of state from high-quality potentials up to fifth order of the chiral expansion (2018). `arXiv:1807.06640`.

[106] A. Nogga, P. Navrátil, B. R. Barrett, J. P. Vary, Spectra and binding energy predictions of chiral interactions for $^7$Li, Phys. Rev. C 73 (2006) 064002.

[107] P. Navrátil, V. G. Gueorguiev, J. P. Vary, W. E. Ormand, A. Nogga, Structure of $A = 10-13$ Nuclei with Two- Plus Three-Nucleon Interactions from Chiral Effective Field Theory, Phys. Rev. Lett. 99 (2007) 042501.

[108] P. Klos, A. Carbone, K. Hebeler, J. Menéndez, A. Schwenk, Uncertainties in constraining low-energy constants from$^3$H $\beta$ decay, Eur. Phys. J. A 53 (8) (2017) 168.

[109] K. Hebeler, H. Krebs, E. Epelbaum, J. Golak, R. Skibinski, Efficient calculation of chiral three-nucleon forces up to N$^3$LO for ab initio studies, Phys. Rev. C 91 (4) (2015) 044001.

[110] E. Epelbaum, W. Glöckle, U.-G. Meißner, The Two-nucleon system at next-to-next-to-next-to-leading order, Nucl. Phys. A 747 (2005) 362.

[111] E. Epelbaum, Few-nucleon forces and systems in chiral effective field theory, Prog. Part. Nucl. Phys. 57 (2006) 654.

[112] K. Hebeler, Momentum-space evolution of chiral three-nucleon forces, Phys. Rev. C 85 (2012) 021002(R).

[113] E. Epelbaum, private communication.

[114] A. Gezerlis, I. Tews, E. Epelbaum, S. Gandolfi, K. Hebeler, A. Nogga, A. Schwenk, Quantum Monte Carlo Calculations with Chiral Effective Field Theory Interactions, Phys. Rev. Lett. 111 (2013) 032501.

[115] A. Gezerlis, I. Tews, E. Epelbaum, M. Freunek, S. Gandolfi, K. Hebeler, A. Nogga, A. Schwenk, Local chiral effective field theory interactions and quantum Monte Carlo applications, Phys. Rev. C 90 (2014) 054323.

[116] P. Navrátil, Local three-nucleon interaction from chiral effective field theory, Few Body Syst. 41 (2007) 117.

[117] M. Piarulli, L. Girlanda, R. Schiavilla, R. N. Pérez, J. E. Amaro, et al., Minimally nonlocal nucleon-nucleon potentials with chiral two-pion exchange including $\Delta$ resonances, Phys. Rev. C 91 (2) (2015) 024003.

[118] V. Durant, P. Capel, L. Huth, A. B. Balantekin, A. Schwenk, Double-folding potentials from chiral effective field theory, Phys. Lett. B 782 (2018) 668.

[119] J. E. Lynn, I. Tews, J. Carlson, S. Gandolfi, A. Gezerlis, K. E. Schmidt, A. Schwenk, Quantum Monte Carlo calculations of light nuclei with local chiral two- and three-nucleon interactions, Phys. Rev. C 96 (5) (2017) 054007.

[120] L. Huth, I. Tews, J. E. Lynn, A. Schwenk, Analyzing the Fierz Rearrangement Freedom for Local Chiral Two-Nucleon Potentials, Phys. Rev. C 96 (5) (2017) 054003.

[121] J. E. Lynn, I. Tews, J. Carlson, S. Gandolfi, A. Gezerlis, K. E. Schmidt, A. Schwenk, Chiral Three-Nucleon Interactions in Light Nuclei, Neutron-$\alpha$ Scattering, and Neutron Matter, Phys. Rev. Lett. 116 (2016) 062501.

[122] B. D. Carlsson, A. Ekström, C. Forssén, D. F. Strömberg, G. R. Jansen, O. Lilja, M. Lindby, B. A. Mattsson, K. A. Wendt, Uncertainty analysis and order-by-order optimization of chiral nuclear interactions, Phys. Rev. X 6 (1) (2016) 011019.

[123] L. I. Schiff, Quantum Mechanics (Third Edition), McGraw-Hill Book Company, New York, 1968.

[124] M. Abramowitz, I. A. Stegun, Handbook of Mathematical Functions with Formulas, Graphs, and Mathematical Tables, Dover, New York, 1972.

[125] E. Feenberg, The Scattering of Slow Electrons by Neutral Atoms, Phys. Rev. 40 (1932) 40.

[126] M. Ostrofsky, G. Breit, D. P. Johnson, The excitation function of lithium under proton bombardment, Phys. Rev. 49 (1936) 22.

[127] H. A. Bethe, A continuum theory of the compound nucleus, Phys. Rev. 57 (1940) 1125.

[128] R. Serber, Nuclear reactions at high energies, Phys. Rev. 72 (1947) 1114.

[129] H. Leeb, H. Fiedeldey, R. Lipperheide, Optical potentials from the scattering cross section by inversion, Phys. Rev. C 32 (1985) 1223.

[130] N. F. Mott, The collision between Two Electrons, Proc. Roy. Soc. A 126 (1930) 259.

[131] C. H. Dasso, S. Landowne, A. Winther, Channel-coupling effects in heavy-ion fusion reactions, Nucl. Phys. A 405 (1983) 381.

[132] S. Landowne, S. C. Pieper, Coupled-channels fusion calculations for $\mathrm{Ni}^{58}+\mathrm{Ni}^{58}$, Phys. Rev. C 29 (1984) 1352.

[133] P. Capel, V. Durant, L. Huth, H. W. Hammer, D. R. Phillips, A. Schwenk, From ab initio structure predictions to reaction calculations via EFT, J. Phys. Conf. Ser. 1023 (1) (2018) 012010.

[134] S. Weber, Three-body forces and nucleus-nucleus interactions, B.Sc. thesis, Technische Universität Darmstadt (2017).

[135] J. W. Negele, D. Vautherin, Density-Matrix Expansion for an Effective Nuclear Hamiltonian, Phys. Rev. C 5 (1972) 1472.

[136] C. Fiolhais, F. Nogueira, M. A. L. Marques (Eds.), A Primer in Density Functional Theory, Vol. 620 of Lecture Notes in Physics, Springer-Verlag Berlin Heidelberg, 2003.

[137] E. Stiliaris, H. Bohlen, P. Fröbrich, B. Gebauer, D. Kolbert, W. von Oertzen, M. Wilpert, T. Wilpert, Nuclear rainbow structures in the elastic scattering of $^{16}$O on $^{16}$O at $E_L$=350 MeV, Phys. Lett. B 223 (3) (1989) 291.

[138] H. G. Bohlen, E. Stiliaris, B. Gebauer, W. von Oertzen, M. Wilpert, T. Wilpert, A. Ostrowski, D. T. Khoa, A. S. Demyanova, A. A. Ogloblin, Refractive scattering and reactions, comparison of two systems:$^{16}$O+$^{16}$O and $^{20}$Ne+$^{12}$C, Z. Phys. A 346 (3) (1993) 189.

[139] Y. Sugiyama, Y. Tomita, H. Ikezoe, Y. Yamanouchi, K. Ideno, S. Hamada, T. Sugimitsu, M. Hijiya, Y. Kondō, Observation of Airy oscillation for the $^{16}$O+$^{16}$O system at Elab = 145 MeV, Phys. Lett. B 312 (1) (1993) 35.

[140] Y. Kondō, Y. Sugiyama, T. Tomita, Y. Yamanouchi, H. Ikezoe, K. Ideno, S. Hamada, T. Sugimitsu, M. Hijiya, H. Fujita, Airy minimum crossing $\theta_{cm}=90$ at Elab = 124 MeV for the $^{16}$O + $^{16}$O system, Phys. Lett. B 365 (1) (1996) 17.

[141] G. Bartnitzky, A. Blazevic, H. G. Bohlen, J. M. Casandjian, M. Chartier, H. Clement, B. Gebauer, A. Gillibert, T. Kirchner, D. T. Khoa, et al., Model-unrestricted nucleus-nucleus scattering potentials from measurement and analysis of $^{16}$O+$^{16}$O scattering, Phys. Lett. B 365 (1) (1996) 23.

[142] F. Nuoffer, G. Bartnitzky, H. Clement, A. Blazevic, H. G. Bohlen, B. Gebauer, W. Von Oertzen, M. Wilpert, T. Wilpert, A. Lepine-Szily, et al., The equation of state for cold nuclear matter as seen in nucleus-nucleus scattering, Nuovo Cim. A 111 (8) (1998) 971.

[143] M. P. Nicoli, F. Haas, R. M. Freeman, N. Aissaoui, C. Beck, A. Elanique, R. Nouicer, A. Morsad, S. Szilner, Z. Basrak, et al., Elastic scattering of $^{16}$O+$^{16}$O at energies E/A between 5-MeV and 8-MeV, Phys. Rev. C 60 (1999) 064608.

[144] Y. Kondō, F. Michel, G. Reidemeister, A unique deep potential for the $^{16}$O+$^{16}$O system, Phys. Lett. B 242 (3) (1990) 340.

[145] I. Tserruya, Y. Eisen, D. Pelte, A. Gavron, H. Oeschler, D. Berndt, H. L. Harney, Total fusion cross section for the $^{16}$O+$^{16}$O system, Phys. Rev. C 18 (1978) 1688.

[146] G. Hulke, C. Rolfs, H. P. Trautvetter, Comparison of the fusion reactions $^{12}$C+$^{20}$Ne and $^{16}$O+$^{16}$O near the Coulomb barrier, Z. Phys. A 297 (2) (1980) 161.

[147] S.-C. Wu, C. Barnes, Fusion and elastic scattering cross sections for the $^{16}$O+$^{16}$O reactions near the Coulomb barrier, Nucl. Phys. A 422 (2) (1984) 373.

[148] A. Kuronen, J. Keinonen, P. Tikkanen, Cross section of $^{16}$O+$^{16}$O near the Coulomb barrier, Phys. Rev. C 35 (1987) 591.

[149] J. G. Duarte, L. R. Gasques, J. R. B. Oliveira, V. A. B. Zagatto, L. C. Chamon, N. Medina, N. Added, W. A. Seale, J. A. Alcántara-Núñez, E. S. Rossi, Jr., et al., Measurement of fusion cross sections for $^{16}$O+$^{16}$O, J. Phys. G 42 (6) (2015) 065102.

[150] J. Hoppe, C. Drischler, R. J. Furnstahl, K. Hebeler, A. Schwenk, Weinberg eigenvalues for chiral nucleon-nucleon interactions, Phys. Rev. C 96 (5) (2017) 054002.

[151] H. D. Vries, C. D. Jager, C. D. Vries, Nuclear charge-density-distribution parameters from elastic electron scattering, Atomic Data and Nuclear Data Tables 36 (3) (1987) 495.

[152] K. Hagino, N. Takigawa, Subbarrier fusion reactions and many-particle quantum tunneling, Prog. Theor. Phys. 128 (2012) 1061.

[153] D. Baye, N. Pecher, Microscopic investigation of the $^{12}$C+$^{12}$C interaction, Nucl. Phys. A 379 (1982) 330.

[154] K. Hagino, N. Rowley, A. T. Kruppa, A Program for coupled channels calculations with all order couplings for heavy ion fusion reactions, Comput. Phys. Commun. 123 (1999) 143.

[155] I. J. Thompson, F. M. Nunes, Nuclear Reactions for Astrophysics: Principles, Calculation and Applications of Low-Energy Reactions, Cambridge University Press, 2009.

[156] C. Y. Wong, Interaction Barrier in Charged-Particle Nuclear Reactions, Phys. Rev. Lett. 31 (1973) 766.

[157] G. C. Wick, The Evaluation of the Collision Matrix, Phys. Rev. 80 (1950) 268.

[158] R. Roth, S. Binder, K. Vobig, A. Calci, J. Langhammer, P. Navrátil, Medium-Mass Nuclei with Normal-Ordered Chiral NN+3N Interactions, Phys. Rev. Lett. 109 (2012) 052501.

[159] D. H. Gloeckner, R. D. Lawson, Spurious center-of-mass motion, Phys. Lett. B 53 (1974) 313.

[160] A. L. Fetter, J. D. Walecka, Quantum Theory of Many-Particle Systems, McGraw-Hill Book Company, New York, 1971.

[161] P. Navrátil, G. P. Kamuntavičius, B. R. Barrett, Few-nucleon systems in a translationally invariant harmonic oscillator basis, Phys. Rev. C 61 (2000) 044001.

[162] P. Navrátil, W. E. Ormand, Ab initio shell model with a genuine three-nucleon force for the $p$-shell nuclei, Phys. Rev. C 68 (2003) 034305.

[163] J. Langhammer, Chiral Three-Nucleon Interactions in Ab-Initio Nuclear Structure and Reactions, Technische Universität Darmstadt, Ph.D. thesis (2014).

[164] H. Hergert, S. K. Bogner, T. D. Morris, S. Binder, A. Calci, J. Langhammer, R. Roth, Ab initio multireference in-medium similarity renormalization group calculations of even calcium and nickel isotopes, Phys. Rev. C 90 (2014) 041302(R).

[165] K. Hebeler, A. Schwenk, Chiral three-nucleon forces and neutron matter, Phys. Rev. C 82 (2010) 014314.

[166] C. Drischler, K. Hebeler, A. Schwenk, Asymmetric nuclear matter based on chiral two- and three-nucleon interactions, Phys. Rev. C 93 (5) (2016) 054314.

[167] V. I. Lebedev, D. N. Laikov, A quadrature formula for the sphere of the 131st algebraic order of accuracy, Doklady Mathematics 59 (3) (1999) 477.

[168] I. Talmi, Nuclear spectroscopy with harmonic-oscillator wave functions, Helv. Phys. Acta 25 (1952) 185.

[169] M. Moshinsky, Transformation brackets for harmonic oscillator functions, Nucl. Phys. 13 (1959) 104.

[170] G. P. Kamuntavičius, R. K. Kalinauskas, B. R. Barrett, S. Mickevičius, D. Germanas, The general harmonic-oscillator brackets: compact expression, symmetries, sums and Fortran code, Nucl. Phys. A 695 (2001) 191.

[171] W. Magnus, On the exponential solution of differential equations for a linear operator, Commun. Pure Appl. Math. 7 (1954) 649.

[172] S. Blanes, F. Casas, J. Oteo, J. Ros, The magnus expansion and some of its applications, Phys. Rep. 470 (2009) 151.

[173] T. D. Morris, N. Parzuchowski, S. K. Bogner, Magnus expansion and in-medium similarity renormalization group, Phys. Rev. C 92 (2015) 034331.

[174] L. L. Foldy, S. A. Wouthuysen, On the Dirac theory of spin 1/2 particle and its nonrelativistic limit, Phys. Rev. 78 (1950) 29.

[175] J. L. Friar, J. Martorell, D. W. L. Sprung, Nuclear sizes and the isotope shift, Phys. Rev. A 56 (1997) 4579–4586.

[176] A. Kallio, On the relation between $t$-matrices in free scattering, nuclear matter and finite nuclei, Phys. Lett. 18 (1) (1965) 51.

[177] A. Erdélyi, Higher Transcendental Functions, Vol. 2, McGraw-Hill Book Company, New York, 1953.

[178] B. A. Brown, The nuclear shell model towards the drip lines, Prog. Part. Nucl. Phys. 47 (2001) 517.

[179] E. Caurier, G. Martinez-Pinedo, F. Nowacki, A. Poves, A. P. Zuker, The Shell model as unified view of nuclear structure, Rev. Mod. Phys. 77 (2005) 427.

[180] L. Coraggio, A. Covello, A. Gargano, N. Itaco, T. T. S. Kuo, Shell-model calculations and realistic effective interactions, Prog. Part. Nucl. Phys. 62 (2009) 135.

[181] B. A. Brown, W. A. Richter, New 'USD' Hamiltonians for the $sd$ shell, Phys. Rev. C 74 (2006) 034315.

[182] E. Epelbaum, H.-W. Hammer, U.-G. Meißner, Modern Theory of Nuclear Forces, Rev. Mod. Phys. 81 (2009) 1773.

[183] R. Machleidt, D. R. Entem, Chiral effective field theory and nuclear forces, Phys. Rep. 503 (2011) 1.

[184] A. Schwenk, B. Friman, Polarization contributions to the spin dependence of the effective interaction in neutron matter, Phys. Rev. Lett. 92 (2004) 082501.

[185] M. Conze, H. Feldmeier, P. Manakos, Special non-central forces for sd-shell nuclei, Phys. Lett. B 43 (1973) 101.

[186] L. Huth, Local interactions and shell-model interactions from chiral effective field theory, Ph.D. thesis, Technische Universität Darmstadt (2018).

[187] Y. Kondo, T. Nakamura, R. Tanaka, R. Minakata, S. Ogoshi, N. A. Orr, N. L. Achouri, T. Aumann, H. Baba, F. Delaunay, et al., Nucleus $^{26}$O : A Barely Unbound System beyond the Drip Line, Phys. Rev. Lett. 116 (10) (2016) 102503.

[188] http://www.nndc.bnl.gov/ensdf/.

[189] Z. Elekes, Z. Dombradi, N. Aoi, S. Bishop, Z. Fulop, et al., Spectroscopic Study of Neutron Shell Closures via Nucleon Transfer in the Near-Dripline Nucleus O-23, Phys. Rev. Lett. 98 (2007) 102502.

[190] A. Schiller, N. Frank, T. Baumann, D. Bazin, B. A. Brown, et al., Selective population and neutron decay of the first excited state of semi-magic O-23, Phys. Rev. Lett. 99 (2007) 112501.

[191] L. Cáceres, A. Lepailleur, O. Sorlin, M. Stanoiu, S. Sohler, Z. Dombradi, S. Bogner, B. A. Brown, H. Hergert, J. Holt, et al., Nuclear structure studies of $^{24}$F, Phys. Rev. C 92 (1) (2015) 014327.

[192] Z. Vajta, M. Stanoiu, D. Sohler, G. Jansen, F. Azaiez, et al., Excited states in the neutron-rich nucleus $^{25}$F, Phys. Rev. C 89 (5) (2014) 054323.

[193] M. Vandebrouck, A. Lepailleur, O. Sorlin, T. Aumann, C. Caesar, M. Holl, V. Panin, F. Wamers, S. R. Stroberg, J. D. Holt, et al., Effective proton-neutron interaction near the drip line from unbound states in $^{25,26}$F, Phys. Rev. C 96 (2017) 054305.

[194] R. V. Carlson, T. Frederico, M. S. Hussein, H. Esbensen, S. Landowne, Dispersion relation for effective interactions, IFUSP/P-802 (1989).

[195] H. Feshbach, Unified theory of nuclear reactions, Ann. Phys. 5 (4) (1958) 357.

[196] H. Feshbach, A unified theory of nuclear reactions. {II}, Ann. Phys. 19 (2) (1962) 287.

[197] C. Drischler, K. Hebeler, A. Schwenk, Chiral interactions up to N$^3$LO and nuclear saturation (2017). `arXiv:1710.08220`.

# Acknowledgments

*It is thanks to them*
*that I live in three dimensions,*
*in a non-lyrical and non-rhetorical space,*
*with a shifting, thus real, horizon.*
(Wisława Szymborska)

First of all, I want to thank Prof. Achim Schwenk for welcoming me in his group, his supervision and his help during these years. I am also deeply grateful for his encouragement and for all the opportunities that he gave me to present my research in schools, conferences, and workshops. Last, but in any case least, I want to thank him for the excellent human quality he showed throughout the process of my PhD studies.

I also want to thank Prof. Pierre Capel, for being always willing to help me and all the time he dedicated to it. All the detailed emails and pleasant discussions helped me understand a little bit better this world called nuclear reactions, encouraging me to always improve my scientific persona.

A big thank-you goes also to Dr. Kai Hebeler, who literally always made time to answer any questions, no matter how naive, with the same implication. Without him, more than half of this thesis would not have been possible.

Special thanks goes to Prof. Pierre Capel, Dr. Kai Hebeler, Dr. Toño Coello, Dr. Joel Lynn, Dr. Lukas Huth, and Prof. Achim Schwenk for proof reading my thesis.

Of course, I cannot forget to thank all the other persons that at some point collaborated with me: Lukas Huth, Jan Hoppe, Johannes Simonis, Joel Lynn, Sulamith Weber, and Baha Balantekin. Along with them, I also want to thank Prof. Artur Polls, and Dr. Isaac Vidaña, who were the first to guide me and help me get through the research world.

I want to make a special mention to Prof. Heiko Hergert for sharing with us the original Talmi code, and answering all our questions related with it.

I also want to acknowledge all the people in the strongint group, who have, directly or indirectly, inspired me: Alex, Arianna, Toño, Christian, Svenja, Jan, Lukas, Philipp, Sebastian, Thomas, Joel, Javier, Sabrina, Marc, Rodric, Johannes, Ingo, Corbinian, Kyle, and Lars.

Talking about inspiration, I cannot forget to mention and thank all the other people at the TU who have also brought it to me in one way or another: Prof. Almudena Arcones, Prof. Hans-Werner Hammer, Samuel Giuliani, Marc Leonhardt, Stefan Schulz, Christina Stumpf, Guillermo Fernández, amongst others that I have been selfish enough to not remember in this moment.

Being lucky to be here, I was also lucky to have time for friendship. Toño, thanks for listening to my complaints, for the coffee breaks, for the soup-escapades, and for all your support. Samu, thanks for all the philosophical talks, flying across half a continent to visit me in Seattle, always having a smile, and (again) for being an inspiration for me. Lukas and Sabrina, thank you for always inviting me on Wednesdays, even though I many times declined, and for being honest friends. Michael, thanks for suffering through the Softskills with me, and for making that our (sometimes sparse) meetings always feel like we had just met yesterday.

To the people who are not here with me: Irene, Miriam, Rubén, thank you for keeping me company in the distance, and for having shared your priceless friendships with me for over 14 years. Albert, thanks for all the chats and for the visits. To all my family, but especially my mother and my sister, you always loved and accepted me exactly as I was, and always made me feel that my dreams were valid; there is nothing in this world that can thank that enough.

Enric, I also have many things to thank you: helping me with my codes, always listening, being happy when things were good and realistic when they were not-so-good... But above all, putting up with me. I don't know how I would have made it without you.

This work was supported by the ERC Grant No. 307986 STRONGINT, and the GSI-TU Darmstadt cooperation, along with the HGS-HIRe school.

# Curriculum vitae

## Personal Data

| | |
|---|---|
| **Name** | Victoria Durant Sanjinés-Uriarte |
| **Date of birth** | 05.03.1988 |
| **Place of birth** | Cusco, Peru |

## Education

| | |
|---|---|
| **2014 – 2018** | Ph.D. in Nuclear Physics, Technische Universität Darmstadt (Darmstadt, Germany)<br>Thesis: *Chiral interactions for nuclear reactions and heavy nuclei.*<br>Supervisor: Prof. Ph.D. Achim Schwenk |
| **2012 – 2013** | Interuniversitary Nuclear Physics M.Sc., Universitat de Barcelona (Barcelona, Spain)<br>Thesis: *Magnetic susceptibility of neutron matter.*<br>Supervisor: Prof. Dr. Artur Polls |
| **2007 – 2012** | Bachlelor in Physics, Universitat de Barcelona (Barcelona, Spain) |
| **2006** | Higher education entrance qualification, IES Puig i Cadafalch (Mataró, Spain) |

# Erklärung zur Dissertation

Hiermit versichere ich, die vorliegende Dissertation ohne Hilfe Dritter nur mit den angegebenen Quellen und Hilfsmitteln angefertigt zu haben. Alle Stellen, die aus Quellen entnommen wurden, sind als solche kenntlich gemacht. Diese Arbeit hat in gleicher oder ähnlicher Form noch keiner Prüfungsbehörde vorgelegen.

Darmstadt, den 12. November 2018

(V. Durant)